



HAL
open science

”On-chip” astronomical instrumentation: bringing polarimetric and spectroscopic capabilities to the detector level

Sophie Bounissou

► **To cite this version:**

Sophie Bounissou. ”On-chip” astronomical instrumentation: bringing polarimetric and spectroscopic capabilities to the detector level. Instrumentation and Methods for Astrophysic [astro-ph.IM]. Université Paris Saclay (COMUE), 2019. English. NNT : 2019SACLS400 . tel-02870363

HAL Id: tel-02870363

<https://theses.hal.science/tel-02870363>

Submitted on 16 Jun 2020

HAL is a multi-disciplinary open access archive for the deposit and dissemination of scientific research documents, whether they are published or not. The documents may come from teaching and research institutions in France or abroad, or from public or private research centers.

L’archive ouverte pluridisciplinaire **HAL**, est destinée au dépôt et à la diffusion de documents scientifiques de niveau recherche, publiés ou non, émanant des établissements d’enseignement et de recherche français ou étrangers, des laboratoires publics ou privés.

“On-chip” astronomical instrumentation : bringing polarimetric and spectroscopic capabilities to the detector level

Thèse de doctorat de l'Université Paris-Saclay
préparée à l'Université Paris-Sud et au CEA

Ecole doctorale n°127 d'Astronomie et d'Astrophysique d'Île de France
Spécialité de doctorat : Astronomie et Astrophysique

Thèse présentée et soutenue à Saclay, le 27 novembre 2019, par

Sophie Bounissou

Composition du Jury :

Alain ABERGEL Professeur, IAS	Président
Etienne LE COARER Chercheur, IPAG	Rapporteur
Alfred KRABBE Professeur, Université de Stuttgart	Rapporteur
Carole TUCKER Professeur, Université de Cardiff	Examineur
Willem JELLEMA Professeur, SRON	Examineur
Louis RODRIGUEZ Chercheur, CEA Saclay (DAp)	Directeur de thèse
Vincent REVERET Chercheur, CEA Saclay (DAp)	Co-encadrant de thèse
Hervé GEOFFRAY Chercheur, CNES	Examineur
Laurent DUSSOPT Chercheur, CEA Grenoble (LETI)	Invité

“On-chip” astronomical instrumentation : bringing polarimetric and spectroscopic capabilities to the detector level

Thèse de doctorat de l'Université Paris-Saclay préparée à l'Université Paris-Sud et au CEA

Ecole doctorale n°127 d'Astronomie et d'Astrophysique d'Île de France
Spécialité de doctorat : Astronomie et Astrophysique

Thèse présentée et soutenue à Saclay, le 27 novembre 2019, par

Sophie Bounissou

Composition du Jury :

Alain ABERGEL, Professeur, IAS	Président
Etienne LE COARER, Chercheur, IPAG	Rapporteur
Alfred KRABBE, Professeur, Université de Stuttgart	Rapporteur
Carole TUCKER, Professeur, Université de Cardiff	Examineur
Willem JELLEMA, Professeur, SRON	Examineur
Louis RODRIGUEZ, Chercheur, CEA Saclay (Dap)	Directeur de thèse
Vincent REVERET, Chercheur, CEA Saclay (Dap)	Co-encadrant de thèse
Hervé GEOFFRAY, Chercheur, CNES	Examineur
Laurent DUSSOPT, Chercheur, CEA Grenoble (LETI)	Invité

Acknowledgements

Après avoir rédigé ma thèse en anglais, je m'autorise un peu plus de liberté en switchant au français qui me semble plus approprié ici.

Voilà! Trois années s'achèvent... et quelles années! Une thèse ça vous change : bien sûr, j'ai énormément appris en sciences, mais j'ai le sentiment d'avoir encore plus grandi sur le plan personnel. Un peu hésitante au début à l'idée d'arriver dans un labo inconnu pour ma thèse, les qualités scientifiques et humaines des personnes au CEA ne m'ont jamais fait regretter ce choix.

Je souhaite tout d'abord remercier les chercheurs qui m'ont fait le privilège d'être dans mon jury de thèse. Merci à Alfred Krabbe et à Etienne Le Coarer qui ont lu mon manuscrit avec beaucoup d'attention. Je salue également la bienveillance et l'intérêt scientifique que m'ont témoignés Carole Tucker et Willem Jellema à la fin de ma thèse et en particulier le jour de ma soutenance. Merci enfin à Alain Abergel qui m'a suivie à l'école doctorale pendant ces trois années et à Hervé Geoffroy du CNES de m'avoir permis de faire ce doctorat au CEA.

Pour réaliser une thèse en R&D dans de bonnes conditions, il faut plusieurs ingrédients. Le tout premier, c'est une idée un peu étrange d'un chercheur qui se dit que ce serait intéressant de creuser dans une direction encore plus ou moins inexplorée.. Merci Vincent R. ! Je me suis éclatée, ce sujet m'a passionnée (et parfois même un peu hantée). Merci de m'avoir fait confiance en me laissant la liberté nécessaire à ma recherche, tout en m'encadrant jusqu'au dernier jour !

Ensuite, la recette d'une thèse implique un directeur de recherche qui vous impressionne par l'étendue de ses connaissances et qui ne compte pas les heures qu'il vous accorde! Merci Louis R. pour tous les échanges que l'on a eus, ils ont vraiment construit ma réflexion et guidé ma recherche. Outre cela, quel bonheur de travailler avec toi ! Tu as raison, c'est essentiel de travailler avec des personnes que l'on apprécie.

Un ingrédient indispensable à cette fameuse recette est un super binôme de labo'. Merci Albrecht P. de m'avoir accompagnée tout au long du chemin. Ton aide, tes conseils et tes anecdotes herscheliennes et filiiennes m'ont été si précieuses. Et puis c'est tellement plus amusant les manip's avec toi ! A quand la prochaine "Ferme à Dédé" par 40°C ?

Pour réaliser une thèse dans de bonnes conditions, il vous faudra aussi un Cyrille D. ! Et oui tout le monde a besoin d'un Cyrille D., qui produit un travail monstrueux et avec une motivation infaillible ... J'ai en mémoire une journée cauchemardesque que l'on avait passée à démonter, remonter, re-démonter, re-remonter, re-re-démonter et encore re-monter un cryostat parce que la colle de la tige qui actionne la

roue cassait à chaque fois à un endroit différent et tu ne désespérais pas... Sache que ta persévérance m'a bluffée ce jour-là! Le DAp a vraiment beaucoup de chance de t'avoir.

Viennent ensuite les collègues du LETI. Merci à Laurent D. qui a suivi et dirigé ma thèse sur le plan technique, je suis très contente et fière que notre collaboration ait pu amener ce projet si loin! Merci à Abdel A. pour sa gentillesse et pour toutes ces discussions qui m'ont appris beaucoup sur la technologie silicium et les simulations. Valérie G., merci pour ta sympathie et tes bons conseils, que ce soit en conf' ou autre! Et enfin, Gilles L., merci pour le temps que tu nous as consacré : ces lonnnnnngues journées en salle blanche ont fini par aboutir à quelque chose, merci mille fois!

Je dois aussi remercier : Obaid A. avec qui j'ai partagé bien des discussions comsoliques, Jean-Luc S. (parce que j'adore tout simplement le personnage! mais aussi...) pour sa bienveillance scientifique, Jérôme M. parce qu'il m'a dessiné de super montures pour mes étalons mais surtout pour sa bonne humeur clairement contagieuse ainsi que Didier D., Samuel R. et Pierre-Antoine F. pour tous leurs conseils d'opticiens! Merci à Sandrine P. même si un projet commun n'a pu aboutir, à Jacques D. pour les discussions sur la spectroscopie et pour son aide sur la polarimétrie et à Suzanne M. et Maud G. pour leur aide à la préparation de ma soutenance. Merci à Vianney L. et Koryo O. pour le suivi qu'ils m'ont consacré pendant ces trois années! Je remercie aussi Olivier L. pour son aide avant soutenance. Merci à Pascale D. pour le soutien qu'elle m'a apporté, même après avoir quitté le CEA!

Pour une thèse qui se déroule dans la bonne ambiance, choisissez également de supers collègues avec qui vous apprécierez partager des moments conviviaux. J'ai nommé : Michel L., Thierry T., Olivier B., Gamil C, Pascal G., Vincent M., Isabelle L., Christian E., Kévin T., Léa B., Mathieu C., Luc D., Patrick M., Eric D., Michel T., Philippe F., Marc S., Ayoub B., Pam-pam B., Paul S., Yannick L., Manu G.,... et good luck à Camille G.! J'adresse un cheers particulier à des collègues qui sont devenus des amis : Diana R., Thibault P., Marin P. et François V. . Merci pour tous ces bons moments passés, je sais qu'il y en aura d'autres! J'ai aussi une pensée pour Jess' (mon ancienne super co-bureau qui est actuellement une super maman) et pour Paula T. et Iacopo B.! Merci aussi à ma Tat' de m'avoir sorti la tête de mon ordi à bien des reprises, t'as été une acolyte parfaite : de running, de spectacles en tout genre, et bien sûr d'apéro!

Je remercie chaleureusement mes famille et belle-famille pour leur soutien. En particulier, merci à mes parents qui m'ont offert la chance de choisir ma voie, en me rappelant souvent de profiter de toutes les expériences de la vie. Mention spéciale à Flo' pour son aide avec la bibliographie, tu m'as filé un vrai coup de pouce!

Last but not least... Baptiste. Il y a approximativement un milliard de raisons pour lesquelles je devrais te remercier! Pour n'en citer qu'une parce qu'elle est particulièrement représentative de ta gentillesse à mon égard : merci de t'être enfilé huit épisodes d'une série la dernière nuit de ma rédaction, juste pour rester avec moi! Tu rends ma vie tellement plus simple, et aussi terriblement plus belle.

Contents

Introduction

1	Advancement of astronomical research due to progress in instrumentation and analytical methods	5
1.1	Introduction of instrumentation for astronomy	6
1.2	Scientific opportunities for future polarimetric and spectroscopic imaging instruments . . .	10
1.2.1	The effects of magnetic fields in the process of star formation	10
1.2.2	The [CII] cooling line as tracer of the ISM	14
1.2.3	The B modes : the new frontier of Cosmic Microwave Background science	18
1.3	Potential for simplification of future instruments	22
2	Bolometers for far-infrared/ (sub)-millimeter observations	25
2.1	Bolometers : more than 100 years of research	27
2.1.1	The invention of the first bolometer	27
2.1.2	General description of bolometers	28
2.1.3	Evolution of the bolometer technology	35
2.1.4	Other detectors in the sub-millimeter field	37
2.2	Bolometers at CEA	40
2.2.1	The PACS bolometers	40
2.2.2	From PACS bolometers to B-BOP bolometers	46
2.2.3	Perspectives	49
3	Optimization of the spectral absorption of polarimetric bolometers for SPICA/B-BOP instrument	51
3.1	Introduction to linear polarization	52
3.1.1	Definition of Stokes parameters	52
3.1.2	Classical measurements of any polarized state	55
3.2	A first step towards on-chip polarimetry	56

3.3	The SPICA/B-BOP polarimetric imager instrument	61
3.3.1	The SPICA mission : scientific objectives and instruments	61
3.3.2	B-BOP : a polarimetric imager	62
3.4	Optimizing the design of the detectors in the three channels of the B-BOP instrument . . .	64
3.4.1	Optimizing the physical parameters of the detectors	65
3.4.2	Minimizing the cross-polarization	66
3.4.3	Adapting the 200 μm - and the 350 μm -channels from the 100 μm - detectors	68
3.5	Perspectives	69
3.5.1	New design of the focal plane	69
3.5.2	Deriving the Stokes parameters from the detectors signal	70
4	Development of a compact spectroscopic imager	75
4.1	State of the art of spectroscopy for far-infrared/sub-millimeter astronomy and new develop- ments towards compact spectrometers	77
4.1.1	Spectrometers for far-infrared/sub-millimeter instruments	77
4.1.2	Towards compact spectro-imaging instruments	86
4.2	Compact spectroscopic imager using Fabry-Perot Interferometer (FPI)	92
4.2.1	Adding the spectral selectivity to the detector	92
4.2.2	Conventional Fabry-Perot Interferometry in the sub-millimeter range	97
4.2.3	Optimizing the spectral finesse of the FPI	101
4.2.4	Coupling the FPI with the detector	111
4.2.5	Conclusions of the chapter	125
5	Experimental validation of the spectroscopic capability of compact Fabry-Perot Inter- ferometers based on dielectric mirrors for combination with bolometer arrays	127
5.1	Building mirrors with dielectric materials for compact FPIs	128
5.1.1	Building the dielectric mirrors in collaboration with LETI	128
5.1.2	Validation of the quality of dielectric layers for mirrors	130
5.1.3	Assembling the mirrors	135
5.1.4	Validation of the theoretical model by Time Domain Spectrometer (TDS) measure- ments at ambient temperature	140
5.2	Validation of the performance of Fabry-Perot etalons based on dielectric mirrors	140
5.2.1	Description of the cryogenic optical train	140
5.2.2	Measuring the finesse of multi-layer silicon etalons	145
5.2.3	Measuring the transmission of multi-layer silicon etalons	154
5.3	A first step towards the coupling of the spectrometer to the bolometer	158

5.4	Conclusions of the chapter and perspectives for the future experiments	162
Conclusion		163
A	Derivation of the Airy formula for Fabry Perot interferometry	169
B	Solution based on micro-structured silicon	173
C	CMB bands defined by the LiteBIRD mission	177
D	Calculation of the spectral and spatial effects of a Fabry Perot located in the focus of a beam for different nominal finesses.	179
E	Upgrade of the FTS Optical Train	181
E.1	Configuration of the system before the upgrade	181
E.2	Upgrade of the optics design	182
E.3	Implementation of the FTS optics upgrade	184
Bibliography		189

Introduction

Up to the recent detection of gravitational waves, light was the main messenger from the Universe. It has brought us an incredible amount of information about celestial objects that are, for now, unreachable. With the discovery that the electromagnetic spectrum is not restricted to the visible light, instrumentation has continuously evolved to help astronomers observing the full spectrum. While the X-rays highlight the violent and energetic reactions related to ionization, the infrared and radio-waves trace the cold Universe (for low redshift). With light as the only probe, one can get the global picture of phenomena like physical processes and chemical composition in a specific region of the sky. Building telescopes sensitive to any wavelength (if possible), in the highest and driest places on Earth was therefore necessary to collect the maximum amount of photons which can travel through the atmosphere. To observe wavelengths that are absorbed by the atmosphere, telescopes fly onboard balloon, aircraft or spacecraft. Every small structure in the sky is investigated by increasing the size of the telescope mirrors and when one single dish cannot meet the spatial resolution required by science, several telescopes are used to artificially create one dish the size of the maximal distance between telescopes. In addition of observing smaller details, it is also possible to observe further in distance : astronomers are, indeed, able to travel in time and even more, to get back to the first light of the history of the Universe.

When travelling towards the Earth, light brings a large number of precious data. The function of an instrument is to grab the fraction of information relevant for astronomical purposes. In particular, besides the different wavelength range, it may be useful to observe the intensity of a source as a function of time, to study one or several specific lines of the spectrum (spectroscopy) or to probe the preferential direction of the electric field of the wave (polarimetry). The two latter aspects are the ones which we are particularly interested in in this thesis. As always, science drives the evolution of instrumentation (the reverse is also true) and it turns out that the requirements are becoming more and more challenging. Indeed, the current need is to have several light analyzing functionalities within the same instrument. This is, for instance, related to the need for mapping the polarization of light or fine-structure lines in star-forming regions. There are even some scientific targets where polarimetry, (low-resolution) spectroscopy, and imaging are required, and preferably in one homogeneous observation. Here, we are, in particular, interested in having

the polarimetric and the spectroscopic capabilities (in a first attempt, independently) brought to the level of the detection array. The idea of having several instrumental functionalities in a very compact form, has become possible only because of the progress in micro-technologies. In our developments, we are benefiting from the expertise of CEA/LETI in the silicon microelectronics field. This fruitful collaboration has resulted in the bolometers for the HERSCHEL/PACS photometer at the beginning of this century and will make achievable the challenging polarimetric detectors for the SPICA/B-BOP instrument. The concept of extending the instrumental capabilities by adding more functionalities within the bolometer array aims at paving the way to detectors which could become the whole instrument. Assuming that multi-function detectors could reach the same performance as current instruments (related to science requirements), one would gain a lot in terms of simplicity, mass and volume budgets, cryogenics autonomy, ...

This thesis studies the possibility to implement the light analysis functions, namely polarimetry and spectroscopy, at the level of the bolometer array. At the beginning of this thesis, the original idea behind the polarimetric pixels had already demonstrated its working principle. The work presented here consists in the optimization of the design and in the characterization of certain performance parameters of the polarimetric pixel. Concerning “on-chip” spectroscopy, I had the chance to select the object of my research since this domain had been sparsely studied in our team. The objective was to develop a concept which will introduce the spectroscopic capability within the pixel array and to experimentally validate this concept with the manufacture of a prototype. In this thesis, the absorption of the detector has been a key notion since the absorber plays the role of the transducer of the electromagnetic radiation. This is the reason why bringing the light analysis functionalities to the pixel array had been only possible by modifying either the design of the absorber or of the interferometric system the absorber is embedded in. Thus, the absorption of the detector has been the figure of merit throughout this work.

This thesis starts from the astrophysical motivation to the experimental work including the development of the theoretical concept.

Chapter 1 introduces some astrophysical and cosmological open questions that formulate the need for combining several instrumental functions, namely polarimetric and spectroscopic imaging, within one instrument.

The bolometer technology is described in chapter 2, from its invention in 1881 to the key milestones of bolometer evolution and the development of other detectors in the sub-millimeter field. This chapter lays the foundation for the next chapters, by also introducing the absorption process within the CEA bolometers. It also describes the reasoning which has led to pixels intrinsically sensitive to polarization.

Chapter 3, as a continuation of chapter 2, describes how the scientific questions arisen after HERSCHEL and PLANCK results, has driven the concept of the B-BOP instrument for the new SPICA mission. In

this chapter, I depict in detail the detector design and present my model and its results. The last part is dedicated to the new design of the pixels achieved by the B-BOP detector team.

Chapters 4 and 5 deal with the introduction of spectroscopy within the detector array. Chapter 4 is focused on the theoretical development of the spectro-imaging detector. From a review of compact spectrometers, I picked one solution which seems to be the easiest to implement with an array while meeting high-spectroscopy performance : the Fabry-Perot interferometer (FPI). We then decided to introduce multi-layer silicon mirrors to improve the efficiency of the current state-of-the-art FPIs. The efficiency and the limitations of the spectro-imaging system are also estimated in this chapter.

In chapter 5, I outline the different steps that make possible the experimental validation of the multi-layer silicon FPI. First, I present the characterization and the assembling of these layers. The experimental cryogenic set-up is then depicted and lastly, results of the measurements and their analysis are shown.

Note that in the rest of this thesis, I will no longer use the pronoun ‘I’, since this work, and especially because it deals with experiments, has benefited from the contribution of several researchers and engineers.

Chapter 1

Advancement of astronomical research due to progress in instrumentation and analytical methods

Contents

1.1	Introduction of instrumentation for astronomy	6
1.2	Scientific opportunities for future polarimetric and spectroscopic imaging instruments	10
1.2.1	The effects of magnetic fields in the process of star formation	10
1.2.2	The [CII] cooling line as tracer of the ISM	14
1.2.3	The B modes : the new frontier of Cosmic Microwave Background science	18
1.3	Potential for simplification of future instruments	22

This chapter is focused on the evolution of astronomical opportunities with progress in instrumentation and methods. It aims at introducing three science topics that instrumentation presented in this thesis could address. In the first part, we point out some milestones that have contributed to breakthroughs in the way astronomers make observations. This historical review is clearly non-exhaustive and is oriented towards what will be presented in this thesis. The second part of this chapter is dedicated to the three specific science cases that remain unsolved and for which innovative instrumentation for spectroscopy and polarization experiments could achieve progress. The very end introduces the next chapters which deal more with instrumentation.

1.1 Introduction of instrumentation for astronomy

Astronomy occurs to be the oldest science since it was the first application of mathematics to an empirical phenomenon, the motion of heavens. Because what happens in the sky was considered as the manifestation of gods on Earth, it also impacted the human's life in practice. In particular calendars have been established thanks to the position of stars and planets ("wanderer" in Greek : at the time this included the Moon and the Sun) within the year. Calendars have organized the civil life and agriculture, by informing farmers about the seasons, for the start of planting, for example. The need for these calendars has justified the invention of rudimentary tools (e.g. sundials) to very complex ones (e.g. astrolabes). Astronomy was also a powerful tool for navigation. The Sun and the stars were indeed good orientation points during long ship journey. Techniques and also instruments (especially on-board reliable chronometers) were developed. Nowadays, stars and planets are no longer used for time measurements and navigation ; astronomy has become exclusively a pure science, justified by the humans wish to understand their place within the Universe.

The evolution of astronomy together with the progress in the field of instrumentation has to be extended to that of physics. This is the reason why this part, which deals with the milestones of instruments for astronomy is interspersed with key historical events in physics and optics. The first breakthrough which marks the start of modern astronomical instrumentation corresponds to the invention of the refractive telescope in 1609. Although there is some doubt about the identity of the actual inventor of this new kind of instrument, Galileo was one of the first to use such an instrument for observations of the heavens while anything so far had been achieved with the bare eye. Refractive telescopes have been progressively improved over the years, but this kind of telescope presents a limitation due to the use of lenses. Indeed, lenses introduce optical aberrations in addition to the mechanical limitations of having large lenses in a telescope. Nevertheless, a solution was proposed to solve the aberration issues by increasing the focal length and by introducing mirrors to fold the induced long focus. The reflective telescope, proposed by Newton, in 1688, for astronomical purpose, overcame all the issues introduced by refractive telescopes. Shortly after (1666), Newton with his famous prism experiment, revolutionized the physics field by understanding that

white light is composed of a set of rainbow colors. Herschel went further, more than one century after (1800), still with a prism that disperses the Sun light. When he used mercury-glass thermometers to measure the radiation of several wavelengths, he noticed that, next to the outermost radiation of the visible spectrum, heat was still produced by an invisible radiation : he discovered the infrared radiation. The illustration of the Herschel experiment is shown in figure 1.1. Later, the ultraviolet (Ritter), radio waves (Hertz), X-rays (Rontgen) and gamma-rays (Villard) were discovered.

In the meantime, the understanding of the nature of light drastically evolved. In the second half of the

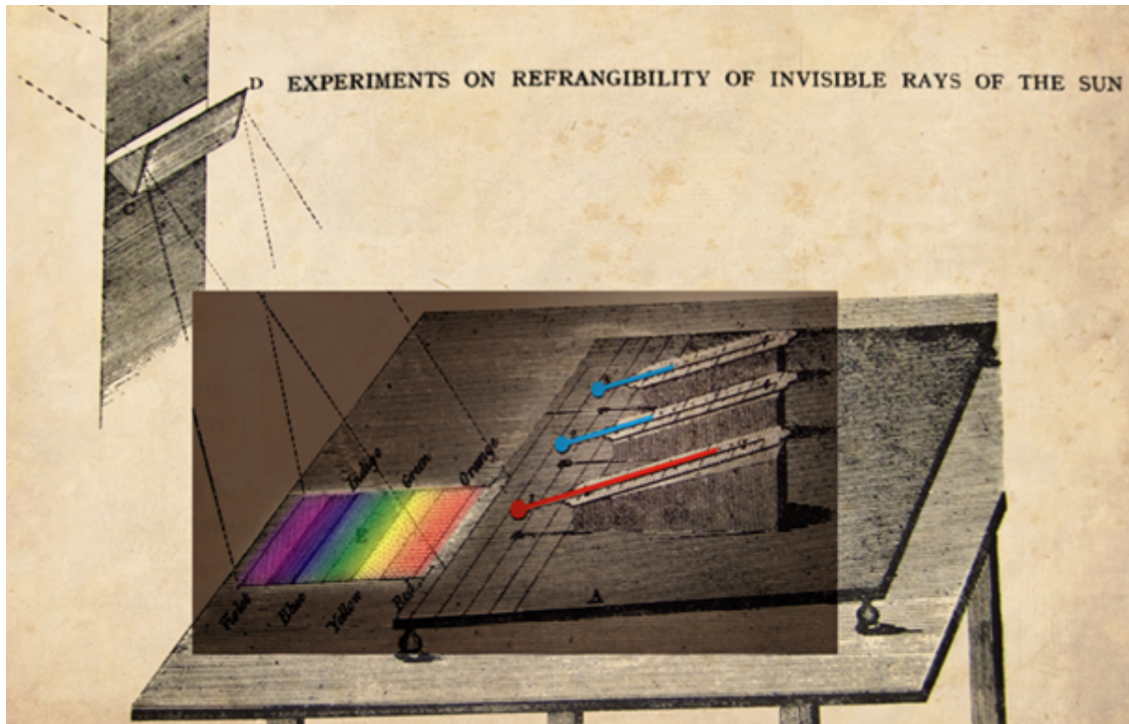


FIGURE 1.1: The Herschel experiment : Sun light is dispersed by a prism and thermometers are in charge of measuring the heat produced by each rainbow color (illustration by Vilmos Thernesz based on the original figure in Herschel (1800)).

19th century, Maxwell understood the relationship between the electric and the magnetic fields, how they influence each other to create and propagate an electromagnetic wave. He developed four equations that unify the physics of electricity and magnetism and the properties of materials. From these equations, he also derived the result that the electromagnetic wave travels at the exact speed of light (first calculated by Romer, in 1676) and concluded that the light was an electromagnetic wave. In astronomy, the dispersion of light by optical elements such as gratings enabled Fraunhofer to measure the spectrum, i.e. the power distribution as a function of wavelength, including the dark lines, of the Sun in 1835. Spectroscopy was invented and appears quickly as a new way to investigate the sky, different from photography. Indeed, it is a powerful tool to learn more about the nature or the evolution of distant astronomical objects, simply by probing their composition. Lines, whether they are emitted or absorbed by the gas, correspond

to unique chemical elements and molecules. Spectroscopy is also the means to observe their distance through cosmological redshift, and their intrinsic motion, by measuring the Doppler effect. The study of the black-body radiation was the next breakthrough in physics which has found applications in astronomy. A black-body has a characteristic spectrum which only depends on its temperature. With Wien's empirical law, the temperature of a black-body can be derived from its maximal emission wavelength through Wien's law :

$$\lambda_{max} \times T = b \quad (1.1)$$

where $b \approx 2898 \mu\text{m.K}$ is Wien's displacement constant. Any body is not necessarily a black-body, but it happens that most astronomical objects can be approximated as a black-body or by a gray-body (i.e. a black body with a lower emissivity). A table of the corresponding frequency, wavelength, energy and temperature for the whole radiation spectrum is presented in figure 1.2. It shows, in particular, that short wavelengths are related to highly energetic events while it is the opposite for longer wavelengths. Then X- and γ -rays are related to the hottest ionized regions while the radio emission traces the cold Universe (assuming no redshift).

The 19th century has seen the start of the production of silver-on-glass mirrors for reflector telescopes. Since

	Frequency f	Wavelength λ	Energy E	Temperature T
Radio	< 300 MHz	> 1 m	< 1 μeV	3 mK
μ-wave	≈ 3 GHz	≈ 10 cm	$\approx 10 \mu\text{eV}$	30 mK
mm	300 GHz	≈ 1 mm	≈ 1 meV	3 K
Far IR – sub-mm	300 GHz – 6 THz	50 μm – 1 mm	1 meV – 20 meV	3 K - 60 K
IR	≈ 300 THz	$\approx 1 \mu\text{m}$	≈ 1 eV	3,000 K
Visible	≈ 500 THz	≈ 600 nm	≈ 2 eV	5,000 K
UV	1 PHz	300 nm	≈ 4 eV	10,000 K
X	≈ 300 PHz	≈ 1 nm	≈ 1 keV	3 MK
γ	> 30 EHz	< 10 pm	> 100 keV	> 300 MK

FIGURE 1.2: Relationship between frequency f , wavelength λ , energy E and temperature T . The wavelength range which this thesis is focused on, has a white background.

then, the size of the mirrors has been increasing and this is still relevant today : the future E-ELT primary mirror will be 39-m in diameter. Nowadays the whole spectrum is exploited since it has been understood that different parts of the spectrum provide various complementary information. For regions of the spectrum which are not accessible from the ground, telescopes are sent onboard balloons, airplanes or spacecrafts. For example, X-rays are completely inaccessible from the ground while the terrestrial atmosphere is perfectly

transparent to radio waves. For far-infrared/sub-millimeter wavelengths (the range we are interested in in this thesis), some windows exist from the ground but require telescopes in the driest and highest places on Earth. The opacity of the atmosphere as a function of wavelength is illustrated in figure 1.3.

Depending on the astrophysical target, photometry, spectroscopy or polarimetry can be performed. Time-

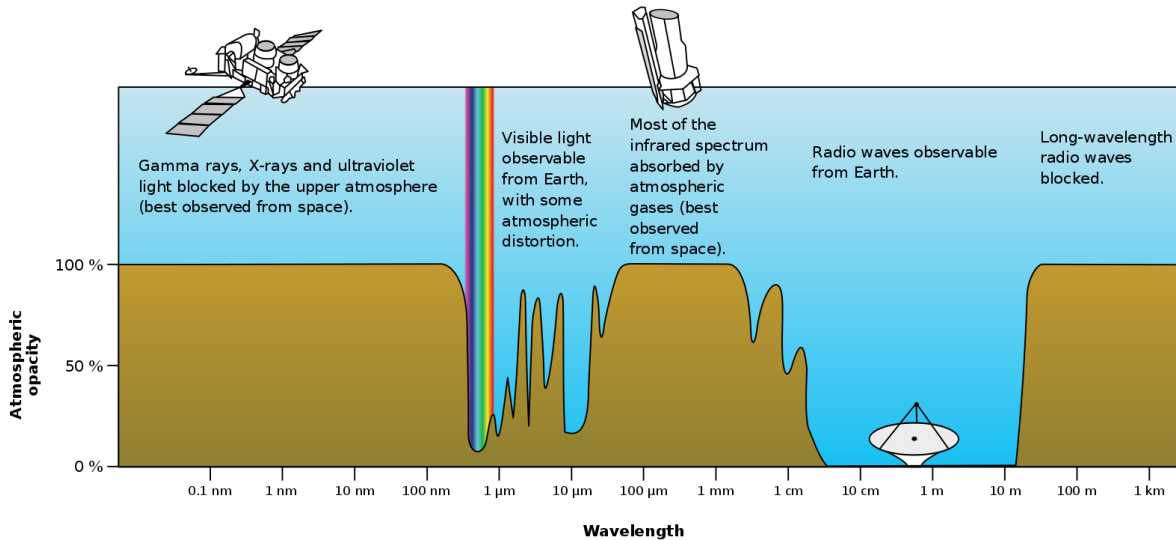


FIGURE 1.3: Atmospheric opacity as a function of the wavelength. Credit NASA

dependent photometry has even made possible the tracking of the supernova evolution by measuring their light curves. Moreover, while instrumentation progress has increased the quantity of collected data, the introduction of new computational methods, such as Fourier Transform theory and the improvement of computing resources have enabled astronomers to process a large amount of data. Another example is the recent use of several radio-telescopes across the world to create one single virtual larger telescope, the Event Horizon Telescope (The Event Horizon Telescope Collaboration, 2019). Very long baseline interferometry drastically improves the resolving power of individual antennae, so much that the equivalent resolving power of the network is comparable to the one of a telescope with a diameter approximating the size of the Earth.

Up to the recent detection of gravitational waves, light has been the main messenger from the Universe. This thesis is focused on the far-infrared/sub-millimeter range, which can trace several kinds of astrophysical sources. A few of them are presented in the next section. Note that the words “far-infrared” and “sub-millimeter” refer to the wavelength range $50 \mu\text{m} - 1 \text{mm}$. Kimmitt (1970) differentiates these words as follows : “the use of ‘far-infrared’ or ‘sub-millimeter’ depends on whether the method is derived from optical or microwave wavelengths”. However, in this thesis, techniques from both optical (especially in spectroscopy) and radio (in polarization) fields are applied to CEA bolometers, thus we use both terms indiscriminately.

1.2 Scientific opportunities for future polarimetric and spectroscopic imaging instruments

In this part, we aim at reporting some of the scientific applications that would require the combination of different instrumental capabilities within one single instrument. Since the detectors that we use are dedicated to sub-millimeter astronomy, we will first focus on astrophysical applications linked to the cold Universe. The two following subsections are motivated by questions about the processes involved in star formation within the Interstellar Medium (ISM). We first describe the requirement of using a polarimetric imager to probe the magnetic field within the filaments in dense molecular clouds where stars may form. The second subsection develops the idea that astronomers would need maps of reliable tracers (as the [CII] cooling line) for a better understanding of the evolution of the gas and dust in the ISM. The last subsection slightly differs from the first ones because we shift our discussion to longer wavelengths to discuss cosmology and more precisely, polarization of the CMB that may require the collection of all the light information (photometry, low-resolution spectroscopy and polarimetry) within one instrument.

1.2.1 The effects of magnetic fields in the process of star formation

“What drives the star-formation process?” is still an open question in astrophysics. The HERSCHEL Space Observatory (Pilbratt et al., 2010), launched in 2009, has delivered valuable data which have contributed to enhance significantly our understanding of the evolution of the ISM and of star formation. One of the main goals of the instruments onboard the far-infrared/sub-millimeter observatory was to map the structure of the gas in molecular clouds. Although large scale filamentary structures were known to exist in some interstellar clouds for a long time (Schneider and Elmegreen, 1979), the systematic nature of the pattern was not expected. HERSCHEL has demonstrated the ubiquitousness of these filamentary structures in the ISM : interstellar clouds exhibit filaments on all scales as shown in figure 1.4 (André et al., 2013). These filaments play a key role in the star formation process : they could be the seeds of prestellar cores and ultimately of protostars, after the fragmentation of gas which leads to the formation of dense cores through gravity.

Other important results in this field have been derived from observations with HERSCHEL : for example, Arzoumanian et al. (2011) and Arzoumanian et al. (2018) found out that the filaments are characterized by a specific width of 0.10 ± 0.06 pc. Thus the ISM, which looks chaotic at first glance, is actually well structured and constrained. The main process which drives the physics within the network of filaments in the ISM is still not well understood and requires deeper examinations. Gravity and supersonic turbulence are strongly involved in the process but the magnetic field may be the missing part of the puzzle (Crutcher, 2012). Indeed results from the PLANCK mission have pointed out that magnetic field is very

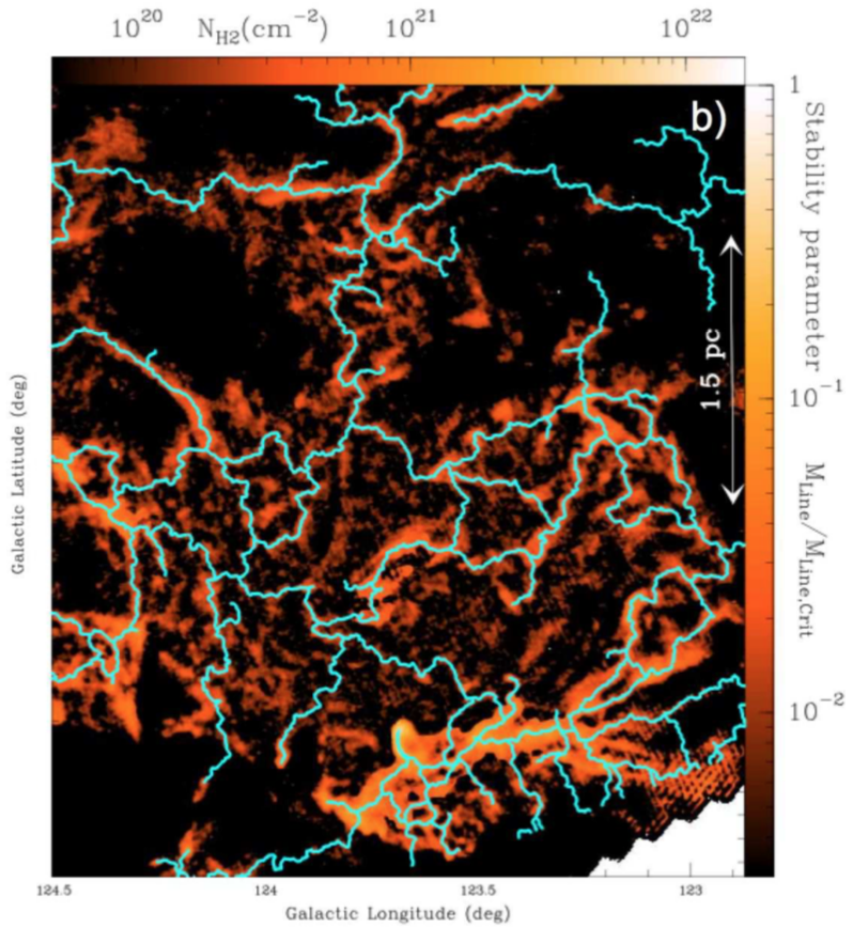


FIGURE 1.4: Column density map of a portion of the Polaris flare translucent cloud, derived from HERSCHEL data where contrast of filaments has been enhanced : the backbone of the filament network is highlighted in blue (André et al., 2013).

well organized : the field tends to be perpendicular to the high-density filaments but looks aligned with the low-density filaments (see figure 1.5). This observation may suggest that the magnetic field shapes the whole filamentary pattern by enhancing the accretion of matter in low-density filaments along field lines (André et al., 2019). Studying the morphology of the magnetic field inside denser filaments may also help to understand why the width is maintained constant whatever the filaments are.

Polarimetry is an indirect tool to observe the effects of magnetic field on the interstellar medium and in fact, the light polarization measured in the Universe can have different physical origins (Hildebrand, 1988; Tielens, 2005). While the effects of irregularly shaped dust grains on starlight were already known through the phenomena of extinction and reddening, Hall (1949) and Hiltner (1949) have first observed another effect : the polarization of starlight by these grains. Indeed the magnetic field tends to align the elongated grains perpendicular to the field lines since the spin axis of grains is the shortest one. As a

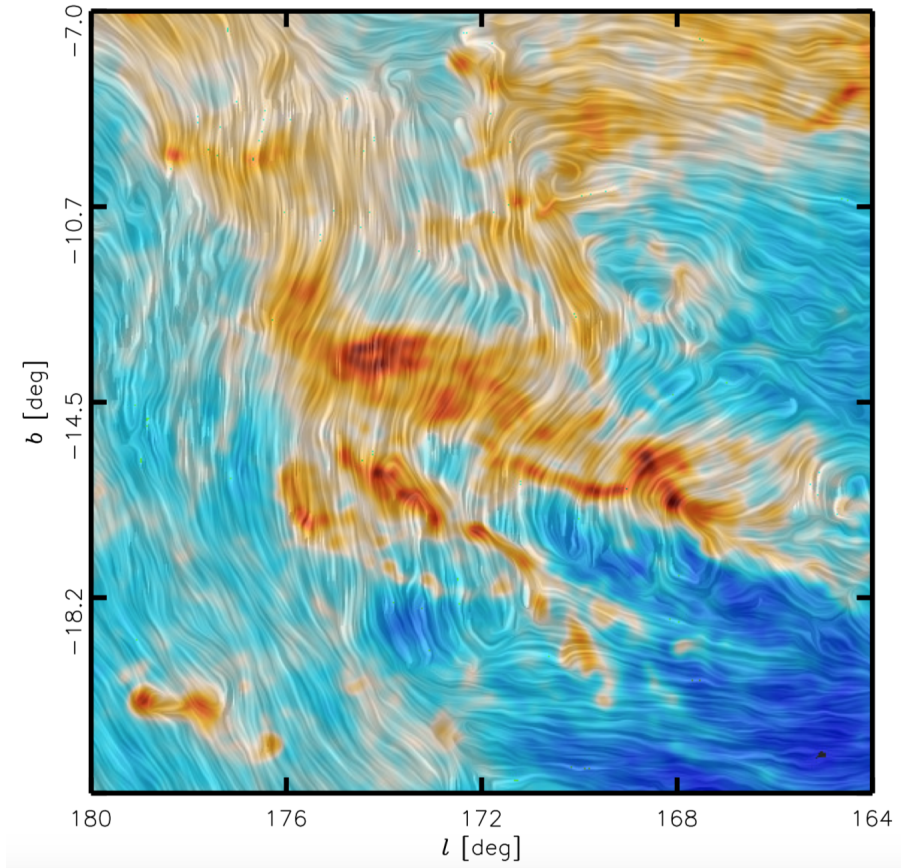


FIGURE 1.5: Column density (colors) from Planck data toward the Taurus molecular cloud. The ‘drapery’ pattern traces the magnetic field, orthogonal to to the thermal polarization (Planck Collaboration, 2016).

consequence grains absorb the unpolarized light of stars preferably in the direction of their alignment, leading to polarization of light parallel to the magnetic field in the UV/visible wavelength range. The induced polarization is often called “dichroic extinction” since it refers to selective attenuation of light in the direction of the alignment of grains (Wood, 1997). Measuring the polarization of light coming from one region of the sky gives access to the orientation of the magnetic field in this region. Another way to probe the magnetic field is to observe the polarization of the thermal emission of the dust grains themselves after they have absorbed the visible and UV radiations. This polarization also finds its origin in the fact that the spin axis of grains is aligned with the field lines. Hence grains will preferably re-radiate energy in the direction of their long axis, which is perpendicular to the field. Since the temperature of the molecular cloud is about a few tens of Kelvins, the emitted radiation lies in the far-infrared wavelength range. Figure 1.6 illustrates the polarizations by dichroic extinction and by thermal emission which are in fact orthogonal and which can be measured in different wavelength ranges. Because both polarizations originate from the alignment of the grains, they strongly depend on the nature of these grains (i.e. composition, size and shape).

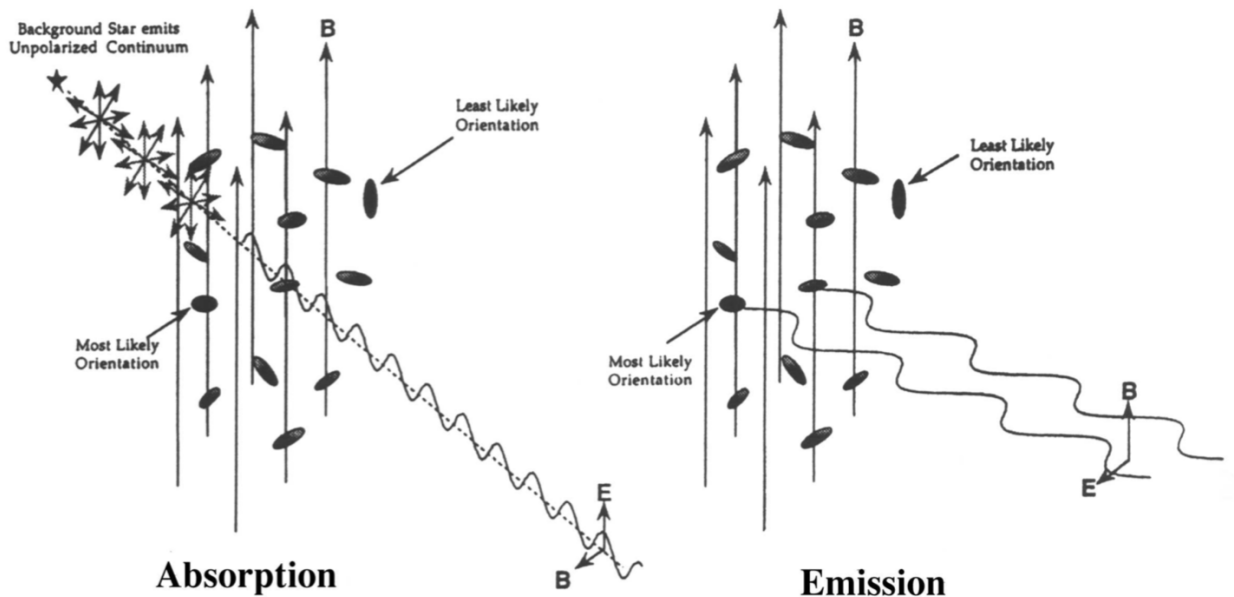


FIGURE 1.6: Polarization of starlight by dust grains, extracted from Weintraub et al. (2000).

Future imaging polarimetry in the submillimeter field aims at examining the thermal polarized emission of dust in order to understand the role of magnetic fields in the evolution of filaments. SPICA (Roelfsema et al., 2018), the European/Japanese telescope scheduled to be launched in 2032, will have an instrument B-BOP dedicated to this purpose for example (see André et al. (2019) for an overview of the main science drivers). B-BOP is an imaging polarimeter that can reach high sensitivity due to the cooling of the primary mirror to 8 K and of the detectors down to 50 mK : the Noise Equivalent Power (NEP) of the detectors is $\sim 1 \text{ aW/Hz}^{1/2}$ (Rodríguez et al., 2018; Adami et al., 2018). This advantage will allow B-BOP to achieve the same signal to noise in polarized maps (a few percent up to 20% of polarization is expected in some interstellar regions) as the PACS photometer (Poglitsch et al., 2003b) of HERSCHEL for total power intensity maps. The main innovation of the B-BOP detectors, compared to the PACS photometer bolometers, is that they are intrinsically sensitive to polarization. They are comprehensively described in chapter 3. These detectors allow a very compact instrument design by integrating one of the optical functions directly into the device. The high spatial resolution with the SPICA telescope is also a strong argument in favor of the imaging polarimeter : significantly better than PLANCK spatial resolution (20-30 times higher due to a slightly larger primary mirror and a different sampling, although they cannot be compared directly because they do not work at the same wavelength (a factor ~ 8 in wavelength)), B-BOP will be able to resolve the magnetic field inside dense filaments. This capability will enable astronomers to trace the morphology of the field, especially within dense filamentary structures where astronomers suspect that the field could change from perpendicular in the outer part to parallel in the inner part of the filaments. Instruments as SPICA/B-BOP, with better performance than previous instruments, will certainly push forward the

boundaries of our current knowledge of the evolutionary stages of filaments and of the formation of dense cores.

1.2.2 The [CII] cooling line as tracer of the ISM

The interstellar medium, that fills the space between stars, is the source of 25% of the visible light coming from a galaxy (Tielens, 2005). It is made of gas and dust (99% of the mass of the ISM is assigned to the gas (Ward-Thompson and Whitworth, 2011)). It is one of the key players that regulates the star formation of a galaxy. Indeed, the star formation rate of a galaxy is directly linked to the gas density through the Schmidt-Kennicutt law (Schmidt, 1959; R.C. Kennicutt, 1998). Understanding this complex medium will help to know more about the stars that are already formed but also to understand how the future stars will form. The “metallic” (see below) ISM originates directly from stars because it results from stellar winds, radiative emission or even supernovae (explosion of massive stars when they die or of white dwarfs); and the future stars will feed and emerge from this rich environment. After the Big Bang, the Universe was made of hydrogen and helium but it has evolved towards increasing complexity with the birth and death of stars which have introduced “metals” (atoms heavier than hydrogen and helium). The metallicity Z defines how metal-rich a galaxy is and precisely corresponds to the mass fraction of metals (as C, O, N, Fe . . .). Similarly, we can define X and Y as the mass fraction of hydrogen and helium respectively. These definitions lead obviously to the equation $X + Y + Z = 1$ everywhere in the galaxy, although the metallicity is not necessarily constant over the full scale of the galaxy. Moreover metals in a galaxy become more abundant through the lifecycles of stars : stars produce heavy elements up to iron during their lives through the stellar nucleosynthesis and they expel these elements to the ISM through stellar winds or at the end of their lives when they explode, leading to an enrichment of the ISM. Observations provide insight into the cycling of matter between stars and ISM. This study requires data over the full electromagnetic spectrum to disentangle the different contributors to the radiation. For example the visible observations highlight the stars but dust tends to absorb the stellar radiation and to re-radiate light in the infrared (illustrated in figure 1.7). These processes lead to dark zones in the visible and to a bright continuum in the infrared. Hence the observations of a galaxy at different wavelengths depict different physico-chemical mechanisms.

Although the ISM generally takes the form of a diffuse warm gas, it also exists as dense and cold molecular clouds in other places, which builds a perfect stellar nursery. The gas and dust of the ISM are heated by stellar photons, X rays or cosmic rays through photo-ionization and photo-electric effects. As a consequence, the ISM becomes stratified depending on the optical penetration depth of the radiation field

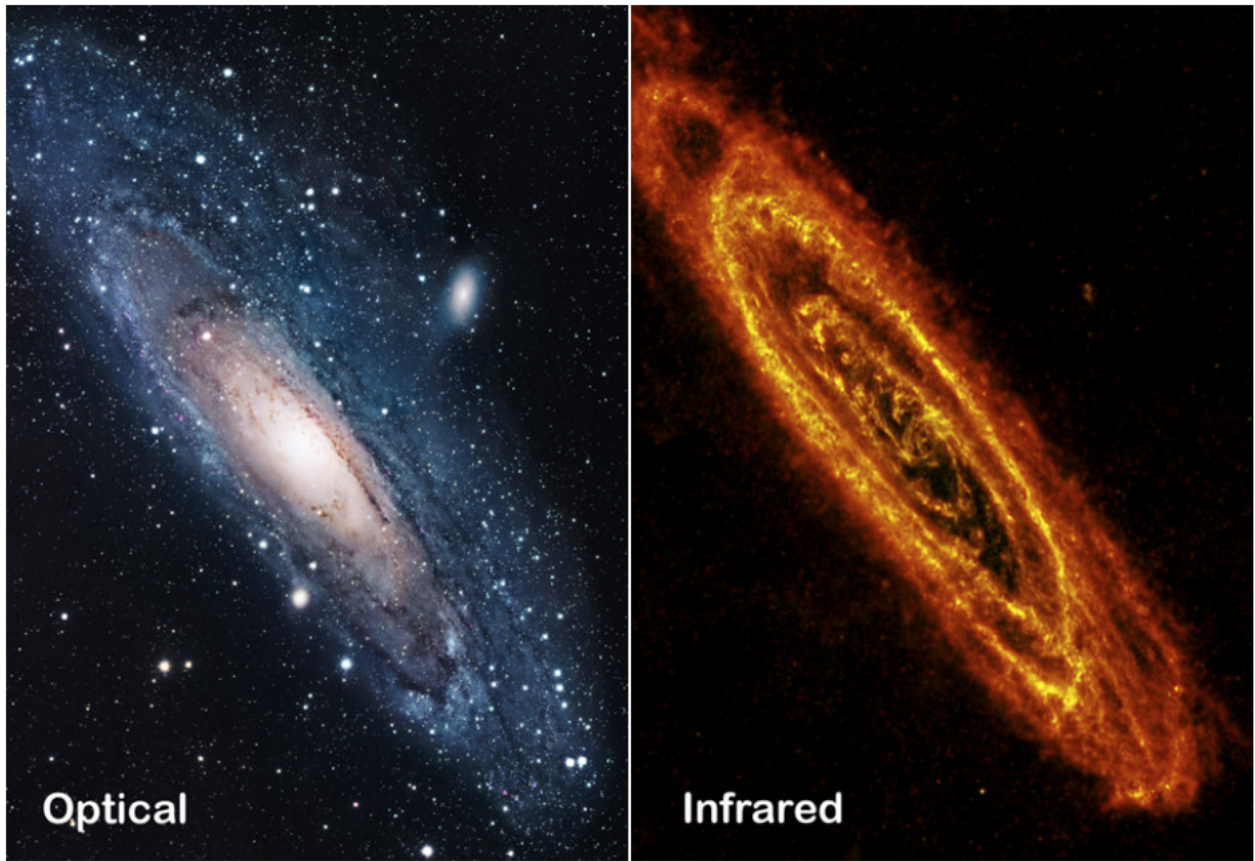


FIGURE 1.7: Andromeda Galaxy (M31) in visible (Image credit : Robert Gendler) and infrared, at $250\ \mu\text{m}$ (ESA/Herschel/SPIRE) : the visible range picture highlights the bright stars of the galaxy while the infrared range one shows the thermal radiation of cold dust due to absorption of the stellar radiation by dust grains.

through the cloud. Astronomers have chosen to describe this morphology as a function of the state of hydrogen : ionized, neutral atomic or molecular. The sketch in figure 1.8 illustrates this three-layers stratification.

The ionized phase corresponds to the environment surrounding stars where the UV radiation from the stars ionizes the hydrogen atoms. In these so-called HII regions, a UV photon with energy greater than $13.6\ \text{eV}$ hits an atom of hydrogen thus removing the electron which will collide and excite other electrons. In this phase the hydrogen species is mostly represented by H^+ , the temperature can exceed $10\ 000\ \text{K}$ and densities can vary from $1\ \text{cm}^{-3}$ in the diffuse regions to $10^5\ \text{cm}^{-3}$ in the most compact regions (Chevance, 2016).

In the atomic phase, the hydrogen molecules have been dissociated (or not been yet formed) and the photons with energy greater than $13.6\ \text{eV}$ have all been absorbed in the previous layer, thus the hydrogen atom can no longer be ionized : the neutral atomic form of hydrogen dominates, the area is called HI region. Nevertheless, the photo-ionization of atoms for which the ionization energy is less than $13.6\ \text{eV}$ can still happen in this region : the atomic phase consists of atoms (H, O, C) and ions (C^+ , Si^+ , S^+). The dominant

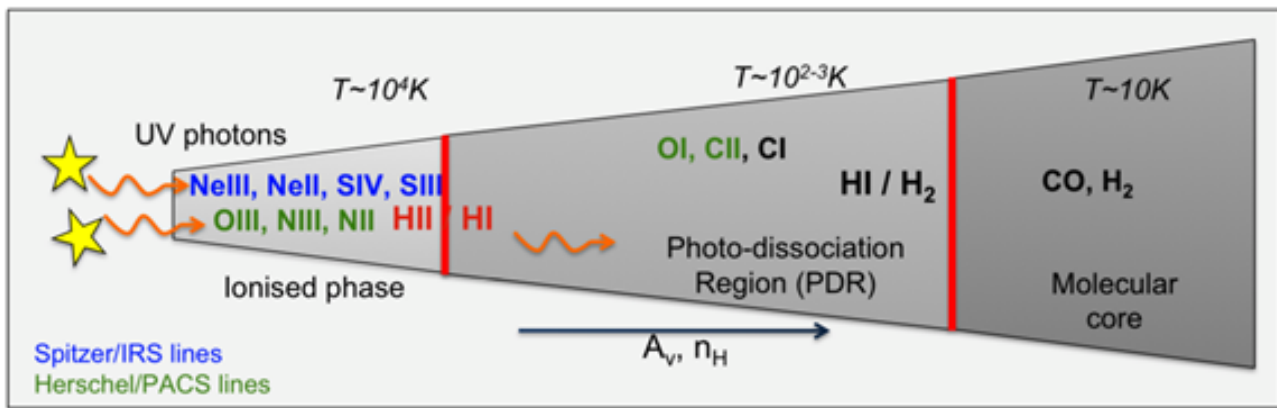


FIGURE 1.8: Sketch of the three structured phases of the ISM : HII region (ionized), Photodissociation region (atomic) and molecular region. UV photons from stars travel the ISM and heat the gas and dust, the optical depth is different for photons depending on their energy. Cooling lines that can be used as tracers for each layer are indicated (Cormier, 2012).

heating in this medium comes from the photo-electric effect by UV radiation on dust grains : a photon will eject an electron from the grain which will excite neutral atoms and other electrons of the gas, leading to an increase of the temperature of the gas. Thus the ISM varies from 100 K in the cold neutral medium (CNM) to 8000 K in the warm neutral medium (WNM) and the density is about 50 cm^{-3} in the CNM while it can fall to 0.5 cm^{-3} in the WNM (Tielens, 2005). The transition region between the ionized region and a molecular core, where star formation may happen, is called the Photodissociation Region or Photo-dominated region (PDR). In this region, atoms such as carbon can still be ionized by far-UV radiation (carbon ionization potential : 11.26 eV) and the molecules are photo-dissociated by the incident photons ; it is the neutral atomic region surrounding molecular clouds (Hollenbach (1990) for more information).

In this stratified model, the molecular phase is the deepest phase into the cloud and it may be the birth-place of stars : stars emerge from the gravitational collapse of these dense and cold molecular clouds. H₂ is the dominant form of hydrogen in this region. Molecules of gas are more easily formed on the surface of dust grains, which act as a catalyst, and then evaporated. The low temperature in this phase increases the efficiency of molecule formation. Although H₂ is the most abundant molecule, other molecules are present such as CO, CS, HCN, O₂ or H₂O (Chevance, 2016). H₂ is protected from UV radiations by its self-shielding while the other molecules mostly rely on the dust to protect them from photo-dissociation. The molecular phase being the deepest phase in the cloud, only a small amount of far-UV and X (through cosmic rays) radiation reaches this zone and bypasses the shielding of molecules to heat the gas (by photo-electric effect on the dust grains or by photo-dissociation of molecules). In these clouds, the temperature goes down to 10 K and the density can reach high values from 100 cm^{-3} up to $1\,000\,000 \text{ cm}^{-3}$ in the dense cores. These low temperatures will also enable star formation since the gravitation will overcome the gas pressure forces (Jeans instability). In short, the cooling of the gas and the shielding of molecules create an environment

suitable for a cradle of stars.

In this three-phase model, a photon from a star removes an electron from a dust grain or from a hydrogen atom of the gas. This electron collides with other electrons and heats the gas. The energy transferred by the electron to the gas can be radiated away by fine structure line emission. Spatial and spectral observations of the emission (continuum and fine structure lines) of the gas and dust help to understand the stages of the evolution of the ISM. Indeed, this emission fully depends on the chemical compositions, on the temperature and on the density of the medium. On one hand, the study of the bright continuum between 10 μm and 1 mm outlines the heating of dust; on the other hand, the fine structure lines trace the cooling of the gas.

Depending on the phase of the medium, there are species which are more suitable than others to use for tracing the ISM cooling. For example, the [CII] 158 μm line, which corresponds to the electronic ground state fine structure transition of C^+ , is often the brightest line, accounting for 0.1-1% of intensity in the far-infrared regions (Stacey et al., 1991). The ionization of C^0 occurs in HII regions but also in photo-dissociated regions since the required energy (11.26 eV) is less than for hydrogen H^0 (13.6 eV). Astronomers often use the [NII] 122 μm and 205 μm lines as complementary data to disentangle the contributions from HII and photodissociation regions to the observed [CII] line flux. However, the luminosity of the fine structure lines strongly depends on the metallicity of the galaxy. Cormier et al. (2015) have shown that in dwarf galaxies as in the Small and Large Magellanic Clouds where the metallicity is low (in comparison to the Milky Way), the [OIII] 88 μm line is the brightest. The observation tools must therefore be adapted to the galaxy. Regarding the molecular phase, because the direct detection of H_2 is quite difficult, astronomers track CO, the second most abundant molecule, which emits one line at 2.6 mm. Nevertheless, the C/CO zone transition is quite different from the H/ H_2 transition since CO is still photo-dissociated in the outer part of the molecular phase, while H_2 is no longer photo-dissociated, due to its shelf-shielding: thus there exists a “dark zone” which is invisible in CO line emission. This means that the emission of the CO molecule only traces a fraction of the molecular phase. With the C^+ ion being present in this area and the excitation still sufficient, the [CII] line can therefore be used to unveil this CO-dark molecular component. In a more general way, the [CII] line can trace the ionized phase and a part of the neutral phase. So, used in combination with other tracers (such as the [NII] line), its observations can help to disentangle the different phases.

In a nutshell, the emission of the [CII] 158 μm line encompasses a large range of conditions of the ISM. It is the reason why instruments like PACS and HIFI onboard the HERSCHEL observatory and FIFI-LS and GREAT onboard SOFIA have chosen this probe; future experiments as SPICA and Co-PILOT will also observe the C^+ cooling line. The large interferometer ALMA is also able to observe the redshifted 158 μm line emitted from the early Universe, leading to a global picture of the evolution of the ISM throughout

time. The Co-PILOT balloon experiment (C^+ observations with PILOT), for instance, aims at mapping the [CII] line over a wide field of view with a $2'$ angular resolution. The main goal of this experiment would be to resolve the boundary layers of molecular clouds in the Milky Way (and other galaxies of the Local Group), as the COBE/FIRAS instrument did (Bennett et al., 1994) but with an angular resolution 200 times better. For this purpose, the instrument onboard the balloon-borne experiment will need to combine arrays of detectors with a spectral capability. In this thesis, we propose a solution for a very compact spectrometer which could be suitable for this kind of scientific target.

1.2.3 The B modes : the new frontier of Cosmic Microwave Background science

In this last subsection about specific science that can be studied with new compact instrumentation, we want to broaden the discussion to open cosmological questions, since the technology choices taken in this thesis are not restricted to sub-millimeter applications. In the following, we discuss the next challenge in the Cosmic Microwave Background (CMB) field : detecting B modes. As will be explained, B-modes detection requires polarimetric imaging in several spectral bands.

In 1948, G. Gamow explained that the atomic species that we can observe in all directions of the universe are the main result of the evolution of the primordial matter at the earliest stages of the expansion of the Universe (Gamow, 1948). Following Gamow's path, R. Alpher and R. Herman (Alpher and Herman, 1948) predicted that this expansion must have cooled down the early extremely hot-and-dense Universe to a temperature of about 5 K. In 1965, A. Penzias and R. Wilson from the Bell Telephone Laboratories in New Jersey accidentally measured an excess noise at a 3.5 K temperature coming from all over the sky (Penzias and Wilson, 1965), that they interpret, with another scientific team from a Princeton laboratory, as being the Cosmic Microwave Background (CMB), the leftover glow from the Big Bang. Shortly after the Big Bang, the Universe was made of a white-hot soup where no light was able to escape. The photons from the highly-ionized plasma (baryons, electrons and photons) were scattered by the electrons, and thus were trapped in this soup, leading to an opaque Universe. As the Universe was expanding, the plasma became cooler and protons and electrons combined to form the first atoms (mostly hydrogen) without being photo-dissociated. Around 380,000 years after the Big Bang, the interaction rate between electrons and photons decreased because of the lower electron density, allowing the photons to travel freely in the Universe. This period is called the period of decoupling between light and matter. The mean free path of photons grew towards reaching the Hubble'radius (i.e. the size of the observable Universe) : the Universe became transparent to light. The CMB corresponds to the radiation of the last scattering surface : photons from the CMB are remnants of the first electromagnetic waves and they saved the information about the spatial distribution of matter 380,000 years after the Big Bang. At this time, the temperature of the Universe was about 3000 K which corresponds to infrared wavelengths but with the expansion of the universe, the temperature dropped down to about 3 K today, the radiation became less energetic and the wavelength has

been stretched to the millimeter range. With the expansion of the Universe, the temperature of the CMB will continue to drop and the wavelength associated to the radiation will be more and more redshifted. Observing today this 3 K-radiation in all directions of the sky appears to be one of the strong evidences of the Big Bang theory because this shows that there was a time where the Universe was in thermodynamic equilibrium and every element of the plasma was at the same temperature. We now know that this CMB radiation that we observe at a distance of 13.8 billion light years from us ($z=1100$), represents 95% of the electromagnetic energy that we receive from the Universe, on a global scale.

The second milestone has been reached by the COBE satellite (1989-1993) which had three scientific instruments onboard. Soon after launch, one of them, the FIRAS (Far-InfraRed Absolute Spectrophotometer) instrument, measured the spectrum of the CMB and showed that it perfectly fits a blackbody spectrum (as defined by M. Planck in 1901) with a temperature of $2.735 \pm 0.06\text{K}$ (Mather et al., 1990), which corresponds to a wavelength peak at about 2 mm; to date it is the best-known blackbody (figure 1.9).

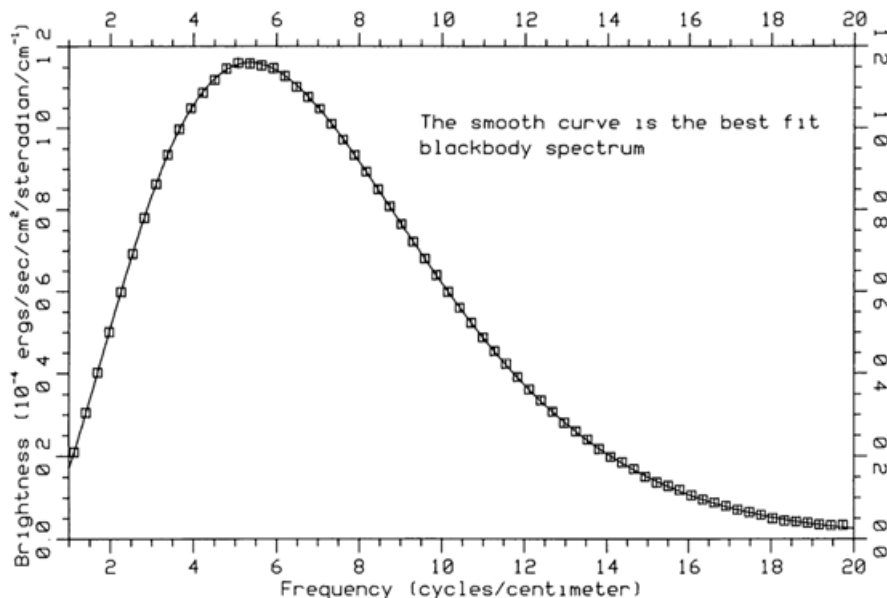


FIGURE 1.9: First spectrum for the CMB from FIRAS observations, compared to a blackbody emission. Data with 1% error bar (Mather et al., 1990).

Later more advanced data processing has refined this value to 2.725 ± 0.002 (Mather et al., 1999). Another instrument, called DMR (Differential Microwave Radiometer), contributed also to the success of the mission by mapping the deviations from the blackbody temperature: the tiny temperature variations are called anisotropies of the CMB. After subtracting the galaxy background and the dipole effect (due to motion of the Solar system), temperature fluctuations ($\Delta T/T$) have been estimated to the order of 10^{-5} from point to point on the sky (Smoot et al., 1992). This discovery has strongly supported the Big Bang theory: the uniformity of the 2.72 K-radiation in all directions of the sky suggests that all the spatial points in the Universe have a common origin but the anisotropies correspond to the early density variations that

are the seeds of the large-scale structures in the Universe (clusters, galaxies and stars) that we see today. The anisotropies of the CMB have also allowed to strongly constrain the six parameters that are needed to fully describe the Universe within the Λ -CDM model (Λ Cold Dark Matter) by using the data from the WMAP (Wilkinson Microwave Anisotropy Probe) satellite (2001-2010) and then from the PLANCK satellite (2009-2013) (Planck Collaboration, 2018) . The anisotropies measured by WMAP and PLANCK are shown in figure 1.10.

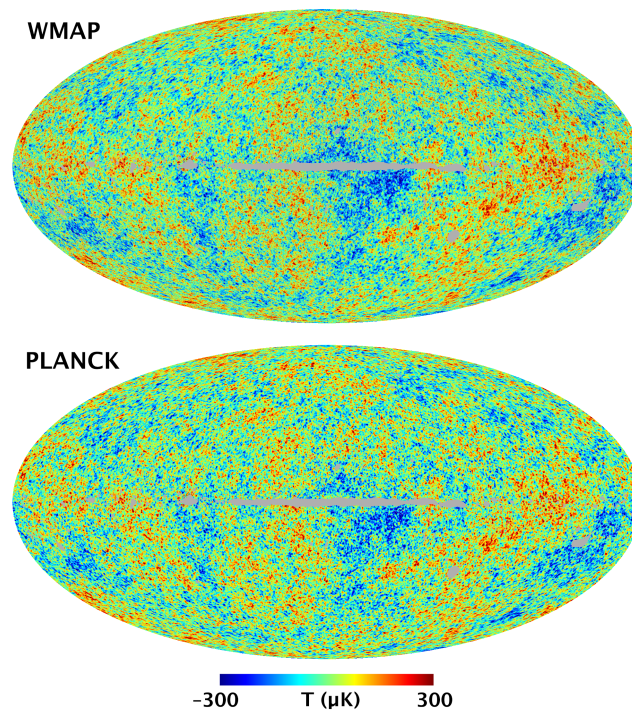


FIGURE 1.10: Anisotropies of CMB at 2.72 K from WMAP and PLANCK satellites [NASA].

Nowadays CMB remains an active field with ongoing studies as cosmologists are facing a new promising topic : the polarization of the CMB. Indeed, the polarization of the CMB is one of the missing pieces that will increase our knowledge of the history of the Universe. Polarization is a different probe than temperature to map the anisotropies ; in a perfectly uniform glow, the radiation would have been unpolarized. This polarization comes from the Thomson scattering at the time of the last scattering period : an electron in an anisotropic plasma sees different intensities depending on the hot and cold spots around it, it oscillates in one preferential direction, producing a polarized wave. The degree of polarization of the CMB is about 10%. The anisotropies of the plasma at the origin of this polarization may be due to density fluctuations (scalar fluctuations) and the polarization is called E-modes, or due to distortions of space by the primordial gravitational waves (tensor fluctuations) and the polarization is called B-modes. The E and B modes can be

differentiated by their properties of symmetry : E is even while B is an odd function (figure 1.11). Detecting

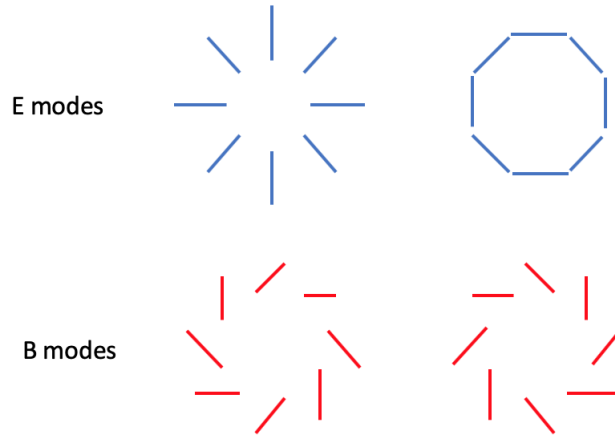


FIGURE 1.11: E and B modes.

the B-modes of the CMB at degree angular scales, will support the theory of the cosmic inflation that would have happened shortly ($\sim 10^{-32}$ s) after the Big Bang and that would have expanded the Universe with an exponential rate, producing gravitational waves. If the E-modes have already been caught by the PLANCK satellite, the B modes are still part of the challenges that cosmology would have to address. The B modes are very difficult to observe because they are considerably faint : the B modes are expected to be more than three orders of magnitude less prominent than the anisotropies of the CMB (see figure 1.12, left). These numbers are the result of predictions but it could occur that these B-modes are much fainter. If we want to push the limits of our knowledge of the history of the Universe, scientific instruments must be always more sensitive. In 2014, the BICEP2 collaboration thought that they had mapped the B-modes of the CMB, but the polarization that they observed was the result of the dust emission of our own galaxy (Ade et al., 2015). To be able to identify such faint sources as B-modes, we need to remove all other contributions to polarization : galactic foregrounds, synchrotron emission, E modes, B modes due to the lensing of E-modes by large scale structures at relatively late time, etc . For this, we need to characterize the emission level of each component and this can only be done by recording the polarization in several spectral channels to discriminate each contribution to the polarization, this is what is presented in figure 1.12, right. The Japanese mission LITEBIRD, planned to be launched in 2027, is one of the candidates competing for the discovery of B-modes. For this, the telescope will have 15 frequency bands from 40 to 400GHz onboard (Suzuki et al., 2018). In this thesis, we present detectors that are sensitive to far-infrared polarization (chapter 3). The working principle of these detectors could be scaled to longer wavelengths for CMB purpose. We could also take benefit from the spectrometric capacity developed in this thesis (chapters 4 and 5) to modify the intrinsic spectral selectivity of these detectors to adapt it to specific bands as it is required for CMB missions (shown in figure 1.12, right).

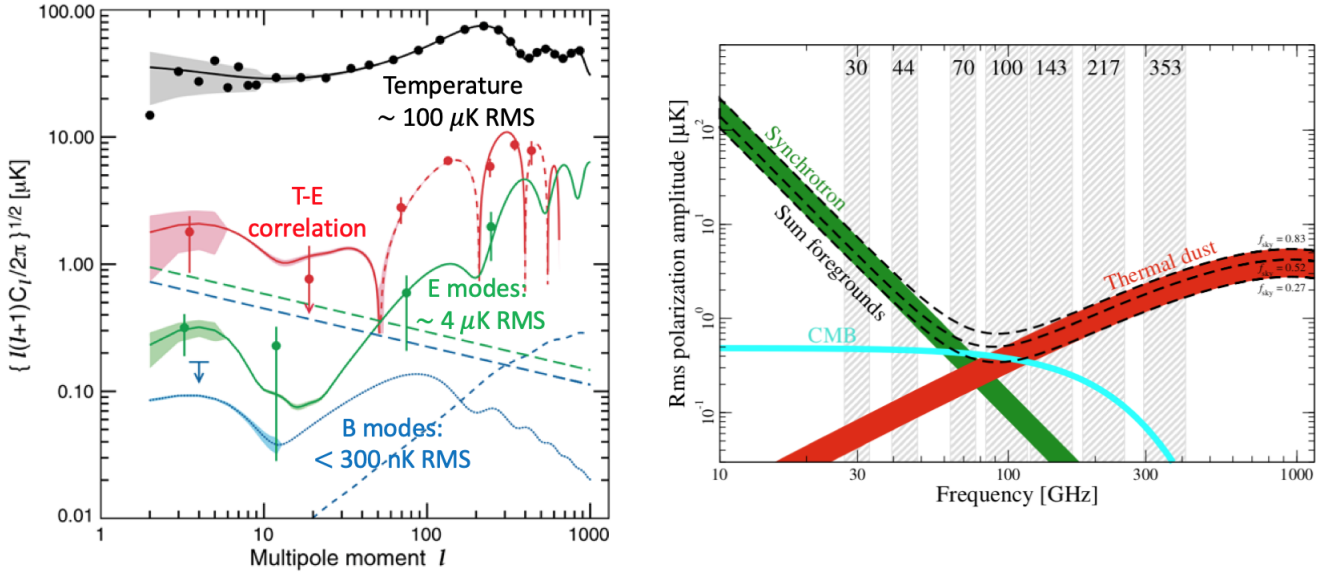


FIGURE 1.12: (Left) Simulated power spectra of anisotropies in intensity and polarization (Page et al., 2007; Piat, 2008); (right) Different contributions to polarization as a function of frequency. Planck channels are shown in grey (Planck Collaboration, 2018).

1.3 Potential for simplification of future instruments

The current and future requirements of astrophysics and cosmology imply having ever more complex instruments. The focal planes must be always larger, the detectors have to be more sensitive from one mission to the next one, and so on. Here we are interested in combining different optical functions in the same instrument, namely imaging, polarimetry and spectroscopy. This means that science targets such as the ones presented above could be addressed. Keeping in mind these objectives, we want to extend the instrument capabilities by adding more functionalities to the simple photometer. However, we decided to do so at the level of the focal plane array. Therefore, we create pixels which are intrinsically sensitive to polarization and we want to add the spectral capability to the detection array (i.e. in a very compact way). In a longer-term, we could imagine to have all functionalities in the same pixels array. A spectro-imaging polarimeter array could for example, be one of the ‘off the shelf’ technology that suits the CMB requirements, providing a scaling of the detectors. In short, this thesis aims at investigating the possibility to have several light analysis functions in the same compact device to simplify the overall instrument. The benefits of compact instruments are quite straightforward : mass, volume, simplicity, ... These advantages are also reinforced by the fact that our instruments work at very low temperature. As a consequence, the total mass of the instrument to cool down must be as low as possible. Nevertheless, combining several instrumental capabilities in a compact way may affect the performance of each individual function. In this

thesis, in addition of presenting the current developments, we will discuss the impact on performance of having these various light analyzing functionalities within the pixels or at least, in the focal plane.

Chapter 2

Bolometers for far-infrared/ (sub)-millimeter observations

Contents

2.1	Bolometers : more than 100 years of research	27
2.1.1	The invention of the first bolometer	27
2.1.2	General description of bolometers	28
	Parameters to optimize	29
	General equations	30
	Noise	32
2.1.3	Evolution of the bolometer technology	35
2.1.4	Other detectors in the sub-millimeter field	37
2.2	Bolometers at CEA	40
2.2.1	The PACS bolometers	40
2.2.2	From PACS bolometers to B-BOP bolometers	46
2.2.3	Perspectives	49

The detection of a natural phenomenon can be usually understood as the conversion of a physical quantity to an electric signal. The method for detecting electromagnetic radiation really depends on the wavelength of the radiation. Moreover we have seen in chapter 1 that observations in various wavelengths ranges bring complementary information of astrophysical sources. As a consequence, the choice of the detector used must be adapted to the observation frequency range in order to get the best from measurements. This thesis is focused on thermal detectors, i.e. bolometers, for far-infrared astronomy, since they are one of the prime choices for detectors in this range (together with KIDs and photoconductors). Detectors based on the same physical principle as bolometers are used for X-rays spectroscopy and are called “calorimeters”. One difference exists however, bolometers for far-infrared detect the intensity of the incoming wave while calorimeters can resolve the energy of individual X-ray photons. Concerning other wavelength domains, although thermal detectors can in principle be used for the whole spectrum, photodiodes are favored for far UV to near IR measurements. These detectors rely on the internal photoelectric effect : when a photon strikes a semi-conductor material, provided the photon is energetic enough, the transferred energy allows the creation of an electron-hole pair which raises the electrical conductivity of the material. Applying a bias voltage to the detector allows one then to measure the change of current. In practice this kind of detection can be used up to 100 μm since at longer wavelengths the incident radiation is no longer energetic enough, compared to the bandgap of most semiconductor. It has to be noted that for the PACS and FIFI-LS spectrometers onboard HERSCHEL and SOFIA respectively, Ge :Ga photoconductors have been mechanically stressed to push forward the cut-off wavelength to 200 μm (Poglitsch et al. (2003a), Fischer et al. (2018)). In the radio wave field, detectors use antennas to couple the wave to the detection system. In this chapter, our goal is to present a brief overview of thermal detectors and to focus on highly-resistive bolometers for far-infrared astronomy, since they are the historical devices and the current technology used at CEA. However, more recent developments such as superconducting bolometers or kinetic inductance detectors will also be presented. We will first try to provide a detailed picture of the invention of the bolometer and then some general characteristics of the bolometer behavior. We will also present some key technological milestones achieved in the field which have led to the current bolometers that we work on at CEA. Lastly, we will come back to the evolution of bolometers at CEA, from PACS bolometers, which have flown with the HERSCHEL space observatory, to the B-BOP technology of the future space mission SPICA. The first section is an overview of the field which also appears in many other thesis (Buzzi (1999); Reveret (2004); Billot (2007) in particular). The last section of this chapter is dedicated to the bolometers that have been thought, designed and built at CEA, from a strong collaboration between DRF/IRFU/DAP in Saclay and DRT/LETI in Grenoble.

2.1 Bolometers : more than 100 years of research

Here we describe in a non-exhaustive way several key events of the bolometer history : from Langley’s invention to the different milestones which have led to today’s bolometers. This section aims at introducing the technology description of CEA silicon bolometers.

2.1.1 The invention of the first bolometer

The bolometer has been invented by an American astronomer, Samuel Pierpont Langley (1834-1906) (see biography by Loettgers (2003) for more details). After trying to improve thermopiles¹ for decades to measure the radiant heat from the infrared spectrum of the Sun, he concluded that the field needed a new instrument, more reliable and more sensitive. In 1881, a paper published in Nature (Langley, 1881), described the new concept of bolometer, or ‘actinic balance’ :

“Two strips of thin metal, virtually forming arms of a Wheatstone’s bridge, placed side by side in as nearly as possible identical conditions as to environment, one only of them being exposed to radiation. Such radiation would slightly warm the strip and therefore alter its electric resistance, and the amount of this change would be indicated by the movement of the needle of the galvanometer placed in the middle circuit of the “bridge” ”.

Then a bolometer converts radiation heating into variations of the electrical impedance and a galvanometer records the change of current flowing through the bolometer. With this simple definition, the bolometer becomes a universal detector that could work, in principle, in every frequency range. Figure 2.1 illustrates the principle of the Langley’s experiment. The top figure shows the ebonite cylinder which contains a series of diaphragms in front of the metallic strips which are located at the end of the tube. The bottom figure sketches the Wheatstone bridge which allows one to measure the variation of the electrical resistance of ‘M’, caused by the incident radiation, via the imbalance of the bridge. The performance of the bolometer was far better than any thermopile : the bolometer allowed Langley to measure changes in resistance that correspond to heating of the metallic part of 10 μK ! Langley found the sensitive instrument he was looking for and used this breakthrough invention to observe the solar spectrum. The details of the experiment are explained in Langley (1900a,c,b) : Langley used a bolometer combined with optics including a prism and called this whole set-up a “spectrobolometer”. In addition of its contribution to the knowledge of water vapor absorption by earth’s atmosphere (Langley, 1902), the measurements made by Langley with its spectrobolometer have announced early signs of the discovery of Planck’s law about black body emission. Indeed, in Langley (1881), he presented his recent results about the solar spectrum, demonstrating that the heat maximum recorded on a bolograph (intensity as a function of the wavelength) was shifted to shorter wavelengths despite his contemporaries’ thoughts. Further measurements of artificial radiations proved that the heat maximum shifts to shorter wavelengths with increasing temperature. Beyond that,

1. based on thermocouples

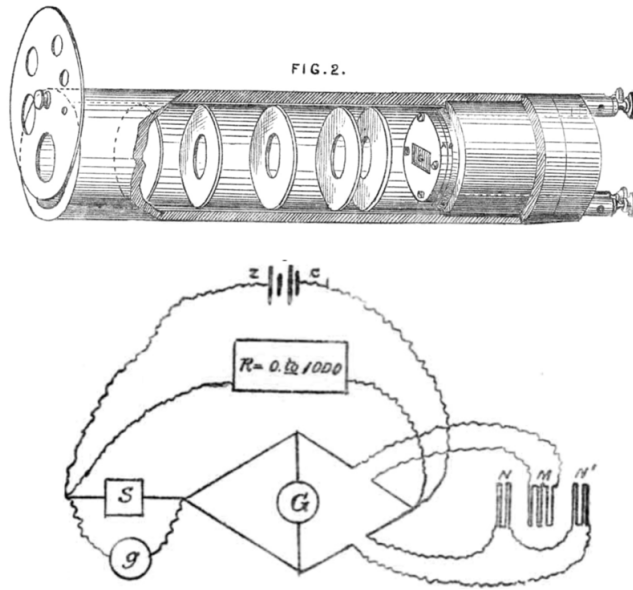


FIGURE 2.1: (Top) Ebonite cylinder with several diaphragms and Langley's bolometer (metallic strips); (Bottom) Wheatstone bridge which is used to measure the variations of the electrical reference M, exposed to light, with respect to reference resistances (Langley, 1881).

Langley extended the scientific observations of the Sun to the infrared region and therefore paved the way to a new research field of astronomy.

2.1.2 General description of bolometers

In this subsection, we describe the overall functioning of a contemporary bolometer. The working principle of these detectors is similar to the one used for Langley's device : the bolometer measures the conversion of radiation to heat, it is a power detector. However, in Langley's experiments the absorber and thermometer were basically the same element while the functions are nowadays decoupled even if the temperature is supposed to be homogeneous in the system. This has the clear advantage to enable the optimization of both elements at the same time.

The bolometer can be basically described by three components : the absorber, the thermal sensor and the heat sink shown in figure 2.2. When a photon hits the absorber, its energy is converted into heat. The thermometer measures the changes in temperature through the changes in its resistance. Note that the critical part (i.e. absorber and thermometer) is thermally isolated from the rest of the bolometer and that finally, the energy is offloaded to the heat sink.

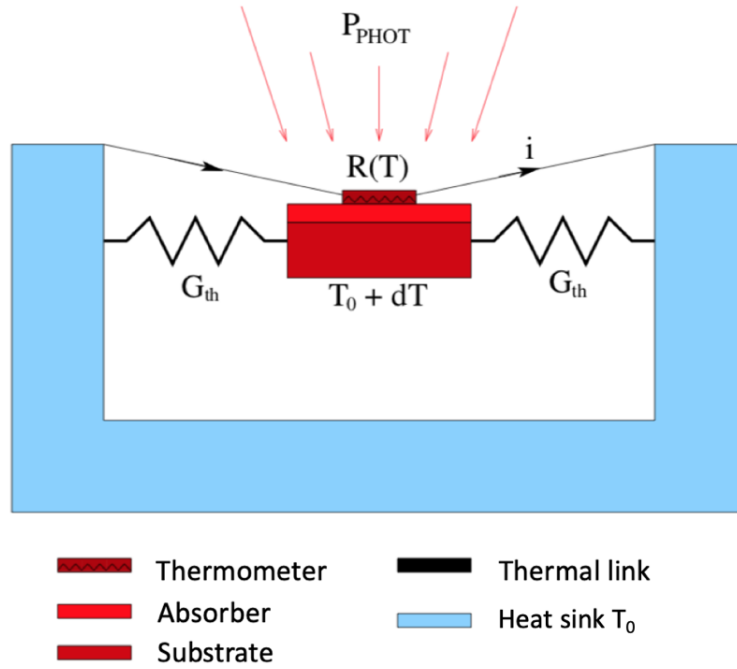


FIGURE 2.2: Description of the different parts that form a bolometer. The incoming wave gets absorbed and converted into heat by the absorber. Then the thermometer measures the temperature rise of the absorber. Note that the central part is suspended and thus thermally isolated. A weak link enables the thermometer to offload the heat to the heat sink. The thermal conductance G_{th} is a parameter to optimize since it accounts for the sensitivity and for the speed of the whole bolometer (adapted from Billot (2007)).

Parameters to optimize

Depending on the application, several parameters can be optimized :

- The absorption of the radiation is a key parameter as it determines how much of the incident light is converted into heat for detection. The optimization of the absorption of the bolometer is the central concern of this thesis and will be largely investigated throughout the manuscript.
- The heat capacity C_{th} for a thermally isolated object is by definition the ratio of the absorbed energy dE to the temperature rise dT : $C_{th} = dE/dT$. To have very sensitive bolometers, we need absorbers and thermometers to react strongly (in terms of temperature rise) to a small amount of energy. Therefore the heat capacity of the system must be minimized. One way for reducing the heat capacity of the absorber is to reduce its mass m since the heat capacity C_{th} is proportional to m through the equation : $C_{th} = m \cdot s$, where s is the specific heat capacity of the material used. Another way to minimize the heat capacity is to work at very low temperature : as suggested by Simon (1935), the sensitivity of the bolometer could be improved by many orders of magnitude when working at low temperature. Indeed, the specific heat capacity s depends, in theory, on the temperature as T^3 for

crystals and as T for metals. In practice, the materials one uses have intermediate T law dependence. As it will be explained later in this chapter (section 2.1.2), the low temperature also reduces the different noise contribution within the system.

- The conductance G_{th} of the thermal link is important too. As we see in figure 2.2, the detection parts are mechanically suspended by the thermal link which also ensures the thermometer to be thermally isolated from the cold bath, in order to be sensitive to a even small amount of radiation. However, the heat sink is necessary for the sensitive part to be cooled down to an equilibrium temperature T_0 , after being heated. The thermal insulation of the absorber is characterized by the thermal conductance G_{th} of the thermal link to heat sink. A priori, we would want to minimize G_{th} but this parameter is also involved in the speed of the system through the thermal time constant $\tau = \frac{C_{th}}{G_{th}}$. The definition of τ shows that : (1) under constant illumination, if the bolometer undergoes a high rise in temperature (C_{th} small), then the system will be fast ; (2) if the thermal link allows fast offloading (G_{th} high), then the system gets back quickly to the equilibrium. Therefore the value of the conductance corresponds to a trade-off between sensitivity and speed.
- The coefficient α characterizes the electro-thermal behavior of the detector. Indeed bolometers measure the variations of the electrical resistance as a function of the temperature $R(T)$. The measurement of the radiation through the change in resistance is relevant when the resistance depends only on the temperature. A bolometer is very sensitive to incident power if it undergoes a strong change in resistance as a response to a small perturbation in temperature. This is a characteristic that bolometers using doped-semiconductors and superconductors achieve (see sections 2.1.3 and 2.1.4). The temperature coefficient $\alpha = \frac{1}{R} \frac{dR}{dT}$, defines then the electrical sensitivity to thermal excitation of the bolometer.

As a consequence, the bolometer physics is really complex since it refers to several scientific fields as detection, optics, solid state physics, thermodynamics, cryogenics, electronics, and so on (Rodriguez (2012)). In a nutshell, we want to have a very low heat capacity C_{th} , a pretty low thermal conductance G_{th} (compromise with detector speed, depending on the applications) and a very sensitive thermal sensor (large $\alpha(R(T))$).

General equations

The following gives a simple description of the bolometers behavior, it is mostly adapted from Richards (1994). The equations account for the global heating of the bolometer through the incident power, the Joule heating and the thermal bath. First we want to derive the general equation of bolometers. Assuming there is an incident power $P_\nu(t)$ that falls onto the bolometer, the system undergoes some changes in temperature and this temperature evolves with the time constant being $\tau = \frac{C_{th}}{G_{th}}$. The incident power $P_\nu(t)$

can be decomposed in two parts as following :

$$P_\nu(t) = P_1 + P_2 e^{i\omega t} \quad (2.1)$$

where P_1 is a constant power which can represent the sky, for example, and the instrumental backgrounds, and P_2 is related to a fainter signal (which accounts for the faint astronomical signal), which oscillates with time at a frequency ω (which can account for chopping in a lab experiment). From this, we can derive the expression of T_b :

$$T_b = T_1 + T_2 e^{i\omega t} \quad (2.2)$$

The resistance of the thermometer evolves with temperature, depending on the nature of the thermometer : if it is a semiconductor, heating the thermometer produces a decrease in resistance while it is the opposite for a superconducting bolometer. The Joule heating corresponding to the power dissipated in the thermometer due to the electrical current flowing in the resistor, is then a function of time that we call here $P_J(t)$ and which is equal to : $R(T) I_{\text{bias}}^2$ with I_{bias} being the bias current in the case of a resistive thermometer. At first order, $P_J(t)$ can be approximate by :

$$P_J(t) = (R(T_1) + \left(\frac{dR}{dT}\right)_{T_1} T_2 e^{i\omega t}) I_{\text{bias}}^2 \quad (2.3)$$

Moreover, the power offloaded through the thermal link to the heat sink :

$$P_{\text{offloaded}}(t) = \overline{G_{th}}(T_b(t) - T_0) \quad (2.4)$$

with $\overline{G_{th}}$ being the average thermal conductance of the offloaded heat between T_0 and T_b . Finally, the variation of energy dE in the absorber is defined by $dE = C_{th} dT$, which means the stored power at time t in the system is :

$$P_{\text{stored}}(t) = \frac{dE}{dt} = C_{th} \frac{dT}{dt} \quad (2.5)$$

The equation that summarizes the input and outputs power is :

$$P_{\text{stored}}(t) = P_\nu(t) + P_J(t) - P_{\text{offloaded}}(t) \quad (2.6)$$

From this, we can derive the general equation of bolometers :

$$C_{th} \frac{dT}{dt} = P_\nu(t) + P_J(t) - \overline{G_{th}}(T_b(t) - T_0) \quad (2.7)$$

For semiconductor bolometers ($\alpha < 0$) and thus constant bias current I_{bias} , the voltage responsivity S of a bolometer is defined as the ratio of the change in voltage to the change in incident power : $S = \frac{dV}{dP}$. S is equal to $\frac{V_1}{P_1}$ here. From the equation of bolometer, we can derive the definition of S . First, we replace each term of equation 2.7 by the corresponding expressions :

$$i\omega C_{th} T_2 e^{i\omega t} + \overline{G_{th}}(T_1 - T_0) + (G_{th})_d T_2 e^{i\omega t} = P_1 + P_2 e^{i\omega t} + I_{\text{bias}}^2 R(T_1) + I_{\text{bias}}^2 \left(\frac{dR}{dT} \right)_{T_1} T_2 e^{i\omega t} \quad (2.8)$$

with $(G_{th})_d = \left(\frac{dP}{dT} \right)_{T_1}$ being the dynamic thermal conductance at T_1 . We can therefore separate the time independent terms (steady state) and the time varying terms :

$$\begin{cases} P_1 + R(T_1) I_{\text{bias}}^2 &= \overline{G_{th}}(T_1 - T_0) \\ i\omega C_{th} + (G_{th})_d &= \frac{P_2}{T_2} + I_{\text{bias}}^2 \left(\frac{dR}{dT} \right)_{T_1} \end{cases} \quad (2.9)$$

From the equation with time varying terms, we can derive the voltage responsivity of the bolometer :

$$S = \frac{V_1}{P_1} = I_{\text{bias}} \left(\frac{dR}{dT} \right)_{T_1} \frac{T_1}{P_1} = \frac{I_{\text{bias}} \left(\frac{dR}{dT} \right)_{T_1}}{(G_{th})_d - I_{\text{bias}}^2 \left(\frac{dR}{dT} \right)_{T_1} + i\omega C_{th}} \quad [V/W] \quad (2.10)$$

By setting the temperature coefficient $\alpha = \frac{1}{R} \left(\frac{dR}{dT} \right)_{T_1}$ and the effective thermal conductance which accounts for the thermal feedback $G_e = (G_{th})_d - I_{\text{bias}}^2 R \alpha$, we get :

$$S = \frac{I_{\text{bias}} R \alpha}{G_e (1 + i\omega \tau_e)} \quad (2.11)$$

with $\tau_e = \frac{C_{th}}{G_e}$ the electrical thermal time constant, which is shorter than the thermal time constant τ for a semiconductor bolometer ($\alpha < 0$) due to the electrothermal feedback. Indeed this latter reduces the change in temperature. Once again, the value of G_e has to be a trade-off between the sensitivity and the speed of the system.

Noise

In this part, the different sources of noise which a bolometer may be subject to are reviewed. First, any noise contribution is expressed in Noise Equivalent Power (NEP), in $W/\sqrt{\text{Hz}}$, which corresponds to “the power which must fall on the detector to raise the output by an amount equal to the root-mean-square (RMS) noise” (Rohlfis and Wilson, 2004) in a one Hz bandwidth, this means that the NEP is the smallest optical power that the bolometer can detect in this bandwidth. Each individual source of noise NEP_i adds

up to the total NEP of the detector following the equation :

$$NEP = \sqrt{\sum_i NEP_i^2} \quad (2.12)$$

The photon noise

The photon noise is related to the quantum fluctuations of photons which fall onto the detector. Assuming a black-body radiation, the square of the RMS fluctuations in the number of photons of this radiation at frequency ν is (Rohlf and Wilson, 2004) :

$$\Delta n_{RMS}^2 = n (1 + n) \quad (2.13)$$

with n being the photon occupation number at frequency ν . For high frequency (visible, near-infrared), the photon noise follows a Poisson distribution, meaning that the photons arrival times are independent and we have : $n \ll 1$ and $\Delta n_{RMS}^2 \approx n$. The fluctuations are then proportional to \sqrt{N} with N the mean number of photons received by the detector (Zmuidzinas, 2003), this is a quantum noise. In contrast, for lower frequency (radiowave), the Bose-Einstein nature of photons must be taken into account with $n = (e^{h\nu/kT} - 1)^{-1}$ (h the Planck constant, k the Boltzmann constant and T the temperature of the photon source). The term in brackets in equation 2.13 can be seen as a correction factor which stands for the correlation of the arrival time of particles (Rieke, 2003). This means that because photons come by groups, they may interfere and create a larger noise compared to the simple Poisson statistics (Lamarre, 1986). In this case : $n \gg 1$, $\Delta n_{RMS}^2 \approx n^2$ and the fluctuations of photons vary with N . The far-infrared/sub-millimeter range is at the borders of these two regimes and for this reason, we keep the photon noise as it is defined in equation 2.13. However, we can turn the RMS fluctuations in the number of photons to a macroscopic quantity expressed in power, the NEP. For this, we must consider the density of states factor ($h\nu^3/c^2$), the photon energy $h\nu$, the collecting area A and the acceptance solid angle Ω of the detector, an extra factor of 2 which accounts for unpolarized radiation and for Nyquist sampling. Finally we have to integrate the product of these quantities over the whole frequency spectrum :

$$NEP_\nu = \int_0^\infty 2h\nu \sqrt{\frac{A\Omega}{\lambda^2} \frac{1}{e^{h\nu/kT} - 1} \left(1 + \frac{1}{e^{h\nu/kT} - 1}\right)} d\nu \quad (2.14)$$

To derive this formula, we have only considered a black body radiation, but in case of a grey body, n must be multiplied by $\epsilon(\nu)$ (< 1), the emissivity of the grey body. To be more rigorous, n should be also corrected by factors $\eta(\nu)$ and $t(\nu)$ which stand for the quantum efficiency of the detector and the optical transmission of the whole system, respectively. The photon noise is the fundamental limit of noise. It mostly depends

on the emission from the telescope and from the atmosphere for ground-based telescopes, while for space telescopes, the astronomical foregrounds (Zodiacal dust, Cosmic Infrared Background and the CMB) can also limit the observations, in addition to the emission of the telescope. An ideal detector has all its intrinsic noise sources reduced (using low temperature, for example) to be less than the photon noise. This is the definition of a Background Limited Infrared Photodetector (BLIP). For HERSCHEL-type telescope, the major thermal background came from the ‘hot’ primary mirror, while for the future SPICA observatory, the thermal emission of the dish will be considerably reduced by cooling it down to 8 K. This is the main reason why the detectors have been required to be that sensitive.

The Johnson noise

The Johnson noise is related to thermal fluctuations of electrons in a resistance R . The $NEP_{Johnson}$ is a white noise, estimated to be :

$$NEP_{Johnson} = \frac{\sqrt{4kTR}}{S} \quad (2.15)$$

with S the responsivity of the bolometer. In practice, R is the equivalent resistor which accounts for the bolometer but also for the load resistor seen in parallel by the detector.

The phonon noise

The phonon noise is related to the fluctuations of the quantum vibrations inside the crystal when the stored energy is dissipated through the thermal link to the heat sink.

$$NEP_{phonon} = \sqrt{4kT^2(G_{th})_d} \quad (2.16)$$

with T the effective temperature of the bolometer and $(G_{th})_d = \left(\frac{dP}{dT}\right)_{T_1}$ the dynamic thermal conductance around T_1 . This thermal noise is frequency independent.

The Johnson noise and the phonon noise are both white noises related to the temperature of the system. The use of low temperature is a strong requirement of the system in order to gain in sensitivity.

The 1/f noise

The 1/f noise stands for the fluctuations of the resistance due to the random position of impurities in the doped material. This adds a noise for the low frequencies.

Other noise contributions are present in a bolometer : read-out noise, microphonic noise, temperature fluctuations of the heat sink, electromagnetic perturbations, ...

2.1.3 Evolution of the bolometer technology

Bolometers have slightly evolved since their invention by Langley up to the middle of the 20th century. One of the first milestone of that century has been achieved by F. Low using, for the first time, semi-conductors as the temperature sensor for the bolometer. Low's bolometer was made of gallium-doped single crystal germanium (Low, 1961), covered by black paint to improve the efficiency of the detection. Because the thermal detectors were operated at low temperature (liquid helium - 2 K), sensitivities close to the theoretical limit were measured with an NEP of $5 \times 10^{-13} \text{ W}/\sqrt{\text{Hz}}$. In his paper, Low also shows the potential of his bolometer if it was operated at even lower temperature : he predicted an NEP of the order of $10^{-15} \text{ W}/\sqrt{\text{Hz}}$ at 0.5 K. In addition, Low paves the way to far-infrared astronomy by installing his bolometer in a cryostat with a 30-cm telescope inside a NASA Learjet aircraft.

New research on the doping of germanium has led to the development of neutron transmutation doped (NTD) germanium sensors (Haller, 1994). The transmutation by neutrons in a nuclear plant ensures homogeneity of dopant species across the crystal. The doping elements are obtained by the neutron capture transmutation of different isotopes naturally present in germanium. The electron donors and acceptors are the two nearest elements of germanium : gallium and arsenic. NTD Ge thermistors have been widely used since they benefit from a low heat capacity and from low noise.

For better performance, composite bolometers were used to optimize independently all the parameters of the bolometer. The absorber has in particular been improved with the invention of the spider-web bolometer (SWB) by JPL (Bock et al., 1995) to be combined with NTD Ge thermistor. First, the light is concentrated by feedhorns located above the spider web and interactions with the absorber are multiplied by an integrating cavity. The gold absorber covers a spider-web silicon nitride (Si_3N_4) structure, which considerably reduces the heat capacity of the absorber by minimizing the mass, without modifying the overall optical performance (one condition however : the holes of the spider web should be significantly less than the wavelength). The bolometer is therefore much faster and is also less sensitive to cosmic radiation because of the low cross-section of the absorber with particles. For this latter reason, the SWB were particularly adapted for space applications and flew with the HERSCHEL/SPIRE and PLANCK/HFI observatories (one bolometer of SPIRE is shown in figure 2.3). For these two instruments, the NEP_{detector} were respectively $3 \times 10^{-17} \text{ W}/\sqrt{\text{Hz}}$ at 300 mK and $1 \times 10^{-17} \text{ W}/\sqrt{\text{Hz}}$ at 100 mK (Holland and Duncan, 2002). However, this technology has one drawback : each thermometer is deposited by hand and hence makes impossible the manufacture of very large arrays with uniform performance.

The solution to this drawback might have been found some years earlier by Downey et al. (1984) who conducted research on monolithic silicon bolometers. The absorber was created by an evaporated film of bismuth on silicon while the sensor was phosphorus and boron - implanted silicon suspended by silicon threads (figure 2.4). The entire detector was obtained by microelectronics techniques in a collective

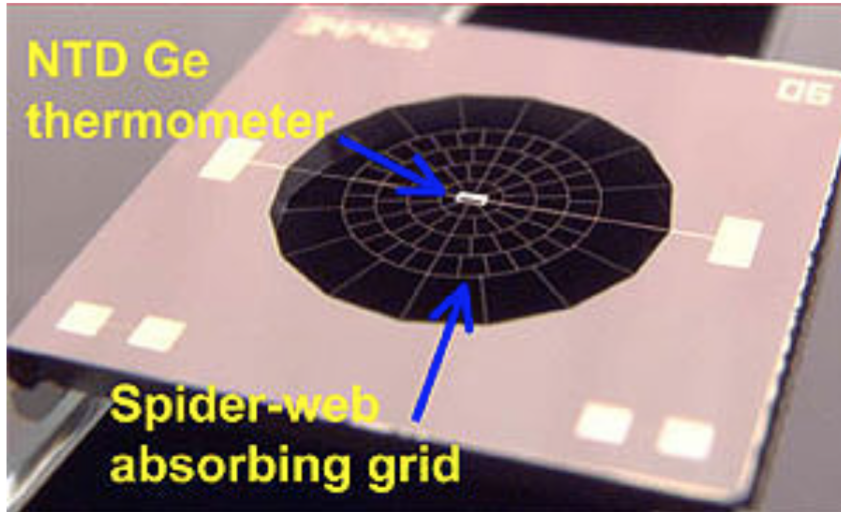


FIGURE 2.3: One spider web bolometer of HERSCHEL/SPIRE (JPL).

manner, which allowed the manufacturing of large arrays. This technique has been studied and improved by

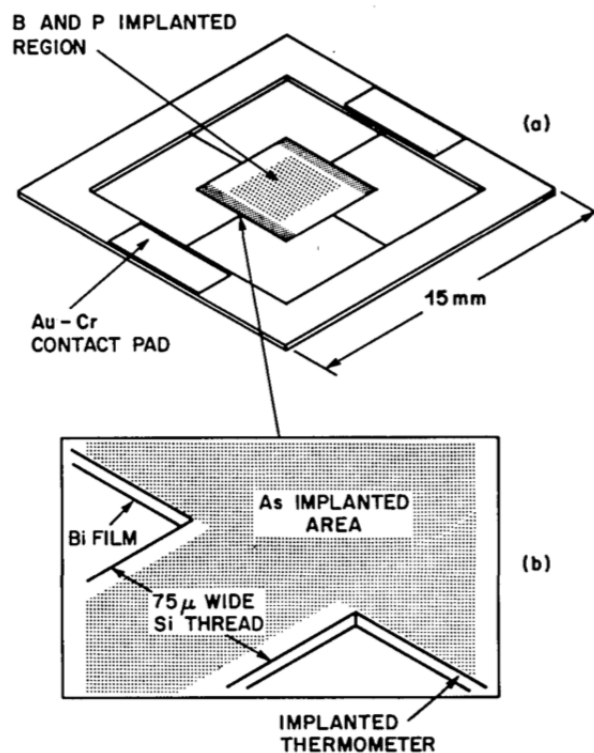


FIGURE 2.4: Monolithic silicon bolometers (Downey et al., 1984).

many labs like the Goddard Space Flight Center (GSFC) with its 'pop-up detectors' (Moseley et al., 2000) installed in the SHARC and SHARC II instruments for the Caltech Sub-millimeter Observatory (CSO) telescope. If SHARC used to have 24 pixels, SHARC II had 12 lines of 32 pixels enabled by the folding of

the silicon membranes to 90° (Li et al., 1999) (see figure 2.5), which led to a filling factor of the focal plane of more than 90% (Dowell et al., 2003). The optical efficiency was also improved by the introduction of a $\lambda/4$ backshort, first introduced for CEA bolometers in this wavelength domain, to achieve more than 75% absorption.

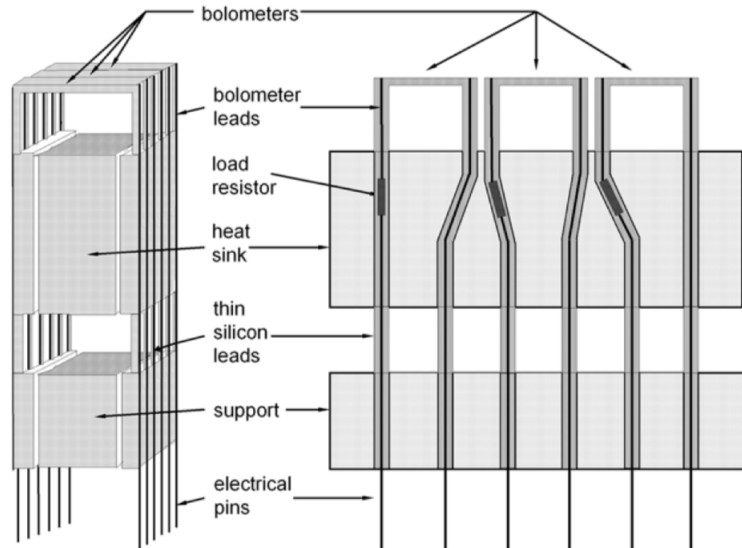


FIGURE 2.5: “Pop-up” bolometer array principle (Rieke, 2003).

The monolithic silicon bolometers have inspired many groups of the worldwide bolometer community. In particular, CEA has started developing these large focal plane arrays at the very end of the 20th century. Before describing in detail the evolution of bolometers at CEA for about 25 years, we introduce other, more or less recent, emerging technologies.

2.1.4 Other detectors in the sub-millimeter field

Here we present the most commonly used sub-Kelvin cryogenic detectors for far-infrared/sub-millimeter applications. They can be split into two families : thermal and non-thermal detectors.

Thermal detectors

Thermal detectors gather resistive bolometers (semiconductors), but also superconducting Transition Edge Sensors (TES) and metallic magnetic calorimeters (MMC).

High-resistivity bolometers have already been partially introduced since they are the historical bolometers. Their characteristic features will be more deeply explained throughout the presentation of CEA silicon bolometers in section 2.2. However, we may add one piece of information for the coming comparison with TES devices about the electro-thermal feedback. Indeed, semiconductor bolometers ($\alpha < 0$) are current-biased

and an electro-thermal feedback guarantees a pretty stable total power ($P_J + P_\nu$). Indeed the increase in temperature due to radiation is converted to a decrease in resistance. The Joule power decreases therefore with $R(T)I_{\text{bias}}^2$ while P_ν increases. The negative electro-thermal feedback tends to speed up the cooling of the bolometer to the thermal equilibrium, this is why we had $\tau_e < \tau$ in section 2.1.2.

A TES device is another kind of sensitive thermometers. It relies on the use of a superconducting material around its critical temperature T_c . The transition in resistivity between the normal and the superconducting states is very sharp (see figure 2.6, (a)), which means that a small amount of energy hitting the detector will lead to a large change in resistance. The temperature coefficient $\alpha = \frac{1}{R} \frac{dR}{dT}$ takes therefore values between 50 and 2000 K^{-1} (Holland and Duncan, 2002), it is 10 to 50 times more than for semiconductors. TES have considerably low resistance (much less than 1Ω) compared to resistive thermometer ($\sim M\Omega$ to $G\Omega$). One other difference to semiconductor is that TES ($\alpha > 0$) are voltage-biased and the change

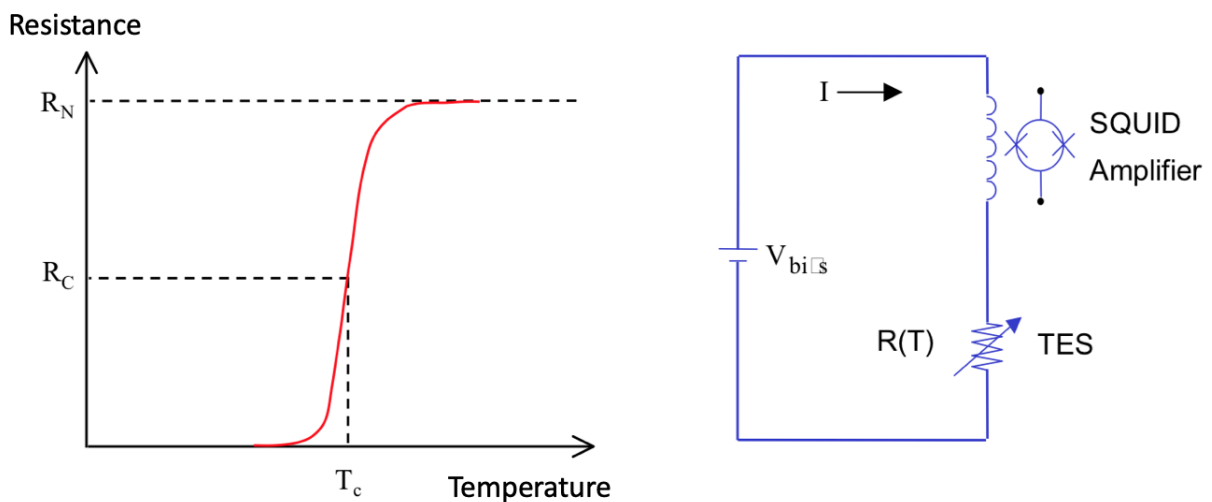


FIGURE 2.6: (a) Resistance as a function of the temperature for a TES device, T_c corresponds to the transition temperature of the superconducting material where the slope is very steep on the normal-superconducting transition; (b) TES is voltage biased and the change in current is read out by a SQUID amplifier (illustration in Reveret (2004)).

in current is read out by the use of a superconducting quantum interference device (SQUID) amplifier as presented in figure 2.6, (b). When energy is deposited in the absorber, the bolometer warms up and the resistance increases ($\alpha > 0$). Because the electric bias power is defined by $P_J = V_{\text{bias}}/R^2$, this means that the rise of P_ν leads to a fall of P_J and powers compensate each other to have around the same total power. This strong electro-thermal feedback (ETF) enables the TES to stay in the transition regime and as in the semiconductor case, but much more drastically, to reduce the time constant. However, any excessive power can make the TES inoperative if this latter leaves the working transition regime. TES have quickly shown performance comparable to those of semiconductors. As an example, Lee et al. (1998) used a titanium-film superconducting bolometers for their composite voltage-biased superconducting bolometer with a strong negative ETF. The measured response time went from 2.6 s to 13 ms (200 times faster) due to the ETF

and a $NEP_{detector}$ of $5 \times 10^{-17} \text{ W}/\sqrt{\text{Hz}}$ at 375 mK was achieved. Nowadays, TES performance is close to $10^{-19} \text{ W}/\sqrt{\text{Hz}}$ (Roelfsema et al., 2018).

The last technology of thermal detectors that we can quote is the metallic magnetic calorimeters (MMC) principle, however they will not be explained in details since they are not represented in the sub-millimeter field, but more widely in the X-ray field, especially for high-resolution spectroscopy (Fleischmann et al., 2004). Here we only aim at giving a short overview of the working principle. MMC use a metallic absorber in contact with a paramagnetic temperature sensor to which a small magnetic field is applied. When the X-ray particle hits the absorber, this leads to a rise in temperature of the calorimeter and also to a decrease in magnetization of the sensor, since the magnetic properties of materials strongly depend on temperature. The change of magnetization of the paramagnetic sensor is read out by a SQUID magnetometer. A schematic representation of the MMC principle is proposed in figure 2.7.

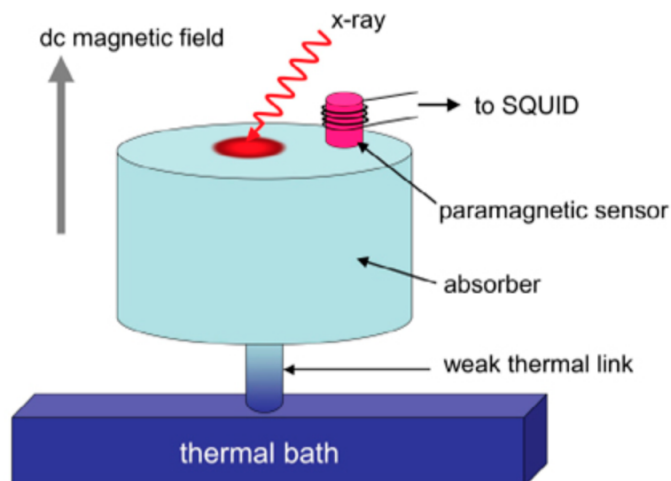


FIGURE 2.7: Schematic representation of a Metallic Magnetic Calorimeter (MMC) (Bandler, 2010).

Non-thermal detectors

One of the most commonly used non-thermal detectors in the sub-millimeter/millimeter community is the Microwave Kinetic Inductance Detector (MKID). These detectors have been invented more recently, in 2003, by a team of Caltech and of JPL (Day et al., 2003). They first appear from the need to have large arrays for the observations of the CMB, without the need for complex multiplexing systems. MKIDs rely on the measurement of the variation of the kinetic inductance of a LC resonant circuit due to radiation. For this, a superconducting thin film is used at a working temperature $T \ll T_c$: a photon with energy high enough can break Cooper pairs and creates excess quasiparticles. Since the complex impedance Z (inductance L and resistance R) depends on the quasiparticle density, the resonance is shifted in frequency

upon incoming radiations, modifying the amplitude and the phase of the signal. The working principle of detection is best illustrated in figure 2.8. By coupling an array of many resonators with different resonance frequencies to a common transmission line, it is possible to perform a simple frequency multiplexing, which enables the production of large arrays (frequency multiplexing of 150 on NIKA2 (Désert et al., 2016)). Contrary to resistive and superconducting bolometers, KIDs do not measure the temperature changes but rather the quasiparticles density in the superconducting element.

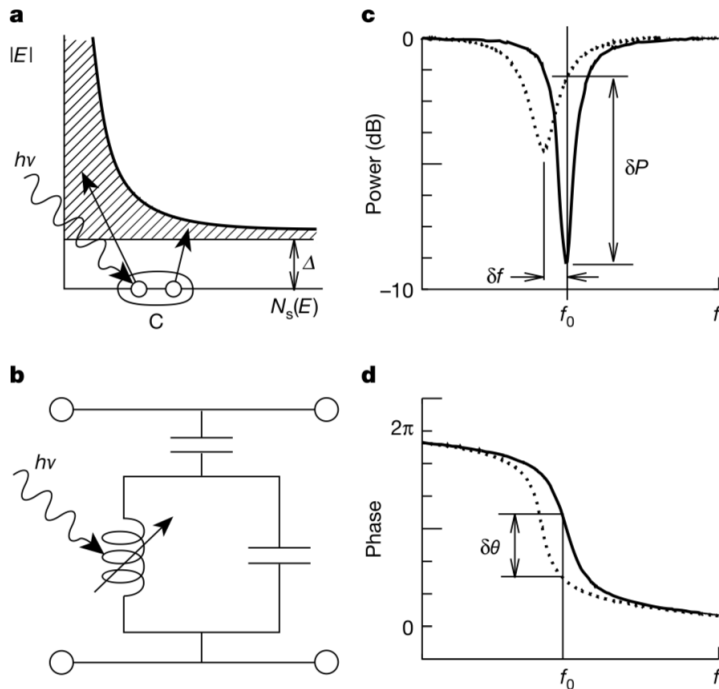


FIGURE 2.8: Detection principle of Microwave Kinetic Inductance Detector (MKID). (a) Photons with energy greater than 2Δ (binding energy of the superconducting thin-film) break Cooper pairs and create quasiparticles. (b) Microwave equivalent resonant circuit (parallel LC circuit) : incoming radiation increases the quasiparticles density and therefore increases the inductance L and adds a series resistance R . (c) Any raise in L and R moves the resonance to lower frequency, the resonance is also broader and shallower. The amplitude of the signal is then modified and so (d) the phase (Day et al., 2003).

2.2 Bolometers at CEA

We describe here the evolution of silicon bolometers, thought and made at CEA, from the involvement in the HERSCHEL/PACS photometer to the imaging polarimeter SPICA/B-BOP.

2.2.1 The PACS bolometers

At the origin of CEA bolometers are the spider-web developed at JPL in the early 1990's. The breakthrough with these new devices was the manufacture of sub-millimeter and millimeter wave individual

detectors by micromachining techniques on silicon or silicon nitride membranes. JPL achieved, at the time, the most sensitive detectors, used them for the BOOMERANG long flight balloon experiment, and their detectors were selected for the HFI instrument on PLANCK, and SPIRE on HERSCHEL.

As seen in section 2.1.3, the basic spider-web bolometer functions were made by :

- a feedhorn and an integrating cavity to collect light,
- a Si_3N_4 micro machined web, to insulate the detector from the cold sink at 100 mK (PLANCK/HFI) or 300 mK (HERSCHEL/SPIRE),
- a thin metallic (gold) layer, adapted to vacuum impedance and deposited on the silicon nitride structure to absorb the far-infrared radiation,
- an NTD germanium thermistor to measure the temperature rise with light absorption.

In 1995, Patrick Agnès, at CEA/LETI, suggested to make use of silicon micromachining techniques developed for MEMS, to produce all-silicon bolometer arrays of high complexity, combining in the detector assembly, an interface to a cold readout circuit. He adapted the four functions depicted above to the geometry of the new detectors and found a way to read them out and multiplex them to save wires when multiplying the number of pixels.

The light absorption

Maxwell's equations show that the absorption of a single thin metal sheet in one way is, in theory, limited to 50% when the metal electric resistivity is adapted to half the impedance of free space (Hadley and Dennison, 1947). However, this limit can be overcome by the use of electromagnetic 'tricks'. For instance in the spider web design, integrating spheres and Winston cones (Winston, 1970) act as light collector. The aperture of the metallic feedhorns constrains the incident angles of the wave. Once inside the Winston cone, the wave reaches the integrating sphere and undergoes several reflections on the surface of the sphere that multiply chances for the wave to be absorbed, resulting in a efficiency rate greater than 50%. Many instruments have used these light traps to increase the absorption of the detector : we can mention the focal plane of PLANCK/HFI with the use of JPL's SWB, which the focal plane is shown in figure 2.9.

However, Winston cones are sometimes abandoned since an earlier concept which has been updated by CEA (among other labs) has demonstrated its efficiency. For this technology, the absorption efficiency is ensured using the principle of resonant absorption established by Gabriel Lippmann at the beginning of the 20th century. Indeed the resonant absorption takes advantage of the reflection on a mirror. The tangential electric field vanishes at the surface of a mirror since the reflective wave is in phase opposition with the incident wave. This produces (E and B) standing waves above the mirror. As it is illustrated in figure 2.10, (left), the E field has a node at the mirror level, at $(2k + 1)\lambda/2$ with k an integer while the standing B

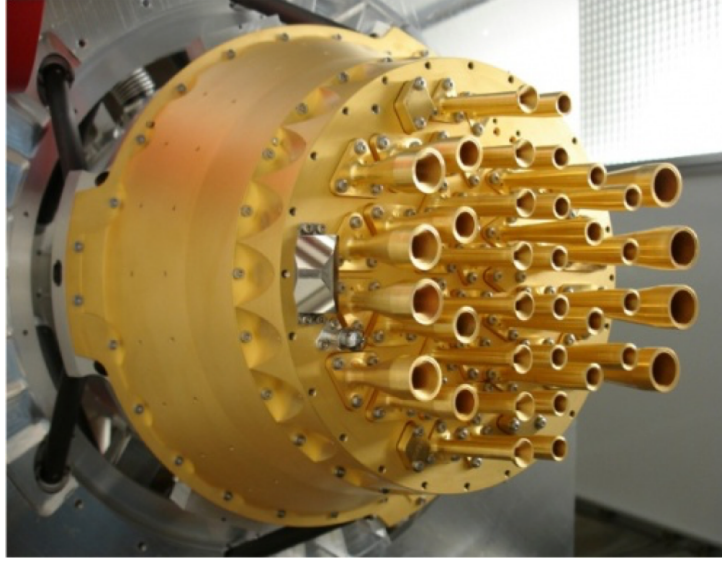


FIGURE 2.9: Planck focal plane. The different sizes of the feedhorns correspond to different frequency ranges (857, 545, 353, 217, 143, 100, 70, 44 and 30 GHz) : the aperture of the horn must be adapted to the wavelength to prevent diffraction of the incoming wave (ESA)

field is exactly $\frac{\pi}{4}$ -shifted compared to the standing E field . This means that at a distance $(2k + 1)\lambda/4$ above the mirror, there is an electrical field anti-node and magnetic field node. As a consequence, all the electromagnetic wave energy is there present in the electric field and can be dissipated if an impedance-matched absorber is located at this position (Hadley and Dennison, 1947; Fante and McCormack, 1988). This situation is illustrated in figure 2.10, (right). The spectral response of the bolometer is thus given by the size of the quarter-wave cavity. Such an architecture produces planar focal planes, similar to the ones of the visible/near-infrared range. Removing feedhorns has therefore enabled a move towards more compact and lighter arrays. The advantage of having no feedhorn is also to have more flexibility in optics but it should be mentioned that these open pixels are subject to more stray light.

The system [absorber/cavity/mirror] can be seen as a two-beam interferometer (direct and reflected waves) comparable to a Michelson Interferometer. The resulting effect is a rather smooth and wide absorption bandwidth. At the absorber level, the incident light and the reflected light are delayed in distance by $2d_{\lambda_0/4}$. This leads to a finesse of 2 which is not very selective in wavelength (see figure 2.11, right). Most of the current detectors now use this quarter wave cavity, even when a horn or a micro-lens is used to concentrate the incoming light. With this setup, the absorption efficiency can be very high, above 90%, for a wide range of wavelength. The resulting efficiency of CEA-type detectors can be observed in figure 2.11.

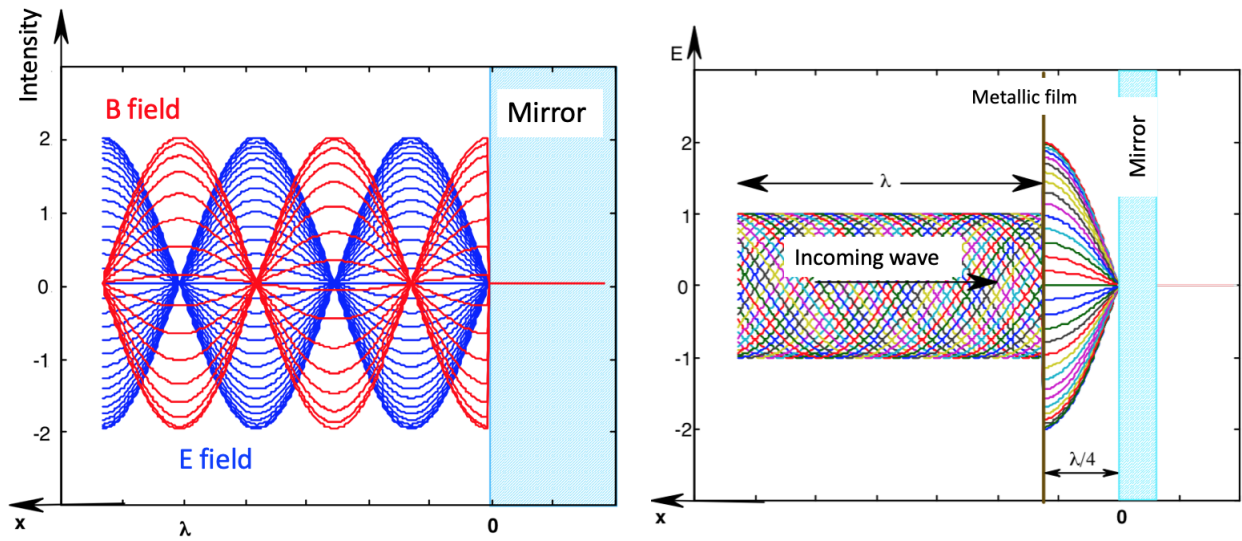


FIGURE 2.10: (Left) Resulting electric and magnetic fields after reflection on a mirror. (Right) Several incoming phase-shifted wave with wavelength λ : all have an electric node at the surface of the mirror. The maxima of the electric fields occur at a distance $\lambda/4$: positioning a vacuum impedance-matched metallic film at this location enables one to absorb 100% of light (Martignac, 1998).

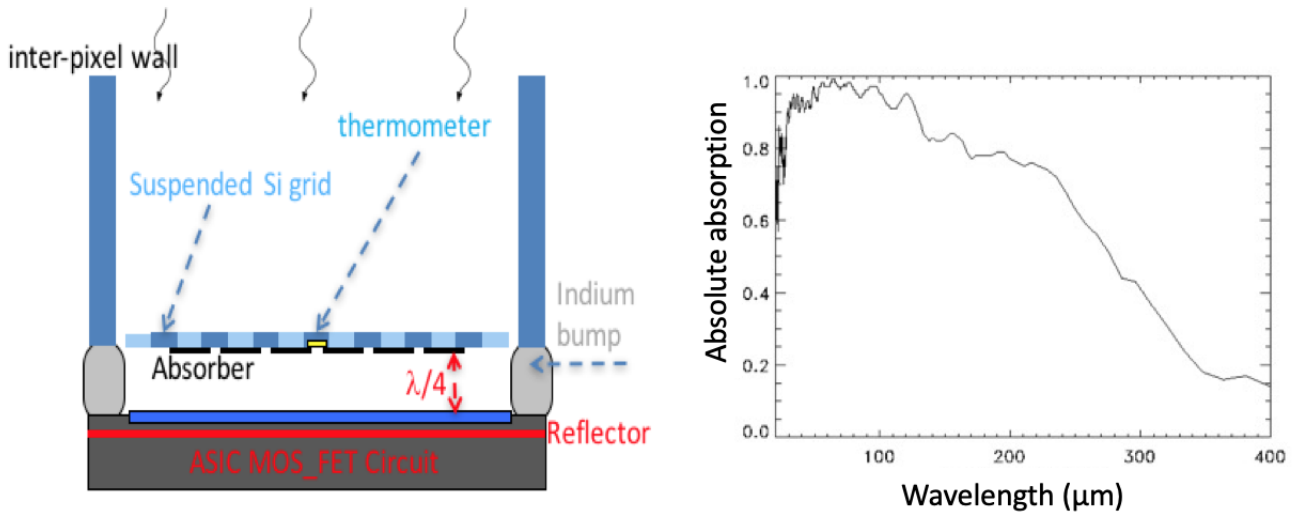


FIGURE 2.11: (Left) The CEA detector optical scheme. Here the indium bumps set the cavity resonance between absorber and backshort reflector ; (Right) Measured absorption when 25 μm bumps are used. (CEA).

The suspended structure

On the CEA Herschel bolometers, the suspended and insulated structure is a 5 μm thick silicon grid covering 72% of the pixel pitch surface. Four legs of $5 \times 5 \mu\text{m}^2$ - section and 700 μm -length insulate the suspended part from a frame of 16×16 pixels at 300 mK, as shown in figure 2.12. The pixel pitch is 750 μm in both directions. In order to reduce the heat capacity, the suspended part of the bolometer is a thin grid whose holes are much smaller than the wavelength, and appear to the wave as a homogeneous

structure of lower refractive index. Moreover the frame is thermally connected to the cold sink, the readout circuit, by indium bumps of $\sim 20 \mu\text{m}$ -height. The readout circuit includes, at its surface, the structured reflector. For the grid material, silicon is preferred to nitride because the crystalline structure has a heat capacity which decreases as T^3 , when cooling to sub-kelvin temperature. For comparison, silicon nitride decreases as T , due to its amorphous structure.

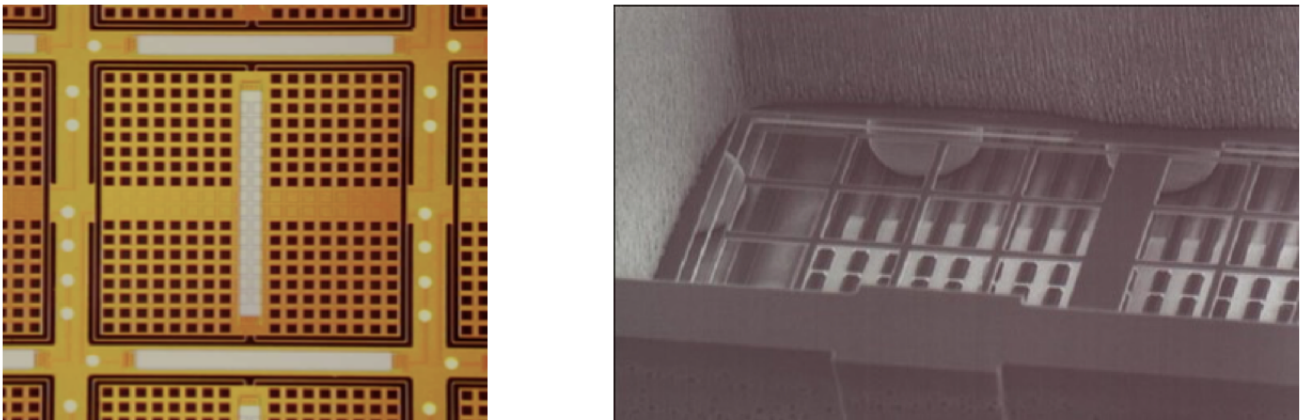


FIGURE 2.12: (Left) Photograph of one pixel within the array : the frame with the horizontal reference thermometers and the suspended grid structure with $5 \mu\text{m}$ thick legs carrying the vertical bolometer thermometer. (Right) Photograph of a part of one pixel observed from the top, which shows the suspended structure made of etched silicon. This picture also provides a direct view of the $20 \mu\text{m}$ -height indium bumps (CEA).

The absorber

The wave absorption is realized by metallic structures matched to the vacuum impedance. As the suspended structure is a silicon grid, the absorbers are square loops deposited around the holes of the grid. This geometry was preferred to other possible patterns (grid, crosses, ...) since a wider absorption plateau with wavelength was predicted by numerical simulations (see figure 2.12). In this configuration, the interaction between absorbing elements on a pixel is dominated by capacitive effects. The absorbers are the largest metallic sub-units on the suspended structure, and the ones with the largest contribution to the global heat capacity. For PACS detectors, superconductive alloys (TiN, WN and TaN), far from T_c , were investigated to reduce the heat capacity. The TiN alloy ($T_c = 4.2 \text{ K}$) was selected. Although the titanium nitride is a superconducting material, absorption is still possible if the incident wave is energetic enough to break Cooper pairs (BCS theory, Hadley (1957)). This occurs for wavelength $\lambda < \lambda_c$ with $\lambda_c = \frac{hc}{3.5 kT_c}$. For TiN, $\lambda_c = 1.8 \text{ mm}$, thus in our frequency range, TiN acts as an absorber. In this thesis, the refractive index of TiN is calculated from (Hilsum, 1954) :

$$n_{TiN} = \sqrt{\frac{1}{2\rho_{TiN}\epsilon_0\omega}}(1 - i) \quad (2.17)$$

with $\rho_{TiN} = 2.4 \times 10^{-6} \Omega.m$ the resistivity of TiN, $\omega = 2\pi f$ the angular frequency and $\epsilon_0 = 8.8 \times 10^{-12} A.s/(V.m)$ the dielectric permittivity of vacuum. By tuning the thickness of the material (and the overall geometry of the absorber), we can match the impedance of the absorber to the one of free space (377Ω) in order to optimize the absorption. However, this is not always suitable, as it will be concluded from calculations in chapter 3.

Finally the quarter-wave cavity is defined by the metal absorbing layer (matched to the impedance of vacuum on the silicon suspended structure) and the low impedance reflector on top of the readout circuit. The indium bumps between the two layers ensure at the same time the size of the cavity, the electrical connection between the thermal sensors and the readout circuit and also the thermal link between bolometers and the cold sink (to the 300 mK cryocooler).

The thermometer

For the thermometer, high impedance (a few $G\Omega$) silicon Phosphorus-doped, Boron-compensated thermal sensors were developed and are still used today. The advantage of using silicon compared to germanium is the possibility to have a full collective process using current doping implantation techniques on silicon wafers. Silicon has also a low heat capacity at low temperature which results in a small thermal time constant. Since at very low temperature (< 1 K) single doped semiconductor such as germanium or silicon are perfect resistors, the conduction is obtained by doubly doping the semiconductor, as far as the doping densities are unbalanced. The resulting physical phenomenon is called the variable range hopping conduction. It has been introduced by Mott and refined by Efros and Shklovskii in presence of a Coulomb gap around the Fermi level. In the most usual case, the electrons jump by tunnel effect, between donors occupied states and empty states at some variable distance. The amount of empty states is linked to the quantity of acceptors in the material. The compensation factor $K = \frac{N_a}{N_d}$, where N_a and N_d are the acceptors and donators density, stands for the mismatch in impurities. The temperature-dependence resistance of doped silicon is described in (Efros and Shklovskii, 1975) :

$$R = R_0 \exp\left(\sqrt{\frac{T_0}{T}}\right) \quad (2.18)$$

where R_0 and T_0 are proper to a thermometer which means that both depend on the doping and on the compensation. This means that the electrical properties of a thermometer can be tuned by adjustments of the doping and especially of the compensation. The weak points of this technique are : (1) a very delicate doping density precision to achieve, rather far from usual micro-electronics requirements and (2) the need to homogenize these dopants in the bulk of the sensor material to mainly avoid systematic deviations from the usual resistance laws and unwanted noise.

The four main functions which define the PACS bolometers have been summarized here. One of the final PACS photometer arrays is shown in figure 2.13.

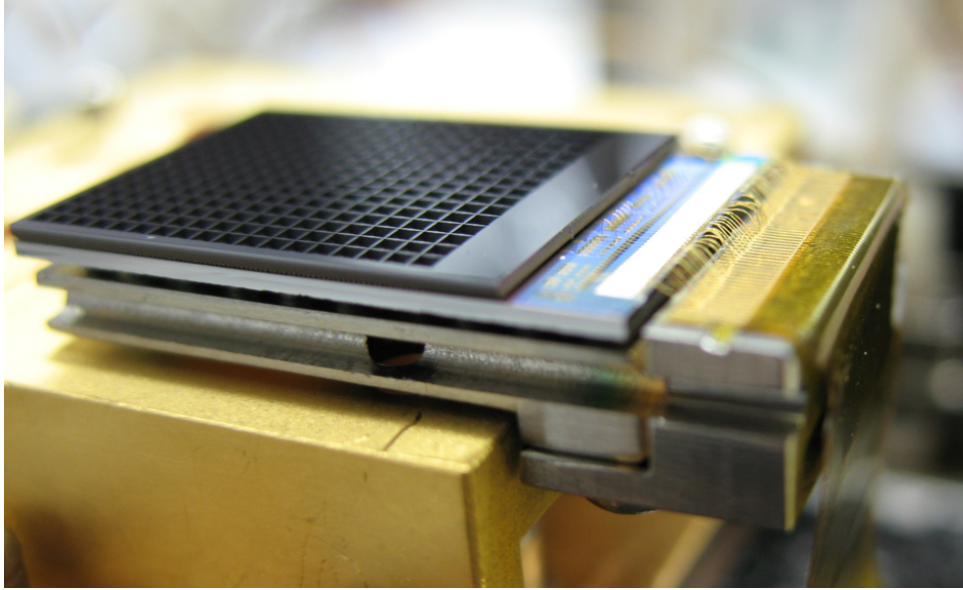


FIGURE 2.13: Photograph of a Herschel/PACS photometer module with 16×18 pixels at the 300 mK thermal stage, connected to the readout circuit (in blue) by indium bumps. We can see details of the gold bondings between the readout integrated circuit and the ribbon cable to the 2 K stage. The two blind pixel rows are under the metalized silicon strip on the bonding side (CEA).

2.2.2 From PACS bolometers to B-BOP bolometers

The PACS photometer has been one of the most used instrument of HERSCHEL, and gave the first image (M51 galaxy) only few hours after recycling the cryocooler. This showed 30 days after the launch, the extraordinary capabilities of the space observatory. The focal plane assembly of 2560 pixels has been, for years, the largest bolometer array in operation. Nevertheless, there was room for improvement : the HERSCHEL development schedule was so tight, that no feedback was possible after experimental tests of the actual detectors.

One improvement is, regarding the new scientific objectives, to achieve a better sensitivity of at least two orders of magnitude (NEP from $\sim 10^{-16} \text{ W}/\sqrt{\text{Hz}}$ to $\sim 10^{-18} \text{ W}/\sqrt{\text{Hz}}$). This is essentially obtained by decreasing the operational temperature. Indeed a reduction of the operating temperature from 300 to 50 mK should be enough to improve sensitivity by a factor of 200, as soon as the thermal sensors are adapted to this temperature in terms of electrical resistance. A better response can also be obtained by geometrical modification of the detectors, i.e. by improving the thermal resistance of the bolometers. For this, one can increase the length of the silicon beam or reduce its section. In any case, the heat capacity must also be reduced in order to prevent any degradation of the detector time constant.

The evolution of the CEA bolometers has followed three milestones.

The first one was to replace the silicon grid by a silicon serpentine structure that absorbs the sub-millimeter radiation. The CEA group made such structures on a $1.5 \mu\text{m}$ - thick silicon-on-insulator (SOI) wafer, with a thermal sensor at the center. Although the temperature is not uniform across the pixel, it should be

maximal at the structure center where the sensor lies (see figure 2.14). The thermal resistance is enhanced by the long and thin strip (shown in green in the picture), and the heat capacity concentrated at the thermal sensor island level. In this scheme, the light absorption is made by dipoles in the two orthogonal directions 2.14.

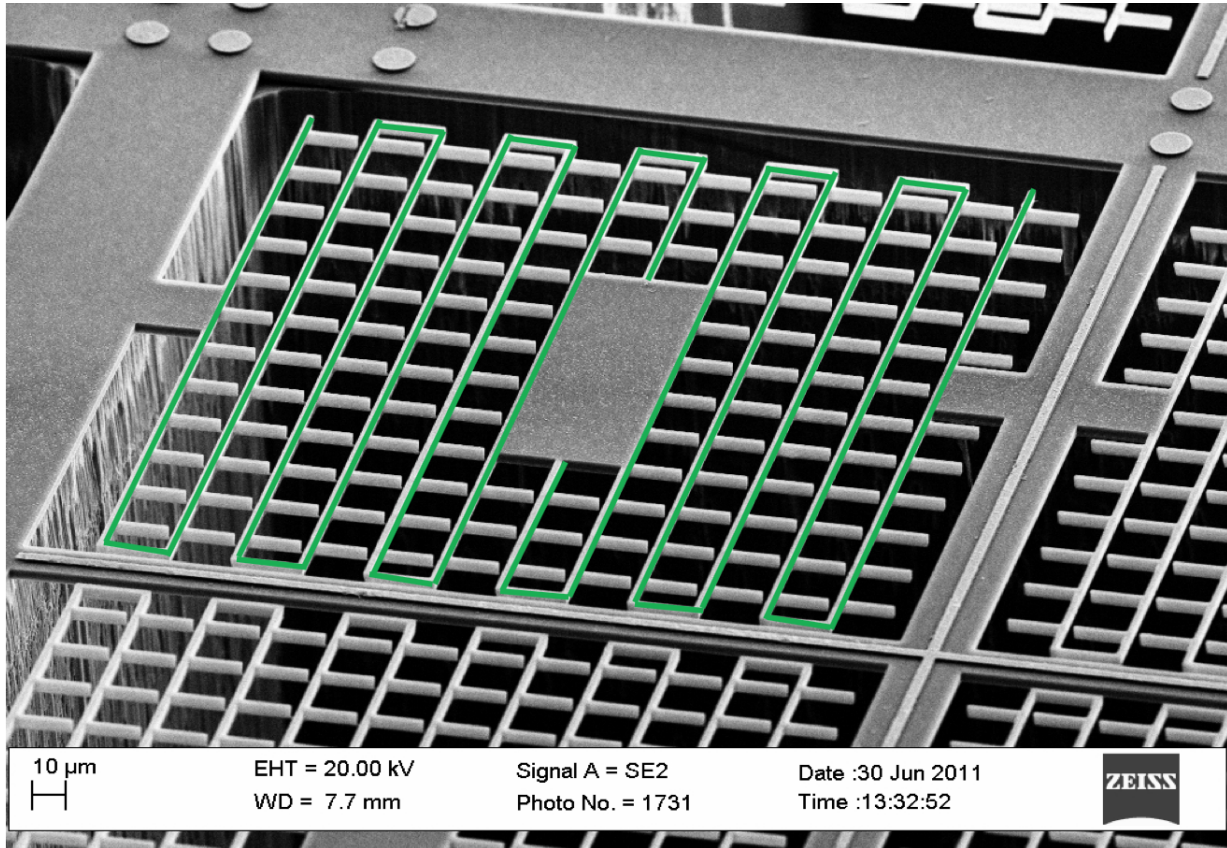


FIGURE 2.14: The serpentine detectors made in 2011 : a long silicon strip (shown here in green) with indentations mimic the silicon grid. Dipoles, deposited on the indentations and on the serpentine are responsible for absorption in the two orthogonal directions. Note that the thermometer is still at the pixel center (CEA).

The second milestone in the detector evolution has been to rethink the conventional thermometer function. Up to this time, the temperature used to vary along the strip and was measured in a single position, at the pixel center. In addition, the Joule power dissipation of the detector bias is concentrated there, and not where the optical power is transformed from electromagnetic energy into heat. Whereas if the temperature sensor (variable resistance) is now distributed along the silicon beam, the electric power will be dissipated everywhere along the beam, and preferentially where the resistance is high : the contact points with the heat sink at both ends. For the next detector iteration, shown in figure 2.15, the support structure carrying the absorbers is also the thermal sensor, cooled by the nails at both ends of the pixel. For this detector, the fabrication process occurs for the first time in our development, “above IC” (IC for Integrated Circuit). This means that the different layers of our detector are grown on a wafer layer by

layer, using material depositions (SiO, metal) and etching.

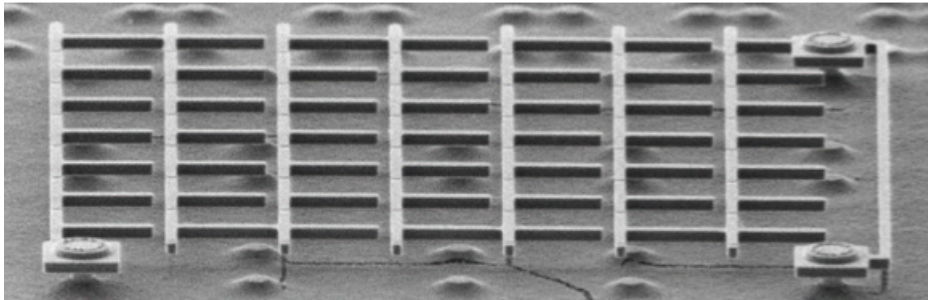


FIGURE 2.15: The strip structure : here the thermal sensor is distributed all along the silicon path with absorbers of the same type as in figure 2.14. Here the cavity above the backshort is filled with Silicon Oxide to reduce the physical height of the cavity, keeping the same resonance (CEA).

Finally, the last key advance, which enabled CEA bolometers to be competitive for a SPICA-type mission, was to introduce new instrumental functionalities at the detector level. In 2014, CEA had the opportunity to build dual-polarization sensitive bolometers, with the two orthogonal directions having the same optical/thermal properties. This marked a turning point since Planck's PSB used to have two grids for each polarization separated by $60 \mu\text{m}$, introducing a small spectral difference that can be seen as a leakage when measuring polarization unbalance, at a very low level, as it is usually done in space observations.

The CEA solution for this detection is a in-pixel double network of absorbing dipoles located as usual at $\lambda/4$ over a reflective layer. Since the working principle of these bolometers is fully described in chapter 3, we will not go into details but it has to be mentioned here that the two networks are in the same plane. Figure 2.16 on the left illustrates one of these pixels; on the right hand side of the same figure is the polarization-sensitive bolometers for millimeter applications.

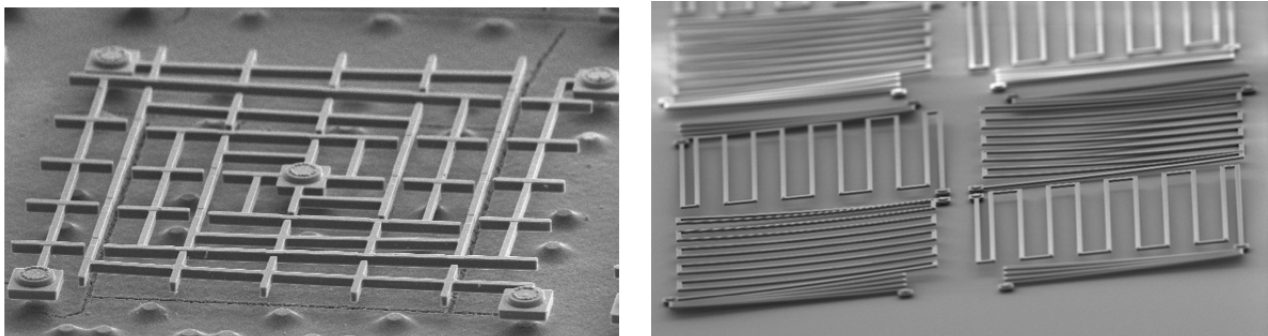


FIGURE 2.16: (Left) A polarization sensitive pixel for the sub-millimeter range : the silicon spirals are the absorbers support as well as the distributed thermal sensor.(Right) A polarization sensitive pixel for the millimeter range : here, there are no spirals because the size of the pixel is close to the wavelength resulting in absorbing dipoles of half of the size of the pixel pitch (CEA).

2.2.3 Perspectives

In this chapter, we have discussed the bolometer technology, in general terms. However, in the rest of this thesis, we focus on the light absorption of detectors, for polarimetry (in chapter 3) or for spectroscopy (chapters 4 and 5) purposes.

The bolometer is a power detector : the efficiency of this kind of detector is expressed through the ratio of absorbed power to incident power. Therefore the absorption is a very critical part since it is the first step of the detection phenomenon and constrains the rest of the measurement. To optimize the absorption, we have investigated what are the parameters that can be tuned. The material, the shape and the dimensions of the absorbers are obviously critical, but the layout of the whole bolometer can also affect the efficiency of the detector. These parameters will be fully tested in the remaining chapters.

Chapter 3

Optimization of the spectral absorption of polarimetric bolometers for SPICA/B-BOP instrument

Contents

3.1	Introduction to linear polarization	52
3.1.1	Definition of Stokes parameters	52
3.1.2	Classical measurements of any polarized state	55
3.2	A first step towards on-chip polarimetry	56
3.3	The SPICA/B-BOP polarimetric imager instrument	61
3.3.1	The SPICA mission : scientific objectives and instruments	61
3.3.2	B-BOP : a polarimetric imager	62
3.4	Optimizing the design of the detectors in the three channels of the B-BOP instrument	64
3.4.1	Optimizing the physical parameters of the detectors	65
3.4.2	Minimizing the cross-polarization	66
3.4.3	Adapting the 200 μm - and the 350 μm -channels from the 100 μm - detectors	68
3.5	Perspectives	69
3.5.1	New design of the focal plane	69
3.5.2	Deriving the Stokes parameters from the detectors signal	70

As described in chapter 1, there are several ways to investigate the Universe. Polarization measurements are one of these tools as they enable one to probe the magnetic field through observations of its effects on matter. In particular, elongated dust grains of the ISM exposed to the magnetic field of the medium tend to align perpendicular to the direction of the B field. The UV/visible unpolarized light from background stars gets polarized by the aligned dust grains medium while the grains, once heated, emit polarized far-infrared light in the direction parallel to the grains orientation. The latter is the scientific target of recent far-infrared polarimeter observatories. By probing the polarization of light (always as a projection on the sky), the structure of the magnetic field in the ISM can be deduced to better understand how it shapes the medium.

3.1 Introduction to linear polarization

So far only linear polarization is expected to carry valuable information on the magnetic field behavior in the ISM. The degree of polarization is foreseen to be of the order of a few percent for the brightest sources, up to 15-20% in some regions. In this section, we provide the necessary background for the understanding of this chapter. We here present the formalism of polarization and describe how linear polarization can be measured. This section has been largely inspired by the book written by Collet (2005).

3.1.1 Definition of Stokes parameters

In this preliminary part, we introduce the Stokes parameters, which are commonly adopted to describe any polarized state of light. For an electromagnetic plane wave travelling in the z-direction (towards us, for example), we can write the two electric field components as being :

$$\begin{cases} E_x(z, t) &= E_{0x} \cos(\omega t - kz + \delta_x) \\ E_y(z, t) &= E_{0y} \cos(\omega t - kz + \delta_y) \end{cases} \quad (3.1)$$

with E_{0x} and E_{0y} the maximum amplitudes of the x and y components respectively, $\omega = 2\pi f$ the angular frequency, $k = \frac{2\pi}{\lambda}$ the wave number and δ_x and δ_y the phases of the x and y components respectively. We set $\delta = \delta_y - \delta_x$, the phase difference of the two orthogonal components.

From the first definitions, we can identify degenerate polarization states which correspond to specific states of the electric field obtained for different combinations of amplitudes and phases. The degenerate polarization states are schematized in figure 3.1. We have linearly horizontally/vertically polarized (LHP/LVP) light if either E_{0y} or E_{0x} is equal to 0. When $E_{0x} = E_{0y}$ and $\delta = 0$ [π], the light is linearly $\pm 45^\circ$ polarized (L+45P/L-45P). Finally, for $E_{0x} = E_{0y}$ and $\delta = \pi/2$ [π], we have right/left circularly polarized light (RCP/LCP). Note that the RCP and LCP light stand for rotation clockwise and counter clockwise

rotations respectively when propagating towards the observer. These specific polarization states simplify any polarization calculation and above all, they lay the foundation of any polarization measurement when defining scientific instruments.

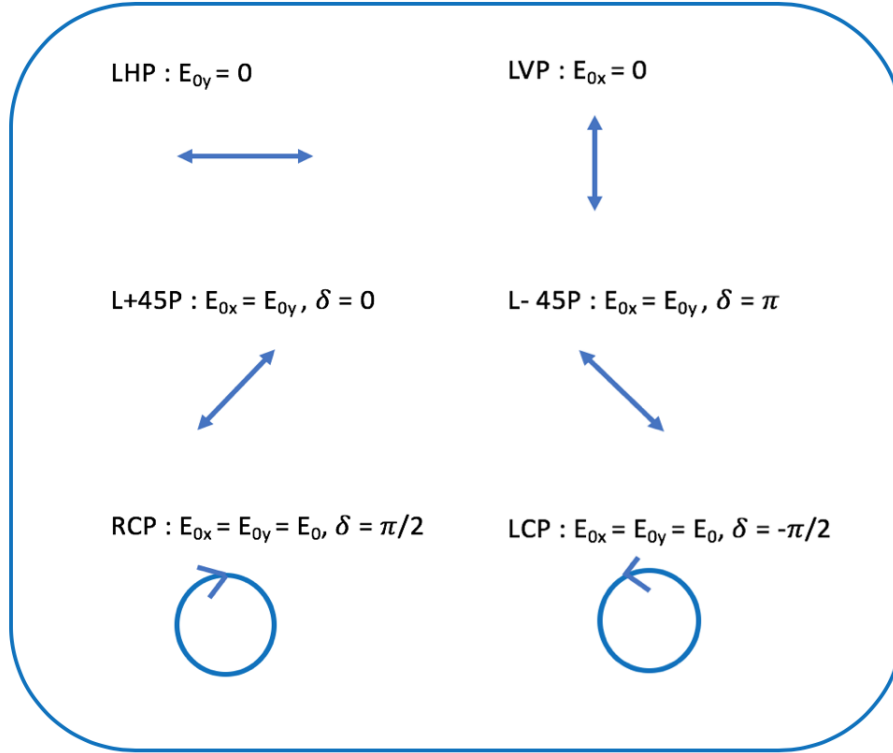


FIGURE 3.1: Degenerate Polarization States : linearly horizontal/vertical polarized (LHP/LVP), linearly $\pm 45^\circ$ polarized (L+45P/L-45P), right/left circularly polarized light (RCP/LCP) (Collet, 2005).

For simplicity, equations 3.1, can be turned into complex notation :

$$\begin{cases} E_x = E_{0x} \exp(i\delta_x) \\ E_y = E_{0y} \exp(i\delta_y) \end{cases} \quad (3.2)$$

We can now define the Stokes parameters in complex notation :

$$\begin{cases} S_0 = E_x E_x^* + E_y E_y^* \\ S_1 = E_x E_x^* - E_y E_y^* \\ S_2 = E_x E_y^* + E_y E_x^* \\ S_3 = i (E_x E_y^* - E_y E_x^*) \end{cases} \quad (3.3)$$

where * refers to the complex conjugate. We use the definitions of equations 3.2 to compute the Stokes

parameters :

$$S = \begin{pmatrix} S_0 \\ S_1 \\ S_2 \\ S_3 \end{pmatrix} = \begin{pmatrix} E_{0x}^2 + E_{0y}^2 \\ E_{0x}^2 - E_{0y}^2 \\ 2 E_{0x} E_{0y} \cos(\delta) \\ 2 E_{0x} E_{0y} \sin(\delta) \end{pmatrix} \quad (3.4)$$

In the following, because it is the commonly used formalism, the Stokes components S_0 , S_1 , S_2 and S_3 will be named I , Q , U and V respectively. The Stokes vector can be easily derived for each degenerative polarization state :

$$\begin{aligned} S_{LHP} &= I_0 \begin{pmatrix} 1 \\ 1 \\ 0 \\ 0 \end{pmatrix}; & S_{LVP} &= I_0 \begin{pmatrix} 1 \\ -1 \\ 0 \\ 0 \end{pmatrix}; & S_{L+45P} &= I_0 \begin{pmatrix} 1 \\ 0 \\ 1 \\ 0 \end{pmatrix}; \\ S_{L-45P} &= I_0 \begin{pmatrix} 1 \\ 0 \\ -1 \\ 0 \end{pmatrix}; & S_{RCP} &= I_0 \begin{pmatrix} 1 \\ 0 \\ 0 \\ 1 \end{pmatrix}; & S_{LCP} &= I_0 \begin{pmatrix} 1 \\ 0 \\ 0 \\ -1 \end{pmatrix}. \end{aligned}$$

These derivations indicate the meaning of each Stokes parameter :

- I is the total intensity of the electric field,
- Q is the preponderance of LHP light over LVP light,
- U is the preponderance of L+45P light over L-45P light,
- V is the preponderance of RCP light over LCP light.

Stokes parameters are very convenient because they can describe any polarization, but also any unpolarized state. Partially polarized light S can be represented by :

$$S = \begin{pmatrix} I \\ Q \\ U \\ V \end{pmatrix} = (1 - \mathcal{P}) \begin{pmatrix} I \\ 0 \\ 0 \\ 0 \end{pmatrix} + \mathcal{P} \begin{pmatrix} I \\ Q \\ U \\ V \end{pmatrix} \quad (3.5)$$

where \mathcal{P} corresponds to the degree of polarization ($0 \leq \mathcal{P} \leq 1$) : $\mathcal{P} = 1$ for completely polarized light while $\mathcal{P} = 0$ for unpolarized light. The degree of polarization of light can be computed from the Stokes parameters by the equation :

$$\mathcal{P} = \frac{I_{pol}}{I_{tot}} = \frac{\sqrt{Q^2 + U^2 + V^2}}{I} \quad (3.6)$$

3.1.2 Classical measurements of any polarized state

Any polarized state can be measured with two optical components : a retarder and a polarizer. The principle of this measurement is shown in figure 3.2. The retarder phase shifts the incident beam described

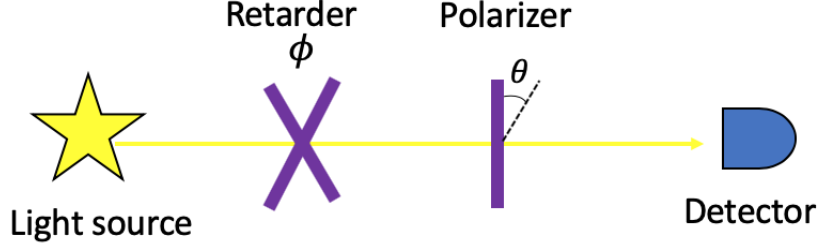


FIGURE 3.2: Principle of measurement of the Stokes parameters

by E_x, E_y : it advances E_x by $\phi/2$ and retards E_y by $-\phi/2$:

$$\begin{cases} E'_x = E_x \exp(i \phi/2) \\ E'_y = E_y \exp(-i \phi/2) \end{cases} \quad (3.7)$$

The polarizer only transmits one direction of the polarization, depending on the axis of the polarizer (described by the projection angle θ). The resulting electric field is :

$$E'' = E_x \exp(i \phi/2) \cos(\theta) + E_y \exp(-i \phi/2) \sin(\theta) \quad (3.8)$$

The intensity \mathcal{I} measured by the detector is therefore :

$$\begin{aligned} \mathcal{I} &= E'' \cdot E''^* \\ &= \frac{1}{2} [[E_x E_x^* - E_y E_y^*] \cos(2\theta) + [E_x E_x^* + E_y E_y^*] \\ &\quad + [(E_x E_y^* + E_y E_x^*) \cos(\phi) + i(E_x E_y^* - E_y E_x^*) \sin(\phi)] \sin(2\theta)] \\ &= \frac{1}{2} [I + Q \cos(2\theta) + (U \cos(\phi) + V \sin(\phi)) \sin(2\theta)] \end{aligned} \quad (3.9)$$

The derivation of the four Stokes parameters from measurements is achieved for different combinations of θ and ϕ :

- $\mathcal{I}(\theta = 0^\circ, \phi = 0^\circ) = \frac{1}{2} (I + Q)$
- $\mathcal{I}(\theta = 90^\circ, \phi = 0^\circ) = \frac{1}{2} (I - Q)$
- $\mathcal{I}(\theta = 45^\circ, \phi = 0^\circ) = \frac{1}{2} (I + U)$
- $\mathcal{I}(\theta = 45^\circ, \phi = 90^\circ) = \frac{1}{2} (I + V)$

I , Q , U and V can be therefore obtained from the four following measurements : $(\theta = 0^\circ, \phi = 0^\circ)$, $(\theta = 90^\circ, \phi = 0^\circ)$, $(\theta = 45^\circ, \phi = 0^\circ)$ and $(\theta = 45^\circ, \phi = 90^\circ)$. However, in this chapter, we only discuss measurements of the linear polarization, which can be achieved by the three measurements : $(\theta = 0^\circ, \phi = 0^\circ)$, $(\theta = 90^\circ, \phi = 0^\circ)$ and $(\theta = 45^\circ, \phi = 0^\circ)$.

3.2 A first step towards on-chip polarimetry

Conventional polarization measurements

As a typical example of an experiment which observes polarization in astronomical sources at sub-millimeter wavelengths, we can cite the PILOT balloon-borne experiment (Bernard, 2005). With three flights (2015, 2017 and 2019), PILOT has completed almost 50 hours of scientific observations of some regions in the Galactic plane and of the diffuse ISM. With a better accuracy and higher angular resolution, the balloon has complemented Planck observations at shorter wavelengths ($\lambda = 240 \mu\text{m}$). PILOT polarization measurements are achieved by use of a rotating half-wave plate and a fixed polarizer/analyzer in front of the detector. The 45° tilt of the polarizer allows the detection of the transmitted and reflected polarization components with two separate focal plane arrays. A sketch of the optics is presented in figure 3.3. By rotation of the half-wave plate, the polarization can be phase-shifted and then split again by the analyzer in two orthogonal directions. In principle, the information of the linear polarization (i.e. the I , Q , U Stokes parameters), is retrieved with at least two angular positions of the half-wave plate. The optics design for polarization follows a classical design; nevertheless less bulky solutions have been brought to experiments. One can mention the Archeops balloon-borne experiment (Benoit et al., 2004) and its three Ortho Mode Transducers (OMTs). Each OMT is made of a polarizer at 45° which sends the two orthogonal polarizations on two distinct detector pixels, in a more compact fashion than traditional optics (figure 3.4). The polarization axis of the three OMTs is rotated by 60° with respect to each other. By scanning these three doubled sensors, the information about linear polarization can be retrieved while minimizing errors since pixels of one OMT observe the same beam on the sky.

First polarization-sensitive bolometers

To push further the concept of compact bolometers for polarization measurements, investigations have been conducted in order to get rid of the polarizer. Indeed, any error of misalignment of the reflection and the transmission focal planes of PILOT-type instruments may introduce systematic measurement errors of the polarized field. For this reason, but among all for simplicity, several labs have progressively developed on-chip polarimeters. The polarization-sensitive bolometers (PSBs) have been first introduced by Jones et al. (2002), from Caltech and JPL. They originate from the “spider-web” bolometer (SWB) technology developed at JPL in the 1990s (Bock et al., 1995) by photolithographic techniques. For the first time,

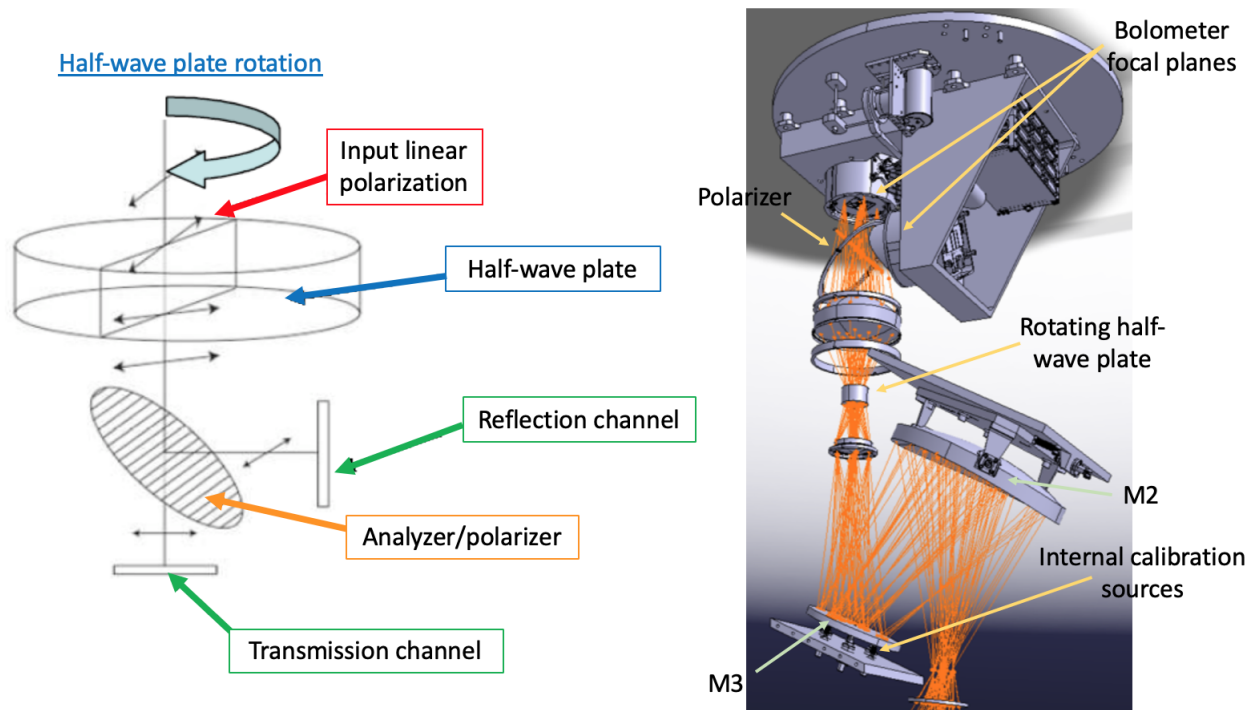


FIGURE 3.3: Principle of polarization measurement on the PILOT balloon (adapted from Engel et al. (2009))

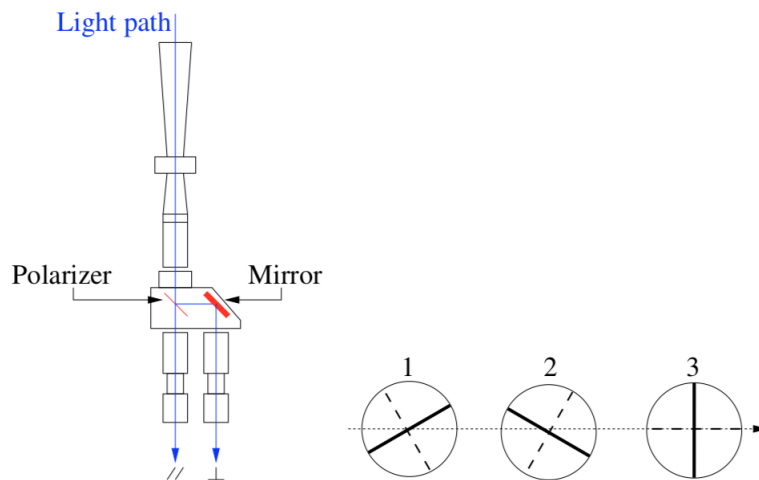


FIGURE 3.4: Measurement of polarization on the Archeops balloon-borne experiment. (Left) Scheme of an Ortho Mode Transducer : light enters the feedhorn, passes through a beam splitter and the two orthogonal linear polarizations are transmitted or reflected to a bolometer ; (Right) Orientation of the polarization for the three OMTs, the arrow corresponds to the scan direction (Benoit et al., 2004)

the membrane absorber is made of a thin metallic mesh, which leads to (1) a smaller heat capacity of the bolometer and (2) a bolometer transparent to cosmic rays. From this development, PSBs have been derived, with the spider-web absorber being replaced by a rectangular grid (see figure 3.5, left). One bolometer has two free standing lossy grids separated by $60 \mu\text{m}$ both thermally and electrically isolated,

each grid being metallized in one single direction (either horizontally or vertically). For one particular grid, only the electric field component which is parallel to the direction of the metallization deposits energy in the grid; the orthogonal component does not interact with the grid. Because the two grids are part of the same bolometer and receive the signal of the same filters and feed structure, systematic effects are therefore minimized. With one PSB pair, it is possible to measure the first two Stokes parameters (I, Q) by the sum and the difference of the signals of one detector; the value of the third one (U) can be derived by having one other PSB pair rotated by 45° with respect to the first. A sketch of the Planck/HFI bolometer focal plane, which uses this technology, is shown in figure 3.5 (Right) where we can see, in addition to the spider-web bolometers, how the PSBs and especially their different polarization axes are configured. One should mention, however, that the cross-polarization of such designed PSBs has been estimated to be of the order of several percent : one grid is not perfectly insensitive to the polarization perpendicular to the direction it was designed for (Lamarre et al., 2010). This adds another constraint on the absorber impedance : while it was only adapted to the overall geometry of the bolometer (corrugated feedhorn and quarter-wave cavity) to maximize absorption in the SWB case, the PSB absorber impedance had also to minimize cross-polarization (Holmes et al., 2008).

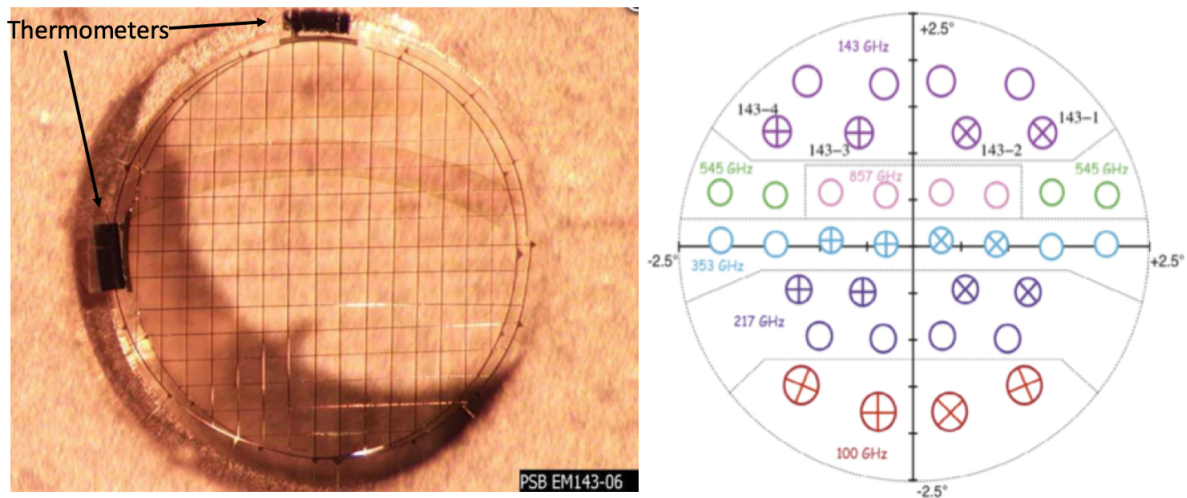


FIGURE 3.5: (Left) One PSB for Planck/HFI : two rectangular grids separated by $60 \mu\text{m}$ (indistinguishable on the picture), each one being metallized in an orthogonal direction, to measure the I and Q Stokes parameters. The two thermometers of the two grids are shown by the arrows (PLANCK collaboration); (Right) Planck/HFI focal plane : 20 spider-web bolometers at five frequencies and 16 PSB pairs at four frequencies (Rosset et al., 2010)

Slot-antenna bolometers

For the sake of homogeneity in the bolometer response, JPL carried out further investigations on PSBs and finally proposed a design with only one level of absorbers (and no longer two grids) arranged in a

planar antenna-coupled bolometers configuration (Bock, 2008). A planar antenna consists of a network of dipole sub-antennas, as depicted in figure 3.6. In this configuration, there are two independent networks of sub-antennas, one for the vertical polarization and one for the horizontal polarization. Slot-antennas of the same network are combined coherently and are connected to a TES bolometer. Because the sub-antennas are in phase, the beam pattern can be controlled before the energy gets dissipated in the TES bolometer. The acceptance solid angle of each pixel is then determined by the array geometry and for this reason, feedhorns are no longer needed. Note that the dipole network is also embedded in a quarter-wave cavity to improve the efficiency of the absorption. As the whole pixel is obtained by photolithography, this makes possible the production of large arrays. The scheme can also be tuned to different wavelength bands simply by scaling the antenna. For the measurement of Stokes parameters, the sum and the difference of the two signals of each planar antenna provide I and Q. By having the two polarization measurements in one plane, issues related to positioning of one grid with respect to the other (in comparison to Planck PSBs design) are reduced. Finally, manufacturing bolometers collectively enables one to produce detectors homogeneous with regard to spectral and thermal responses. In Bock (2008), the cross-polarization is measured to be 3%.

CEA's new bolometers for the SPICA/B-BOP instrument, which this chapter is focused on, have been inspired by the JPL planar antenna-coupled bolometers.

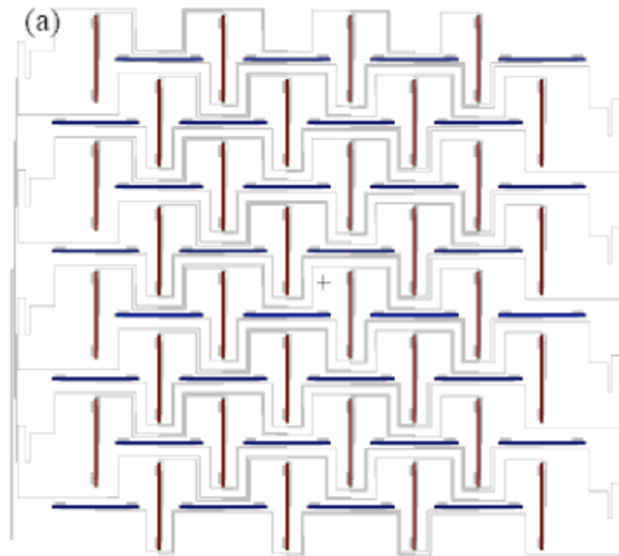


FIGURE 3.6: Schematic of a planar antenna : two interleaved networks of sub-antennas (blue and red) which are each sensitive to one direction of polarization. Each network is connected to a TES bolometer (not shown here) (Bock, 2008).

Other example of emerging designs in the KIDs and TESs field

Before moving on to the CEA polarization sensitive bolometers, we still want to mention recent developments in the KID and TES field to introduce the polarization measurement within the pixel.

As an example of newly designed KIDs, the lumped-element kinetic inductance detectors (LEKIDs, Doyle et al. (2008)) have made possible the single polarization measurement within one pixel because the wave is directly absorbed by a meandered inductor which is polarization sensitive by geometry (McCarrick et al., 2014). The concept has been extended to dual polarization (McCarrick et al., 2016, 2017). Like in the single polarization case, the inductors act as the absorbers; however the two orthogonal polarization are detected by using two orthogonal resonators in one pixel : one has the shape of a hairpin while the other looks like two hairpins to avoid any crossover (figure 3.7). Despite a design asymmetry, the geometry is optimized in order for the two orthogonal antennae to have the same spectral response.

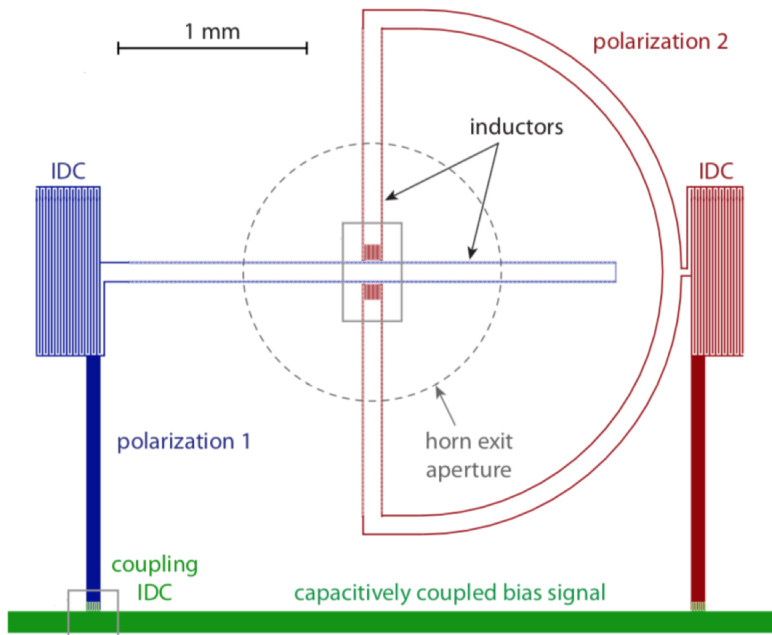


FIGURE 3.7: Sketch of a dual polarization LEKID pixel : each pixel has two orthogonal inductors sensitive to orthogonal polarizations (McCarrick et al., 2017)

Researches in the TESs field have resulted in the design of a new pixel : a multi-chroic dual polarized sinuous antenna (Suzuki et al. (2012), for example). The pattern of the antenna, presented in figure 3.8, enables broadband absorption in the millimetre-wave range. The signal, after antenna-coupling, is transmitted to on-chip filter banks where distinct TES bolometers can therefore disentangle the two orthogonal polarizations and the frequency bands. In both cases (LEKID and sinuous antenna TES), with pixels axis which differ by 45° , it is possible to recover the three first Stokes parameters.

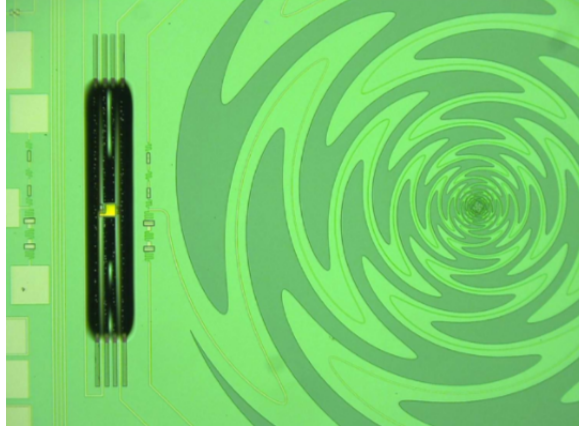


FIGURE 3.8: Photograph of a multi-chroic dual polarized sinuous antenna TES bolometer. The sinuous antenna is shown in dark green on the right of the figure while the black rectangular on the left is the TES bolometer (from Suzuki et al. (2012))

3.3 The SPICA/B-BOP polarimetric imager instrument

In this section, we aim at describing the SPICA mission, its scientific objectives and instruments, especially the polarimetric imager B-BOP, which CEA is in charge of.

3.3.1 The SPICA mission : scientific objectives and instruments

The SPace Infrared telescope for Cosmology and Astrophysics, SPICA mission (Roelfsema et al., 2018) is a joint space project of Japan and Europe which is expected to be launched in the early 2030s (satellite design in figure 3.9 (left)). This mission has been pre-selected as one of the M5 candidates of ESA (European Space Agency). Phase A study will last up to the final selection at the end of 2021.

This space infrared observatory follows the path of the ISO and HERSCHEL satellites by exploring the Universe in the 12-350 μm wavelength range and thus will extend the study of the origin and early-evolution of planets, stars and galaxies. By observing in the far-infrared/ sub-millimetre range, we can have access to the cold dust, where galaxies, stars and planets are formed and grow. To reach these challenging scientific goals, sensitivities of the observations need to be considerably improved in comparison to the last space observatory HERSCHEL. This is achieved by pushing the technological limits of the telescope. The major advance is the cooling down of the 2.5-meter primary mirror to below 8 K (80 K for HERSCHEL). So far, it was not possible to have such a large and cold mirror. The progress on this technical aspect and the use of ultra-sensitive detectors will lead to the collection of data with unprecedented sensitivities (2 orders of magnitude compared to HERSCHEL). To optimally exploit this progress for science, SPICA will have three instruments on board : SMI, SAFARI and B-BOP. Figure 3.9 (right) shows how the unvignetted field of view in the focal plane is shared by the three instruments, nevertheless note that this configuration might change during the coming months. The SPICA Mid-infrared Instrument (SMI) is a spectrometer/camera

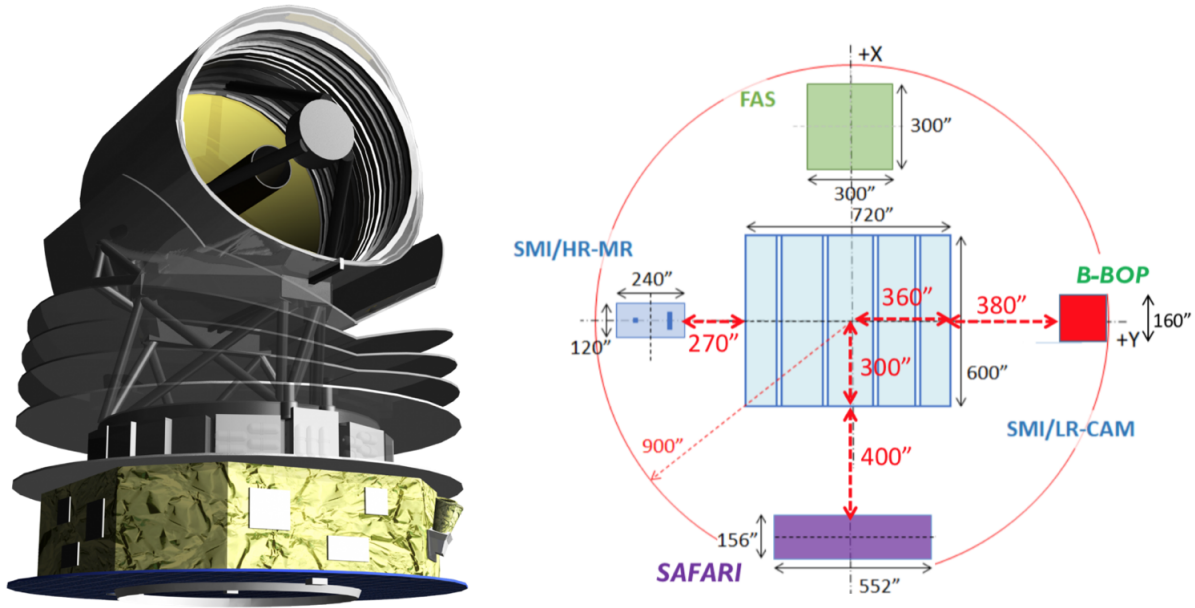


FIGURE 3.9: (Left) The SPICA Infrared telescope for Cosmology and Astrophysics SPICA (JAXA); (Right) This scheme shows how the three instruments of SPICA (SMI, SAFARI and B-BOP) share the unvignetted field of view at the level of the pick-off mirror. The exact arrangement might still change during the coming months. (JAXA/SPICA team)

which observes in the 12-36 μm range. The spectrometer can reach a large range of resolving powers (from 50 to 28,000) in three modes where the imaging capability decreases with spectral resolution. The SPICA Far-IR Spectrometer (SAFARI) works in the 34-230 μm range at different spectral resolutions : from 300 in the low resolution mode to 2000-11,000 in the high resolution mode. More details will be given on these two spectrometers, in chapter 4. The B-BOP polarimetric imager is described more precisely, in the next section.

3.3.2 B-BOP : a polarimetric imager

The design of the B-BOP instrument, previously called POL (Rodriguez et al., 2018), has been driven by the need to map the magnetic field (through polarization) inside Galactic filamentary structures. The specificity of this instrument is to use detectors which are intrinsically sensitive to polarization. Due to the large focal plane and to the polarizing detectors, B-BOP will combine both imaging and polarimetric capabilities. To achieve science objectives, it will be possible to observe simultaneously filaments, for example, in three different wavelength ranges centred around 70 μm (initially 100 μm), 200 μm and 350 μm . The three focal planes are presented in figure 3.10 on the left. To take full advantage of the low temperature of the primary mirror at 8 K, the detectors will be cooled down to 50 mK with a dedicated hybrid adiabatic demagnetization refrigerator (ADR)/helium sorption cooler to achieve a sensitivity (NEP) better than $3 \times 10^{-18} \text{ W}/\sqrt{\text{Hz}}$. The different cooling stages follow a Russian doll configuration down to 50 mK, this is

presented on the right hand side of figure 3.10. The design of the B-BOP detectors enables the implementation of a very compact imaging polarimeter by getting rid of the conventional analyzer/polarizer. This also eliminates any systematic effect due to misalignment between separate focal planes for each polarization. In addition, because astronomers only look after linear polarization of light, three different measurements ($(\theta = 0^\circ, \phi = 0^\circ)$, $(\theta = 90^\circ, \phi = 0^\circ)$ and $(\theta = 45^\circ, \phi = 0^\circ)$) should be sufficient and we should in principle, get rid of the retarder. However, in practice, an achromatic half-wave plate could be necessary to disentangle the scene polarization from the instrumental self-polarization. A partially polarized rotating source is also considered for this calibration.

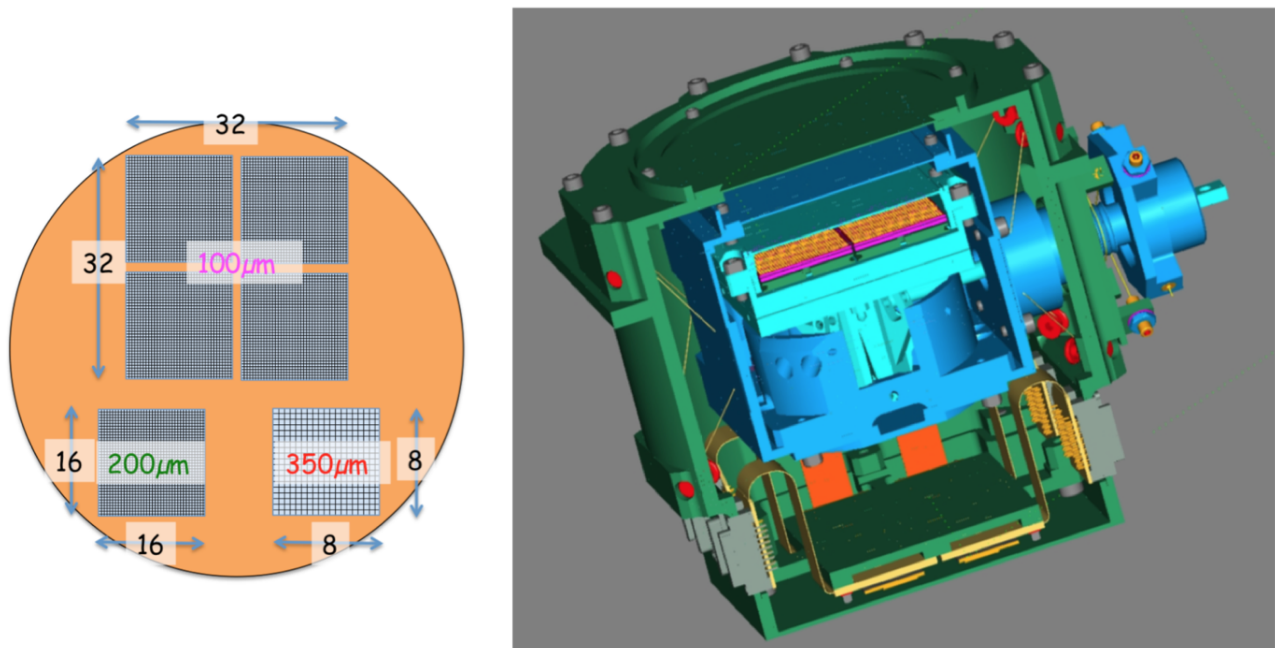


FIGURE 3.10: (Left) B-BOP focal plane with its three bands : 70 μm (initially 100 μm), 200 μm and 350 μm ; (Right) the Russian doll focal plane array structure : 50 mK stage (light blue), 300 mK stage (dark blue) and 1.7 K stage (green). The 50 mK and 300 mK stages are suspended by Kevlar wires (B-BOP team)

The B-BOP detectors are directly part of the legacy of the HERSCHEL/PACS instrument and of the bolometer technology initiated at CEA/LETI. These bolometers use structured absorbers, with integrated thermometers, suspended above a quarter-wave cavity made of silicon oxide (11 μm) and vacuum (2 μm). For B-BOP needs in polarization, “each pixel consists of two orthogonal arrays of dipole antennas supported by four interlaced spirals, which fill all the pixel surfaces” (CEA patent), as described by Adami et al. (2019). Thermometers are essentially made of silicon unbalanced doping with phosphorus (P) and boron (B) to increase the conductivity at very low temperature (Adami et al., 2018). Figure 3.11 shows a photograph of one pixel (same pixel in the left and right figures) of the first array produced to test the mechanical feasibility of the suspended spirals for the working principle of the B-BOP detectors. On the left figure, we can see the four silicon spirals : the two red and the two blue ones meet in the central

nail respectively. Branches with the same color are sensitive to the same polarization direction. Titanium nitride (Aliane et al., 2018) is deposited on top of silicon beams, which are in the same plane as the silicon backbone, to form the orthogonal dipole antennae. Green dipoles are supported by the blue arms while the yellow dipoles are supported by the red arms. In this way, spirals of the same color carry the signal of one single polarization direction and the two others carry the signal of the other one : the two polarizations are thermally decoupled from each other. It must be emphasize that in contrast to JPL slot antennas which work as a phased array, the energy absorbed by the unconnected dipoles is locally dissipated in each dipole and the heat conducted to the thermometer so there is no significant directivity of the whole pixel.

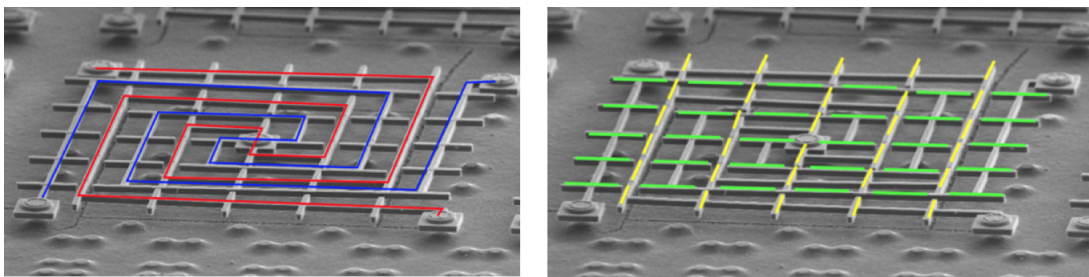


FIGURE 3.11: Photographs of one single pixel : (Left) blue and red spirals are two different thermometers, each one of them carries one polarization signal; (Right) green and yellow antenna absorbers are dipoles in two orthogonal directions.

3.4 Optimizing the design of the detectors in the three channels of the B-BOP instrument

This section aims at optimizing the design of the B-BOP detectors through electromagnetic simulations. This work has been published in the Journal of Low Temperature Physics (Bounissou et al., 2018) and it is the reason why the following is broadly inspired by this paper. Since the 100 μm pixel has been simulated firstly and will still be the proof-of-concept of the manufacturing for the ESA phase A study, its electromagnetic model is presented here in the first part. However, for scientific reasons, the first shortest wavelength band has been recently shifted to 70 μm and the same analysis could easily be applied to this case. The second part is an adaptation of the work presented in Reveret et al. (2010) to the 200 μm and 350 μm focal planes. In this chapter, we only focus on the electromagnetic behavior of the pixels by optimizing the spectral response of the polarizing pixels in each band. This study is a preliminary work that initiates the spectroscopy developed in the chapters 4 and 5. This chapter ends with perspectives concerning the evolution of the now called Stokes pixels.

3.4.1 Optimizing the physical parameters of the detectors

3D electromagnetic simulations using the electromagnetic wave module of the COMSOL Multiphysics software have been performed to predict the electromagnetic response of the detectors designed for the B-BOP instrument. In these calculations, the chosen criterion is the optical absorption as a function of the wavelength over the three different spectral bands of B-BOP. Only calculations for the 100 μm band are developed here.

Silicon bolometers as they are currently thought at CEA, involve two resonances. The vertical resonance is related to the quarter-wave cavity while the horizontal resonance is determined by the structured shape of the absorbers (antennas). The quarter wave cavity is defined by the stack of layers shown in the cross-section depicted in figure 3.12 (left). This is a schematic view of what we observe in figure 3.11. Due to the large computer resources required in 3D simulations of a full pixel, we have chosen to focus on one unit cell of the pixel, defined by four (half-) dipoles (as presented in figure 3.12 (right)), assuming a periodical pattern and thus an infinite pixel.



FIGURE 3.12: Left : Stack of the different layers defining the $\lambda/4$ cavity (thicknesses : Si : 1.5 μm , vacuum cavity : 2 μm , SiO₂ cavity : 11 μm). Right : The unit cell with four (half-) TiN absorbers, pattern seen from above the detector. The yellow and green dipoles correspond to the antennas (same color) of the figure 3.11, right.

Several parameters concerning the dimensions of the dipoles can be optimized : the length, the thickness and the width (thus the impedance) and the distance between two horizontal (/vertical) dipoles in a line. For this optimization, we send an electromagnetic wave polarized in one direction (one of the two axis directions defined by the dipoles) and compute the amount of energy effectively absorbed by the dipoles which should be 100% sensitive to the polarized radiation. In this part, we have chosen to present results for the dipoles optimization about the length and the impedance for the 100 μm band.

In figure 3.13 (top) the optical absorption as a function of the wavelength is presented for different lengths of dipoles. The quarter wave cavity as described in 3.12 (left) is adapted for the 100 μm band and we get the best absorption for a length of dipoles equal to 40 μm . Further simulations for the determination of

the optimal length have led to $\sim 35 \mu\text{m}$ which corresponds to $\sim \lambda/3$. For clarity of the figure, we only present here results of simulations obtained for a length of dipoles varying in steps of ten microns. It must be emphasized that an optimal length of $\sim \lambda/3$ is quite different from the optimal length in the case of a single antenna ($\sim \lambda/2$), which means that a dipole embedded in an antenna network can only be optimized as part of the overall system.

The optimization of the impedance as a parameter of the dipoles is shown in figure 3.13 (Bottom). Hadley and Dennison (1947), Fante and McCormack (1988) have demonstrated that a screen located a quarter wavelength above a reflector will absorb 100% of incoming light if and only if the surface impedance matches the free space impedance ($Z_0 = 377 \Omega$). Moreover, when a more complex absorber (network of antennas) is embedded in a quarter wave cavity of SiO_2 and vacuum (figure 3.12, left), the optimized impedance is quite different. Figure 3.13 (bottom) shows that we should decrease the impedance by a factor of 2 (and thus multiply the thickness of the absorbers by a factor of 2) in order to be almost 100% efficient over the whole bandwidth. The main reason for this shift of optimum surface impedance is the Si/vacuum/ SiO_2 cavity, but the resonance is also reinforced by the network of antennas designed for the $100 \mu\text{m}$ band.

Similar simulations use the distance between two horizontal (/vertical) dipoles in a line as a parameter : the dipoles need to be as close as possible. In practice, the minimum distance between these dipoles will be tailored to the technological feasibility of the process.

3.4.2 Minimizing the cross-polarization

In the previous part, we have shown how the length and the impedance of the dipoles could be optimized. Optical simulations can also predict performances for the detector as a function of the width of dipoles : a priori the wider the dipoles, the more efficient the detectors. However, because increasing the width of the dipoles induces cross-polarization, we need to find a trade-off between cross-polarization and technological feasibility. For this purpose, we simulate an incoming wave linearly polarized in one of the two directions of the unit cell, presented in figure 3.12 (right) and calculate the power dissipated by Joule heating in the parallel and orthogonal sets of dipoles separately. The cross-polarization is then defined as the ratio between the absorption of the orthogonal dipoles, that should not be sensitive to the incoming wave, over the total absorption of the unit cell (exactly $:10 \cdot \log_{10}(\text{this ratio})$ in dB). Figure 3.14 shows the cross-polarization in a logarithmic scale over the $100 \mu\text{m}$ band for different width w of dipoles. We choose $w = 2 \mu\text{m}$ as the optimal width. This dimension is technologically achievable and should meet the scientific requirement (we remind that we want to be able to observe a few percent of polarization) : 1/1000 of cross-polarization is expected for this value.

In this section, we have shown several results obtained by electromagnetic simulations. First, the quarter

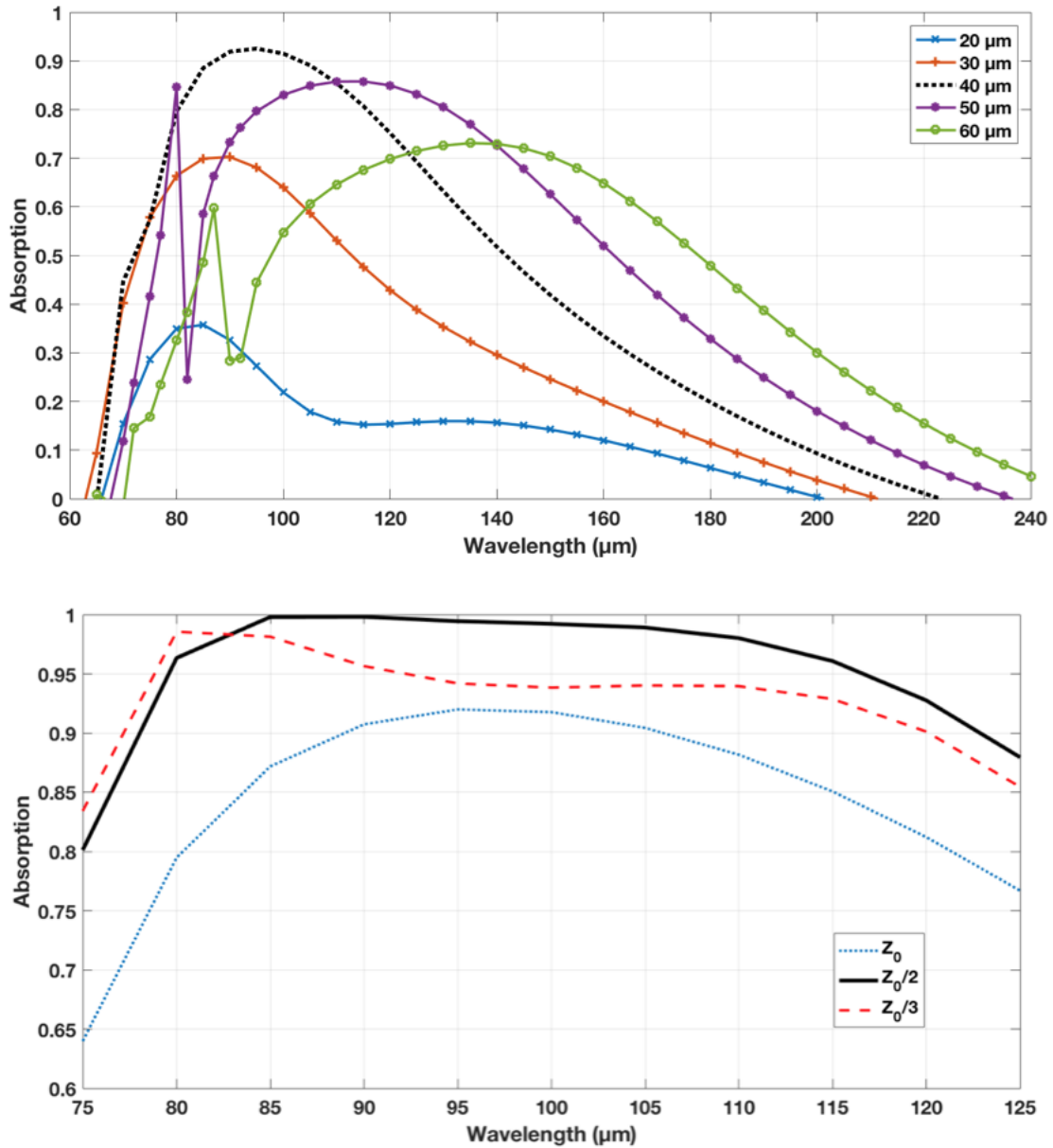


FIGURE 3.13: Top : Optimization of the length of the dipoles for the 100 μm band : optimal length is around $\lambda/3$ when matching the free space impedance Z_0 . Bottom : Optimization of the impedance of the absorbers for the 100 μm band : when matching an impedance $Z_0/2$, the absorption is optimized (almost 100%) over the bandwidth (dipoles length equal to 35 μm) because we have a multilayer cavity.

wave cavity as initially designed, is adapted to the 100 μm band and dipoles with a length of $\sim 35 \mu\text{m}$ ($\lambda/3$) are needed. We have chosen a spacing between two horizontal (/vertical) dipoles, facing each other, of 8 μm , which leads to a unit cell dimension of 43 μm . This choice has been driven by geometric specifications. Indeed, the silicon spiral (4 μm - width) for one polarization can pass between two dipoles (facing each other) of the other polarization and we have left a distance of 2 μm on each side of the silicon arm. As a consequence of this design, the cross-polarization is found negligible for a dipole width of 2 μm regarding

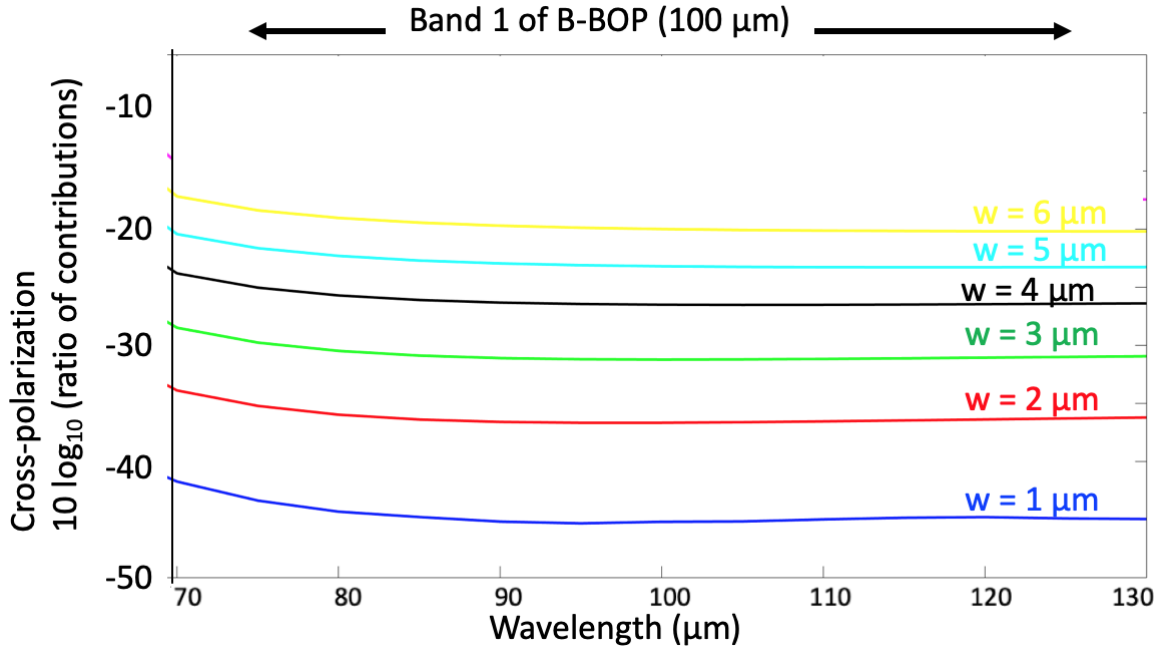


FIGURE 3.14: Computed cross-polarization in dB over the 100 μm band for different width of dipoles. The cross-polarization is less than 1/1000 for $w = 2 \mu\text{m}$.

the scientific requirements. To compute the thickness t of TiN that we need to deposit, we must take into account the filling factor of each dipole and so, this calculation leads to : $t = \rho_{TiN} * l / (Z * dl)$, where ρ_{TiN} is the resistivity of TiN ($= 2.4 \times 10^{-6} \Omega.m$) and l , Z and w are respectively the length, the impedance ($= Z_0/2$) and the width of the dipoles : thus, we need 220 nm of TiN for each dipole. This design will ensure a high absorption efficiency ($> 95\%$) over a large bandwidth (80-115 μm).

3.4.3 Adapting the 200 μm - and the 350 μm -channels from the 100 μm - detectors

The previous study needs to be reiterated for the 200 μm and 350 μm detectors. However, the backshort distance is fixed because it is not possible to have taller nails than those in the 100 μm design (risky technology), so we have to adapt the 100 μm bolometer to the 200 and 350 μm with another solution. Reveret et al. (2010) has successfully adapted the detector to longer wavelengths by adding a silicon layer in front of the bolometer with an airgap in between. This result will be explained in more details in chapter 4. With a software which optimized the airgap (AG) between the detector and the silicon layer and the thickness of this Si layer (AR), we find efficient absorption with AG = 10 μm and AR = 4 μm and AG = 10 μm and AR = 13 μm for the 200 μm and 350 μm respectively (see figure 3.15). Note that in each case the design of the antennae dipoles has been adapted to the wavelength band.

This solution has been initially chosen since it is a simple way to shift the optimal wavelength band. However, since this PhD work, CEA/DAP in collaboration with CEA/LETI have investigated a more

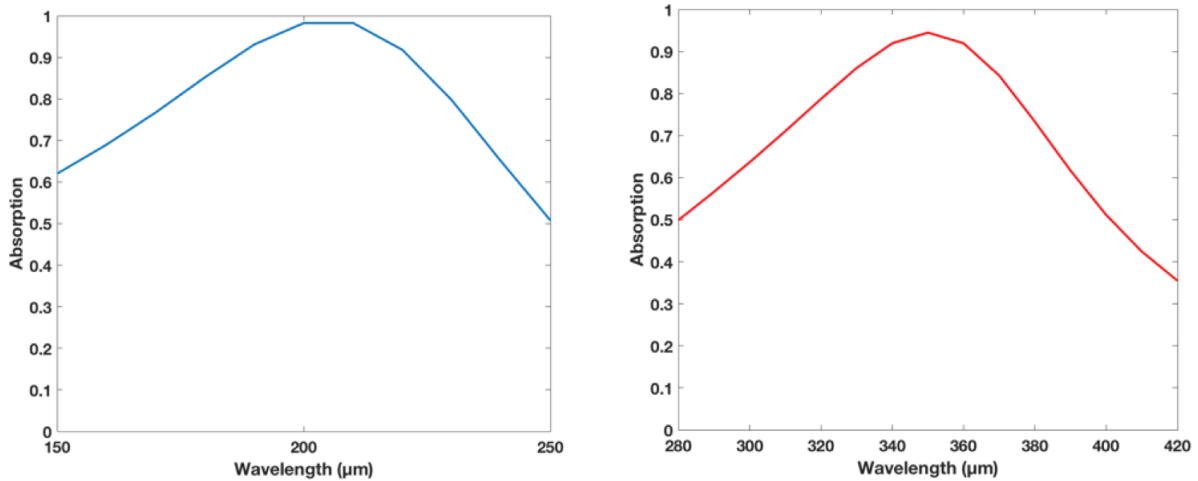


FIGURE 3.15: Left : Optical absorption for the 200 μm with $\text{AG} = 10 \mu\text{m}$; $\text{AR} = 4 \mu\text{m}$. Right : Optical absorption for the 350 μm with $\text{AG} = 10 \mu\text{m}$; $\text{AR} = 13 \mu\text{m}$.

complex solution which relies on the development of high impedance surfaces (HIS) to replace the backshort mirror. HIS use periodic structured patterns to reflect the wave in a frequency band, without a phase shift of 180° . In contrast to perfect electric conductors used so far as the backshort mirror, HIS then do not need to be distant from the absorber by a quarter-wave cavity but rather to be close to the absorber. This solution, by optimizing the HISs, would modify the working spectral band.

3.5 Perspectives

The study, presented here, has been conducted at the beginning of this PhD project has paved the way to more complex analysis which has piloted the manufacturing of the detectors at CEA/LETI.

3.5.1 New design of the focal plane

The design of the CEA polarization sensitive bolometer is slightly different from the first prototype pixels of figure 3.11. The computations to optimize the pixel design have enabled the emergence of a new pixel definition. Since the size of one pixel is fixed to $\sim 750 \mu\text{m}$, which is a constraint from the technology side, we had to find a way to fill an area of $\sim 750 \mu\text{m} \times 750 \mu\text{m}$ with a grid of $\sim 35 \mu\text{m}$ length dipoles. This condition has led to the ‘centipede’ design presented in figure 3.16 produced by the B-BOP team, which has shown to be the best compromise considering the optical efficiency but also the detector speed and the mechanical stability.

CEA has then further advanced the development of pixels for the detection of partial linear polarization. The choice has been made to take full advantage of the strategy of sampling of the telescope point spread function. Indeed, because two orthogonal (0° and 90°) probes of the polarization are not sufficient to de-

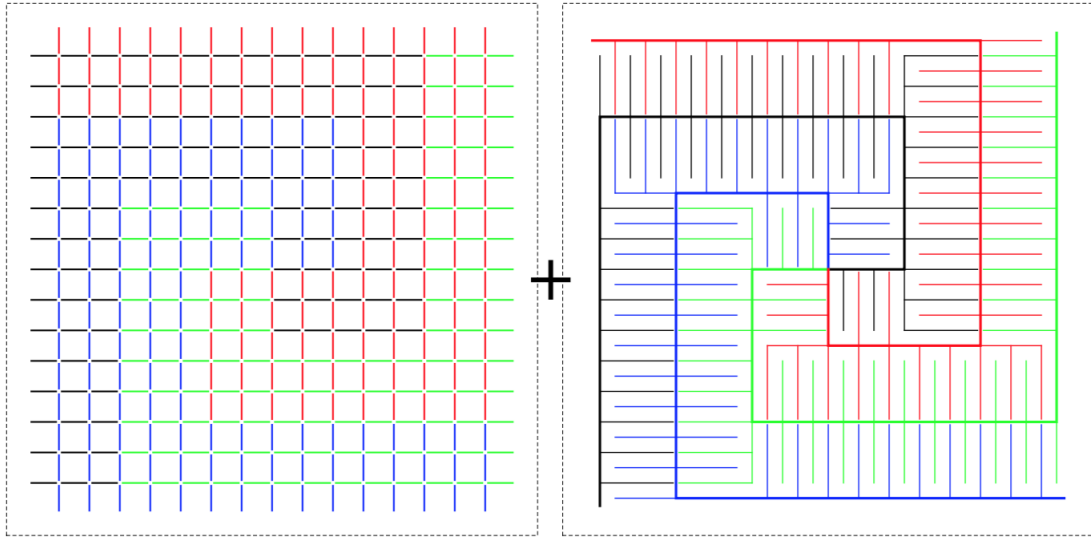


FIGURE 3.16: Design of one CEA polarization sensitive bolometer for the initial 100 μm band of the SPICA/B-BOP instrument : antennae dipoles(left) are supported by thermometer spirals (right). Green and black dipoles gather the information on the horizontal polarization direction, red and blue ones on the vertical direction. Silicon spirals are distributed in a ‘centipede’ configuration to limit the effects on the detector speed while filling the whole area with dipoles. The black spiral supports the black dipoles and so on. (Design by A. Poglitsch)

to determine the direction of the E-field (there is an angle ambiguity), the B-BOP detector team has introduced pixels based on the same design but with dipoles rotated by 45° which give access to the 45° and 135° directions. Note that although the 135° dipoles do not bring more information since only three measurements are necessary, these dipoles will bring redundant data to strengthen the results from the other dipoles. These pixels, named Stokes pixels, are illustrated in figure 3.17. Having several of these Stokes pixels in the Airy disk enables one to have simultaneous measurements of the intensity (I) and of the linear polarization (Q and U) of the same spatial element on the sky, as depicted on the bottom panel of figure 3.17. To measure the circular polarization, a quarter-wave plate would be required, but since this is not part of the scientific expectations, the circular polarization will appear as unpolarized light.

3.5.2 Deriving the Stokes parameters from the detectors signal

In this part, we derive the Stokes parameters I , Q , and U from the signal of the four dipole directions d_1 , d_2 , d_3 and d_4 in one pixel. The goal is to use the Stokes parameters to get back to the total intensity of the signal I_{tot} (which is equal to I), to the polarized intensity I_{pol} (and thus the degree of polarization \mathcal{P}) and finally to θ the angle of polarization compared to the 0° -axis of the Stokes pixels.

From equation 3.9, we know that the intensity measured by a polarizer is :

$$\mathcal{I} = \frac{1}{2} [I + Q \cos(2\theta) + U \sin(2\theta)] \quad (3.10)$$

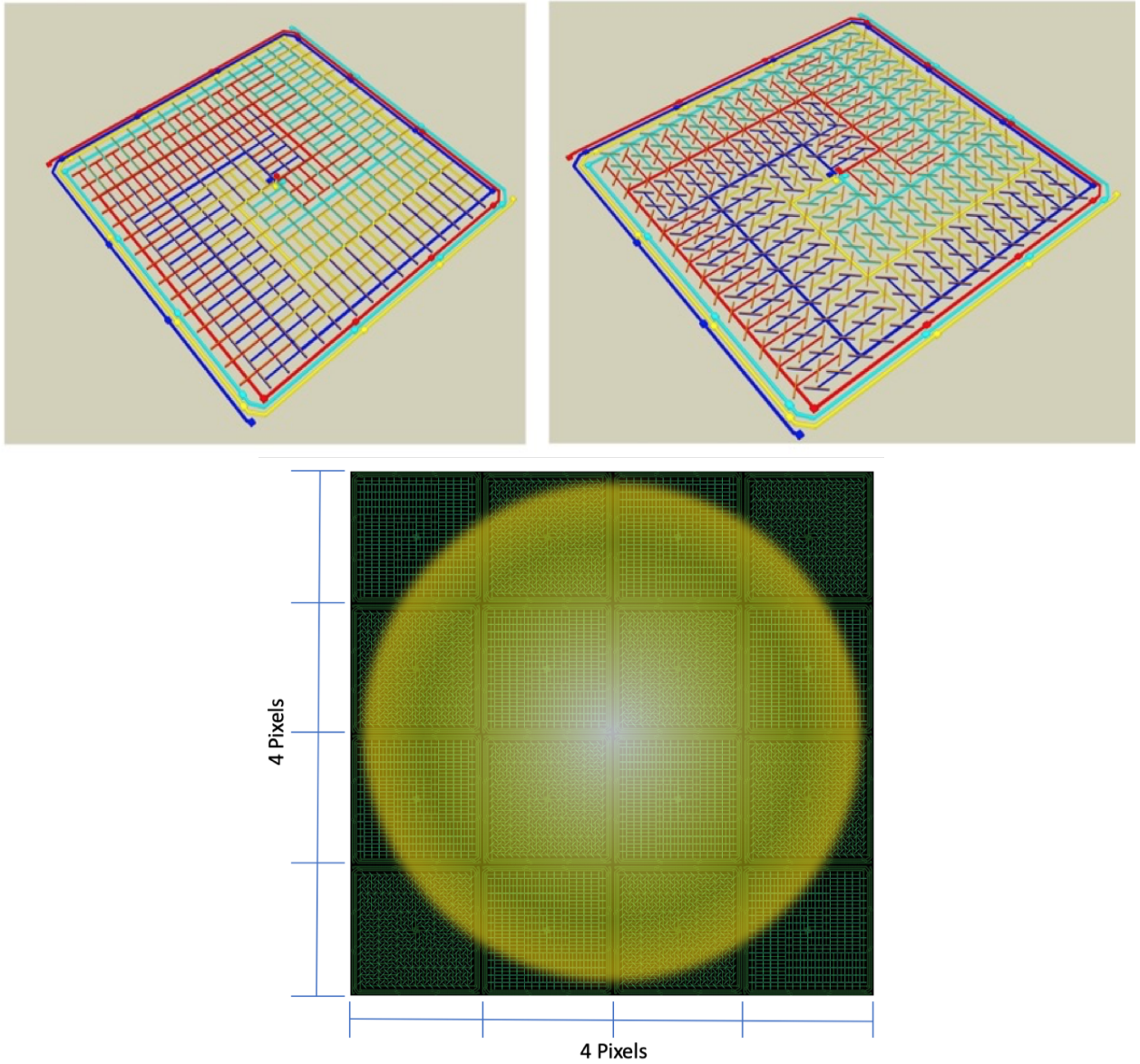


FIGURE 3.17: (Top) Stokes pixels : (Left) 0° and 90° and (Right) 45° and 135° orientations pixels. (Bottom) yellow circle : Airy disk (first dark ring of the diffracted pattern) which covers both kinds of Stokes pixels (Design by O. Adami)

Note that here we only deal with linear polarization. We can therefore compute the intensity signal received by the four Stokes pixels :

$$\begin{cases} d_1 = \frac{1}{2} [I + Q \cos(2\theta) + U \sin(2\theta)] \\ d_2 = \frac{1}{2} [I + Q \cos(2(\theta + \frac{\pi}{4})) + U \sin(2(\theta + \frac{\pi}{4}))] = \frac{1}{2} [I - Q \sin(2\theta) + U \cos(2\theta)] \\ d_3 = \frac{1}{2} [I + Q \cos(2(\theta + \frac{\pi}{2})) + U \sin(2(\theta + \frac{\pi}{2}))] = \frac{1}{2} [I - Q \cos(2\theta) - U \sin(2\theta)] \\ d_4 = \frac{1}{2} [I + Q \cos(2(\theta + \frac{3\pi}{4})) + U \sin(2(\theta + \frac{3\pi}{4}))] = \frac{1}{2} [I + Q \sin(2\theta) - U \cos(2\theta)] \end{cases} \quad (3.11)$$

I is obtained easily with $\frac{d_1 + d_2 + d_3 + d_4}{2}$, but the three parameters I , Q , and U can all be derived by matrix calculations. If we set :

$$D = \begin{pmatrix} d_1 \\ d_2 \\ d_3 \\ d_4 \end{pmatrix}; \quad A = \frac{1}{2} \begin{pmatrix} 1 & \cos(2\theta) & \sin(2\theta) \\ 1 & -\sin(2\theta) & \cos(2\theta) \\ 1 & -\cos(2\theta) & -\sin(2\theta) \\ 1 & \sin(2\theta) & -\cos(2\theta) \end{pmatrix}; \quad S = \begin{pmatrix} I \\ Q \\ U \end{pmatrix} \quad (3.12)$$

A is called the Mueller matrix, it represents the polarizing elements. From equations 3.11, we have therefore :

$$D = A S \quad \Longleftrightarrow \quad S = (A^t A)^{-1} A^t D \quad (3.13)$$

with A^t the transpose matrix of A . The derivation of Q and U is straightforward and the polarized intensity I_{pol} and the degree of polarization \mathcal{P} can be computed. Finally the angle of polarization θ with respect to the 0° -axis of the Stokes pixels is obtained by the argument of Q and U which are both related to the linear polarization through $\theta = \frac{1}{2} \arctan \left(\frac{U}{Q} \right)$. We remind that Q is the preponderance of LHP light over LVP light and U is the preponderance of L+45P light over L-45P light. These definitions give the figure 3.18.

Up to now, we did not take into account noise measurements. This can be achieved by adding a vector

$$N = \begin{pmatrix} n_1 \\ n_2 \\ n_3 \\ n_4 \end{pmatrix} \text{ to } D \text{ by writing } D = A S + N.$$

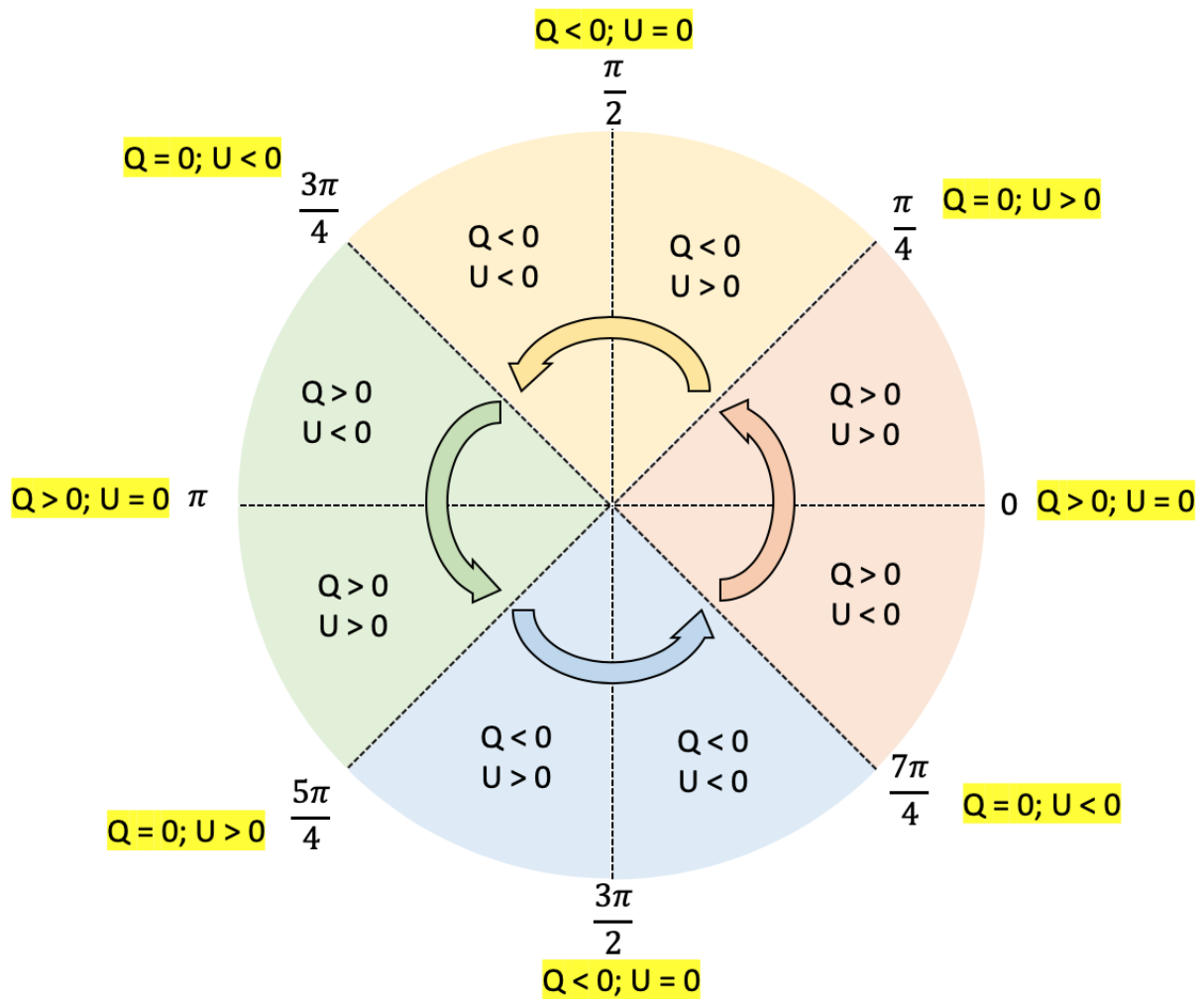


FIGURE 3.18: Values of the angle of polarization θ as a function of values of Stokes Q and U .

Chapter 4

Development of a compact spectroscopic imager

Contents

4.1	State of the art of spectroscopy for far-infrared/sub-millimeter astronomy and new developments towards compact spectrometers	77
4.1.1	Spectrometers for far-infrared/sub-millimeter instruments	77
	Diffraction gratings	79
	Fourier Transform Spectrometers	80
	Fabry-Perot Interferometers	82
	Heterodyne spectrometers	84
	Imaging capability for conventional instruments	85
4.1.2	Towards compact spectro-imaging instruments	86
	Limitations for any telescope applications	86
	Towards on-chip spectrometers	87
4.2	Compact spectroscopic imager using Fabry-Perot Interferometer (FPI) . . .	92
4.2.1	Adding the spectral selectivity to the detector	92
	The choice of the spectrometer	92
	Properties of the Fabry-Perot interferometer	93
4.2.2	Conventional Fabry-Perot Interferometry in the sub-millimeter range	97
	Examples of instruments using FPIs	97
	FPI based on metallic mesh mirrors	99
4.2.3	Optimizing the spectral finesse of the FPI	101
	FP developments in other labs	101
	High Resistivity Float Zone silicon for cryogenic FPI	102
	Modeling with thin film theory	103

	Improving the reflectivity of mirrors	105
	Definition of the stack for the FPI	108
4.2.4	Coupling the FPI with the detector	111
	Combining the spectrometer to the detector	111
	Spectral and spatial scanning	117
	Imaging with a spectrometer located in the focal plane	119
4.2.5	Conclusions of the chapter	125

The two following chapters are dedicated to the development of a compact spectrometric imager. This instrument could be named a “spectro-bolometer” after Langley’s instrument but, unlike the inventor of bolometers who performed spectroscopy using a single bolometer, we here tried to combine the spectroscopy and imaging capabilities into a all in one compact device. In this chapter, we present the theoretical development of the spectro-imager that we have decided to build at CEA. The experimental implementation of this instrument is addressed in chapter 5. We first recapitulate the state of the art of the technologies used for spectrometers in the far-infrared and then highlight the current trend to compact instruments in many fields. From this, we describe the spectrometer that we have chosen to use in combination with the bolometer array within a compact device : a Fabry-Perot interferometer. We state the performance that we would expect from such a spectrometer and study the behavior of the coupled device.

4.1 State of the art of spectroscopy for far-infrared/sub-millimeter astronomy and new developments towards compact spectrometers

In this section, we first review the most common spectrometer types for far-infrared astronomical applications (and in many other fields). We also present the different existing scanning modes which are sometimes required to derive the spatial and the spectral information. We then provide some of the reasons which motivate the development of compact instruments, especially in space astronomy. Lastly, we non-exhaustively review progresses made towards compact spectroscopy and spectro-imaging since the aim of this section is to provide the background of our research.

4.1.1 Spectrometers for far-infrared/sub-millimeter instruments

In 1666, Isaac Newton showed, that, unlike what his contemporaries thought, the white light is not colored by the prism, but is in fact dispersed by it. The material which forms the prism fully determines the refraction of colors, i.e. how they are separated. His famous experiment, with two prisms, was the demonstration that white light was composed of many colors and that colors were not a property of materials but a property of the light itself. More than a century after, Herschel also used a prism for the discovery of the infrared radiation. Nowadays, prisms are not frequently used for instruments in space (but the future SPICA/SMI instrument will use one for the low resolution mode (Roelfsema et al., 2018)) since their performance have been exceeded by other techniques, but their historical contribution laid the foundation of spectroscopy. Table 4.1 (Swinyard and Wild, 2013) lists the technologies developed for mid- and far-infrared spectroscopy, their performances and their involvements in some of the past instruments.

Type	Resolution-determining element	Achieved resolution, $\lambda/\Delta\lambda$	Wavelength range, $\lambda/\mu\text{m}$	Mission-instruments
Prism	prism size and material	≈ 25	8 to 22	<i>IRAS-LRS</i>
Grating	grating size	100	2.5 to 12	<i>ISO-PHOT-S</i>
		200	42 to 198	<i>ISO-LWS</i>
		1500	2 to 43	<i>ISO-SWS</i>
		1500 to 2000	57 to 210	<i>Herschel-PACS</i>
		4000	5 to 28	<i>JWST-MIRI</i>
Fabry–Perot	quality of etalons	9 000	42 to 198	<i>ISO-LWS</i>
		20 000 to 30 000	11 to 44	<i>ISO-SWS</i>
Fourier transform	mirror travel range	≈ 200 to 1000	100 to 100 000	<i>COBE-FIRAS</i>
			200 to 670	<i>Herschel-SPIRE</i>
Heterodyne	LO stability / spectrometer	$> 10^6$	530 to 610 157 to 600	<i>SWAS, ODIN</i> <i>Herschel-HIFI</i>

FIGURE 4.1: Review of spectrometers of mid-and far-infrared spectroscopy in astronomy and their contributions to past instruments (Swinyard and Wild, 2013).

We will therefore focus on these instruments, namely gratings, Fourier Transform Spectrometers (FTS), Fabry-Perot Interferometers (FPI) and heterodyne spectrometers, that came after prisms and which are more common nowadays for studying light decomposition. These types of instruments, which are all based on interference of light, are still involved in current and future experiments in astronomy. In the following, for each kind of technology, efforts were made to provide additional details (resolving power, spectral bands, imaging,...) in relation to a recent space instrument whose working principle was based on the respective technology. It could be also mentioned that the spectrometers quoted by Swinyard and Wild (2013) are not an exhaustive list : for instance, filter banks find applications in astronomy and they are of particular interest for new developments of on-chip spectrometers. In this section, we only discuss spectrometers such as gratings, FTS, FPI and heterodyne. Filter banks, for instance, will be illustrated later in this chapter with some examples of on-chip applications.

Before explaining the particularities of each kind of technique used in spectrometry, we may need to recap some crucial definitions to quantify the performances of spectrometers.

First, the instrumental profile of spectrometers describes the response of the instrument to monochromatic radiation. Since spectroscopy aims at providing the contribution to intensity of each wavelength, the instrumental profile of a spectrometer should be perfectly known before any use (achieved by calibration of the system). The performance of a spectrometer is mainly described by its ability to discriminate wavelengths. The resolution limit corresponds to the minimal full width half maximum (FWHM) $\delta\lambda$ (in wavelength), $\delta\sigma$ (in wavenumber) or $\delta\nu$ (in frequency) that an instrument can isolate. From this, we can define the resolving power \mathcal{R} of an instrument, which is the ratio of the spectral parameter to the resolution limit,

namely $\lambda/\delta\lambda$, $\sigma/\delta\sigma$ or $\nu/\delta\nu$ (Bouchareine, 1994). Note that the resolving power \mathcal{R} will be written in cursive letter throughout this thesis while the reflectivity of any surface will be referred to by R . One can also define the finesse of an instrument, which describes the resolving power of the spectrometer in first order and one has : $\mathcal{R} = k\mathcal{F}$, with k the order number. Finally, the Free Spectral Range (FSR) (noted $\Delta\lambda$, $\Delta\sigma$ or $\Delta\nu$) of a spectrometer corresponds to the wavelength range where the collection of the spectral information can be unambiguously achieved.

Diffraction gratings

A grating is an optical component that has slits arranged in a periodic pattern. Each slit diffracts light and the waves interfere constructively in different directions depending on the wavelength. The result is similar to the dispersion of light by a prism, but it originates in fact from interferences of the different waves coming from all individual slits. The number of lines on the grating N is a fundamental parameter of the spectrometer since it also corresponds to the number of waves that interfere (related to the finesse \mathcal{F} of the spectrometer). We note d the spacing between two slits or grating constant. If L is the total length of the grating, then $L = Nd$. The grating constant d is also involved in the formula which links the diffraction angle i_{2k} corresponding to the direction of constructive interferences, to the incident angle i_1 of the radiation λ (Bouchareine, 1994) :

$$d (\sin i_1 + \sin i_{2k}) = k\lambda \quad (4.1)$$

where k is the order number. This equation implies that for a single wavelength, the energy is shared between several orders, leading to a weaker signal for one specific order. It also predicts that orders may overlap and thus mix several wavelengths of different orders. The order number determines the free spectral range $\Delta\lambda = \lambda/k$, which means that $\Delta\lambda$ is small for high values of k . The use of high orders gratings requires a strong filtering to avoid any confusion in the signal, although in any case, filtering is a necessary step. Regarding performance, the resolving power of a grating corresponds to the product of the finesse \mathcal{F} by the order number k which can be derived to be :

$$\mathcal{R} = k\mathcal{F} = \frac{L (\sin i_1 + \sin i_{2k})}{\lambda} \quad (4.2)$$

according to equation 4.1. The resolving power depends therefore on the wavelength, on the incident and the diffraction angles, but also on the length of the grating. The last point suggests that the longer the grating, the higher \mathcal{R} : however building long gratings is not straightforward and represents a mechanical challenge. Indeed, to reach the theoretical resolving power, the precision of the surface of the grating has to be better than $\lambda/4$ over the whole area. This constraint does not only concern the surface quality but also

the position of the grooves on the grating. Although the technical requirements are demanding, gratings are frequently used for spectrometers in the far-infrared field. Among all kinds, blazed gratings are the most common : the grooves look like reflecting staircases and they have the considerable advantage of concentrating light in one specific diffracted order for a limited band of the spectrum. The right angles of the blazed gratings allow one to work with high incidence, leading to high resolution according to equation 4.2. The HERSCHEL/PACS spectrometer (Poglitsch et al., 2003b) used three orders of a diffraction grating in three spectral bands : the first order covered the 105-210 μm band, the second the 72-105 μm band and the third the 55-72 μm band. The 30-cm grating allowed the instrument to reach high spectral resolving power $\mathcal{R} \sim 1000\text{-}4000$ depending on the order and on the wavelength. Moreover, because the imaging capacity is not immediate with a diffraction grating, the PACS spectrometer used an integral field unit (IFU) which added the imaging capability at the cost of a more complex optics. The IFU included an image slicer to re-arrange the 5×5 pixels image of the sky in order to provide a 1×25 pixels row input for the grating. Thus, because the energy is dispersed over the spectral channels, the photon noise experienced by each individual detector corresponds to a smaller fraction of energy compared to multiplexing spectrometers, for example.

Fourier Transform Spectrometers

“About ten years ago, when large digital computers became widely available, an old spectroscopic method was revived. [...] many problems are now being done which previously were considered possible only in theory.” (Hochheimer and Bradley, 1969)

While the invention of the first Fourier Transform Spectrometer (FTS) dates back to 1891 by Michelson (with considerable progresses achieved by Rubens in 1910, see Connes et al. (1988)), their expansion is recent and started with the recent progress of computers. FTS are another kind of interferometers. Here we only discuss about one type of FTS, the Michelson Interferometer, and use the term ‘FTS’ to refer to the Michelson. Figure 4.2 explains the working principle of spectrometers based on Fourier Transform (FT) analysis. In contrast to the grating where N waves interfere, depending on the number of grooves, FTS relies on two wave-interference. Indeed, the beam at the entrance of the FTS is divided into two by a beam splitter, the transmitted part and the reflected part are both reflected on mirrors (one is fixed, the other is movable) and then reflected and transmitted respectively by the beam splitter. At the output of the FTS, the two waves interfere and the sensor detects the resulting intensity for particular positions of the movable mirror. Interferograms are obtained by moving this mirror while the other mirror is fixed. In doing so, the optical path difference (OPD) is altered for each position of the movable mirror and the detector can measure the resulting interference fringes. The spectral information is coded into the interferogram since each data point of the measurement is a linear combination of different wavelengths. Applying Fourier Transform to the interferogram enables one to derive the spectrum. It can be the spectrum of the radiating

source used to illuminate the FTS or the transmission spectrum of a sample to test, assuming the reference (source) is known.

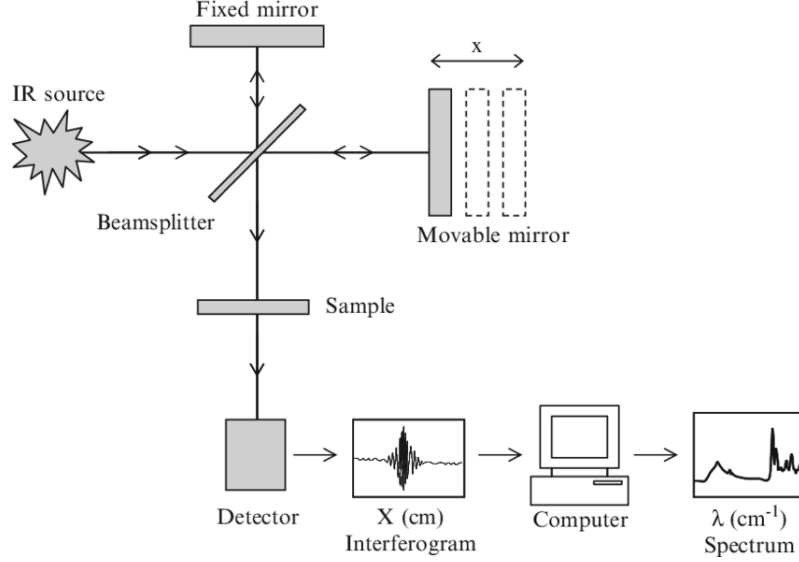


FIGURE 4.2: Working principle of Fourier Transform Spectrometers (FTS) : a source of radiation illuminates the FTS; the beam-splitter splits the incident beam into two beams; the transmitted and the reflected beams are both reflected on mirrors (fixed mirror and movable mirror on the sketch); finally, the beams recombine after reflection or transmission, respectively, by the beam-splitter. The outcoming wave passes through the sample to test and the resulting interferogram is detected and recorded in the computer. By applying a Fourier Transform (FT) to the interferogram, we can derive the spectrum of the source through the sample. The transmission can be calculated by measuring the spectrum of the source without sample and by computing the ratio of the spectra of the sample to the reference (Ojeda and Dittrich, 2012).

Interferograms obtained with FTS are well understood and can be mathematically explained by the Fourier Transform theory. The interferogram I as a function of the OPD δ for a monochromatic radiation λ is calculated to be (Kimmitt, 1970) :

$$I(\delta) = A_0(\lambda) \left[1 + \cos\left(\frac{2\pi\delta}{\lambda}\right) \right] \quad (4.3)$$

where $A_0(\lambda)$ is the total light intensity that illuminates the FTS. If the spectrum of the source through the sample is perfectly monochromatic, the interferences pattern consists in a simple cosine. In most of the cases, interferences are more complex and the interferogram can be represented by the sum (or more precisely the integral) of the contributions from all wavelengths :

$$I(\delta) = \int_0^{\infty} A_0(\lambda) \left[1 + \cos\left(\frac{2\pi\delta}{\lambda}\right) \right] d\lambda \quad (4.4)$$

$$I(\delta) = I_0 + I_1(\delta) \quad (4.5)$$

The interferogram is then the sum of a constant offset I_0 and of a modulated part $I_1(\delta)$ which contains the spectral information. In practice, δ is not infinite and is limited to $D_{max}/2$ where D_{max} is the maximal travelling distance. The limit of resolution is therefore $\delta\sigma = \frac{1}{2D_{max}}$, since $2D_{max}$ corresponds to the maximal travel (in OPD) of the FTS. The resolving power is $\mathcal{R} = \frac{2D_{max}}{\lambda}$. These equations will be used in chapter 5 in more details, as we only aim here at giving a brief overview of the system.

Equation 4.4 shows that FTS does not act as a dispersive element like gratings. Indeed spectrometers that are used as monochromators measure the spectrum in a spectral width $\delta\lambda$ and can potentially scan the spectrum to derive the spectral information on a wider band. However, interferometers such as FTS multiplex wavelengths : the spectrum is not obtained directly from measurements but requires to apply a Fourier Transform. The fact that wavelengths are multiplexed can present an advantage in measuring time efficiency which is known as the Fellgett advantage (Fellgett, 1958) : if the noise of the measurement is limited by the detector noise, the Signal-to-Noise Ratio (SNR) is improved for FTS in comparison to monochromators. When the photon noise limits the measurements, the FTS does not improve the SNR since the noise applies to each wavelength, is mixed through the FTS and will pollute each spectral element after Fourier Transform. In particular, if only parts of the full spectrum are of interest, the combination of a background-limited detector and a monochromator gain an advantage over the FTS.

Nowadays, FTS are very common onboard instruments. For example, the HERSCHEL/SPIRE spectrometer (Griffin et al., 2010) used an FTS, in a Mach-Zehnder configuration which slightly differs from the Michelson configuration (gain in signal) but the working principle is similar. This FTS enabled one to cover two overlapping bands in two focal planes : 194-313 μm and 303-671 μm . In general, FTS are more suitable than monochromators for broad band spectroscopy (depending on detector characteristics) and they deal with considerably more light (\sim half of the light for a Michelson). The resolving power \mathcal{R} for SPIRE was about 1300 at short wavelengths and about 370 at long wavelength. As already mentioned, improving the spectral resolution of an FTS requires to increase the maximal travelling distance, which implies to have a bulkier instrument. In addition, imaging is possible with an FTS, assuming each optical component is large enough to receive all the collimated directions corresponding to the different positions on the sky.

Fabry-Perot Interferometers

Fabry-Perot Interferometers (FPI) are also often used in far-infrared astronomy. Etalons are a specific type of FPI : they are a slab made of one transparent material with parallel reflective surfaces. The ‘real’ spectrometer uses two parallel mirrors separated by a transparent cavity which can be tuned. In both cases, there is a cavity defined by the thickness d and by the refractive index n of the material of this cavity, as well as two reflective surfaces, characterized by an amplitude coefficient of reflection $r \leq 1$ (and then a power reflection coefficient $R = r^2 \leq 1$), surrounding the cavity. The mirrors are optimized to be reflectors with $R \approx 1$ and with minimum losses in the material. When a polychromatic radiation enters in the cavity,

the waves undergo multiple reflections and most of them are reflected back, but for one specific wavelength (and its harmonics), all partial waves from any number of reflections arrive at the second mirror in phase and are transmitted. Wavelengths λ , for which this condition is fulfilled, are related to d by the equation :

$$d = \frac{k\lambda}{2n \cos \theta} \quad (4.6)$$

where k is a positive integer which accounts for the number of half-wavelengths of the standing wave between mirrors and θ the incident angle of the incident radiation with respect to the normal. In other words, wavelengths which are adapted to the resonance of the cavity are transmitted through constructive interferences while other wavelengths are not through destructive interferences. To obtain a full spectrum (in a narrow-band), the size of the cavity d has to be adjusted in order to tune the resonant wavelength. Although the etalon has been invented by C. Fabry and A. Perot in 1897 (see Fabry and Perot (1901)), the interferences resulting from an infinite number of waves were already described by J. B. Airy in 1835. The transmitted energy T through the FPI is (Hernandez, 1986) :

$$T = \frac{1}{1 + \frac{4R}{(1-R)^2} \sin^2(\Delta\phi/2)} \quad (4.7)$$

where $\Delta\phi = \frac{2\pi}{\lambda}\delta$ corresponds to the phase shift and $\delta = 2nd \cos \theta$ is the optical path difference between two successive reflected beams inside the cavity (see appendix A).

For FPI, unlike gratings and FTS (where the number of waves N that interfere is limited), interference occurs, in theory, of an infinite number of reflected waves. In practice, this number is limited, especially by the reflectivity of mirrors, by their surface quality and by their misalignment errors. The transmission plot looks like a Dirac comb : there is an Airy function for every $\lambda_k = 2dn \cos \theta/k$ (equation 4.6), with k a positive integer. The sharpness of the fundamental ($k = 1$) peak is defined by the finesse \mathcal{F} (related to the mean number of waves N that interfere at the output of the FP). \mathcal{F} is also linked to the free spectral range $\Delta\lambda$ (here the spectral distance between two transmitted peaks) and the limit of resolution $\delta\lambda$ through the equation :

$$\mathcal{F} = \frac{\Delta\lambda}{\delta\lambda} \quad (4.8)$$

The resolving power of a peak is $\mathcal{R} = k\mathcal{F}$, with k being again, the order of the resonant wavelength inside the cavity (for the fundamental $k = 1$ and for any harmonics $k > 1$). In the case where \mathcal{F} is not limited by the parallelism or by the quality of mirrors, it mostly depends on the reflectivity of mirrors R and the reflective finesse can be expressed as (Hernandez, 1986) :

$$\mathcal{F}_{\mathcal{R}} \approx \frac{\pi\sqrt{R}}{(1-R)} \quad (4.9)$$

This formula is only valid for high R . High resolution FPI are really efficient for narrow-band spectroscopy but are rather unsuitable for broad-band spectroscopy like for spectral energy density (SED) (except for low-finesse FPI).

High \mathcal{R} spectroscopy with FPI requires the use of filters to remove the unwanted harmonics which are transmitted through the interferometer. Some instruments used diffraction gratings to sort the orders of the FPI. For example, the Long-Wavelength Spectrometer (LWS) (Clegg et al., 1996) that was one of the four instruments onboard the ISO satellite and operated over the 45-180 μm band used the combination of Fabry-Perot and grating. For the medium resolution (~ 200), only the grating was used but higher resolving powers ($\sim 10^4$) were possible by the insertion of a Fabry-Perot Interferometer into the collimated beam. Although the LWS did not benefit from the intrinsic imaging capability of the FPI, these multi-waves interferometers are really suitable for imaging extended sources dominated by narrow emission lines, especially if they are positioned in a collimated beam. As for the FTS, they should be large enough to cover all the directions of the collimated beam that come from different positions on the sky. However, because the FPI are very compact, this considerably limits the volume of the instruments.

Heterodyne spectrometers

Heterodyne spectrometers are fundamentally different from optical spectrometers based on interference and direct photon detection. They originate from radio detection technology. In heterodyne spectroscopy, a local oscillator (LO) produces a stable monochromatic signal with a frequency f_{LO} close to the frequency f_S of the observed signal. The two frequencies are then optically combined in a non-linear device, called a mixer, which results in a new signal at frequencies $2f_S$, $2f_{LO}$, $f_S - f_{LO}$ and $f_S + f_{LO}$ (Swinyard and Wild, 2013). The highest frequencies are filtered out and the lowest frequency is kept for processing. $f_S - f_{LO}$, called the intermediate frequency (IF), is then amplified to be detected by an electronic spectrometer. This way, the heterodyne spectrometer has shifted the frequency range of the observation in a range where amplifiers are optimized, without any loss of the spectral or phase information. This operation is necessary since no amplifiers work at those high-frequencies f . The heterodyne process is sketched in figure4.3.

Heterodyne spectroscopy enables one to reach extremely high resolution. The Heterodyne Instrument for the Far-Infrared (HIFI) (Graauw et al., 2010) on HERSCHEL was working between 157 μm and 625 μm (480-1910 GHz) at a resolution \mathcal{R} of $\sim 10^5 - 10^7$ (corresponding to a velocity resolution of 0.03 - 3 km/s). Imaging with heterodyne spectrometers can be limited, especially onboard a space telescope, since they require large volume and high electrical power. However, some recent instruments have combined high resolution spectroscopy with small detection arrays (7 pixels per sub-array in the SOFIA/upGREAT

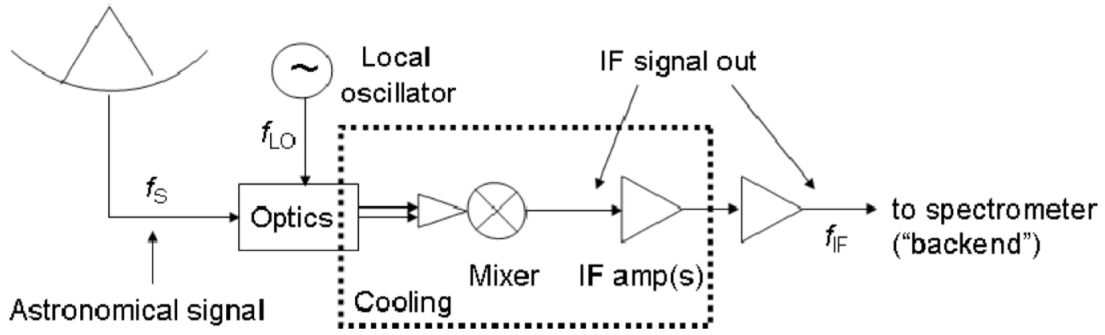


FIGURE 4.3: Principle of heterodyne spectrometers : the astronomical signal f_S interferes with a signal f_{LO} (close to f_S) from the local oscillator of the instrument. The resulting signal $f_S - f_{LO}$ is amplified and sent to the electronic spectrometer (Swinyard and Wild, 2013).

instrument, see Risacher et al. (2018)).

Imaging capability for conventional instruments

As explained before, not all of the four kinds of instruments presented are inherently compatible with a 2d-imaging capability. For example, gratings require the addition of an image slicer to instantaneously measure the spectrum of all spatial pixels of a 2d array. Spectro-imaging instruments aim at deriving a 3D data cube with two spatial dimensions and one spectral dimension, in other words, the spectrum of each spatial pixel of an image is derived. However, in astronomy, some solutions exist to counter the lack of spatial information of some spectrometers. Indeed, any instrument can get the spatial information on the sky by performing a spatial scanning (Sellar and Boreman, 2005). For spectrometers which only enable one point in the field-of-view (FOV), the image can be scanned in a whiskbroom-scanning mode (see figure 4.4 for the schematic view of all modes). This can be a direct solution for any conventional spectrometer. For instruments which accept a slit aperture in their focal plane, one of the two spatial dimensions is obtained by the definition of the instrument. The other dimension is derived by scanning the sky in a pushbroom mode. This mode is very appropriate for gratings so that they disperse a 1-dimension slit image in the perpendicular direction of the diffraction. The framing mode consists in having the 2-dimension spatial information but also the spectral information in one instrument (Ferrec, 2010). This can be achieved for example, by dichroics which discriminate the spectral information and send each colored image on a different array. In practice, performing spectroscopy with dichroics would require many arrays, thus one should not expect high resolution or wide band. Another application is to have a filters array combined with a micro-lens array in front of the detector in order to get the same image in each sub-array but at a different color. Nevertheless, this is only possible for very large arrays and while in the near-infrared field, one can reach a high number of pixels in one array, this is not true for thermal bolometers. The example

of the image slicer combined with the grating is an alternative to the micro-lens array. The filter bank (including Fabry-Perot filter) is also a solution which works in the framing mode. Finally, the last mode called windowing mode, is similar to the framing mode, but still requires a spatial scanning since the 3D datacube is not fully derived from the instrument. For instance, wedge filters provide different spectral responses in one direction of the 2d-array and have to scan the sky in this direction.

This short overview summarizes the different modes to scan the sky for imaging spectroscopy. If these

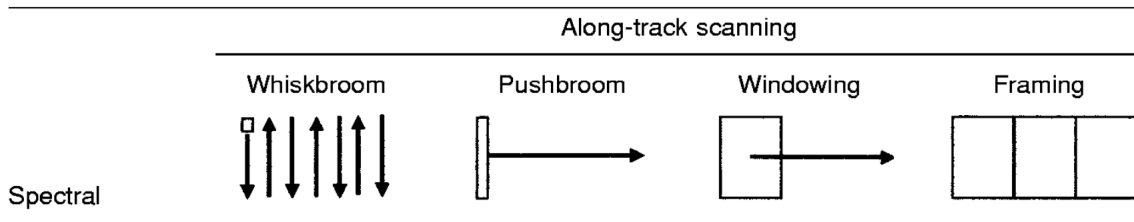


FIGURE 4.4: Scanning modes for imaging-spectrometers (extracted from Sellar and Boreman (2005)).

methods are commonly used in astronomy, they may be adaptable to other applications, too. For example, the pushbroom or the windowing modes can also work for cameras in aerial imaging or on conveyor belts for airport safety. Although there are some solutions to compensate for the lack of intrinsic imaging of the instrument, adding this capability to the spectrometer presents several advantages. Among those, the first one is to have several pixels observing the same spectral feature in the case of an extended source. This allows one indeed, to disentangle the contribution of individual pixels response to the observation. In addition, having a 2d-array working in the windowing mode makes it possible to build a full survey of a particular region with redundant observations of the same sky pixels from one shot to the other for the sake of overlapping.

From the traditional spectrometers presented above, only heterodyne spectrometers do not look perfectly suitable for imaging since each individual spatial pixel is already very power consuming. Gratings can produce the spectra of a sliced image, FTS can image to a certain extent while it is straightforward with filter banks and FPI.

4.1.2 Towards compact spectro-imaging instruments

Similarly to what was invented for polarimetry, we want to achieve spectroscopy at the level of the bolometer array (without degrading the imaging part). We aim at integrating the spectrometer close to the chip and almost performing what is known as ‘on-chip spectroscopy’.

Limitations for any telescope applications

In this part, we focus on the context of experimental applications for space, balloon or airborne telescopes, even if the arguments in favor of compact instruments are also true for a ground-based telescope.

We briefly discuss all kinds of advantages that compact instrumentation benefits from.

Compact instruments help to reduce the allocated volume on-board telescopes, which is already limited. The mass, which is related to the volume is, in general, also minimized when integrating the spectrometer into the focal plane. This has a direct impact on the cryogenic part since a compact system might require less time and less energy to be cooled down. As another consequence, having less mass also reduces the parasitic heat load through the mechanical suspension. Moreover, one of the main advantage is to have a simpler system than conventional optics : if the spectrometer is already combined to the detector, the instrument acts like one monolithic system. By doing so, it is no longer needed to test each individual subsystem (spectrometer and detector) and finally the whole system, but rather only the detection module (providing the latter is an already proven technology). The induced benefit is to assemble together with the spectrometer the detector at manufacturing time. Lastly, we should mention that compact instruments is a strong requirement for applications such as the safety field (monitoring) for example, where the camera must be portable.

A priori, some spectrometers such as gratings and FTS are bulkier than others. However, efforts have been made to make these instruments more compact. For instance, FTS arms can be folded to save space in a cryostat, as it will be done with the SPICA/SAFARI FTS (Roelfsema et al., 2018). But the research goes further in the field of compact spectrometers(-imaging) as presented in the next part.

Towards on-chip spectrometers

Here we present some compact spectrometers/spectro-imaging detectors. We do not aim at listing all the emerging technologies, but rather to show with a few examples, for each kind of conventional spectrometer, how it is possible to minimize the dimensions of a conventionally instrument.

Several laboratories have used gratings above the detector to add the spectral capability to the detector (pushbroom mode). As an illustration, we can cite the Delft University of Technology¹ which has introduced a concept of planar double-grating spectrometer made from lithography, mounted on the surface of a CCD sensor (dimensions of the system : 3 x 3 x 11 mm) for the visible range (Grabarnik et al., 2007). The two gratings are facing each other, enabling the dispersion of a non-collimated beam by the two consecutive gratings and finally the detection of the light coming from the initial entrance slit. A curved mirror between the two gratings focuses the light on the detector. The dimensions of the system can be estimated in figure 4.5, where the schematic ray tracing is also depicted. The resolution has been measured to be 3 nm within 300 nm bandwidth and the throughput, as a compromise with the spectral resolution, is about 9%.

Fourier Transform Spectrometers have also benefited from intensive research to reduce the dimensions of the overall system without degrading the performance too much. ONERA² has developed an on-chip static

1. Delft, Netherlands

2. Office national d'études et de recherches aérospatiales, Palaiseau, France

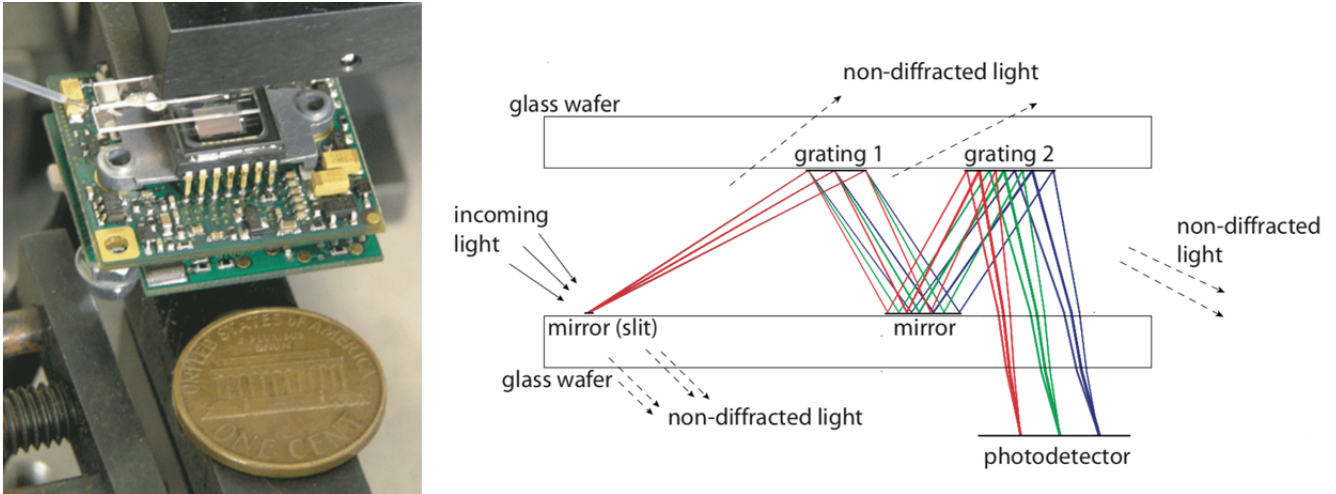


FIGURE 4.5: Planar double-grating spectrometer principle (Grabarnik et al., 2007).

Fourier Transform Spectrometer, called μ -SPOC (initial concept depicted in Rommeluere et al. (2008)). Conventional static FTS have one main advantage which is the stability of the instrument in comparison to other FTS with moving optical parts, but in addition, μ -SPOC is very compact. The spectrometer is directly integrated into the detector by etching a wedge into the CdZnTe substrate instead of the traditional uniform substrate thinning (see figure 4.6). A Fizeau interferometer is formed by the two reflective surfaces of the wedge generating the OPD modulation. The low refractive index of the CdZnTe ($n \approx 2.70$) allows an approximation of the wedge by a two-wave interferometer (i.e. a static FTS). μ -SPOC can be used in a windowing mode to derive the full 3D datacube. The on-chip spectrometer resolution is limited by the maximal height of the wedge which determines the maximal OPD.

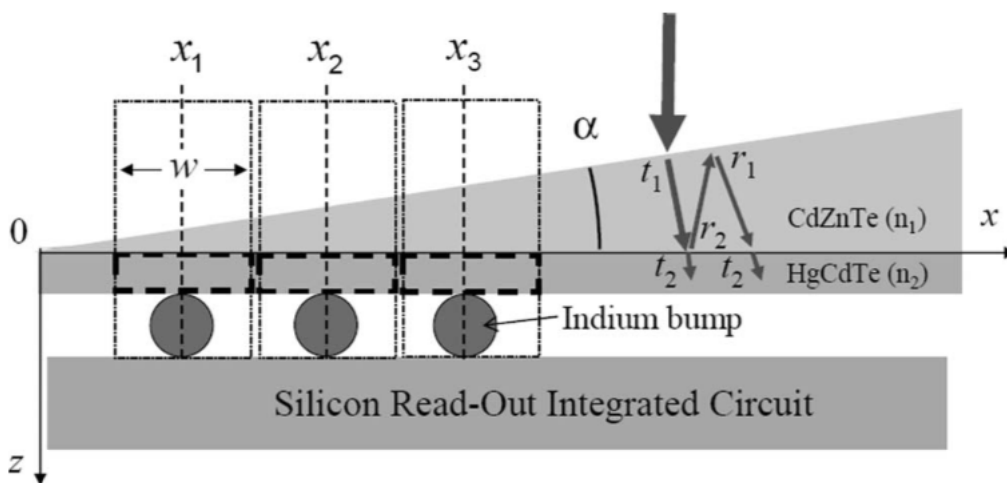


FIGURE 4.6: Stationary Fourier-transform spectrometer obtained by etching the CdZnTe substrate in a wedged shape (Rommeluer et al., 2008).

In a totally different way of spectroscopy based on Fourier transform, IPAG³ first introduced the concept of Stationary-Wave integrated Fourier-Transform Spectrometry (SWIFTS) (Le Coarer et al., 2007). The idea of this new kind of spectrometer has been inspired by Lippmann colored photography (Lippmann, 1891, 1894) and is based on the intensity detection of a standing wave. For this, two experiments using a waveguide can be set up : in the Lippmann configuration, the standing wave is created by reflection of light on a mirror, while in the Gabor configuration (counter propagative mode), the light is divided upstream of the spectrometer and a standing wave is produced inside the waveguide by interferences between the two opposite streams. The evanescent field of the standing wave is then sampled and diffused by gold nanowires deposited along the waveguide, enabling to probe only a small fraction of light (without disturbing the stationary wave). The scattered light is finally detected by a CCD. While the Gabor SWIFTS gives a Fourier interferogram, the Lippmann SWIFTS derives a Lippmann interferogram, similar to conventional Fourier interferograms, but with a dark fringe at the zero path difference (on the mirror). The resolution is only limited by the length of the waveguide, which is the reason why this technology can reach high resolving power ($\mathcal{R} = 40,000$ in the visible range). Lastly, the SWIFTS spectrometer can perform imaging by using a set of parallel waveguides glued on a detector array (Le Coarer et al., 2010).

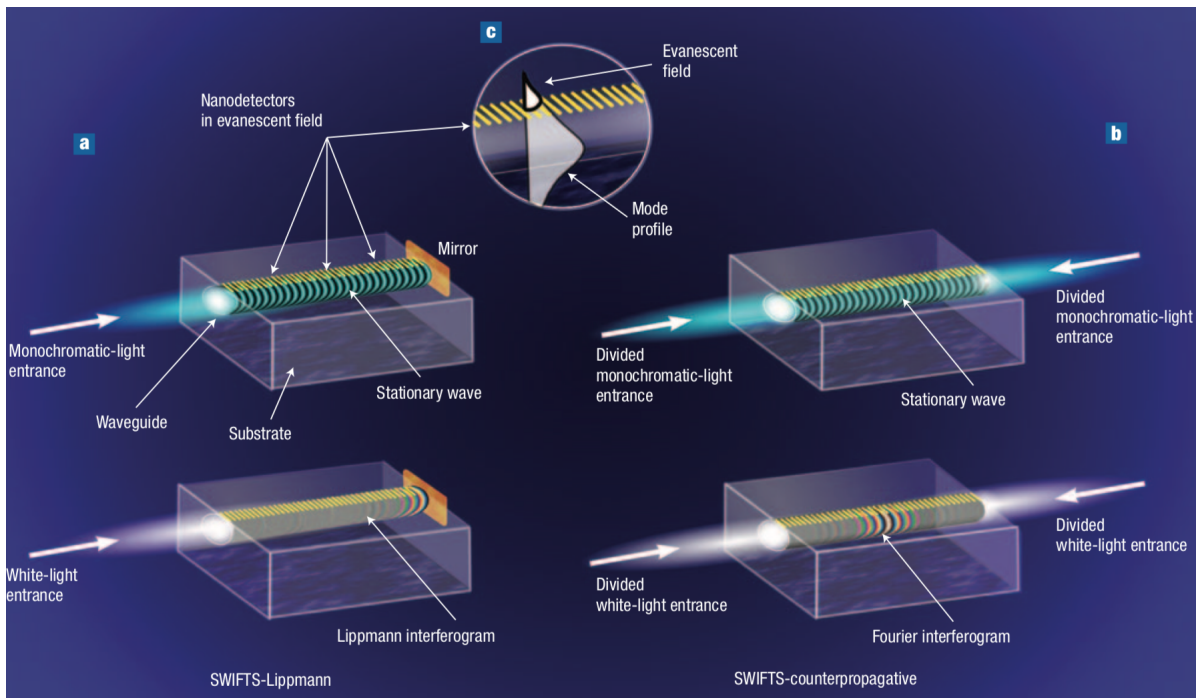


FIGURE 4.7: Stationary-Wave integrated Fourier-Transform Spectrometry (SWIFTS) principle. (a) the Lippmann configuration : the standing wave is obtained by the reflection of the forward propagating wave onto a mirror ; (b) the Gabor configuration : the wave is split in two beams which are introduced at each end of the waveguide and interfere to form a standing wave ; (c) gold nanowires sample and diffuse a small fraction of the energy (the evanescent field) (Le Coarer et al., 2007).

Illustrations of hyperspectral cameras which use Fabry-Perot interferometry can be given. As one example, IMEC⁴ has experimented with this solution through different filter arrangements. For one of them (figure 4.8), the idea was to go beyond the Bayer filter imaging (Bayer, 1976), which already mimics the human eye behavior. Instead of having three colored filters (red, blue and green), the IMEC hyperspectral sensor is sampled by 4x4 filter cells, where the sixteen filters are Fabry-Perot monochromators with various cavity sizes (Geelen et al., 2014). The spatial sampling follows the Nyquist criterion at the level of the cell in such a way that every pixel of the cell observes the same spot on the sky but at a different wavelength. This configuration does not require any scanning to obtain the 3D data cube. However, the spectral bandwidth is limited by the number of filters used in one cell. IMEC proposed two other solutions

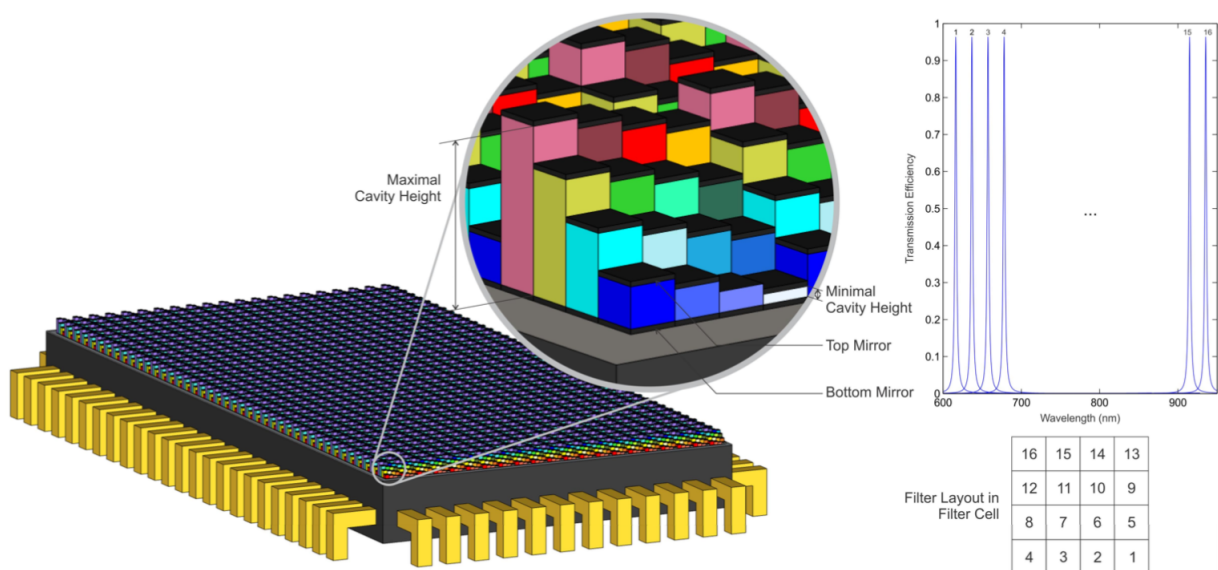


FIGURE 4.8: IMEC hyperspectral sensor based on CMOS imager (Geelen et al., 2014).

that need scanning or other optics but with larger bandwidths (Lambrechts et al., 2014). One of the other arrangements looks very similar to μ -SPOC since a staircase-like structure is used : each row of pixels observes a different wavelength related to the height of the stair (i.e. thickness of the FP cavity). Here the windowing mode is also required to achieve spectral and spatial measurements of a scene, but this technology could be favored if, for example, the instrument flies over the scene to observe. The other arrangement presented by IMEC does not need scanning but uses an optical duplicator such as a micro-lens array. It consists in subdividing the detector array into 32 squares of 256 x 256 pixels with each sub-array having a different filter. The use of a microlens array upstream of the hyperspectral camera allows one to image the scene in 32 spectral bands.

Eventually, we cite two instruments in the field of sub-millimetre astronomy which plan to perform

4. Institut de microélectronique et composants, Louvain, Belgium

on-chip spectroscopy from ground-based telescopes : SuperSpec (Hailey-Dunsheath et al., 2015) from Caltech⁵ and DESHIMA (Endo et al., 2012) from the Delft University of Technology. While an engineering demonstration at the Large Millimetre Telescope (Mexico) is scheduled in the fall of 2019 for SuperSpec, Deshima has already been set up on ASTE (Chile) at the end of 2017. These two instruments are based on microwave technology : lithography enables one to have superconducting filter banks coupled with large arrays of KIDs on a single chip. The working principle is explained in figure 4.9. The wave is absorbed by a wideband antenna, which is coupled to a lens to improve the efficiency of the system. The signal is transmitted through a superconductive microstrip line (without being dissipated) and reaches the narrow-band resonators. Each resonator is adapted to a slightly different frequency from channel to channel. Finally, the wave is dissipated in the microwave kinetic inductor detectors. Similarly to a grating, superconducting microresonators can disperse light from a wideband source over filter banks (DESHIMA : 332-377 GHz (49 channels) in 2017 and 220-440 GHz (347 channels) planned for 2020), but in a very more compact way. With this emerging technology, resolving powers of $\mathcal{R} \sim 500$ are achieved. Concerning the imaging capability, the first DESHIMA instrument hosts 5 spatial pixels. Nevertheless, the next generation (MOSAIC) should have 25 pixels which correspond more or less to the current limit of the array size (due to the size of one spatial pixel, see figure 4.9).

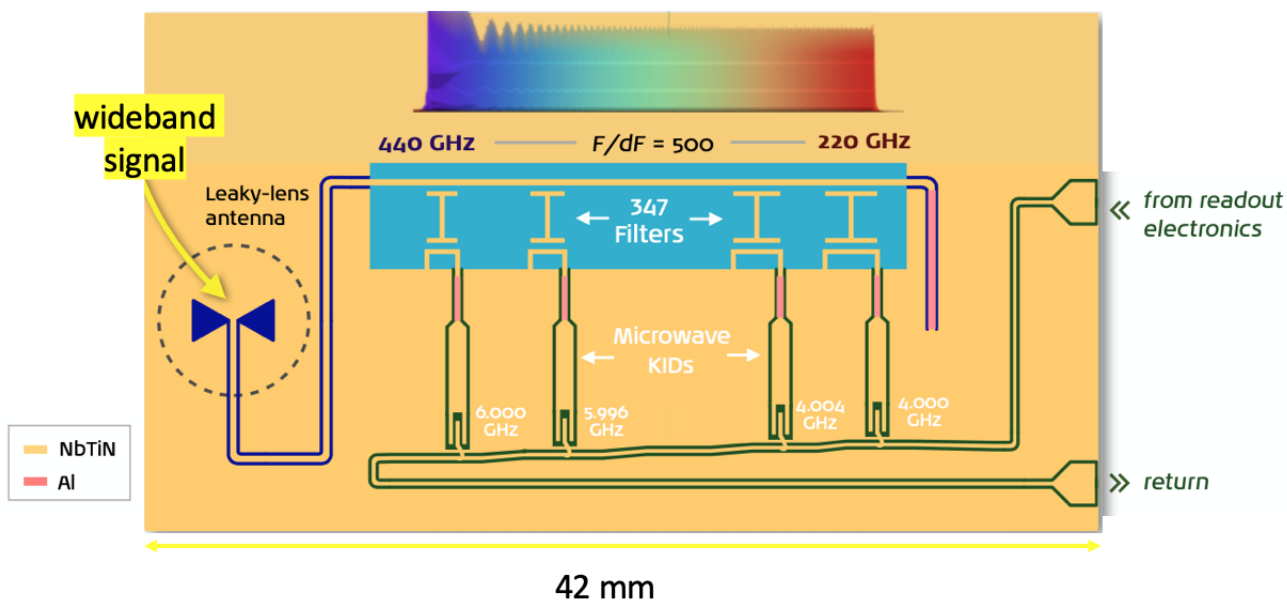


FIGURE 4.9: Sketch describing the working principle of DESHIMA : superconducting filter banks coupled with large arrays of KIDs (adapted from Akira Endo presentation at LTD18 workshop).

5. California Institute of Technology, Pasadena, CA, USA

4.2 Compact spectroscopic imager using Fabry-Perot Interferometer (FPI)

The first section of this chapter has provided an initial overview of all the technologies available which might be relevant to consider if we want to add the spectral selectivity to the bolometer array. In this second part, we explain why we selected the Fabry-Perot interferometer as the solution for a compact spectroscopic imager. Then, we identify one issue that affects the efficiency of the conventional spectrometer so far and propose a solution to counter this. We also try to improve the performance, namely the resolving power, of the chosen spectrometer. Finally, we present the expected performance of the coupled spectro-imaging system. This thesis aims at paving the way for developments toward compact spectro-imaging devices based on CEA type bolometers.

4.2.1 Adding the spectral selectivity to the detector

Here we justify the choice that we made to select the Fabry-Perot Interferometer as the best candidate to be combined with the detector array to form a whole instrument. We also provide more details about FPI which might help for the experimental work.

The choice of the spectrometer

Among all the ‘on-chip’/compact solutions that have been already investigated for different applications, many were not usable in our study. For example, the filterbanks of DESHIMA and SuperSpec spectrometers are not compatible with the CEA technology since they only suit radio type developments as in the case of KIDs. We can neither choose a technological solution that will require a large amount of pixels like the solution which uses microlenses array (Lambrechts et al., 2014) because our detectors do not have a sufficient number of pixels. As the imaging capability has always been a priority in CEA instruments (HERSCHEL/PACS and future SPICA/B-BOP) for science purpose, we discard the solutions which do not enable imaging or enable only a slit image. Solutions like FTS or Fabry-Perot seem to be the easiest interferometers to implement with the bolometer array. For instance, tuning the quarter-wave cavity of the bolometer with a mechanism such as microelectromechanical systems (MEMS) would have changed the optical path difference of the so-built two-wave-interferometer, in a way similar to Michelson interferometers. Nevertheless, this solution has not been selected for two reasons. The first one is that the modulation of the quarter-wave cavity would have been limited to of order one millimetre, which considerably reduces the achievable resolving power. The second one is that modifying the internal geometry of a detector requiring more than one hundred manufacturing steps is not achievable within a three year PhD project. For these reasons, we then decided to focus our research on solutions which add interferometers (FTS or FPI) above the detector array, in a similar fashion to μ -SPOC.

One solution, deeply investigated in our group, was proposed first in Reveret et al. (2010). In this paper, authors showed that adding a silicon layer above the detector allowed them to build a slightly more complex system where constructive interferences are experienced by wavelengths out of the spectral working range of the bolometer. This modification allowed them, in particular, to build from a detector array in the HERSCHEL/PACS range ($\sim 200 \mu\text{m}$) a new system suitable for observations at higher wavelengths (in the $450 \mu\text{m}$ atmospheric window). For our PhD project, we could have then used this principle to build a staircase made of silicon, where each stair, combined with the detector, optimizes a more or less narrow spectral band. In doing so, each row of the array would have been sensitive to a specific band and by scanning the scene in the windowing frame, we could derive the spectral information for each pixel of the scene. To achieve this, the exact thickness needed for each stair can be derived from calculations based on Maxwell equations and thin film theory.

For higher resolution spectroscopy and for being able to address a larger range of applications, we have chosen a solution which is not far from this solution : the Fabry-Perot interferometry. Indeed, if we think of the silicon layer as an etalon, the FP mirrors are made of the interfaces vacuum/silicon with a low reflectivity coefficient (around 70% for a quarter-wave silicon layer, see later in this part). In order to have a device tunable and not static, we decided to introduce a cavity (in our case, a vacuum cavity) between two dielectric mirrors. By tuning this cavity it is therefore possible to scan the spectrum but also to scan the range of resolutions. This allows us to target several scientific applications with one kind of instrument : low- but also high-resolution spectroscopy. We have also refined the mirror design in order to reach higher reflectivity (and thus higher finesse/resolution) with low-loss materials. As explained before, FPI are very efficient for narrow-band spectroscopy (individual lines), in particular with background-noise limited detectors. Finally, we take full benefit of the FP advantage to be easily compatible with imaging capability of the detector array.

Properties of the Fabry-Perot interferometer

In this part, we complete section 4.1.1 and aim at giving more details on the Fabry-Perot interferometry in order to lay the foundations for the definition of the system and for the requirements of the experimental set-up.

The Fabry-Perot is a multi-wave interferometer which only transmits wavelengths that are defined by $\lambda_{k'} = \frac{2nd}{k} \cos \theta$ (equation 4.6), where n is the refractive index of the cavity, d is the cavity spacing, θ is the angle of incidence and k is the order. The comb of the transmitted wavelengths for a plane wave, is given by the Airy function :

$$T = \frac{1}{1 + \frac{4R}{(1-R)^2} \sin^2(\Delta\phi/2)} \quad (4.7)$$

where $\Delta\phi = \frac{4\pi}{\lambda}nd\cos\theta$ is the phase shift. The derivation of the Airy function from the calculation of the multiple reflections inside the cavity is demonstrated in appendix A. Figure 4.10 displays the transmission of the FP for different values of the reflectivity R . It is shown that the width of the peak depends on the reflectivity : high reflectivity mirrors lead to sharp transmission peak.

For an extended source, bright rings are observed when the condition $\Delta\phi/2 = p\pi$ is fulfilled, with p the

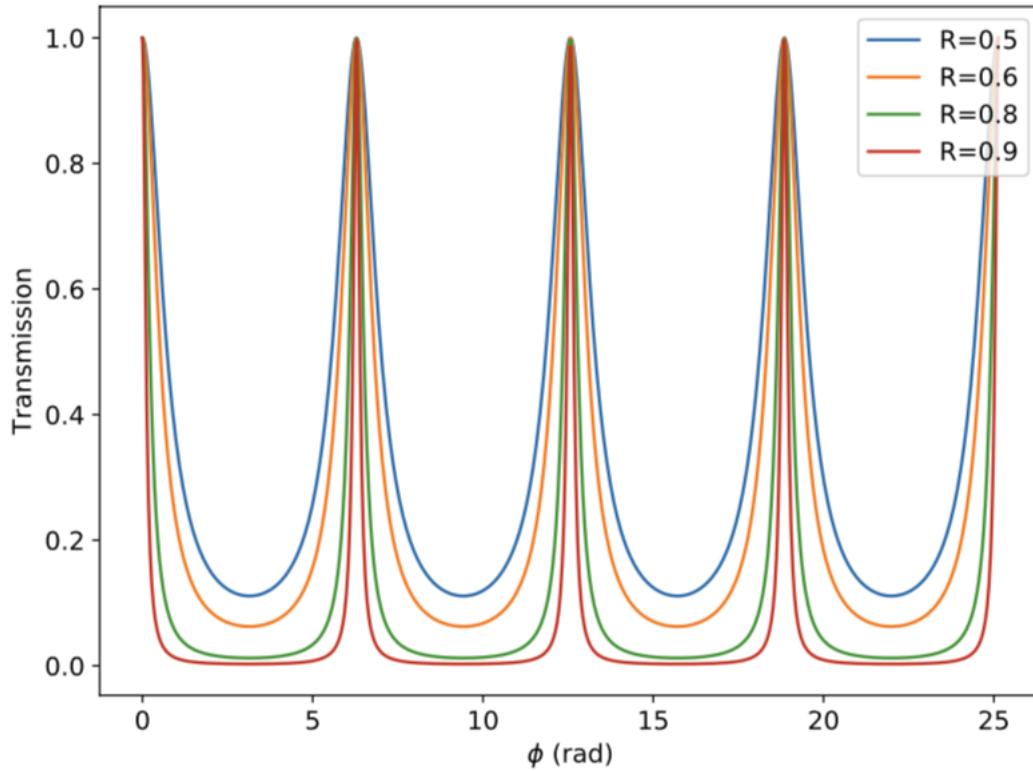


FIGURE 4.10: Transmission of the Fabry-Perot Interferometer as a function of the optical path difference in radians for different values of the reflectivity R , the transmission of a multi-wave interferometer is given by the Airy function.

ring number. To be able to observe the fringes pattern, the collimated beam that comes out from the etalon needs to be focused on a screen by the mean of a convergent lens (we note f' the focal length). The radius r of each individual ring can be therefore calculated as $r \approx f'\theta \approx f' \times \sqrt{2(1 - \frac{p\lambda}{2nd})}$. The concentric rings that Charles Fabry and Alfred Perot obtained for the green mercury line are shown in figure 4.11.

From equation 4.7, we can also derive the expression for the reflective finesse :

$$\mathcal{F}_R = \frac{\pi\sqrt{R}}{(1-R)} \quad (4.10)$$

However, this parameter only takes into account the reflectivity of the mirrors. Another parameter that, in fact, tends to broaden the transmission peaks needs to be estimated for mirrors requirements : the flatness finesse \mathcal{F}_F which stands for the errors of flatness of the mirrors surface but also of parallelism of the two

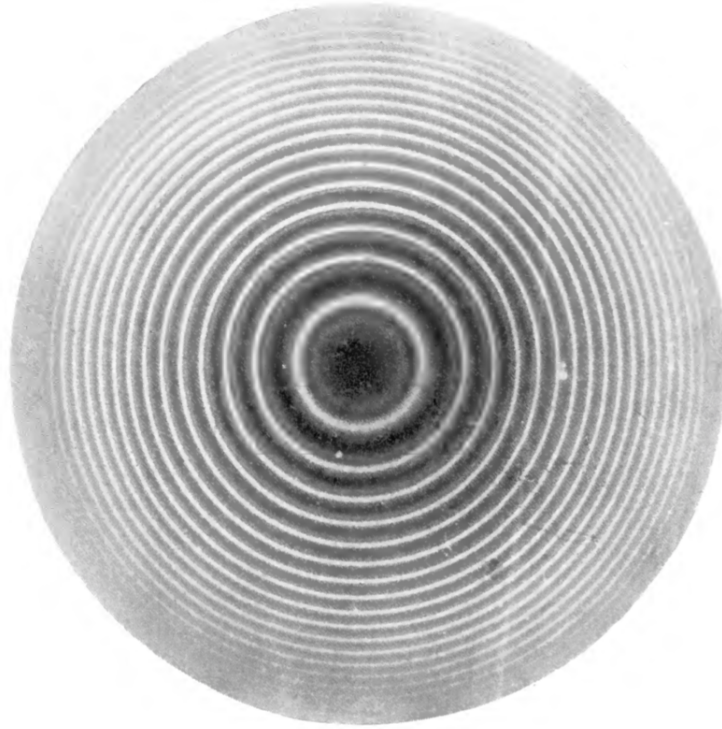


FIGURE 4.11: Interference rings obtained by C. Fabry and A. Perot with their ‘new form of interferometer’ observing a green mercury line (Fabry and Perot, 1901).

mirrors. One can also think of the reflective finesse \mathcal{F}_R as the parameter that defines the integral under the curve of one transmission peak. The flatness finesse \mathcal{F}_F describes how the total integral is distributed : the transmission peak will be high and sharp for ideal mirrors ; whereas the transmission peak will be lower and broader if the mirrors do not meet the flatness specifications since the contribution of wavelengths to the resonance will be different. For the case where mirrors quality limits the resolving power of the FP, there is one consequence, depending whether the observed line is resolved with the FPI. If the line is wider than the degraded FP profile, then we loose resolving power, while if the line is not resolved, light is lost because only a part of the FP profile is tuned to that narrow line. Moreover the integral conservation is verified (for wide line), up to a certain degradation of the mirrors flatness : if this latter is too important, scattering or walk-off may occur within the system leading to losses in the etalon. The two finesse \mathcal{F}_R and \mathcal{F}_F are related to the total finesse \mathcal{F} by the equation :

$$\frac{1}{\mathcal{F}^2} = \frac{1}{\mathcal{F}_R^2} + \frac{1}{\mathcal{F}_F^2} \quad (4.11)$$

In practice, any defect that degrades the performance of the FPI can be represented by a finesse term and added to this expression. There are additional defects which are not quantified here like the walk-off, the diffraction and the aperture effects, these parameters are described in Parshley et al. (2014). In addition

to describing the final FP profile (not only the reflectivity of mirrors), \mathcal{F} also stands for the averaged number of round trips made by the light between the plates (Brooker, 2003) and the quantity $2nd \cos \theta \mathcal{F}$ is therefore the effective longest OPD which can still interfere. Having the total finesse only limited by the reflectivity of the mirrors brings constraints on the quality of the mirrors and the setting in parallelism. To be far from limitations of the finesse by flatness errors, the deviation of the plate from a perfect plane Δd , should fulfill the condition : $\Delta d \ll \lambda/(2\mathcal{F})$ (Bacon and Monnet, 2017). Moreover, the total finesse \mathcal{F} gives access to the minimal spectral width that can be resolved by the FP, or instrumental width, $\delta\lambda$ through the equation :

$$\delta\lambda = \Delta\lambda/\mathcal{F} \quad (4.12)$$

with $\Delta\lambda$ being the free spectral range (FSR), the distance that separates two consecutive orders k and $k+1$ and is equal to $\Delta\lambda = \frac{2nd \cos \theta}{k(k+1)}$, according to equation 4.6. From this last equation, we learn that the FSR is inversely related to the order of the FPI. The finesse \mathcal{F} is a constant for each etalon, it is the figure of merit of a FP. It should not be confused with the resolving power \mathcal{R} which varies and tends to increase when scanning the higher orders. \mathcal{R} is related to \mathcal{F} by the equation :

$$\mathcal{R} = k \times \mathcal{F} \quad (4.13)$$

with k the order of the etalon. Equation 4.12 also shows that, for a given etalon finesse, $\Delta\lambda$ and $\delta\lambda$ vary in the same direction. This means that the use of high resolving power ($\delta\lambda$ small) limits the FSR ($\Delta\lambda$ small). As a consequence, when a very high resolution is not needed, it might be helpful to work at smaller orders to have a large stopband which avoids the need for sharp filters.

In equation 4.7, one parameter has not been taken into account : the absorption of mirrors. Indeed, if the material which the mirrors are made of, exhibits even a weak absorption, the total absorption of the FP may not be negligible due to the \mathcal{F} round trips inside the cavity. Adding the relation $A = 1 - (R+T)$ to the demonstration of appendix A allows one to quantify the effect of absorption by computing the maximal transmission T_{max} (for $\Delta\phi/2 = p\pi$) (Button, 1982) :

$$T_{max} = \frac{T^2}{(A+T)^2} = \left(1 + \frac{A}{T}\right)^{-2} \quad (4.14)$$

For example, assuming an etalon reaches a reflective finesse of ~ 40 without being limited by the flatness of the mirrors (i.e. $\mathcal{F} \sim \mathcal{F}_R$), the reflectivity of mirrors needs to be greater than 0.92 (one of the two solutions of the quadratic equation in R derived from the definition of \mathcal{F}_R as a function of R , equation 4.10). Then if the absorption A by a single-pass is equal to 0.01, the transmission of one mirror is $T = 0.07$ which leads to a maximal transmission of the etalon $T_{max} = 0.76$ according to the equation 4.14. A seemingly low value of the mirrors' absorption per single pass can therefore lead to very high absorption of the etalon

due to the many bounces inside the cavity. When building an etalon made from metallic mirrors, there is a trade-off to do between finesse and absorption : indeed, the higher the reflectivity, the greater the finesse but also the stronger the absorption.

4.2.2 Conventional Fabry-Perot Interferometry in the sub-millimeter range

We now describe some far-infrared/sub-millimeter instruments that perform spectroscopy with Fabry-Perot Interferometers to probe fine structure lines of the ISM. All of them use free-standing metal mesh mirrors which have been invented in the sixties. We therefore give more technical details about this type of mirrors.

Examples of instruments using FPIs

Fabry-Perot interferometers are a kind of spectrometers which are really common in far-infrared instrumentation, especially for the probing of fine structure lines that trace the gas and dust in the different phases of the ISM. Here one gives examples of instruments that use FPI : FIFI (Poglitsch et al., 1991) and KWIC (Stacey et al., 1993) onboard the Kuiper Airborne Observatory (KAO), FORCAST (Parshley et al., 2014) and the future HIRMES (Douthit et al., 2018) onboard the Stratospheric Observatory For Infrared Astronomy (SOFIA), SPIFI (Bradford et al., 2002) for the ground-based telescope James Clerk Maxwell Telescope (JCMT) on Mauna Kea in Hawaii and LWS (Clegg et al., 1996) onboard the ISO satellite, launched in 1995. The FPI technology has been chosen for all kinds of telescopes.

For almost all these instruments, several FPIs are used in series. In general, a High-Order FPI (HOFPI) gives the high resolution of the instrument, a Mid-Order FPI (MOFPI) sorts orders of the HOFPI and a Low-Order FPI (LOFPI) those of the MOFPI. Finally a bandpass filter can be used to sort the orders of the LOFPI. One may mention that for the ISO/LWS instrument and for the SOFIA/HIRMES instrument, the FPIs are used in combination with a grating to sort the order of the high-resolution spectrometers. In instruments where FPIs are used in series, the different FPIs are located at different position of the optical train and they can be therefore cooled down to different temperatures. Moreover, due to their higher resolutions, the HOFPI and the MOFPI are used in a collimated beam. However, the LOFPI can be used near the focus for saving room, since it has a low resolving power and thus a short pathlength. In papers mentioned earlier, several advantages of FP spectroscopy are reminded. Instruments that use FPIs benefit from the intrinsic 2-dimensional mapping capability of the spectrometer. It is then possible to convert an imager into a spectro-imaging facility. The wide range of spectral resolutions that a FPI can cover is also a strong advantage of this kind of spectrometer : instruments like the SOFIA/HIRMES have resolution \mathcal{R} which varies from 600 to 100,000. Finally, as noticed by Bradford et al. (2002), FPIs are very compact compared to gratings : a high resolution of 10,000 at 370 μm requires a cryogenic pathlength of about 1.8

m ($\sim \lambda\mathcal{R}/2$) at that particular wavelength for the grating but only a few centimeters for the FPI due to the many round trips inside the cavity.

An example of the transmission of the JCMT/SPIFI instrument is given in figure 4.12. The figure shows on the same plot the transmission of the two FPIs (HOFPI and LOFPI) and of the bandpass filter made by Cardiff University. It illustrates how the filters complement each other : the HOFPI is the filter that defines the high resolution of the whole instrument, the LOFPI is in charge of suppressing the unwanted orders of the LOFPI and the bandpass filter finally sorts out the orders of the LOFPI. These filters in series allow the instrument to reach a very high resolution of $\mathcal{R} = 6000$ with three compact optical elements. The main resulting drawback is the low transmission which goes down to 0.41 after passing through the HOFPI ($T_{HOFPI} = 0.70$), the LOFPI ($T_{LOFPI} = 0.75$) and the bandpass filter ($T_{BP} = 0.78$). The drop in transmission is due to the absorption of the reflective surfaces of the FPI, that are in fact metallic meshes (metallic meshes are also used for the filters). The single mesh absorption A (in the paper noted a) ~ 0.01 can be responsible for the low total transmission of the FPI, as described in the previous section.

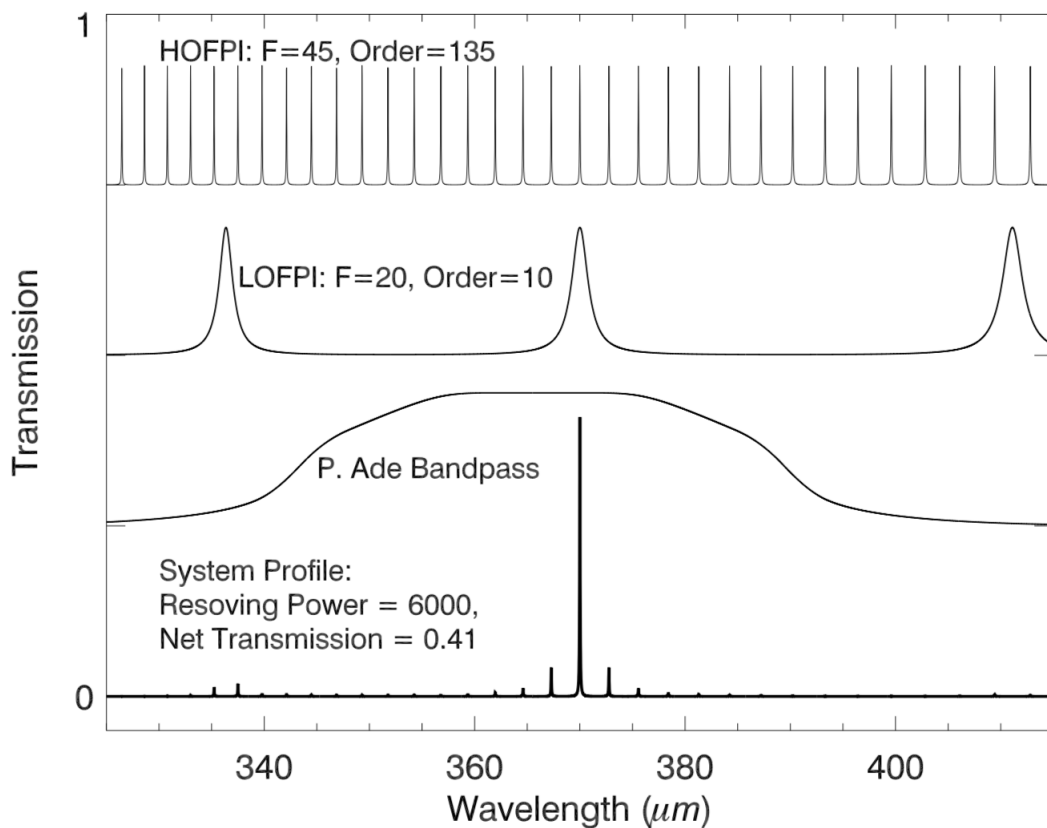


FIGURE 4.12: Transmission of JCMT/SPIFI optical components. The spectral profiles of the HOFPI ($\mathcal{R} = 6000$), LOFPI and bandpass filter are plotted (each offset and plotted at 1/4 vertical scale). The bold line is the product of the three filters. Transmission at $370 \mu\text{m}$: $T_{HOFPI} = 0.70$, $T_{LOFPI} = 0.75$ and $T_{BP} = 0.78$ which result in a total transmission of $T = 0.41$ (losses in the window, mirrors or thermal IR filters are not included) (Bradford et al., 2002).

Figure 4.13 outlines how the etalon transmission varies inversely with the etalon finesse for different absorption per pass A .

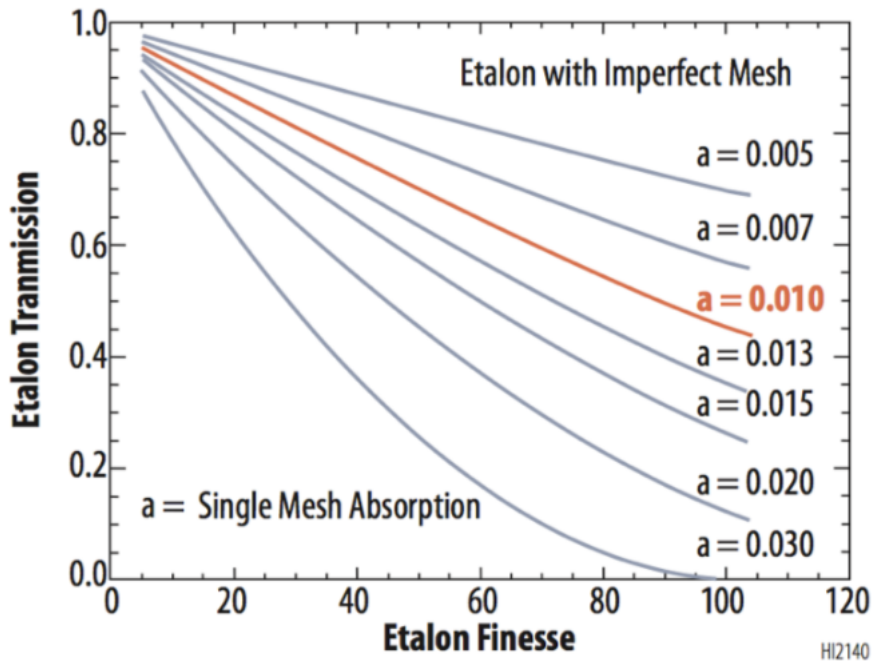


FIGURE 4.13: Computed etalon transmission as a function of the etalon finesse for different single mesh absorption A (in the plot noted a) in a metallic FPI . Transmission and finesse vary inversely due to the absorption of the individual meshes. This effect depends on the value of a (Douthit et al., 2018).

Since $\mathcal{R} = k \times \mathcal{F}$, the resolving power can be increased by two means. The first one is to have an already high value of the finesse \mathcal{F} , but as seen before, a high finesse leads to a low maximum transmission. This is why the finesse is kept “small” (< 60) in conventional FP interferometry and that one then prefers to increase the order of the FPI. However, higher orders induce narrower free spectral ranges, this therefore requires strong filtering and for this reason several FPIs are used in series. In the ISO/LWS instrument that used a grating to sort the order of the FPI, the finesse had been intentionally increased to $\mathcal{F} = 100$ to reach $\mathcal{R} = 10,000$ (i.e order $k = 100$) in order to enable the grating to spectrally resolve the orders of the FPI (Davis et al., 1995). This had a strong consequence : the peak transmission dropped down to 25% (for $R = 0.98$ and $A = 0.01$ in equation 4.14).

FPI based on metallic mesh mirrors

“This effect [transmission within narrow lines] is the more pronounced as the reflecting power f becomes more nearly equal to unity ; now the reflecting power of silvered glass increases with the thickness of the silver film, and approaches that of the compact metal, which is about 0.90 ; but at the same time the

quantity of light absorbed by the silver film increases. If this absorption did not exist, the intensity I_0 of the maxima would be always equal to that of the incident light; the existence of the absorption limits the thickness of the silver films that can be employed, and this thickness must depend upon the intensity of the light at command.” (Perot and Fabry, 1899)

The issue that Charles Fabry and Alfred Perot had to face with their etalon is similar to what the far-infrared FP interferometry needs to deal with nowadays. So far the FPIs are all made of free-standing metal meshes. Initially the grids were formed by electro-deposition of nickel, but they are now built by UV photolithography (Ade et al., 2006). They were first introduced by R. Ulrich, K. F. Renk, and L. Genzel who reported two structures that can be used as filters (Ulrich, 1967). The first mesh is made of a metallic grid while the other (its complementary) is made of squares of metal : both are shown in figure 4.14.

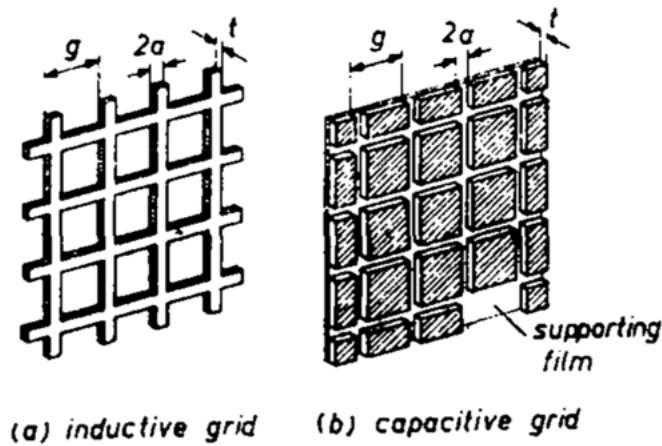


FIGURE 4.14: The inductive and the capacitive two-dimensional grids (Ulrich, 1967).

Because it is possible to make the analogy with the theory of equivalent circuits, the metallic grid is referred to as the ‘inductive grid’ and its complementary as the ‘capacitive grid’. They are both part of what is called the Frequency-Selective Surface (FSS) that subsumes filters whose optical properties depend on the geometry of the meshes. In the following, one only details the theory related to the inductive grids since far-infrared FPI instruments rely on this technology. The first consideration is that the grid constant g (see figure 4.14) must be smaller than the wavelength λ to work in the non-diffraction regime. In short, the inductive grids transmit short wavelengths and reflect long wavelengths and therefore act as a high-pass filter in transmission. The reflection of the so-built filter is commonly used to form the mirrors of the Fabry-Perot interferometer. In Ulrich (1967), Ulrich et al. (1963) and Sakai and Genzel (1983), the authors estimate the theoretical reflection coefficient of these metal-mesh mirrors and quantify the absorption A of the inductive grid due to ohmic losses. As it can be seen in the following equations, both coefficients

depend on the mesh parameters :

$$\begin{cases} R = 1 - \left(\frac{2g}{\lambda} \ln \frac{g}{2\pi a}\right)^2 \\ A = \frac{g}{\pi a} R \left(\frac{4\pi\epsilon_0 c}{\lambda\sigma}\right)^{1/2} \end{cases}$$

where g and a are the grid constant and the radius of the circular wires of the inductive grid respectively, c is the speed of light, ϵ_0 the permittivity of free space, λ the wavelength and σ is the conductivity of the material. However, these parameters are also involved in the maximal peak transmission T_{max} :

$$T_{max} \approx 1 - \frac{\lambda^{3/2}}{6ag(\ln(\frac{g}{2\pi a}))^2(\frac{4\pi\epsilon_0 c}{\sigma})^{1/2}} \quad (4.15)$$

4.2.3 Optimizing the spectral finesse of the FPI

In the frame of this thesis, we evaluated first the capabilities of a spectrometer associated with detectors in the scheme proposed by (Reveret et al., 2010) for wavelength adaptation. The idea was to have a single dielectric layer in front of each detector (or in front of each pixel row, like in a staircase configuration). However, the finesse, and thus the performance, of such a dispositive is very limited, as already described. To increase the spectroscopic skill of this scheme, we decided to start at CEA the development of “real” Fabry-Perot interferometers in order to add the spectroscopic selectivity to the detector. Whereas the far-infrared state-of-the-art FPIs are all made of metallic meshes, we explored the possibilities of using dielectric materials to make the reflective surfaces of the FPI. This approach has been already widely developed in other domains of spectroscopy (e.g. visible, UV). The main reason for this is to avoid any ohmic losses which are introduced by metallic mirrors. In having such mirrors, we could have potentially higher transmission and thus a more efficient spectrometer to couple to the detector. In this part, we only deal with the spectrometer, the study of the spectro-imaging device will come later in this chapter. Here, we first present parallel developments of FPIs using dielectrics, in other laboratories. We also introduce the material from which our interferometer is made of, namely high-resistivity float zone silicon. Then, the mathematical model which has been used to improve the performance of the system is explained in detail. Finally, we show the technological solutions which have been considered during this thesis.

FP developments in other labs

A short overview of the current developments in other sub-millimeter laboratories indicates that FP spectroscopy, although the physics is more than 100 years-old, keeps being challenging. Many researches are

indeed, dedicated to the improvement of FPIs. For example, we can mention a group at Cornell University⁶ (Cothard et al., 2018) which has worked on the combination of inductive and capacitive meshes to obtain a uniform reflectance and thus a uniform finesse over a wide bandwidth (800 μm - 1.5 mm). In addition, they demonstrated the potential of using anti-reflection coated silicon substrate to support the meshes without reflecting a large amount of light. In parallel, they “explore the use of superconducting meshes instead of the traditional gold meshes”. Since the low transmission of FPs based on metallic meshes originates from ohmic losses in the metal, using superconducting material as mirrors would counter this issue. Indeed, below the critical temperature, the ‘electrons’ of the superconductors can move freely without collisions, leading to no absorption. However, this solution could be limited to the millimeter domain because Cooper pairs in a superconductor have generally a low binding energy in comparison to the gap required for $\lambda \sim 150\mu\text{m}$ which is about 8 meV (i.e. $T_c \sim 56$ K). Another example of research in the FP field is given by the work of the University of Lethbridge⁷ in collaboration with SRON⁸ (Naylor et al., 2017). They have designed a monolithic pendulum scanning mechanism which can change the angle of incidence of a fixed etalon. This system makes possible the scanning of the spectrum by tuning the angle of incidence of the collimated beam. The ‘walk-off’ effect that FPs usually suffer originating from the oblique incidence, is reduced by having the conventional inductive meshes mounted on a highly resistive silicon substrate (high refractive index in the Snell’s law). This system simplifies the actuation and the metrology required by traditional scanning FP.

In parallel of these developments, one notices a new trend to build optics made with silicon, like lenses and anti-reflective coatings, based on structured silicon (Caltech or Cardiff University⁹ to name a few).

High Resistivity Float Zone silicon for cryogenic FPI

Our development at CEA is based on the use of dielectric mirrors to replace the metallic meshes systematically used so far. We have chosen to work with silicon, and more specifically with high resistivity float zone (HRFZ) silicon in order to reduce the losses in the material. The float zone method allows the silicon to reach high-purity and thus high-resistivity (for more details see Nakajima and Usami (2009)). For our experiment, we will use silicon with resistivity greater than 1 k Ω .cm.

Dai et al. (2004) present measurements with a terahertz time-domain spectrometer (TDS) performed on HRFZ silicon with a resistivity greater than 10 k Ω .cm. They firstly show that the index of refraction n_{Si} is almost perfectly constant and equal to 3.4175 ± 0.0001 over the 0.5 - 4.5 THz band (67 - 600 μm). From the TDS measurements at room temperature, they also define an upper limit to the intrinsic power absorption coefficient α of the HRFZ silicon : α is less than 0.01 cm^{-1} in the frequency band 0.2 -1 THz

6. Ithaca, NY, USA

7. Lethbridge, Alberta, Canada

8. Netherlands Institute for Space Research, Groningen, Netherlands

9. Wales, UK

(300 μm - 1.5 mm) and less than 0.025 cm^{-1} in the frequency band 1-2 THz (150 μm - 300 μm). The use of low temperature, which cannot be avoided in the far-infrared field, might also increase the resistivity of the material and thus further reduce the losses. Pracht et al. (2012) derived from measurements the conductivity of doped silicon over a large frequency band ($2\text{-}25 \text{ cm}^{-1}$). The results are shown in figure 4.15 : the real conductivity σ_1 which is responsible for the power dissipation in the material, first increases around 150 K (because of the density and mobility of carriers) but then dies off under 80 K (because the density is getting lower at low temperature). This effect should then be reinforced at very low temperature ($\sim 4 \text{ K}$) with HRFZ silicon in the focal plane. By using highly resistive silicon ($> 1 \text{ k}\Omega\cdot\text{cm}$) for the cryogenic FPI, we expect the peak transmission to be considerably improved with respect to the state-of-the-art FPI, because of no absorption (or at least very small absorption).

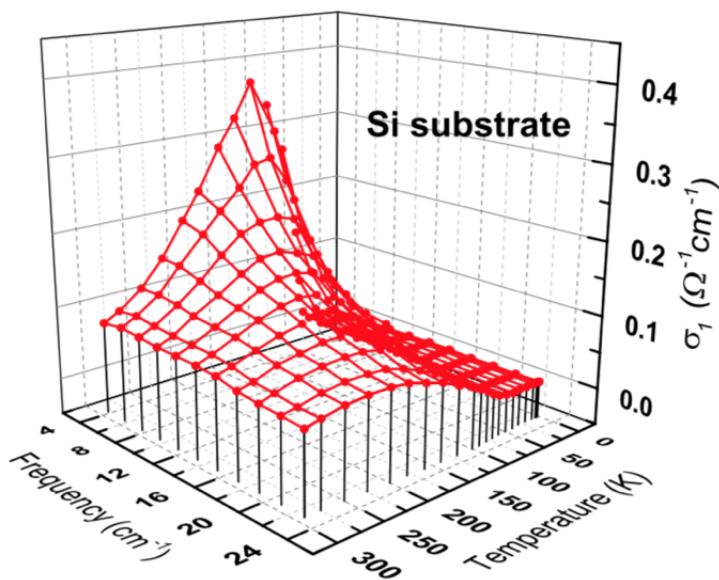


FIGURE 4.15: Real part σ_1 of conductivity with respect to frequency and temperature for silicon (extracted from Pracht et al. (2012)).

Modeling with thin film theory

Before describing the different technological solutions that we have investigated for the development of the all-silicon spectrometer, we first introduce the mathematics used for the modelling. The different layers of the spectrometer have been simulated with a model based on thin film theory. It relies on the computation of propagative fields within a stack of layers. Calculations are derived for the particular case of a plane wave. Here we only give a summary of equations used for derivation of the transmission of the

FPI (for more details see Macleod (2010)). In thin film theory, each layer j is defined by its thickness d_j and by its refractive index n_j as shown in figure 4.16. The transmitted amplitude a_j^+ and the reflective

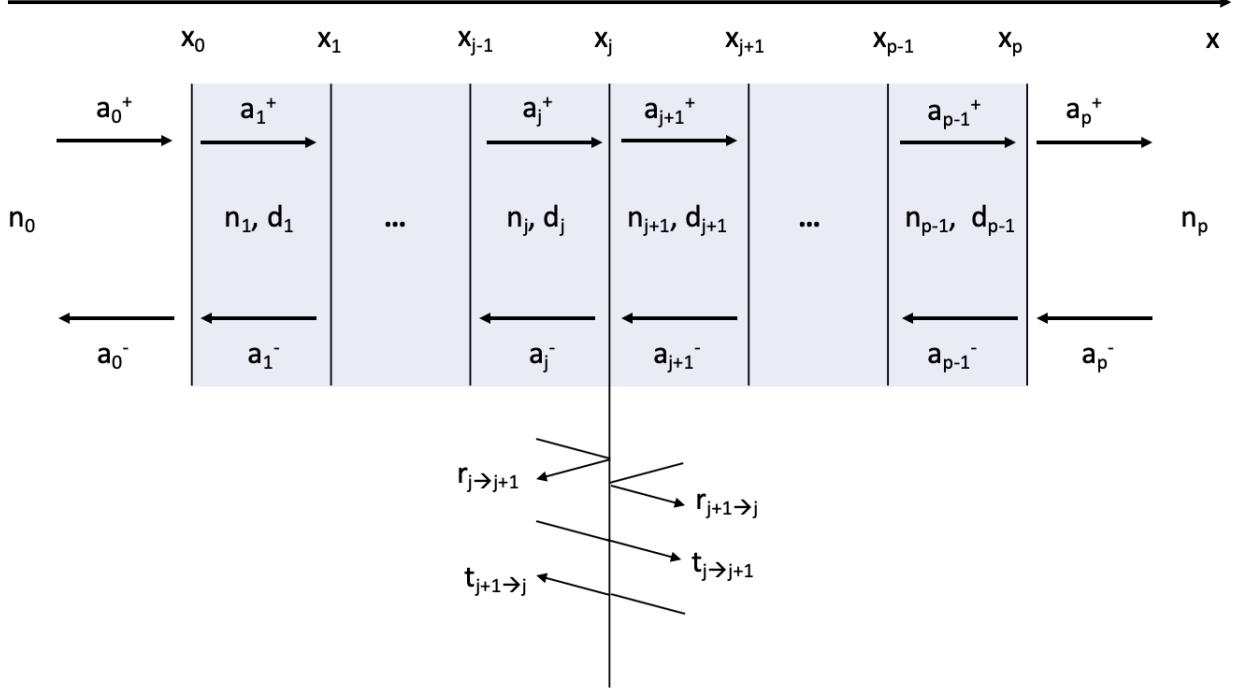


FIGURE 4.16: Definition of the wave amplitudes propagating inside a thin-film stack. Each layer j is represented by its thickness d_j and its refractive index n_j . a_j^+ is defined as the transmitted wave amplitude of the layer j while a_j^- is the reflected wave amplitude of the same layer. The layer optical thicknesses are assumed to be much smaller than the coherence length of the incident beam.

amplitude a_j^- can then be calculated for each layer j as a function of the surrounding layers and of the Fresnel coefficients. Moreover, knowing that the tangential components of the total electric field E_j and of the total magnetic field H_j are proportional to $(a_j^+ + a_j^-)$ and $n_j (a_j^+ - a_j^-)$ respectively, we get the following equation :

$$\begin{pmatrix} a_0^+ + a_0^- \\ n_0 (a_0^+ - a_0^-) \end{pmatrix} = \prod_{j=1}^p \begin{pmatrix} \cos \delta_j & \frac{i}{n_j} \sin \delta_j \\ i n_j \sin \delta_j & \cos \delta_j \end{pmatrix} \begin{pmatrix} a_p^+ + a_p^- \\ n_p (a_p^+ - a_p^-) \end{pmatrix} \quad (4.16)$$

with $\delta_j = \frac{2\pi n_j d_j}{\lambda}$ at normal incidence and n_0 and n_p the refractive indexes of vacuum and of the substrate respectively. Assuming $a_p^- = 0$ (i.e. the illumination only comes from the left side) in figure 4.16, the equation 4.16 becomes :

$$\begin{pmatrix} a_0^+ + a_0^- \\ n_0 (a_0^+ + a_0^-) \end{pmatrix} = \prod_{j=1}^p \begin{pmatrix} \cos \delta_j & \frac{i}{n_j} \sin \delta_j \\ i n_j \sin \delta_j & \cos \delta_j \end{pmatrix} \begin{pmatrix} 1 \\ n_p \end{pmatrix} \cdot a_p^+ = \begin{pmatrix} B \\ C \end{pmatrix} \cdot a_p^+ \quad (4.17)$$

By computing the B and C components, one can therefore define the amplitude reflection r and transmission factor t by :

$$\begin{cases} r = \frac{a_0^-}{a_0^+} = \frac{n_0 \cdot B - C}{n_0 \cdot B + C} \\ t = \frac{a_p^+}{a_0^+} = \frac{2 \cdot n_0}{n_0 \cdot B + C} \end{cases} \quad (4.18)$$

From the amplitude coefficients, one can derive the intensity factors R and T of a stack of layers :

$$\begin{cases} R = r \cdot r^* = \left(\frac{n_0 \cdot B - C}{n_0 \cdot B + C} \right) \cdot \left(\frac{n_0 \cdot B - C}{n_0 \cdot B + C} \right)^* \\ T = \frac{Re(n_p)}{n_0} t \cdot t^* = \frac{4 \cdot n_0 \cdot Re(n_p)}{(n_0 \cdot B + C) \cdot (n_0 \cdot B + C)^*} \end{cases} \quad (4.19)$$

From a simple matrix calculation, the thin film formalism allows one to derive the transmission and reflection coefficients of a potentially complex structure.

Improving the reflectivity of mirrors

In the frame of this thesis, we decided to develop dielectric mirrors for FP spectroscopy. As the CEA/LETI which we work closely with, is very used to work with silicon, and for the promising properties of silicon, we investigated the feasibility of mirrors made of silicon. One of the advantage of silicon in optics is its high refractive index ($n_{Si} = 3.41$), we can get the reflection coefficient of silicon for a semi-infinite plane (only valid for this case), following the Fresnel formula :

$$R_{Si} = \left(\frac{n_{Si} - 1}{n_{Si} + 1} \right)^2 = 30 \quad (4.20)$$

However, for example, for silicon mirrors with a quarter-wave thickness (explained later in this part), separated by a half-wave cavity, the mirrors reflectivity is $\sim 70\%$. It should be mentioned that for low values of R , the relationship 4.10 which links the reflectivity of mirrors and the finesse no longer applies. One way to improve the reflectivity of the mirrors and thus the finesse, is to choose dielectrics with higher refractive index like germanium ($n_{Ge} = 4$), but the range of reflectivities becomes very limited : the reflectivity of a germanium quarter-wave layer is about 78% at $\lambda = 160 \mu\text{m}$. Instead of this, we have preferred to design Bragg mirrors based on silicon. Bragg mirrors are made of a stack of multiple layers of dielectrics and can, in fact, reach very high reflectivity (Koshida, 2008). The working principle relies on the multiple reflections on the different interfaces that produce constructive interferences assuming each layer of the overall system follows a specific layout. Indeed, the stack must be composed of several layers of a high refractive index material (H) interleaved with layers of a low refractive index material (L). Each layer must have a quarter-wavelength optical thickness : $t = \lambda/4n$. The reflections within the stack are

shown in figure 4.17. From Maxwell's equations, one learns that a wave which travels from (H) to (L) does not experience any round-trip phase shift at the interface but is π -shifted when traveling from (L) to (H). Moreover since each layer is $\lambda/4n$ -thick, the phase shift through each layer is $\pi/2$. These two effects lead to constructive interferences for the proper wavelength λ and a consequence is that the more layers there are, the more reflective the system is.

The system of mirrors made of the alternative of (H) and (L) can be represented by the following notation :

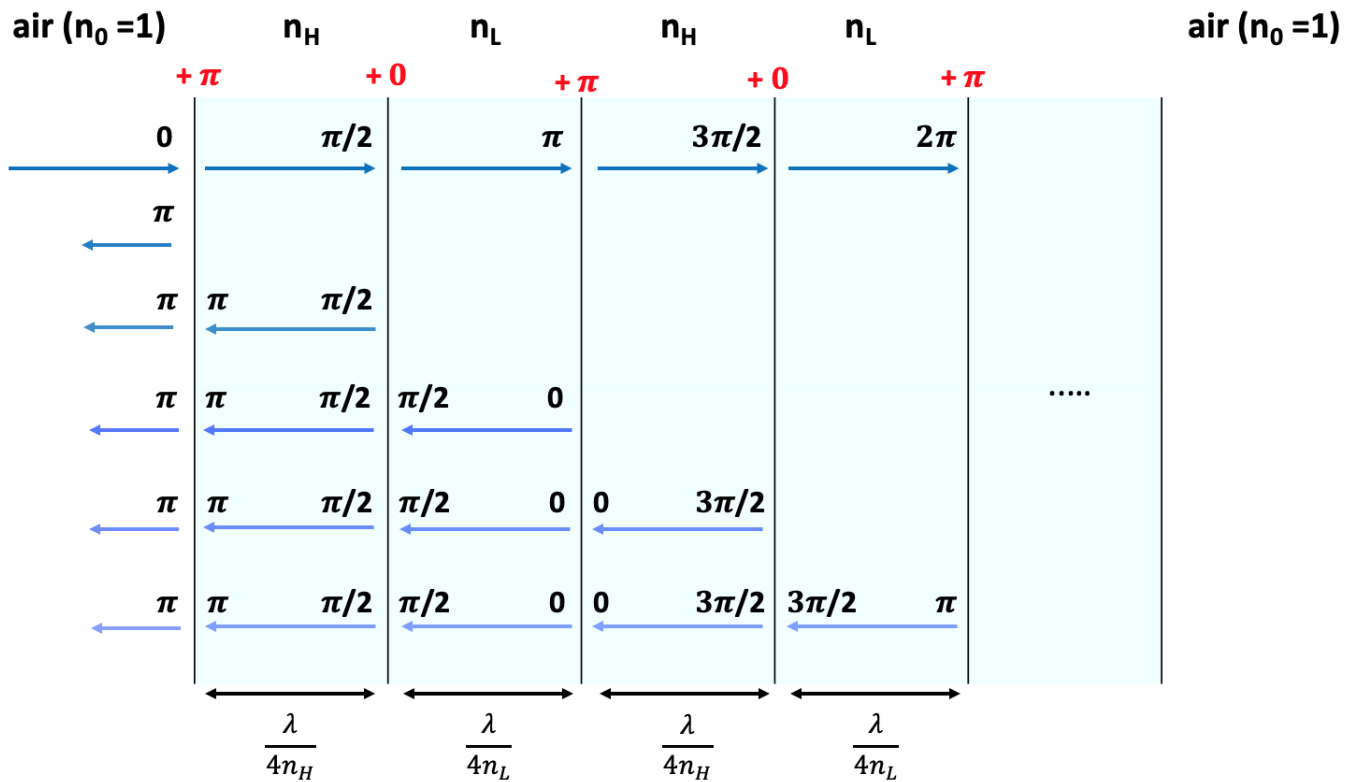


FIGURE 4.17: Principle of Bragg mirrors : several high refractive index material (H) layers interleaved with layers of low refractive index material (L). Each layer is $\lambda/4n$ -thick, so the wave is delayed by $\frac{\pi}{2}$ in it for the specific wavelength λ . The multiple reflections within the layers result in constructive interferences that allow the whole stack to reach high reflectivity. Note that the wave experiences a phase shift at the interface when travelling from (L) to (H) (in red on the sketch).

$$n_0/HLH...HLH/n_0 \quad (4.21)$$

which can also be noted :

$$n_0/(HL)^N H/n_0 \quad (4.22)$$

where N is the number of times (HL) is repeated within the stack. Therefore, from equation 4.17, one can derive the vector :

$$\begin{pmatrix} B \\ C \end{pmatrix} = \prod_{j=1}^{2N+1} \begin{pmatrix} 0 & \frac{i}{n_j} \\ i n_j & 0 \end{pmatrix} \begin{pmatrix} 1 \\ n_0 \end{pmatrix} = \begin{pmatrix} i \frac{n_0}{n_H} \left(\frac{n_L}{n_H}\right)^N \\ i n_H n_0 \left(\frac{n_H}{n_L}\right)^N \end{pmatrix} \quad (4.23)$$

The reflectivity coefficient is given for the specific wavelength λ by the equation :

$$R = \left(\frac{1 - \frac{n_H^2}{n_0} \left(\frac{n_H}{n_L}\right)^{2N}}{1 + \frac{n_H^2}{n_0} \left(\frac{n_H}{n_L}\right)^{2N}} \right)^2 \quad (4.24)$$

We can present some significant results derived from the previous analysis . In figure 4.18, the reflectivity of several mirrors (HLH) ($N=1$) for $n_H= 3.41$ and for different values of n_L at $\lambda = 160 \mu\text{m}$ are plotted. The results are compared with a single $\lambda/4$ - thick layer of silicon and germanium : Bragg mirrors considerably improve the reflectivity over single layers. From this, one can conclude that the reflectivity and the bandwidth increase with the index ratio n_H/n_L .

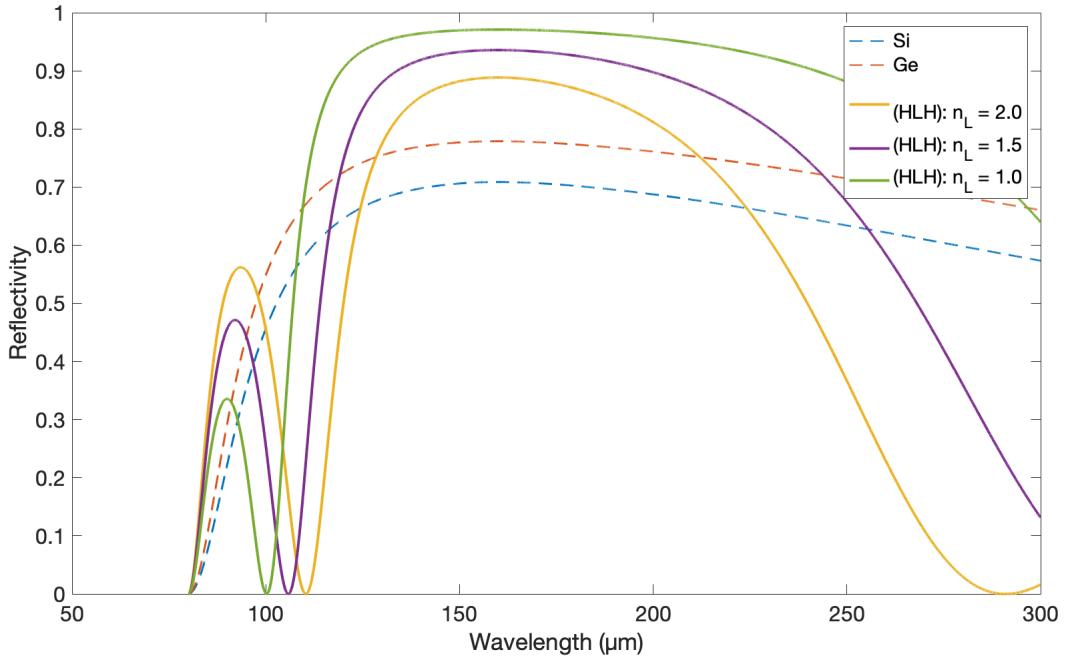


FIGURE 4.18: Reflectivity as a function of wavelength for different values of n_L in a (HLH) Bragg mirror for $\lambda = 160 \mu\text{m}$. (H) is silicon ($n_H = 3.41$). The reflectivity and the bandwidth increase with the index ratio n_H/n_L . The reflectivities of a single $\lambda/4$ -thick layer of silicon and germanium are also plotted for comparison.

Figure 4.19 shows the effect of the multiplicity N of layers (HL) on the reflectivity. As expected, the reflectivity increases with N , while the bandwidth becomes narrower but sharper.

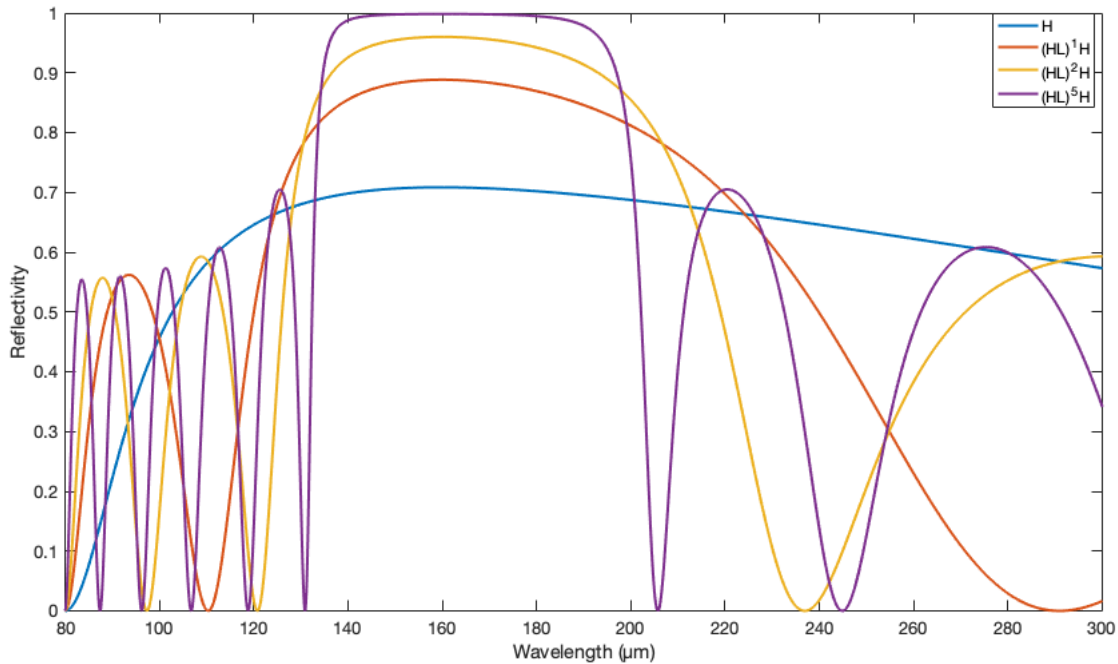


FIGURE 4.19: Reflectivity as a function of wavelength for different values of N in a $(HL)^N H$ Bragg mirror for $\lambda = 160 \mu\text{m}$. (H) is silicon ($n_H = 3.41$) and (L) has been chosen to be a material with $n_L = 2.0$ (to highlight the improvement in reflectivity with increasing N). The reflectivity increases with N but becomes also sharper with N .

One should finally mention that odd numbers of quarter-wave layers provide the same phase shift, which means that Bragg mirrors layers can be $(2p + 1)\lambda/(4n)$ -thick. To give an order of magnitude, for silicon at $160 \mu\text{m}$, Bragg layers are $12 \mu\text{m}$ -thick at first order, $35 \mu\text{m}$ -thick at second order, $59 \mu\text{m}$ -thick at third order, and so forth.

Definition of the stack for the FPI

The final definition of the stack of the etalon has been the result of discussions with CEA/LETI. We planned to build a FPI with the following structure : $(HLH)/ D /(HLH)$, where one mirror corresponds to the (HLH) stack and D is the cavity of the etalon. We chose this three-layers mirror layout for the first prototype to prove that Bragg mirrors are meaningful for our application. Furthermore, limiting the reflectivity of mirrors allows one to get a “reasonable” etalon finesse since a higher finesse, in the case of a more complex stack, could be difficult to measure. It is also important to note that Bragg mirrors for far-infrared spectrometer are nowadays achievable only because the manufacturing of these very thin layers ($< 100 \mu\text{m}$) is possible by etching silicon wafers with sufficient accuracy.

We have firstly oriented the calculations of Bragg mirrors towards $\lambda = 160 \mu\text{m}$, but the studied wavelength range has slightly evolved with the different technological solutions under study.

Solution based on micro-structured silicon

This part is presented in appendix B. It is not shown in detail in this chapter since micro-structured silicon mirrors have not been used for the final prototype. However, we want to emphasize that structuration of silicon can lead to a material with an effective refractive index intermediary between silicon and air refractive indices. This is the reason why we investigated first micro-structured silicon as the low-refractive index material. As it will be explained later in this chapter, this promising solution could have other direct applications.

Solution based on vacuum quarter-wave gap

In order to quickly have a simple prototype which completes a proof of concept, we decided to keep the layout (HLH)/D/(HLH) assuming that we can replace the micro-structured silicon layers by simple airgaps (to be more accurate, vacuum gaps). The idea is then to have spacers between silicon sheets with all layers adjusted to an optical thickness of a quarter-wavelength. While we initially aimed to build a spectro imager for the 160 μm wavelength, we chose to move the resonance of our demonstrator to 320 μm to facilitate the manufacture of the layers, since for Bragg mirrors the thickness of layers is proportional to the targeted wavelength. Hence, we had to grind down the silicon sheets for mirrors and spacers only to twice the thickness of what would be needed for 160 μm which seemed less of a risk and challenge for the mechanical grinding process, when the thickness of layers should be of order less than 100 μm . For the spacers, we opted for rings also made from silicon to avoid any issues with differential thermal expansion during the cool-down to 4 K. The final optical design was therefore : (H/L/H)/2L/(H/L/H), (H) being the full silicon sheets and (L) being vacuum, defined by the silicon rings. The overall stack is depicted in figure 4.20.

Concerning the thicknesses, we picked $t_{Si} = 71 \mu\text{m}$ for the silicon sheets, $t_{vac} = 80 \mu\text{m}$ for the silicon spacers and the FP cavity (2L) is therefore $D = 160 \mu\text{m}$. While $t_{vac} = 80 \mu\text{m}$ corresponds to the conventional quarter-wave thickness required by the Bragg mirror theory, the thickness $t_{Si} = 71 \mu\text{m}$ results from fulfilling the quarter-wave condition in third order (only the odd orders produce effective mirrors). This solution was selected to reduce the risks of breaking the sheets in grinding and assembly, for the first prototype. The impact of the change in thickness is quantified in figure 4.21 which compares the reflectivity of a stack (HLH) for $t_{Si} = \lambda/4$ and $t_{Si} = 3\lambda/4$. The principal effect is a reduction of the bandwidth by a factor 3. Assuming we are able to manufacture such thin layers, we might have an etalon equally efficient over almost 400 μm around $\lambda = 320 \mu\text{m}$. The technological details of the manufacturing are provided in chapter 5; here, we only present the general design and the computed results.

The resulting transmission of FPI based on mirrors with $t_{Si} = 3\lambda/4$ has been computed in figure 4.22 for different cavity size D_{FP} . In the calculation, we assumed that the silicon is a lossless material, but this strong hypothesis should still be experimentally verified. Based on this assumption, the maximal transmission of the FP reaches 100% efficiency over the whole bandwidth. As expected, the finesse is

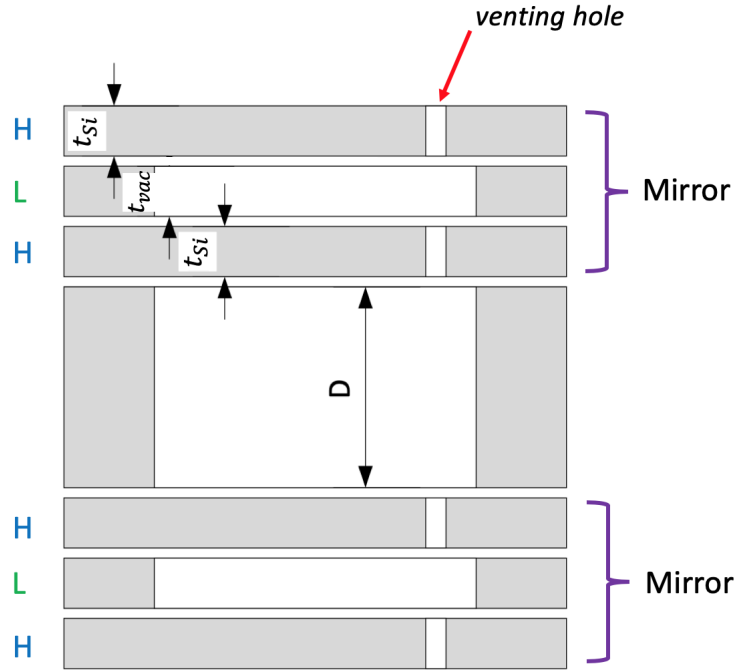


FIGURE 4.20: FPI design based on Bragg mirrors for $\lambda = 320 \mu\text{m}$. Each mirror follows a (HLH) configuration where (H) is full silicon while (L) is vacuum. For $\lambda = 320 \mu\text{m}$, we picked the following thicknesses : $t_{Si} = 71 \mu\text{m}$ for the full sheets and $t_{vac} = 80 \mu\text{m}$ for the silicon rings. The mirrors are separated by a half-wave cavity ($160 \mu\text{m}$) which is made of two quarter-wave silicon rings. Venting holes have been drilled in the full sheets to prevent any deformation or damage from differential pressure during pumping or venting, when used in its dedicated cryostat.

the highest for the wavelength λ which the mirrors are made for, and gets gradually degraded for other wavelengths. Moreover, the transmission bandwidth of the FP is limited to $\sim 260\text{-}400 \mu\text{m}$ because the mirrors become transparent for these two extreme wavelengths (see in figure 4.21). At these wavelengths, the cavity spacing does not have any key role, since the two mirrors are transparent whatever the distance between them. In brief, the fact that the overall system is complex suggests that in addition of the response of the FP as a function of the cavity size, the spectral behavior of each subsystem (i.e. the mirrors) must be understood. Regarding this effect, the metallic mirrors have an advantage : the FP based on Bragg mirrors requires a strong filtering as it does not only exhibit Dirac combs at the resonant wavelengths. However, the filtering requirements will be considerably relaxed for example in the case of $t_{Si} = \lambda/4$ since the mirrors are efficient over a very large bandwidth.

In this part, the design of the Fabry-Perot spectrometer and its expected performance have been presented. The experimental prototype will be described in detail in chapter 5. The following section is dedicated to the coupling of the CEA bolometer (as presented in chapter 2) with the chosen spectrometer. It should be mentioned that although the detection device is a thermal sensor, only the electromagnetic aspects have been studied.

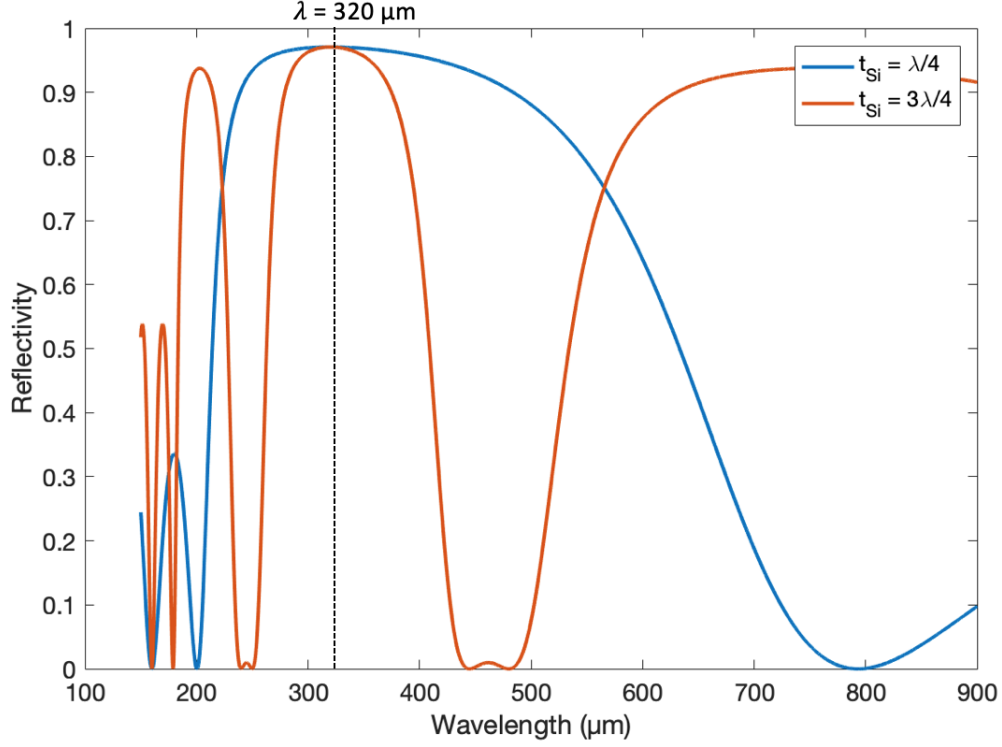


FIGURE 4.21: Computed reflectivity of dielectric mirrors in a H/L/H configuration (Bragg mirrors). The high refractive index (H) is silicon ($n_{Si} = 3.4$) and the low refractive index (L) is vacuum ($n = 1$). In both cases, the vacuum thickness is $t_{vac} = 80 \mu\text{m}$. The silicon thickness t_{Si} is equal to $23\mu\text{m}$ ($k = 0$ and $t_{Si} = \lambda/4$) on the blue curve and to $71 \mu\text{m}$ ($k = 1$ and $t_{Si} = 3\lambda/4$) on the red curve. The reflectivity is then affected by the layer thickness. Increasing the thickness by a factor 3 decreases the bandwidth where mirrors are efficient reflectors by a factor 3.

4.2.4 Coupling the FPI with the detector

Paving the way for developments toward compact spectro-imaging devices based on CEA type bolometer in the far-infrared field is the final purpose of this thesis. The dielectric Fabry-Perot interferometer should be suitable to add the spectral selectivity to a bolometer array since it is compatible with imaging (to a certain extent) and it is very compact. The idea is to bring the spectrometer close to the detector : the optimal distance has been computed to be of the order of half the wavelength (explained later in this section). Figure 4.23 sketches the layout of the spectro-imaging device. The quarter-wave cavity of the detector has been simplified for clarity : it is only made of an absorber located at $\lambda_{cav}/4$ from the backshort mirror. From now on, λ_{FP} and λ_{cav} denote the wavelengths which the FP geometry and the detector cavity are respectively adapted for. In this section, λ_{FP} and λ_{cav} are not necessarily equal.

Combining the spectrometer to the detector

In the following, results from calculations based on thin film theory are depicted. As already mentioned, the matrix computations stand for the propagation of a plane wave. In the context of instrumentation with

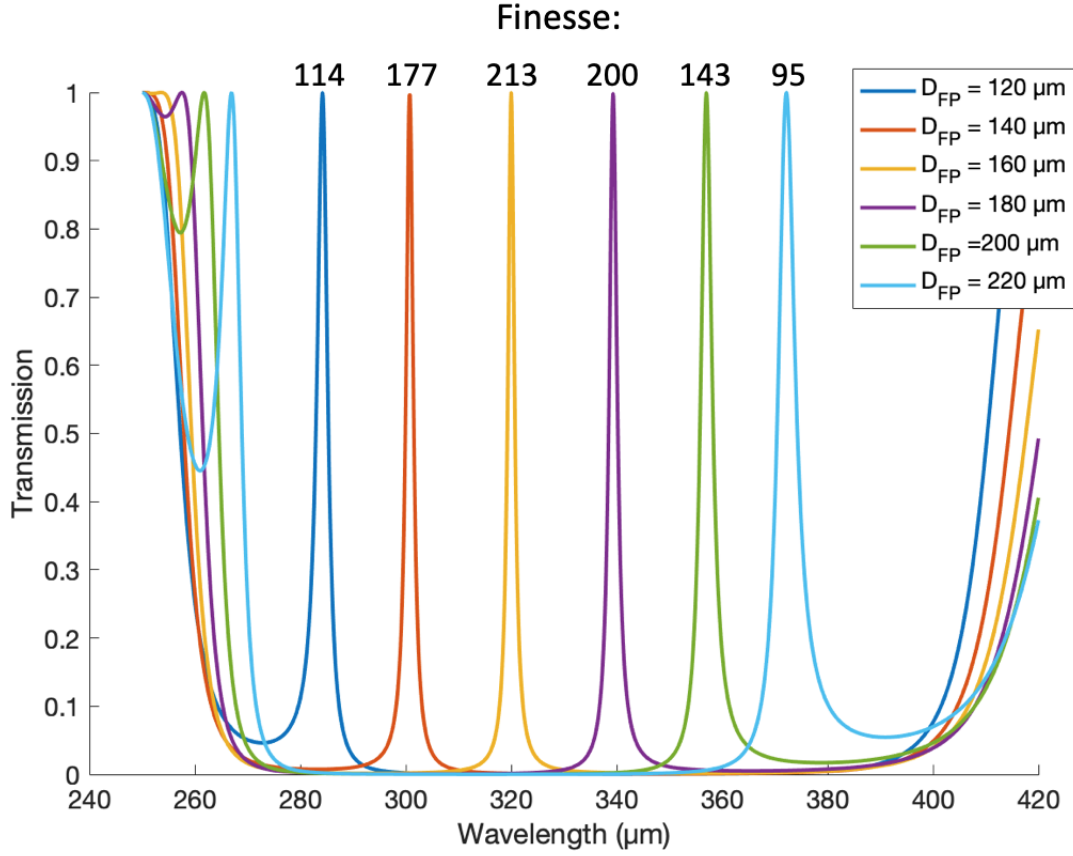


FIGURE 4.22: Computed transmission of the FPI presented in figure 4.20 for different cavity sizes of the FP D_{FP} . The finesse of each transmission peak has been computed and added on the plot above each peak : as expected the finesse is the highest for the wavelength that the mirrors geometry is adapted for. Note that the bandwidth on which the FP acts as a narrow-band filter is limited (on the left and right) due to total transmission of the mirrors of the FP that one could already observe in figure 4.21.

an FPI close to the detector, the assumption of a plane wave is not fully correct due to the focus ; however here we assume this is approximately fulfilled for high f-numbers (which is often true for our applications, since the detector pixel can be large). In order to observe the effect of coupling of the spectrometer to the detection device, the reflection coefficient is derived from equation 4.16. The last layer p of the coupled system ends with a backshort mirror, the consequences are therefore : a_p^- is not null but $a_p^+ + a_p^-$ is, since the tangential electric field vanishes at the surface of a mirror. In addition, $n_p(a_p^+ + a_p^-) = 2n_p a_p^+$, from the previous statement. The amplitude reflection is still :

$$r = \frac{a_0^-}{a_0^+} = \frac{n_0 \cdot B' - C'}{n_0 \cdot B' + C'} \quad (4.25)$$

with $B' \neq B$ and $C' \neq C$ since one has :

$$\begin{pmatrix} a_0^+ + a_0^- \\ n_0 (a_0^+ - a_0^-) \end{pmatrix} = \prod_{j=1}^p \begin{pmatrix} \cos \delta_j & \frac{i}{n_j} \sin \delta_j \\ i n_j \sin \delta_j & \cos \delta_j \end{pmatrix} \begin{pmatrix} 0 \\ 2 \cdot n_p \end{pmatrix} \cdot a_p^+ = \begin{pmatrix} B' \\ C' \end{pmatrix} \cdot a_p^+ \quad (4.26)$$

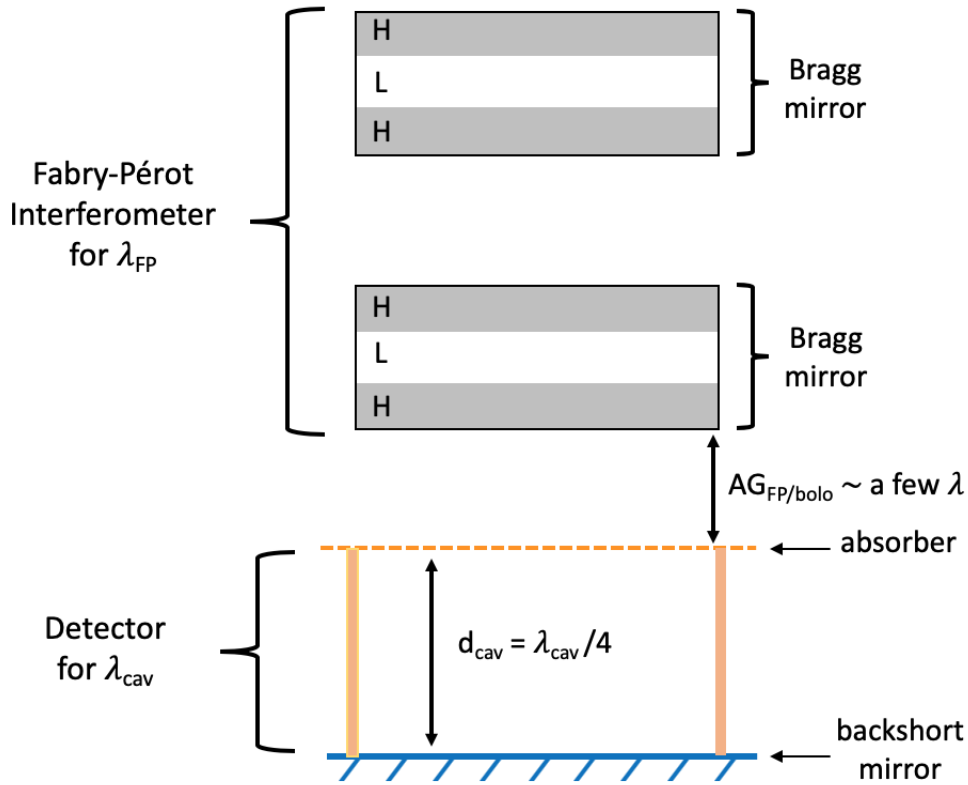


FIGURE 4.23: Coupling of the FPI with a simplified detector. The FPI is based on Bragg mirrors as described previously while the detector is represented by an absorber above a quarter-wave cavity closed by a backshort mirror. The resonant wavelengths λ_{FP} and λ_{cav} of each individual system are not necessarily equal. The bolometer and the FPI are separated by an order of wavelength.

The absorption of a device can be deduced from the reflection calculation, assuming there is no transmission through the backshort mirror : i.e. $A = 1 - R$. In figure 4.24, we compare the absorption of the bolometer and of the bolometer in combination with the FPI. The simulated bolometer is a simple vacuum quarter-wave cavity with $\lambda_{cav} = 100\mu\text{m}$, while the FPI is the one already described with $\lambda_{FP} = 320\mu\text{m}$. From this, we conclude that the absorption of the spectro-imaging device cannot be described by the product of the transmission of the FPI times the absorption of the bolometer. The system acts rather as a coupled resonator system with a high quality factor which makes the absorption 100% efficient. The strong consequence is to have a system that absorbs twice as much light as the simple detector at $\sim \lambda_{FP}$.

To be accurate, the resonant wavelength of the whole device is slightly shifted compared to λ_{FP} ($\sim 319\mu\text{m}$), for a still not completely understood reason. The finesse is also enhanced to 226 (213 for the single FP). For this example, we have picked the distance between the absorber and the FP to be $AG_{FP/bolo} = 160\mu\text{m}$ ($\sim \lambda/2$) but there are some other optimal distances which are shown in figure 4.25. The first noticeable result from this figure is that the resonant wavelength of the etalon λ_{FP} does no longer correspond to the optimum wavelength for the combined system : it is either a bit less or a bit more than $320\mu\text{m}$. Moreover, there is a kind of symmetry of the resonances with two islands (in yellow on the 2D map) around 320

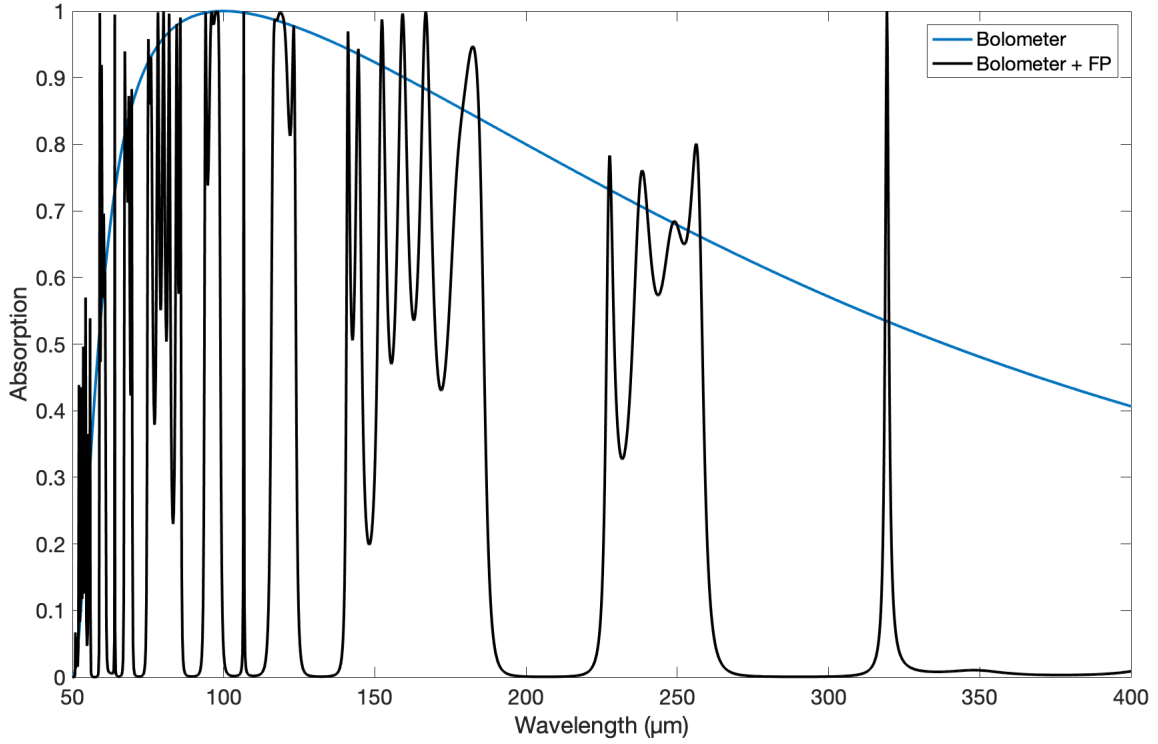


FIGURE 4.24: Absorption of the bolometer (in blue) and of the bolometer in combination with the FP (in black). The FPI is a resonator that enhances the response of the absorber at $\sim 320 \mu\text{m}$ since the absorption is two times better for the spectro-imaging device than the bare bolometer at this particular wavelength. The finesse of the absorbed peak is 226.

μm . The existence of these optima is not well understood yet. However, one can notice that the symmetric pattern has a $\lambda/2$ periodicity according to the value $AG_{FP/bolo}$. Note that in a different case where the detector is adapted to λ_{FP} , the system absorbs 100 % of the light at exactly $320 \mu\text{m}$, whatever the distance $AG_{FP/bolo}$ is.

In order to understand the resonances within the coupled system, we ran some simulations which are based on the finite element method (with COMSOL Multiphysics). The purpose of these calculations was to study the behavior of the electromagnetic field in our system. For this, we first simulated a FP ($\lambda_{FP} = 320 \mu\text{m}$) coupled to a vacuum $80 \mu\text{m}$ -thick cavity detector corresponding to $\lambda_{cav} = 320 \mu\text{m}$. In this case, we know (and this is checked by computation) that, whatever the distance between the FP and the absorber $AG_{FP/bolo}$, the detector absorbs 100% light at exactly $320 \mu\text{m}$. The second step of this experiment is to simulate a coupled system, still with $\lambda_{FP} = 320 \mu\text{m}$, but with a detector adapted to $\lambda_{cav} = 100 \mu\text{m}$ (i.e. a detector quarter-wave cavity of $25 \mu\text{m}$). For this specific case, the detector is not adapted to the etalon and we know (only by computation, figure 4.25) that one of the two values for the optimal wavelength is $\sim 319 \mu\text{m}$ for a particular $AG_{FP/bolo}$ which we choose to be $160 \mu\text{m}$ ($\lambda_{FP}/2$). To compare both cases, we plot in figure 4.27, the norm of the electric field along the cross-section of the coupled system. In the two configurations, the electric fields look similar ; however there is a slight difference in the behavior of

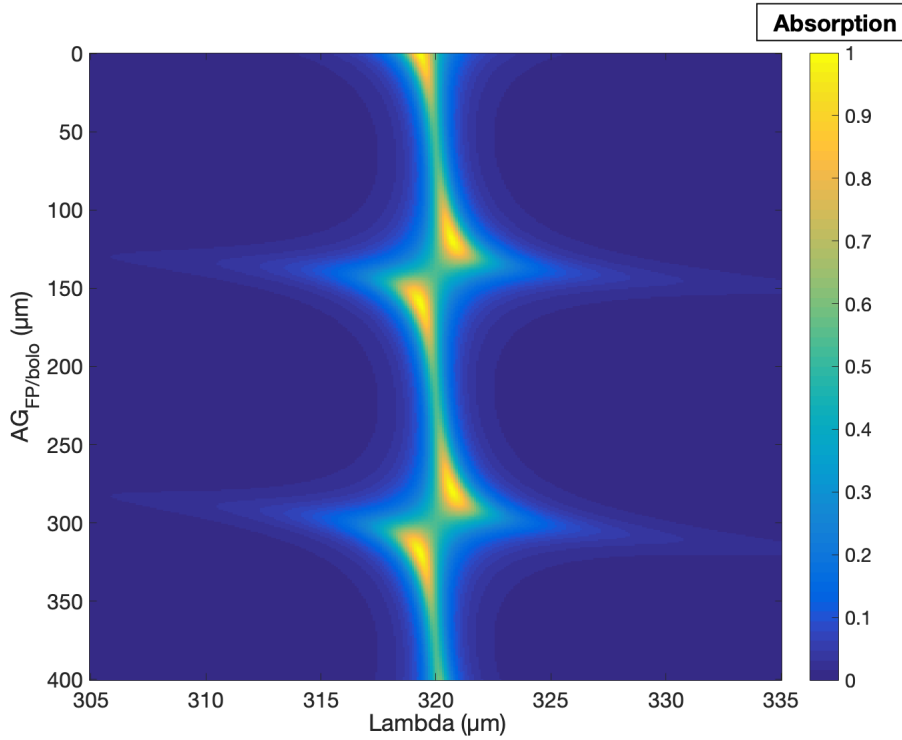


FIGURE 4.25: Absorption of the coupled system (bolometer and FPI) as a function of the wavelength around 320 μm and for different values of the airgap $AG_{FP/bolo}$ (vacuum gap). Here, the size of the detector cavity is 25 μm (i.e. $\lambda_{cav} = 100 \mu\text{m}$).

the electric field between the absorber and the closest mirror of the FP. Indeed in this region, when the detector is adapted to λ_{FP} , the norm of the electric field is flat, meaning that there is no wave which goes back from the reflection after the absorber; in contrast, when the detector does not match λ_{FP} , there are oscillations in the area between the absorber and the closest mirror of the FP, suggesting that there is a reflected wave which goes back to the FP. In other words, when $\lambda_{cav} \neq 320 \mu\text{m}$, the coupled system acts as a new interferometer.

In a totally different field, Burmeister et al. (2010) also experienced this effect. They studied the coupling of two optical cavities through the transmission of a three mirror system. In our combined system, the three mirrors are the two FP mirrors and the backshort mirror of the detector. Similarly, the absorption of our system corresponds to a loss in the system, which for them, is the transmission through the two optical cavities. As presented in the top figure 4.27, each mirror m_i ($i = 1, 2$ or 3) is represented by its reflectivity ρ_i and transmission τ_i . In this example, $|\rho_1|^2 = 0.7$, $|\rho_2|^2 = 0.8$ and $|\rho_3|^2 = 0.9$. Φ_1 and Φ_2 are called the detuning parameters of each cavity (with Φ_1 and Φ_2 in $[-\pi, \pi]$). In a similar way to what we did, they compute the electric field amplitude and plot the transmission of the overall system as a function of the detuning parameters Φ_1 and Φ_2 . The middle figure 4.27 exhibits the same kind of symmetric pattern than in figure 4.25 with a π -periodicity (equivalent to our $\lambda/2$ -periodicity, in phase shift). To explain this, they calculate the compound mirror reflectivities $\rho_{m_1 m_2}$ and $\rho_{m_2 m_3}$ of the first cavity as seen from mirror m_3

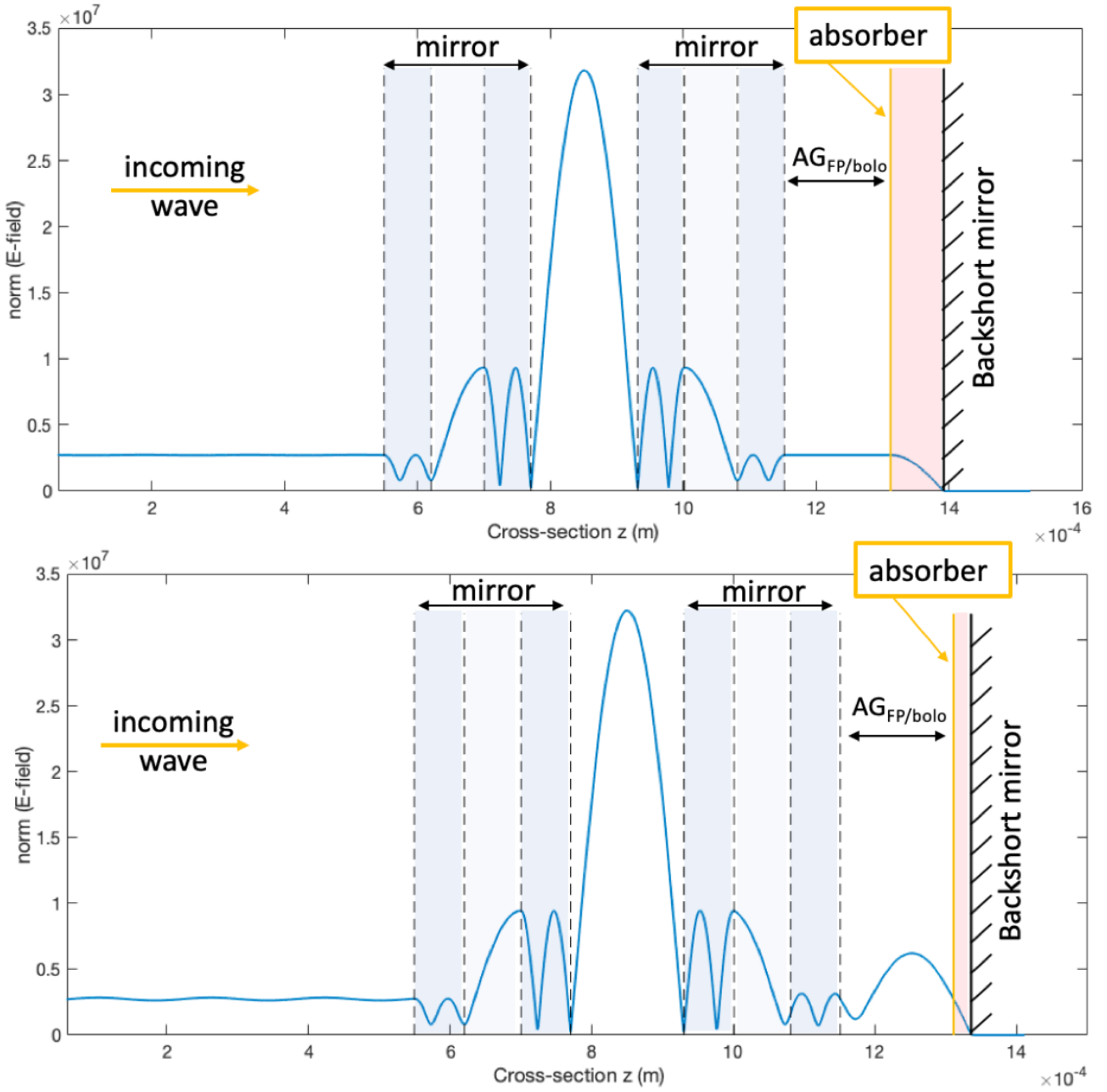


FIGURE 4.26: Norm of the electric field along the cross section of the coupled system. The detector cavity is colored in light red : (top) 80 μm of cavity gives $\lambda_{cav} = 320 \mu\text{m}$, (bottom) 25 μm -thick cavity for $\lambda_{cav} = 100 \mu\text{m}$. In both figures, $AG_{FP/bolo} = 160 \mu\text{m}$ although there is no constraint on this distance in the first case. The electric field is plotted for $\lambda = 320 \mu\text{m}$ in the top figure and $\lambda = 319.3 \mu\text{m}$ in the bottom one : these wavelengths exhibit 99,9% and 99,8% of absorption respectively.

and of the second cavity as seen from m_1 respectively. In the bottom figure 4.27, they show that there is a maximum of transmission for the detuning $\pm\Phi_1$ which corresponds to $|\rho_{m_1 m_2}|^2 = |\rho_3|^2$ and for the detuning $\pm\Phi_2$ which gives $|\rho_{m_2 m_3}|^2 = |\rho_1|^2$. This strong result yields that the system is efficiently coupled when the impedances of the two cavities are perfectly matched. The optimal values of Φ_1 and Φ_2 are confirmed by the middle figure.

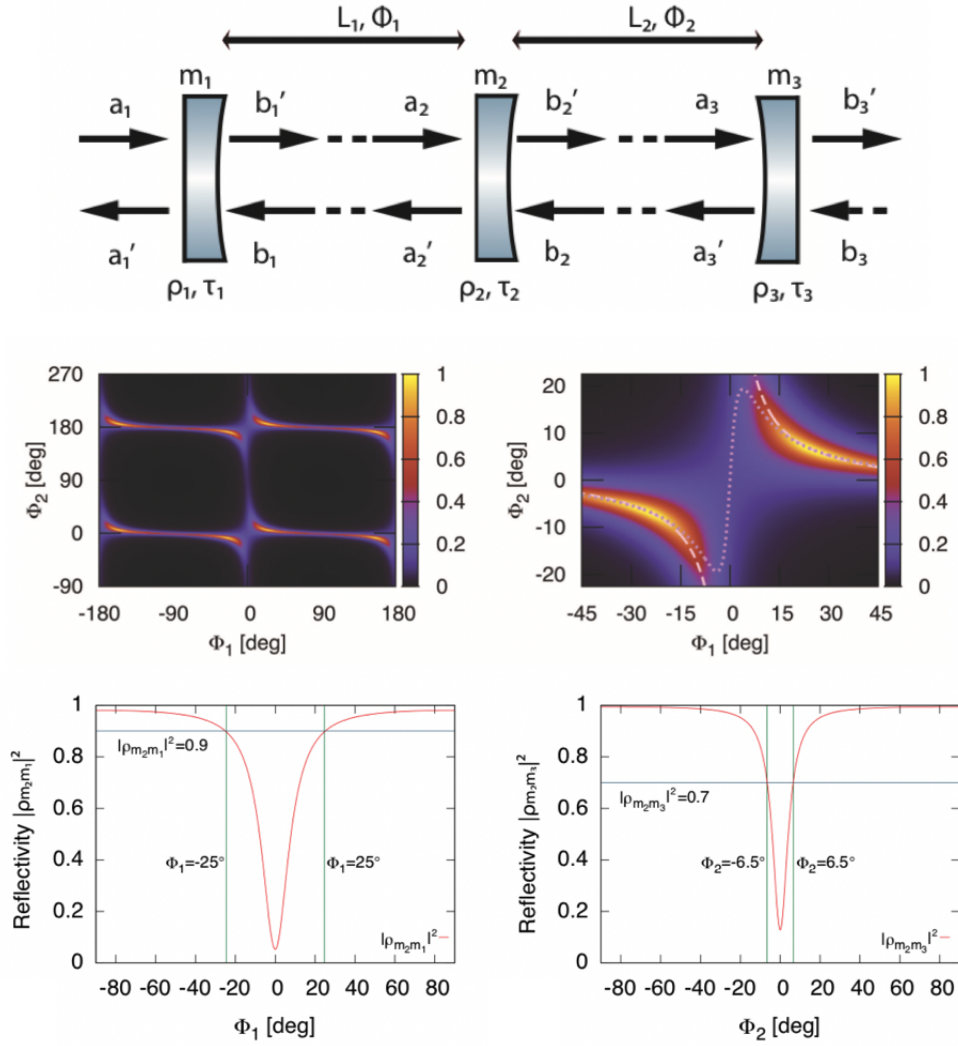


FIGURE 4.27: Results extracted from Burmeister et al. (2010). (Top) Sketch of the two optical cavities made from a three mirror system. Here, the mirrors are represented by reflection and transmission amplitude coefficients ρ_i and τ_i respectively for each mirror m_i ($i = 1, 2$ or 3). In the paper, $|\rho_1|^2 = 0.7$, $|\rho_2|^2 = 0.8$ and $|\rho_3|^2 = 0.9$. L_1 and L_2 correspond to the length of the two cavities formed by the three mirrors and Φ_1 and Φ_2 are called the microscopic detuning parameters of each cavity (with Φ_1 and Φ_2 in $[-\pi, \pi]$). (Middle) transmitted power through the loss-less three mirror cavity as a function of the detuning Φ_1 and Φ_2 . The figure on the right is a zoom-in. (Bottom) Compound mirror reflectivities $|\rho_{m_1 m_2}|^2$ and $|\rho_{m_2 m_3}|^2$ as a function of the detuning parameters Φ_1 and Φ_2 respectively.

Spectral and spatial scanning

Before discussing the two ways (the spectral and the spatial scanning) to derive a 3D datacube for fine-line mapping, we want to present preliminary results which could be applied to a CMB experiment. For this application, fixed-cavity FPs with a moderate finesse should be considered as wide-band filters. One could, for instance, have different etalons adapted to specific bands, each etalon being above one bolometer array to define a CMB spectral channel. A low finesse can be obtained to a certain extent, assuming that the reflectivity of the interferometer mirrors can be degraded. This can be achieved by having low contrast refractive index materials or simply low refractive index materials (the micro-structured silicon might be

a solution to tune down the value of the refractive index, see appendix B). The LiteBIRD CMB bands are detailed in the appendix C. To give an example of what could be performed with a FP etalon coupled to a detector, we have worked on the lower channel (in wavelength) of LiteBIRD : the 670-842 μm band (402 GHz). For this example, we chose a detector cavity of 180 μm which makes the detector sensitive to a wide band around $\lambda_{cav} \sim 720 \mu\text{m}$ (blue dashed curve in figure 4.28). Then, in order to have a low finesse etalon, some low-reflectivity mirrors should be assembled. For this, we chose a simple FP configuration with one layer per mirror, this layer being made of a material with refractive index $n = 1.7$ (micro-structured silicon, for example). The thickness of the material is chosen to be equal to $\lambda/4n$ and the FP is located at a distance $\lambda/2$ away from the detector. Note that this distance has been derived from the map of figure 4.25, although this is not fully understood. The resulting absorption of the coupled system (detector + FP_{simple}) is shown in red in figure 4.28. As expected the “finesse” is rather low, but one can also notice that the edges of the absorption around the CMB band (defined by vertical black dashed lines) are not sharp. To counter this, we decided to investigate a more complex structure. This kind of filters is explained in detail in books such as Macleod (2010). It consists in having a stack with several FP interleaved by low-index quarter-wave cavity. Here, one FP is represented by (H 2L H), with (H) being the material with $n = 1.7$, (L) being vacuum, and (H) and (L) are both quarter-wave thick. Therefore, for a four times repeated FP, the complex stack gives the following representation :

$$n_0 / (H \ 2L \ H) \ L \ (H \ 2L \ H) \ L \ (H \ 2L \ H) \ L \ (H \ 2L \ H) / n_0 \quad (4.27)$$

The resulting absorption of the coupled system (detector + FP_{complex}) is illustrated with the yellow curve in figure 4.28. One can clearly see that the complex stack enables us to define a cleaner window for the 402 GHz : the system is almost 100% efficient over the band and reflects the light outside this band. This method could be applied to other spectral channels, assuming the detector is sensitive in this range. As already mentioned, this work is preliminary and we could examine a way to suppress the absorption below 600 μm and above 1 mm. However, this approach could bring solutions to define specific bands for science purpose like CMB experiments.

We now present two technological applications which can be used to perform fine-line spectroscopy (such as C⁺ line) mapping. For this, we need to have the spatial and the spectral information in order to derive a 3D datacube (x, y, λ). This is possible with two kinds of scanning.

On one hand, the spectral scanning is the one commonly used for FPI, where a cryo-mechanism tunes the size of the cavity. In this case, the FPI has the same spatial dimensions than the bolometer array and for a defined cavity, the instrumental profile is the same for all pixels. On the other hand, a spatial scanning allows one to derive the same information. The principle is to have various small fixed-cavity etalons with each etalon being above a group of pixels. Depending on the position on the array, each group of pixels

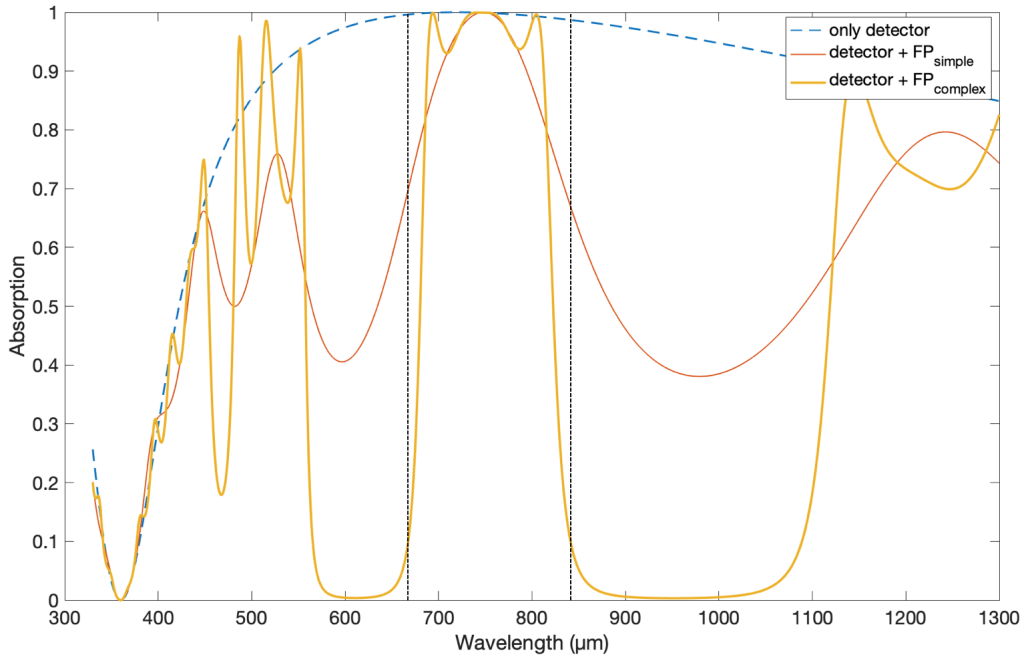


FIGURE 4.28: Optimization of the absorption in the 670-842 μm CMB band. Blue dashed line is the absorption of a quarter-wave cavity detector adapted for $\lambda_{cav} = 720 \mu\text{m}$; Red curve corresponds to the coupling of this detector with an etalon (HLH) where (H) is a material of refractive index $n = 1.7$ and (L) is vacuum. Finally, the yellow curve stands for the coupling of the same detector with a more complex structure : $(L (H 2L H))^4$.

observe one specific spectral channel. To derive the same 3D datacube as for the spectral scanning, the spatial scene (i.e. the sky) would need to be scanned in a windowing mode. This solution is similar to one of the IMEC solutions with colored sub-arrays (Lambrechts et al., 2014). In this case, the spectral band is limited by the size of the bolometer array. The configuration of the FPI above the bolometer array is depicted in figure 4.29 for both scanning methods.

Imaging with a spectrometer located in the focal plane

In the calculations performed all along this chapter, we assumed a plane wave propagating towards the coupled system. However, this assumption is not strictly correct : because the bolometer array is used for imaging, the beam focuses onto the detector. In the following, a Gaussian beam is used to study the converging beam at the output of a Fabry-Perot. The approximation of the converging beam by a Gaussian beam is motivated by the fact that the beam profile along the direction of propagation is a Gaussian and because the electric field amplitude profiles across the direction of propagation have also a Gaussian shape. Therefore, the intensity distribution is Gaussian whatever the cross-section of the beam as illustrated in figure 4.30. This approximation is only valid in the paraxial regime, where we do not have high incidence angles. Note that this study is a first attempt to take into account the focus. These calculations could be

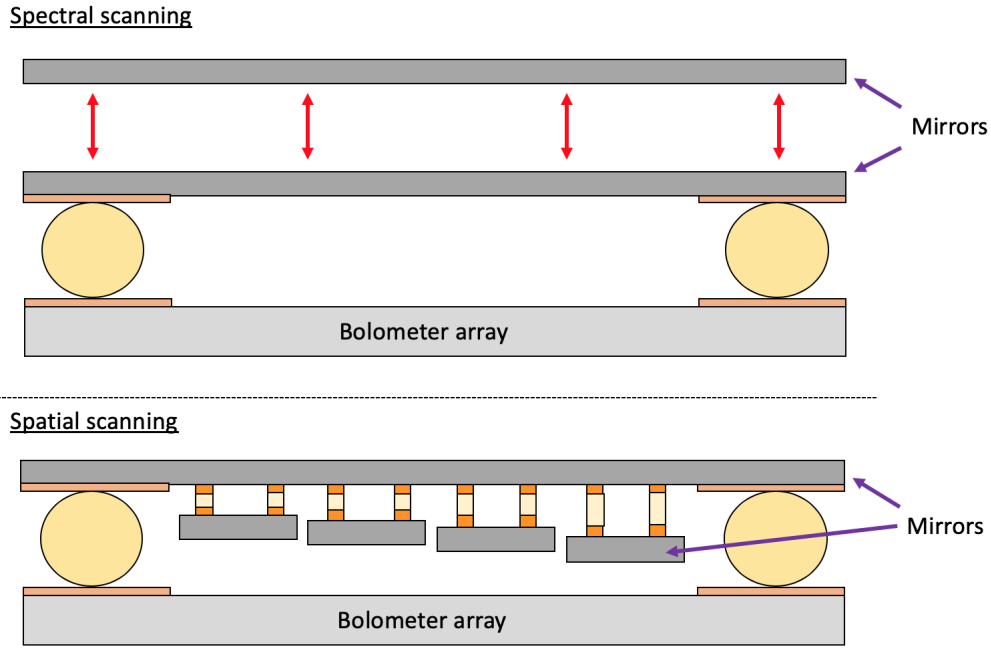


FIGURE 4.29: Two possible scanning methods. (Top) Spectral scanning : the upper mirror of the FPI is actuated by a cryo-mechanism (for example by a piezoelectric motor) to tune the cavity size and then spectrally scan the absorption. (Bottom) Spatial scanning : Several fixed-size cavity etalons stand above the bolometer array. Each group of pixels observe a specific wavelength (related to the size of the etalon cavity). The spatial scene needs to be scanned over the sky.

$f_{\#}$	1	4	6	8	10	100
θ (deg)	28	7.2	4.8	3.6	2.9	0.29

TABLE 4.1: Examples of several values of the maximum angle of incidence θ as a function of the f-number $f_{\#}$

refined with a 3D simulation, which would also include the detector, since we have seen that the spectral response of the whole system does not only depend on the FP. By the simulation here, we want to quantify the degradation of the imaging and of the spectroscopic performance due to the Fabry-Perot near the focus.

First, to have an idea of the order of the beam divergence, we should recall the meaning of an important parameter for an optical system, the f-number $f_{\#}$. It is defined by the ratio of the focal length to the diameter of the optics and is sufficient to describe the divergence of the beam. In our field of applications (astronomy), $f_{\#}$ takes low values ; for example, the HERSCHEL space observatory had a $f_{\#}$ of 8.70 (Pilbratt et al., 2010). Table 4.1 gives examples of values of the incidence angle as a function of the f-number, derived from the relationship $\theta = \frac{1}{2f_{\#}}$ [rad]. As presented in this table, instruments for astronomy have to deal with small incidence angles. However, because of the many reflections inside the cavity, we have to calculate the effect of the FP on the beam.

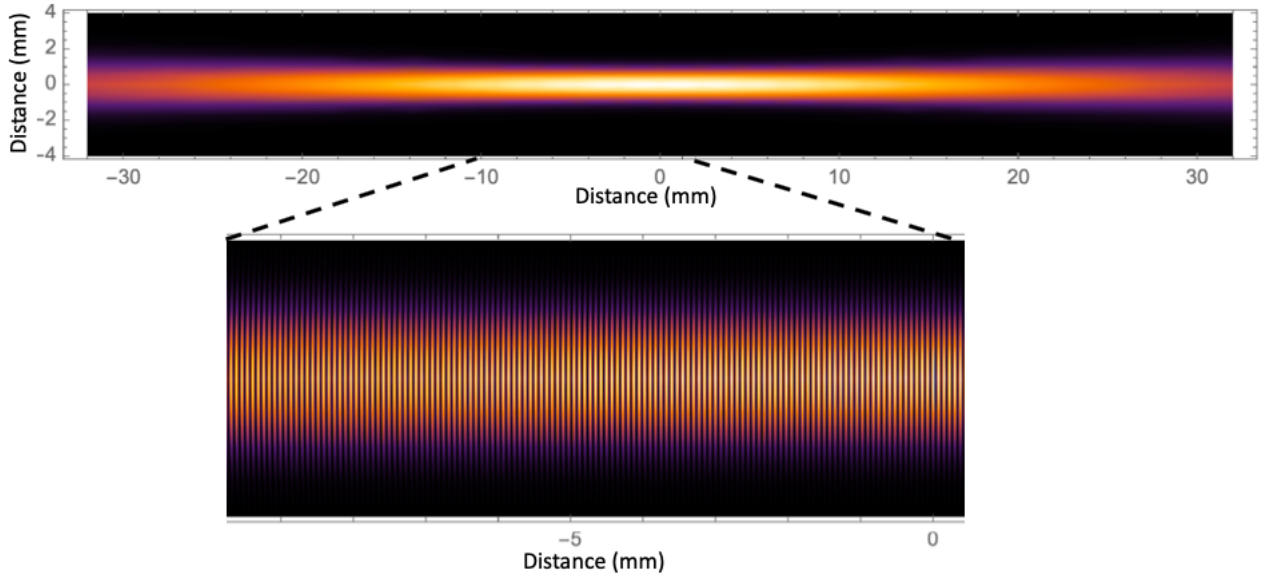


FIGURE 4.30: (Top figure) Intensity of a Gaussian beam along its propagation direction. The optimal focus is at 0 mm. (Bottom figure) Zoom in of the upper figure, which highlights the wavelength period for $\lambda = 158 \mu\text{m}$ (in intensity) : two bright fringes are separated by $\lambda/2$.

In the following simulation, the spectrometer is really simplified : it consists of two reflective surfaces with zero thickness, which means that the mirrors only induce a 180° -phase shift. Here, we work at $\lambda = 160 \mu\text{m}$ (FP cavity of $80 \mu\text{m}$) and with mirrors reflecting 97.9 % of light (which corresponds to a finesse of ~ 150 , typical value of the finesse experimentally obtained (see chapter 5)). Next, a telecentric optics is assumed, ensuring that each point of the focal plane will see a light cone whose axis is parallel to the optical axis. This is the reason why the computation is performed, independently of the position in the focal plane. The electric field of a Gaussian beam is described through the equation (Kogelnik and Li, 1966) :

$$E_G(r, z) = E_0 \frac{w_0}{w(z)} \exp(-i(kz - \psi(z)) - r^2(\frac{1}{w(z)^2} + \frac{jk}{2R(z)})) \quad (4.28)$$

where :

- r is the radial distance from the central axis of the Gaussian beam,
- z is the distance along the propagation axis,
- $k = \frac{2\pi}{\lambda}$ is the wavenumber,
- $w(z)$ corresponds to a measure of the decrease of the electric field amplitude with the distance from the z axis and more precisely $w(z)$ is the radius at which the electric field amplitude falls to $1/e$ ($1/e^2$ in intensity),
- w_0 is the waist radius corresponding to $z = 0$ (where should be placed the focal plane without the FP) ,
- $R(z)$ is the radius of curvature of the beam at z ,
- $\psi(z)$ is the Gouy phase, an extra phase shift that stands for the difference between the Gaussian beam

and an ideal plane wave.

The following equations describe $w(z)$, $R(z)$ and $\psi(z)$:

$$w(z) = w_0 \sqrt{1 + \left(\frac{\lambda z}{\pi w_0^2}\right)^2} \quad (4.29)$$

$$R(z) = z \left(1 + \left(\frac{\pi w_0^2}{\lambda z}\right)^2\right) \quad (4.30)$$

$$\psi(z) = \arctan\left(\frac{\lambda z}{\pi w_0^2}\right) \quad (4.31)$$

To define the Gaussian profile which mimics the converging beam, the first step is to match the full width at half maximum (FWHM) of the Airy disk obtained by Fraunhofer diffraction of the optics to the FWHM of the Gaussian beam. The Gaussian FWHM can be derived, after calculations, to be $w(z)\sqrt{2\ln(2)}$ for any z , and to be $w_0\sqrt{2\ln(2)}$ in the waist. 2×2 pixels (pixel pitch : $750 \mu\text{m}$) of the focal plane cover the Airy disk, according to the Rayleigh criterion. We remind here, that our two objectives are the following :

- to observe the degradation of the FWHM of the beam after travelling through the FP,
- to quantify the degradation in finesse due to the focus.

For the first test, we compare the FWHM of the Gaussian beam without FP (intensity I_G) and the FWHM of the Gaussian beam after the many bounces inside the FP cavity (intensity $I_{G_{FP}}$, formula derived from appendix A), through the derivation of the intensity as a function of the radial distance from the center axis of the beam r :

$$\begin{cases} I_G(r) = |E_G(r, z = 0)|^2 \\ I_{G_{FP}}(r) = (1 - R)^2 \left| \sum_k R^k E_G(r, z = (k - \text{off}) \times d) \right|^2 \end{cases}$$

with R the reflectivity of the mirrors, *off* the offset of the focus and d the pathlength equal to two times the size of the cavity (one round trip). For the Gaussian beam, the maximum of intensity is obtained at $z = 0$ in the waist, while for the Gaussian beam through the FP, the position of the optimal focus has changed due to the many bounces inside the cavity and thus has been optimized. It can be demonstrated that the optimal focus has moved forward at a distance of $\sim 6.2 \text{ mm}$. Note that the pathlength d is also slightly shifted from the initial $160 \mu\text{m}$, due to the fact that the phase velocity of the Gaussian beam is greater than the speed of light. As a consequence, the pathlength is shortly increased. The resulting profiles are shown in figure 4.31 with each intensity being computed in its optimized focus. The result is that the FP at a finesse of ~ 150 has a small impact on the profile : indeed, the FWHM is broaden by a factor 4.1%.

For the second test (degradation in finesse), we compare the profile of two waves travelling through the FP : a plane wave and a gaussian beam (the one computed above with its optimized offset *off* d). The

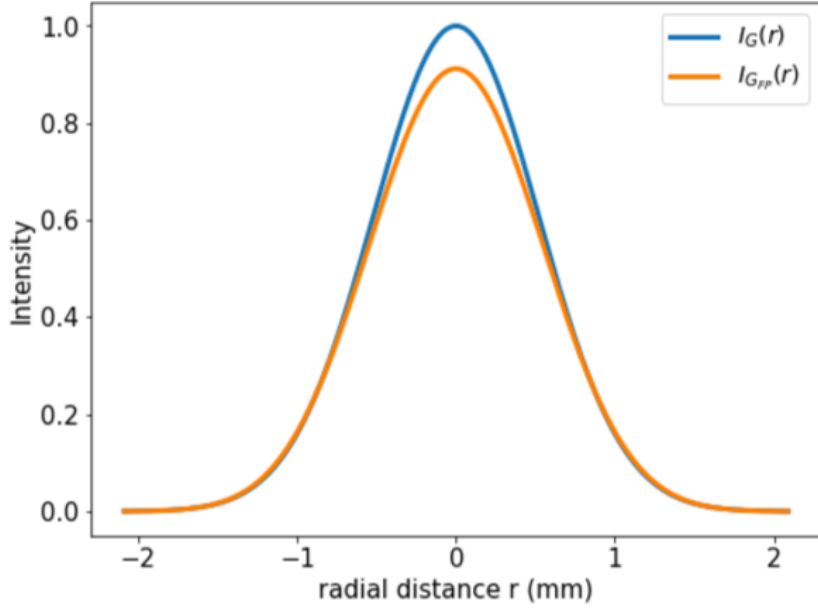


FIGURE 4.31: Intensity with respect to the radial distance from the center axis of the beam. (Blue) Normalized intensity of a gaussian beam in the waist. (Orange) Computed intensity of a gaussian beam through a FP of finesse ~ 150 , in the optimum focus ($off = 39$). For comparison : $\max(I_G(r)) = 1.0$ and $\max(I_{G_{FP}}(r)) = 0.91$, and $FWHM_G = 1.23$ mm and $FWHM_{G_{FP}} = 1.28$ mm

plane wave is simply given by :

$$E_{PW}(z) = E_0 \exp(-ikz) \quad (4.32)$$

and then the intensity of the plane wave once passed through the FP, at any focus off , is :

$$I_{PW_{FP}}(d) = (1 - R)^2 \left| \sum_k R^k E_{PW}(r, z = (k - off) \times d) \right|^2 \quad (4.33)$$

Figure 4.32 presents the resulting profiles of the plane wave and of the Gaussian beam through the FP as a function of the pathlength (twice the FP cavity size) d . From this calculation, the finesse for the gaussian beam \mathcal{F}_G is derived to be 137.8. Therefore, the diverging beam enables us to reach $\sim 92\%$ of the plane wave finesse.

To sum up this part, the Gaussian beam calculations give an idea of how having a high-finesse spectrometer in a focusing beam affects the performance of the imaging and spectrometer system, assuming a telecentric system. We have seen that the presence of the spectrometer offsets the optimal focus. When taking into account this necessary shift of the focal plane, we can compute the degradation of the FWHM of the beam and of the finesse of the device. For a spectrometer with a finesse of 150, the FWHM is 4.1% larger than in the absence of the FP and the finesse is 92% the one of a plane wave that has travelled through the FP. Appendix D gives more results concerning the performance degradation for different nominal finessses (from 50 to 350). From this, we learn that having the FP in the focus does not significantly deteriorate

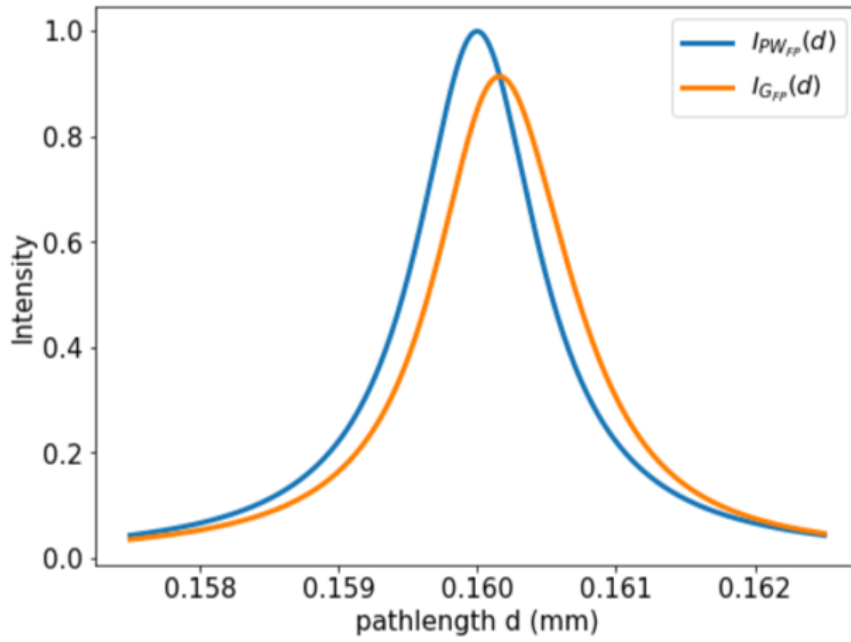


FIGURE 4.32: Intensities with respect to the pathlength d after passing through the FP. (Blue) Spectral profile for a plane wave, (Orange) for a gaussian beam. As expected with $R = 97.9\%$, $\mathcal{F}_{PW} \sim 150$ ($= 149.2$) while $\mathcal{F}_G = 137.8$.

the performance of the system, at least for a low finesse. These results must be considered regarding the degradation that can be accepted in spatial resolution, but also in spectral resolution, especially because it looks like this latter declines faster than the FWHM. However, it also confirms that the plane-wave approximation, applied throughout this thesis, of the low-focusing wave is close to the real situation and can still lead to representative results. Nevertheless, high resolving spectroscopy can still be achieved with several FPI in series, as it is already done in many instruments (see section 4.2.2 of this chapter). The improvement should in addition, come from the introduction of silicon mirrors to reduce the loss in the whole interferometer.

4.2.5 Conclusions of the chapter

In this chapter, we have proposed a solution to introduce spectroscopy within the imaging device. Our idea was to couple a Fabry-Perot interferometer to the bolometer array. For this and in order to overcome the drawbacks of conventional metal mesh based mirrors, we chose dielectric materials to build loss-less mirrors. Based on a close collaboration with CEA/LETI, we decided to implement silicon mirrors. While single silicon layers are not efficient mirrors, Bragg mirrors, with their complex stack of layers, can be very good reflectors. With a simple three-layer silicon/vacuum/silicon mirror, it is possible to reach a theoretical FP finesse of about 200 at $\lambda = 320 \mu\text{m}$, without any loss in the system (to be checked in the next chapter). The coupled system FP/detector has also shown promising properties. Indeed, interferences within the whole device make possible the absorption of spectral lines at wavelength far from the broad-band range of the detector. However, efficient absorption of the spectro-bolometer can only occur when the two optical cavities made by the mirrors of the system are impedance-matched. The technological solution proposed here, could be applied to low-resolution experiments (like for CMB) or to high resolution spectroscopy. For the latter, we have demonstrated that a spectro-imaging device could be used at low-resolution ($\mathcal{R} < 350$), while other higher order FPIs could be used in a collimated beam. The following chapter presents the experimental work which has been achieved in the course of this thesis to test, as best as possible, the theoretical results presented above.

Chapter 5

Experimental validation of the spectroscopic capability of compact Fabry-Perot Interferometers based on dielectric mirrors for combination with bolometer arrays

Contents

5.1	Building mirrors with dielectric materials for compact FPIs	128
5.1.1	Building the dielectric mirrors in collaboration with LETI	128
5.1.2	Validation of the quality of dielectric layers for mirrors	130
5.1.3	Assembling the mirrors	135
5.1.4	Validation of the theoretical model by Time Domain Spectrometer (TDS) measurements at ambient temperature	140
5.2	Validation of the performance of Fabry-Perot etalons based on dielectric mirrors	140
5.2.1	Description of the cryogenic optical train	140
5.2.2	Measuring the finesse of multi-layer silicon etalons	145
5.2.3	Measuring the transmission of multi-layer silicon etalons	154
5.3	A first step towards the coupling of the spectrometer to the bolometer . . .	158
5.4	Conclusions of the chapter and perspectives for the future experiments . . .	162

In this chapter, we present the experimental work performed to test the spectroscopic capability of compact Fabry-Perot Interferometers based on dielectric mirrors for the sub-millimeter wavelength range. It is mostly dedicated to the spectroscopic development since the experimental combination of FPI with a detector has only been taken up at the very end of this PhD project. However, some elements are provided at the end of this chapter, they describe the final experimental work which is currently ongoing at CEA. In the following, we first describe the manufacturing of the mirrors which have been used to assemble several Fabry-Perot etalons. Measurements performed at warm temperature have allowed us to validate the theoretical model used all along these chapters. Then the cryogenic measurements to test the etalons are presented, as well as the derived analysis and the spectral performance of the etalons. Finally, we introduce the steps that we are currently following to set up the test of the whole device including the detector.

5.1 Building mirrors with dielectric materials for compact FPIs

The manufacture of mirrors which have been designed for compact spectroscopy with Fabry-Perot interferometry and which are detailed in chapter 4, is outlined here. It has required several steps to meet the specifications concerning the mirrors quality, before being able to assemble the whole structure for competitive spectroscopy.

5.1.1 Building the dielectric mirrors in collaboration with LETI

The Fabry-Perot we want to build for far-infrared/sub-millimeter astronomy is based on dielectric mirrors as it is usually done in the field of optics. For the mirrors, we have chosen silicon since it has a high refractive index ($n_{Si} \sim 3.41$) which enables us to reach high reflectivity and presumably low loss at the same time. Moreover, silicon is also a material that CEA/LETI is really used to work with, which facilitates the process. In addition to the choice of the material, we decided to design mirrors following a Bragg mirror configuration. This mostly consists in having mirrors based on a stack of alternated high (H) and low (L) refractive index materials, with each layer being $\frac{(2k+1)\lambda}{4n}$ thick, with k an integer. Figure 4.17 explains how the $\frac{(2k+1)\lambda}{4n}$ -thick layers produce constructive interferences. After many discussions and attempts with CEA/LETI about feasibility of different configurations, we have converged on a consensus for the choice of the stack of materials : pure silicon has been selected as the high refractive index material and the low refractive index material will be air (or more exactly vacuum). One etalon mirror will therefore be a three-layer sandwich made of silicon, vacuum and silicon. In order to create some ‘vacuum layers’, we machined spacers which are, in fact, silicon rings. Initially, we wanted to build a FP etalon whose fundamental resonance is at $\lambda = 160 \mu\text{m}$ to make a proof-of-concept with actual astrophysical applications like C^+ line observations. Nonetheless, for mechanical robustness reasons, we decided to build a prototype

for spectroscopy at $\lambda = 320 \mu\text{m}$. With this choice, we can double all the layer thicknesses, which scale linearly with wavelength, while all other parameters remain unchanged. Moreover, for the same reasons, we picked $k = 1$ in the thickness formula for silicon sheets, instead of $k = 0$ to have more solid silicon layers. Then the corresponding Bragg mirror thicknesses are $80 \mu\text{m}$ for silicon spacers ($n_{vacuum} = 1$) and $71 \mu\text{m}$ for silicon sheets. Even though the issue of layer thickness has not been investigated in depth, the possibility of manufacturing $23 \mu\text{m}$ -sheets should not be discarded right away. It would also have the advantage to give a clean signal over $400 \mu\text{m}$ without need for strong filtering (see figure 4.21). We now summarize the different steps that we went through before meeting the specifications for the mirror quality.

The first batch of silicon sheets and spacers was manufactured in November 2018, some of them are pictured in figure 5.1. They proceed from two silicon wafers ground with objectives in terms of thickness of $80 \mu\text{m}$ for spacers and of $71 \mu\text{m}$ for sheets. After grinding, the achieved thicknesses were measured to be $79.7 \mu\text{m}$ and $72.1 \mu\text{m}$ respectively. Then each sample has been cut from the wafers with size $25 \text{ mm} \times 25 \text{ mm}$ by a diamond saw and corners have been removed with a laser for the samples to be less bulky. Finally, some 16 mm diameter-holes have been cut in the $80 \mu\text{m}$ -wafer pieces with the laser to create the vacuum spacer and smaller holes have been drilled, also with the laser, throughout the silicon sheets to allow the air to be vented once the whole structure will be assembled. We remind that the etalon would be operated in a cryostat at low pressure and low temperature ($4 - 77 \text{ K}$). Specific invar holders have been designed to support the etalons at cold temperature. Invar was chosen for its low coefficient of thermal expansion (CTE).

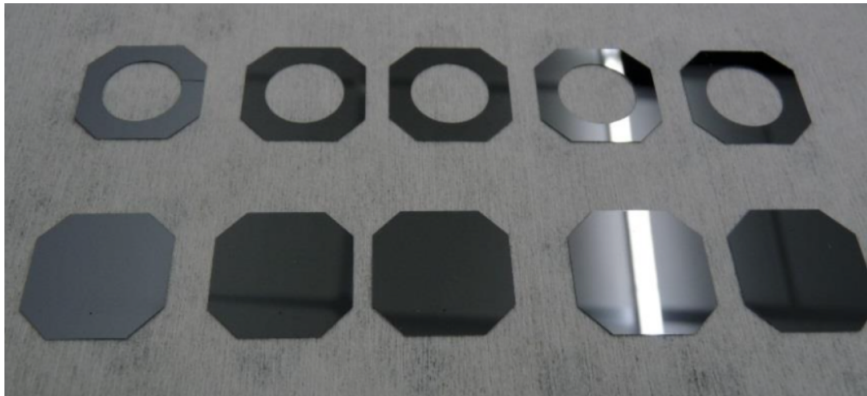


FIGURE 5.1: Picture of silicon layers : the sheets are $71 \mu\text{m}$ -thick and the spacers are $80 \mu\text{m}$ -thick. Samples measure $25 \text{ mm} \times 25 \text{ mm}$. The corners have been cut in order to have moderate size samples; laser has cut 16-mm holes to create spacers and small venting holes in the full sheets.

5.1.2 Validation of the quality of dielectric layers for mirrors

The FPI mirrors as described in the previous section consist of an assembly of silicon and vacuum layers : the overall assembly is a stack (H/L/H)/2L/(H/L/H), where (H) refers to the high refractive index material (i.e. silicon) and (L) means the low refractive index material (i.e. vacuum). In particular, we chose to use two 80 μm spacers to form the 160 μm cavity. With this configuration, theory yields a finesse of ~ 215 (see figure 4.22).

As explained in chapter 4, to be more representative of the total finesse \mathcal{F} , we need to consider the flatness finesse $\mathcal{F}_{\mathcal{F}}$ in addition of the reflective finesse $\mathcal{F}_{\mathcal{R}}$ as suggested by the following equation (also equation 4.11) :

$$\frac{1}{\mathcal{F}^2} = \frac{1}{\mathcal{F}_{\mathcal{R}}^2} + \frac{1}{\mathcal{F}_{\mathcal{F}}^2} \quad (5.1)$$

The flatness finesse stands for the defaults of flatness and of parallelism of each layer within the mirrors. For example, the transmission curves in figure 4.22 only depend on the reflectivity of the mirrors (which corresponds to the red curve in figure 4.21) and implicitly assumes perfectly flat/parallel surfaces. In practice, this means that if we do not want the total finesse to be limited by the quality of mirrors, we must have $\mathcal{F}_{\mathcal{R}} \ll \mathcal{F}_{\mathcal{F}}$. In our case, this means that we want $\mathcal{F}_{\mathcal{F}} \gg 215$. Defining Δd as the deviation from the averaged surface (root mean square) due to non-parallelism or to surface roughness, $2\Delta d$ will be the deviation from the averaged surface experienced by the wavefront after reflection. Therefore, $\mathcal{F}_{\mathcal{F}}$ is defined as $\frac{\lambda}{2\Delta d}$ and from this, we can derive the specifications about the quality of the mirrors : $\Delta d \ll \frac{\lambda}{2\mathcal{F}_{\mathcal{R}}} \sim 0.7 \mu\text{m}$. In theory, we would have required Δd to be much smaller than 0.7 μm but in practice, we might expect a quality of the order of 1 μm for the mirror surfaces. According to the equation 5.1, the total finesse would be already degraded to ~ 156 , assuming we manage to reach a 0.7 μm roughness and parallelism over the whole area and degraded to 128 for $\Delta d = 1 \mu\text{m}$. The estimation of the quality of dielectric mirrors has been decomposed into two experiments : evaluation of the parallelism of the sides of every layer by tests with an autocollimator and evaluation of the flatness of each surface of layers with a Fizeau interferometer. In case where specifications are not met, these measurements will help us to quantify the degradation of the final finesse \mathcal{F} .

Tests with the autocollimator

The experiment with autocollimator is illustrated in figure 5.2. We have first tried to use a flat mirror as a reference to collimate the beam on its surface. We would have then collimated the beam on one of the surfaces of the sample and derived from there the angular displacement. This method turned out to be not suitable for the parallelism experiment since measurements are not reproducible. Indeed some pockets of air

get caught between the flat mirror and the sample and cannot be removed. This has two consequences : the first one is that samples tend to float and slip on the reference mirror, the second one is that any pressure onto the silicon sample changes the air distribution and thus leads to a different angular measurement. To counter this phenomenon , we replaced the flat mirror surface reference by mercury, because this liquid is dense enough to support the sample, reflective enough to be used as the reference of the collimation and finally no air gets stuck between the liquid and the sample. Note that if there is a wedge (and this is what we investigate when we look for non-parallelism effects), the wedge might be underestimated by the measurements as it could dive below the liquid surface. Similarly to what we have tried with the flat mirror as the reference, we collimate the beam on the mercury surface, then drop the sample on the liquid surface and measure the angular displacement of the collimation. This method turned out to be reproducible. We found the wedge to be about $7''$: for a sample with a 25 mm diameter, this corresponds to a shift in height $\sim 0.8 \mu\text{m}$. Knowing that the $7''$ are within the measurement error of the autocollimator, we might consider that the silicon sheets meet the specifications in terms of parallelism. Eventually this test was not possible with silicon spacers since their surface was too small : the reflection of spacers, when compared to the reference, was consequently too faint to be observed. We assume the parallelism is similar in the case of spacers to the one for full sheets, even if they do not come from the same wafer, but because they come from the same process.

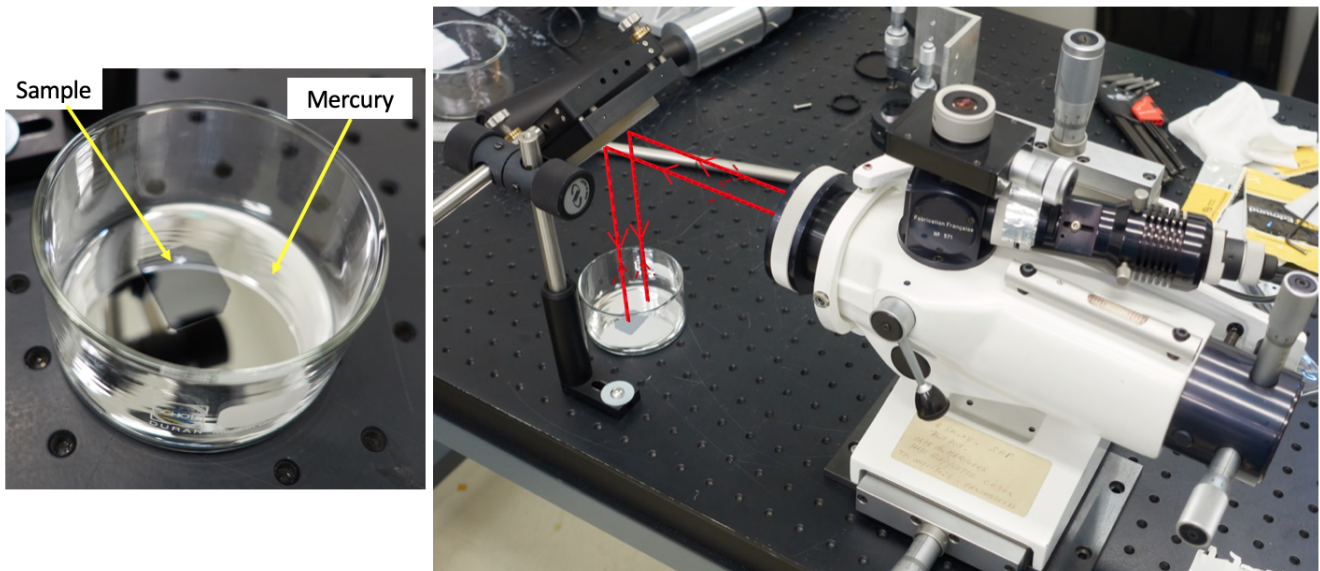


FIGURE 5.2: Experimental set-up for the parallelism tests. (Left) A full sheet sample floats on a mercury bath. (Right) Autocollimator's method : the reference is done with the collimation of light on the mercury surface, then the sample is dropped on the liquid bath and finally the angular displacement is measured. Mercury has been used for the repeatability of the experiment. We measured a $7''$ wedge (within the measurement error) for the silicon full sheets, which corresponds to a height difference of less than $1 \mu\text{m}$.

The Fizeau experiment

The second experiment used for the characterization of the silicon samples was the Fizeau interferometer. The principle of the Fizeau experiment is depicted in figure 5.3 (*top left*). A source illuminates a reference flat where a part of the light is reflected and the other part is transmitted to the test flat. Light is reflected at the surface of the test flat and can therefore interfere with the reflected wave from the reference flat. The interference fringes that we observed then result from the various optical path differences (OPD) that have been experienced by the wave due to (1) a wedge intentionally created to observe fringes, (2) flatness surface deformation. In the frame of this work, we built a Fizeau interferometer at CEA, the schematics of the experiment is presented in figure 5.3 (*top right*). A 1 mm-diameter laser ($\lambda = 633$ nm) is expanded through two beam expanders (x3 and x20) to reach an expected beam diameter of 60 mm. Then the wave is partly reflected at the surface of a beam-splitter. A part of the wave is transmitted to the silicon sample under test, which rests on another beam-splitter. This second beam-splitter is not used as a beam splitter but rather as a reflecting surface with a surface quality of $\lambda/10$ (i.e. $0.06 \mu\text{m}$), which acts as our reference flat. It has been chosen with a reflectivity coefficient of 30% ($R = (\frac{n_{Si} - 1}{n_{Si} + 1})^2$), similar to the one of silicon when it is optically thick (compared to the wavelength). The wave transmitted through the first beam splitter is then reflected back at the surface of the sample but also at the surface of the reference flat (this was for comparison, in theory). The interferences must thus display the OPD at the surface of the sample, in comparison to the reference surface. In practice, this comparison was not possible, still due to the air layer under the silicon sample that prevents us from observing fringes on the sample and on the reference flat at the same time, because the wedge induced by air was too severe. Initially, our goal was not only to measure the roughness of the surfaces but also to have another measurement of the parallelism of sheets. This last experiment could not be achieved for this air reason and the mercury did not help this time because it was very difficult to obtain steady interferences with the liquid at $\lambda = 633$ nm. In a nutshell, the Fizeau experiment has been a suitable tool to quantify roughness at the surface of the sheets, but also larger scale deformation. Figure 5.3 (*bottom*) is an example of the fringes we obtained with one silicon sheet (*left*) and one silicon spacer (*right*). The fringes on the pictures can be considered as a height map : for instance, the points of a surface which are embedded within a continuous red part have the same altitude. This means that if we remove the averaged wedge that introduces equally distant fringes, we can derive the overall deformation map of the surface of sheets and spacers. Note that a doubt still remains concerning the direction of curvature deduced from fringes. More recently, we have used a commercial interferometer (Zygo) which automatically computes the apparent shape of surface without any ambiguity on the direction in which the sample is curved. Figure 5.4 shows an example of the two sides of one full sheet and of one spacer, obtained with the Zygo interferometer. For all the samples, we have found that there is always one smooth side and one grainier. The latter might be the direct result of the wafer grinding to the required thickness. The Peak-to-Valley (PV) has been measured to be between $0.5 \mu\text{m}$ and

1.8 μm for all the samples. However, this upper limit is likely to be lower because, as we can notice from the shape of samples derived from Zygo measurements, the samples show a three-points symmetry, which corresponds to the three-points support (shown in figure 5.5) that we used to hold the samples, without any effect of air. The silicon is then deformed under its own weight and we might consider that the surface quality of all the samples is good enough for our use.

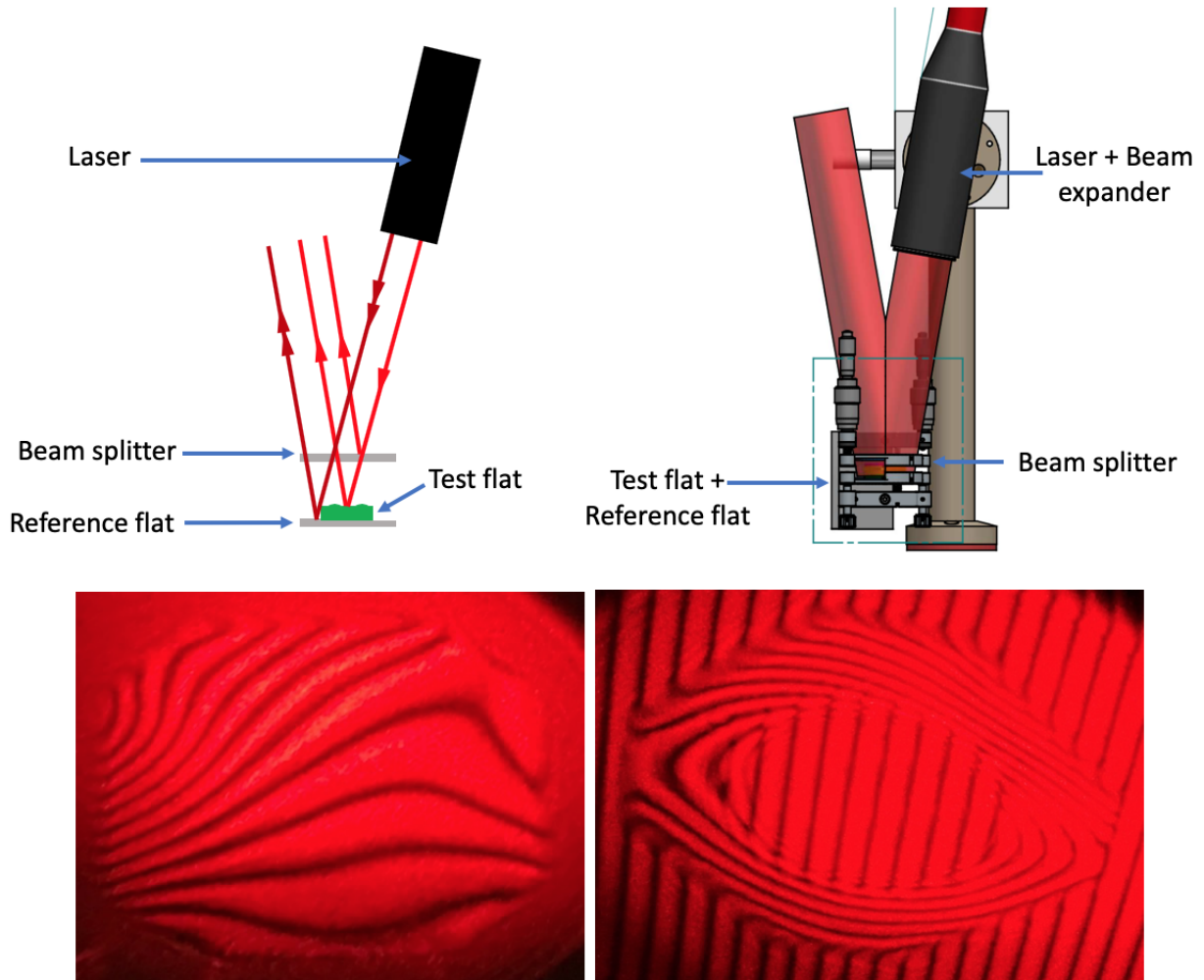


FIGURE 5.3: (Top left) Principle of the Fizeau interferometer used to test the optical surface of a sample in comparison to a reference surface, as built at CEA. (Top right) Fizeau interferometer built at CEA with a laser, a beam expander, a beam splitter and the sample above the reference. Some micrometer screws allow to cautiously adjust the fringes at the sub-micron precision (sketch by C. Delisle). (Bottom) Pictures of the fringes on one silicon sheet (left) and one silicon spacer (right). The full sheet lies on a mercury bath to get rid of the air under the sample; the spacer rests on the beam splitter and fringes from this reference can also be observed even if we cannot deduce the presence of any wedge because of the air under the sample. Only the smooth sides of full sheet and spacer are shown here, the more grainy sides from grinding are shown later in this part.

From the tests with the autocollimator, we can conclude that the samples meet the specifications for parallelism . Indeed, a wedge of $7''$ was measured (within the precision of the instrument). On the other

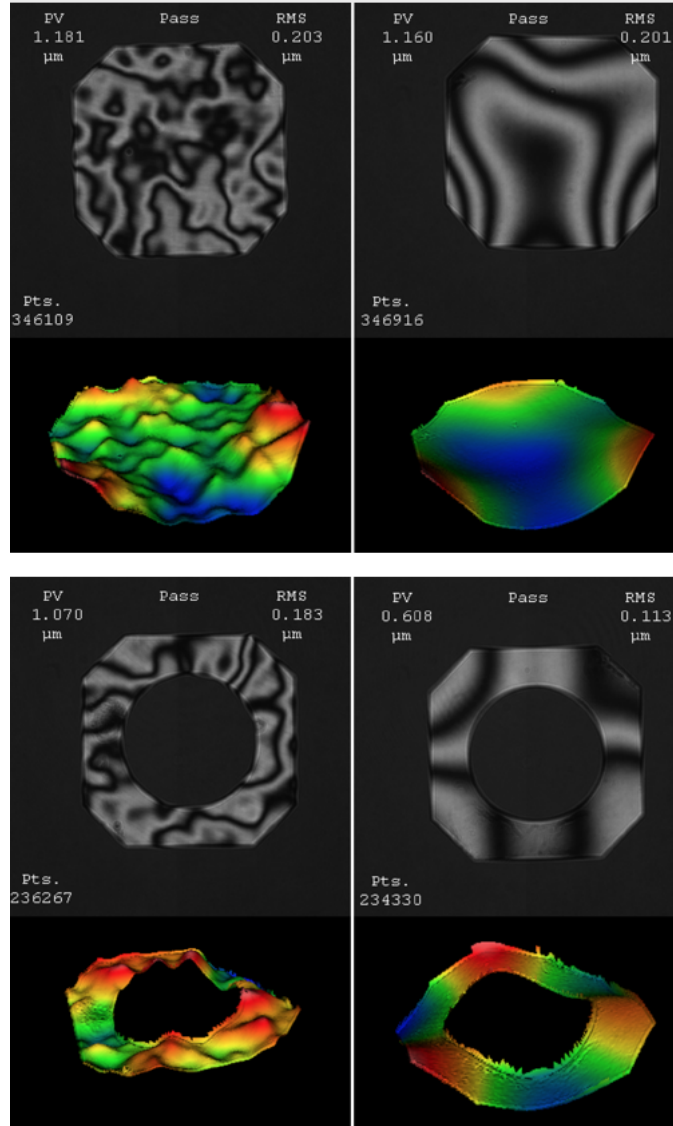


FIGURE 5.4: Data from the Zygo interferometer. The top four pictures are derived from surface measurements of one silicon sheet. The bottom four pictures come from surface measurements of one silicon spacer. In each group of images, the first row corresponds to the fringes observed on the two sides of the same sample and the second row is the shape of the surface deduced from fringes measurement of the first row. Note that for every sample (full sheet or spacer), there is always one smooth side (already presented in figure 5.3 (bottom)) and one grainy side. The latter probably results from the ground side of the silicon wafer. The Peak-to-Valley (PV) varies from $0.5 \mu\text{m}$ to $1.8 \mu\text{m}$ for all the samples.

hand, the Fizeau experiment has demonstrated that the samples are rather flat : the PV has been measured between $0.5 \mu\text{m}$ and $1.8 \mu\text{m}$ for all the samples. Nevertheless, we should therefore keep in mind these values since we have seen in section 5.1.2 that these typical deformations can quickly degrade the total finesse of the spectrometer.

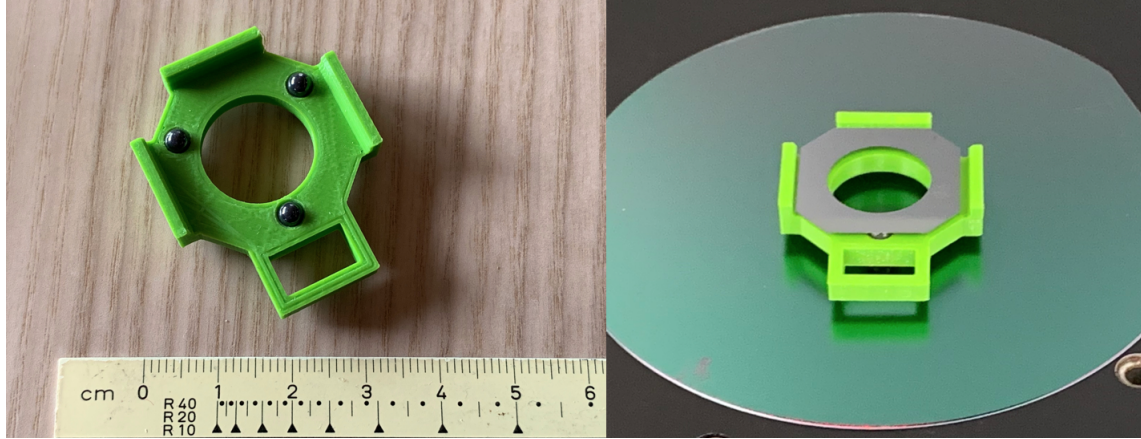


FIGURE 5.5: Three-points holder specially built for the Zygo measurements.

5.1.3 Assembling the mirrors

After the validation of the quality of the different layers that form the mirrors and ultimately a Fabry-Perot interferometer, the assembly step is critical. One of the main issues that we had to face was induced by the laser cut we performed on all the samples. We remind that the laser has been used for the silicon full sheets (corners and venting holes) and spacers (corners and the 16-mm hole of the ring). Figure 5.6 is best appropriate to illustrate our issue : the top figures are pictures of one sheet and the bottom figure comes from observations of the spacer. When we observed the samples at the microscope, we noticed that the laser cut had a huge effect. One can see on the top figures that, indeed, the laser cut produces a different effect than the cut by the wafer saw of the silicon crystal. The latter is definitively cleaner than the cut by laser : the laser indeed introduces some rims due to fused material on the edge of the sheet. In the figure below, we took a picture with a microscope in horizontal set-up to observe one spacer from the side and try to quantify the damage caused by the laser cut. The conclusion is striking : the laser leaves residual matter which increases the thickness of the spacer from the targeted $80\ \mu\text{m}$ to more than $100\ \mu\text{m}$ in some places of the edges. As all the samples were affected by this phenomenon, the assembly was therefore not realistic with this batch of samples.

We have then found a fast track solution which relies on mechanical cuts with a wafer saw made by CEA/LETI. All sample corners have been manufactured this way. In addition, the spacers have been redefined : one spacer is now made of four small silicon trapezoidal pieces (see figure 5.7 (top right)). This has the advantage to create the hole required for the vacuum ring, but the huge drawback of being difficult to assemble and of introducing instability in the whole system when mounting. However, because the silicon ring was not a continuous ring, we did not have to drill a hole within the full sheets because air can still vent from the sides of the spacers. Finally, after cleaning every mechanical invar part and every silicon

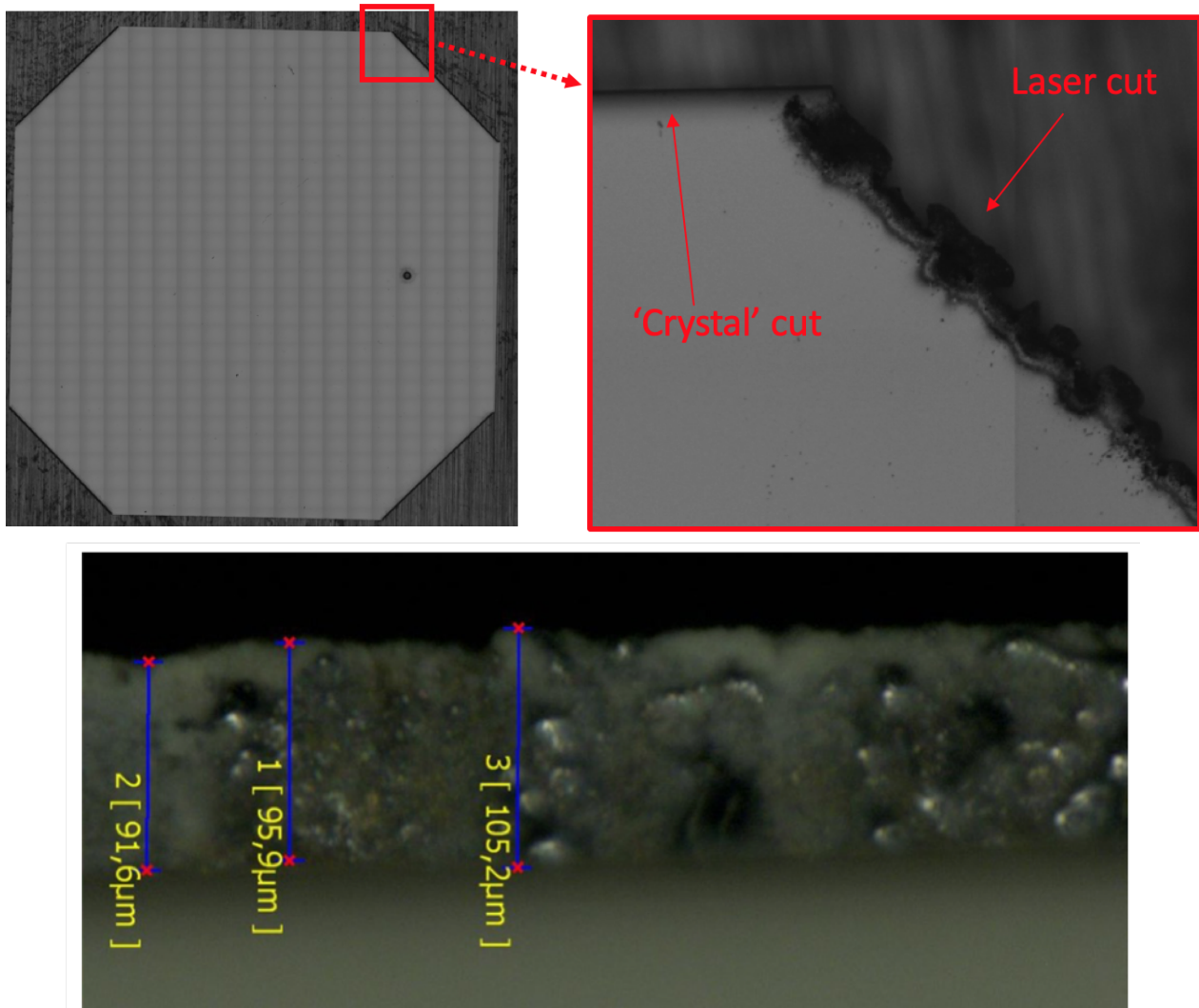


FIGURE 5.6: (Top) (left) Picture of one silicon sheet where the venting hole can be observed; (right) zoom-in on the edges of the sample where two different cuts are shown : the wafer saw (along the crystal axis) produces a very clean edge, while the laser introduces some material rims due to the warming-up by the laser. (Bottom) Photo of a spacer taken by a microscope in horizontal set-up, i.e. the microscope looks at the edge of the sample. One can note that some matter has been deposited on the edge leading to an increase in thickness from the targeted 80 μm to more than 100 μm in some places of the edge.

element with acetone and isopropanol in ultrasonic baths, layers have been assembled following the scheme (H/L/H)/(2L)/(H/L/H) as found optimal by our simulations, where each (L) layer is made of four small sheets. Figure 5.7 shows the pictures of the first mounting achieved at the end of March 2019. As the first etalon built, the notation 'FP1' will be used throughout this chapter.

A more adapted technique has been investigated to find out a solution to avoid the thick rims caused by the laser cut, while bearing in mind that the etalon should be easily mountable. First thoughts were in favor of shorting the pulse durations of the laser, typically in the femto-second range rather than in

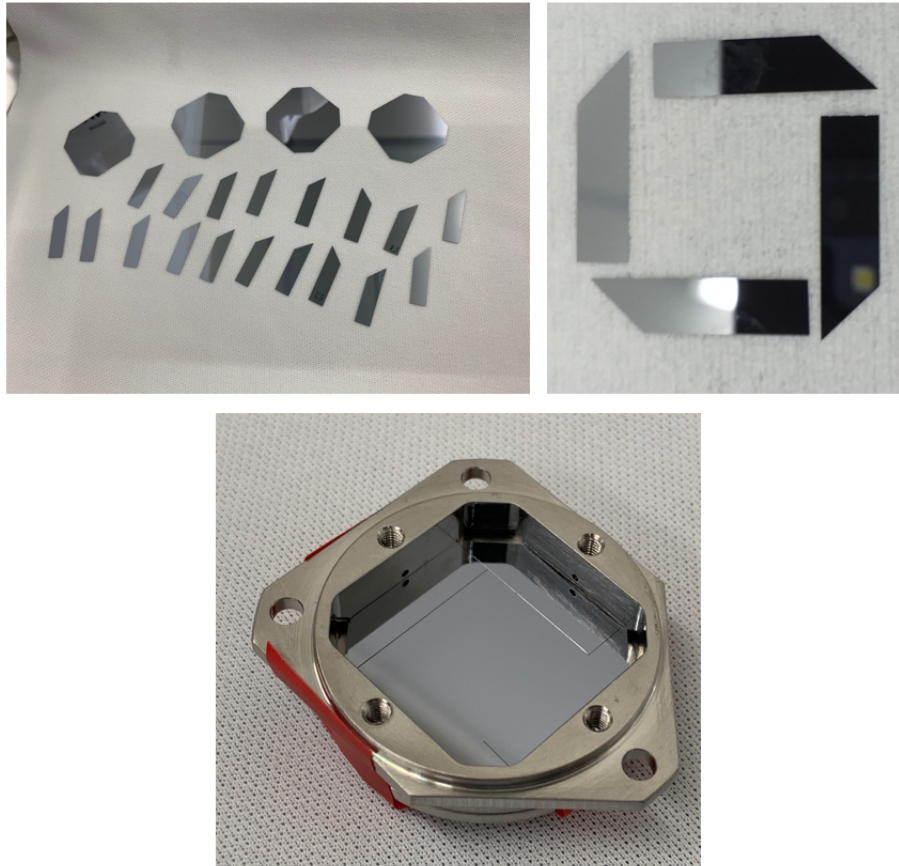


FIGURE 5.7: (Top left) Set of needed silicon sheets (and two additional small sheets) to build one etalon in the (H/L/H)/L/L/(H/L/H) layout, (Top right) Four small silicon trapezoidal pieces that act as a ring spacer. (Bottom) Assembly of the different parts in their mechanical invar parts.

the nanosecond range as the one used by CEA/LETI. In theory, such short pulses could have heated the silicon so quickly that the matter could only evaporate and thus would not leave any rim on the edges of the sample. Instead of a femto-second laser, we decided to choose and trust another innovative technology called the Laser MicroJet ((Synova S.A., 2019), (Vuichard S.A., 2019)). The principle of this cutting method is presented in figure 5.8 : it combines low-pressure water jet and laser. Used this way, the water contains the laser beam similarly to an optical fiber, cools down the work piece and removes debris from the surface. The water thus compensates for the thermal damage and deposition induced by the conventional laser. The impressive results from this technology are compared to the conventional laser cut in figure 5.9. We consequently used this technology to build the spacers as it was previously designed (i.e. as continuous rings) and also to drill the venting holes throughout the silicon in the full sheets. In addition, a special care has been given to select the best layers ($PV \leq 1 \mu\text{m}$) for the sheets, but also for the spacers. For this reason, we expect the performance of the second assembly to be better than those of FP1. The second mounting arrived at the end of May 2019, which we call ‘FP2’.

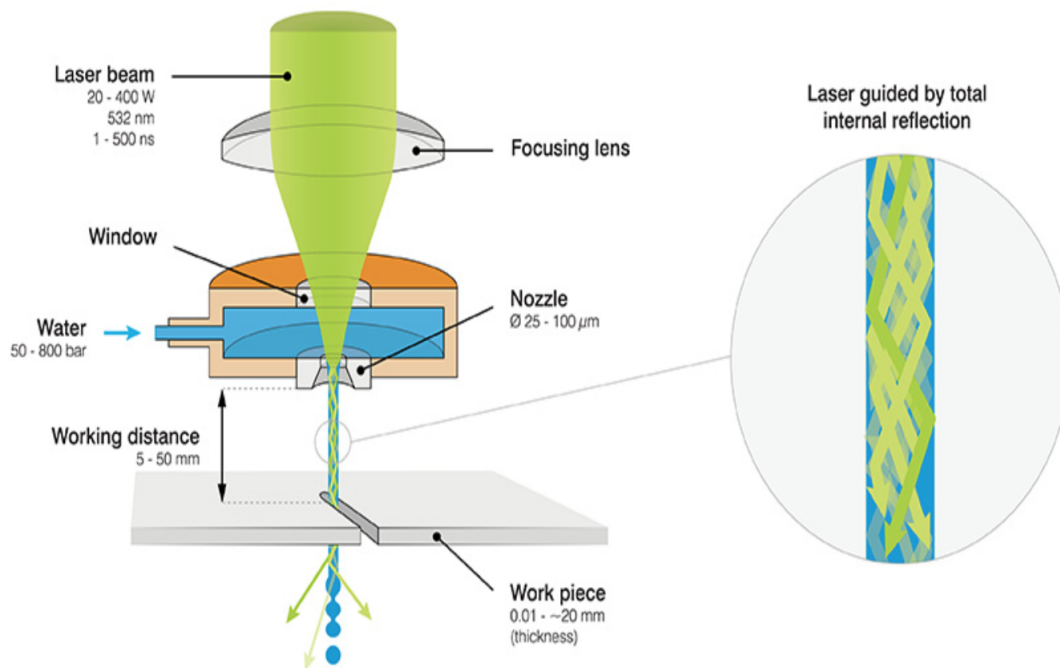


FIGURE 5.8: Synova innovative technology principle : the Laser MicroJet combines low-pressure water jet and nano-second laser. In addition of containing the laser within a constant beam diameter over a long distance, the water jet provides continuous cooling to the material. The laser jet technology prevents the material to experience thermal damage or deposition, in contrast to the conventional laser. Note that if the water reservoir is pressurized to 50-800 bar, the nozzle is so thin (25-100 μm -diameter) that the resulting force is negligible ($< 0.1 \text{ N}$) (extracted from (Synova S.A., 2019)).

Finally, the last improvement that we performed concerns the quality of the holders. Figure 5.10 shows the different parts : the silicon stack is maintained between the red and the magenta parts. The support by three pads, rather than a full ring, was chosen to be less sensitive to deformations of the rings in the mount, which may occur between room temperature and cryogenic temperatures due to residual stress in the material. After building the first assembly (FP1), we noticed with the Fizeau interferometer that these two three-pads pieces tended to deform the silicon mirrors just by laying down on the silicon sheet. Therefore, the three-pads parts have been corrected by lapping to the sub-micron precision, in order to have three flat pads but also in the same plane to avoid any distortion of the silicon layers. The third and last assembly is called FP3. In theory the performance of FP3 should be even better than those of FP2, however, for this etalon, we could not have all the layers meeting the specifications about peak-to-valley flatness better than $1 \mu\text{m}$.

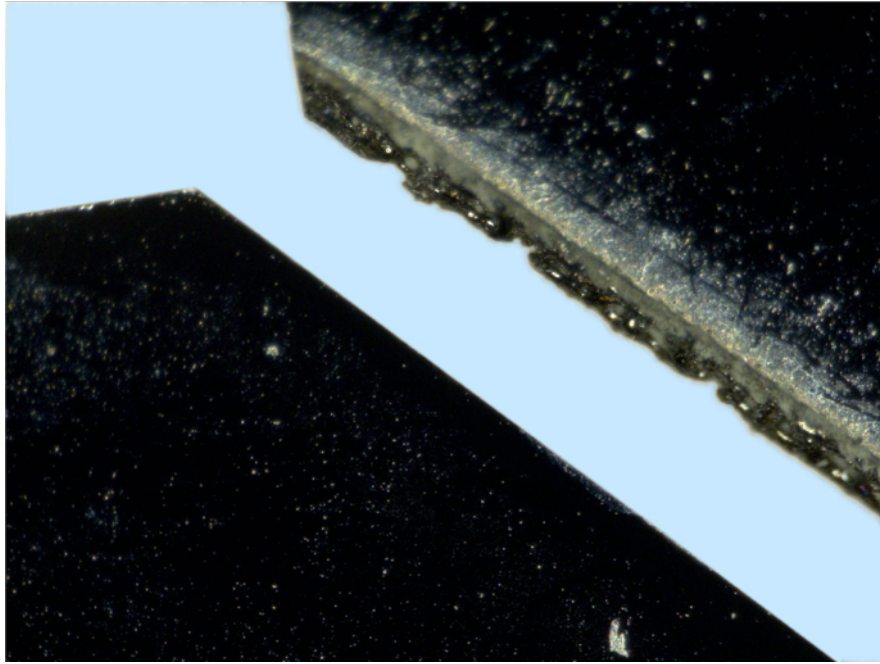


FIGURE 5.9: Comparison of two laser cut methods on two silicon sheets observed under the microscope : in the bottom left part, the Laser MicroJet technology ; in the top right part, the conventional laser cut made by CEA/LETI.

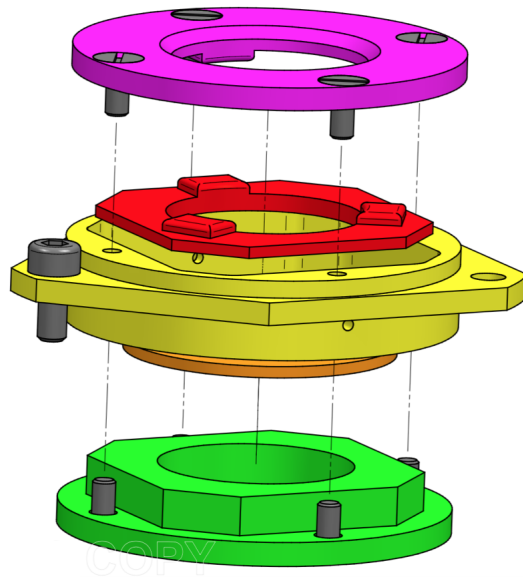


FIGURE 5.10: Mechanical holders for etalons. The red and magenta parts maintain the multi-layer silicon structure. Three-pads have been designed on these rings to avoid any deformation of the stack. Etalons are used at 4-77 K. The mechanics is made of invar because it has a low coefficient of thermal expansion (mechanical design by J. Martignac).

5.1.4 Validation of the theoretical model by Time Domain Spectrometer (TDS) measurements at ambient temperature

Measurements with a Time Domain Spectrometer (TDS) at ambient temperature have been performed to check the spectral transmission of the etalons at low-spectral resolution. The working principle of a TDS is described in Neu and Schmuttenmaer (2018). Figure 5.11 compares the measure of FP1 by the TDS to the computed transmission derived from thin film simulations, over a large bandwidth. As it will be explained in the next section, narrow-band filtering was required at cold temperature with the Martin-Puplett interferometer, thus the TDS makes possible the comparison of the model and of the measure over a large bandwidth. The figure teaches us that the model predicts very well the spectral behavior of the all-made silicon FP1. A slight difference can still be observed between the theory and the experiment which might be explained by the fact that thicknesses of the wafers were not measured within the sub-micron precision all over the wafer. In the model, we took as thicknesses the ones measured at the wafer level : 79.7 μm for the silicon rings and 72.1 μm for the full sheets. It should be mentioned that the narrow line expected around 320 μm cannot be resolved by the TDS because of its intrinsic resolution (46 at 320 μm , due to the limited maximal delay of 48 ps), but we can still observe a sinc function which is the nominal shape of unresolved fine-lines (this is emphasized with the yellow square window in the figure). The results presented in this figure concern the transmission of etalon FP1, but similar results are obtained for the other etalons.

5.2 Validation of the performance of Fabry-Perot etalons based on dielectric mirrors

After assembling several etalons, we tested them at low temperature with a cryogenic Fourier Transform Spectrometer. The experimental set-up and measurements are presented hereafter, with a particular emphasis on the data analysis. The objective is to experimentally check the principle of multi-layer silicon mirrors for FP spectroscopy at sub-millimeter wavelengths. This implies to measure its spectral profile with sufficiently high resolution and, above all, to demonstrate a high transmission. The experimental validation of the lossless behavior, or at least of the small loss, of the etalon is the main purpose of this section. In this part, we will also check that the dielectric etalon response can be shifted in accordance with the variations of the cavity size.

5.2.1 Description of the cryogenic optical train

The optical bench (see appendix E) can be described as a set of three cryostats, shown in figure 5.12. The light from a blackbody source first enters into the Fourier Transform Spectrometer cryostat, then goes to the sample cryostat and finally reaches the detector in the bolometer cryostat. In this part, we emphasize

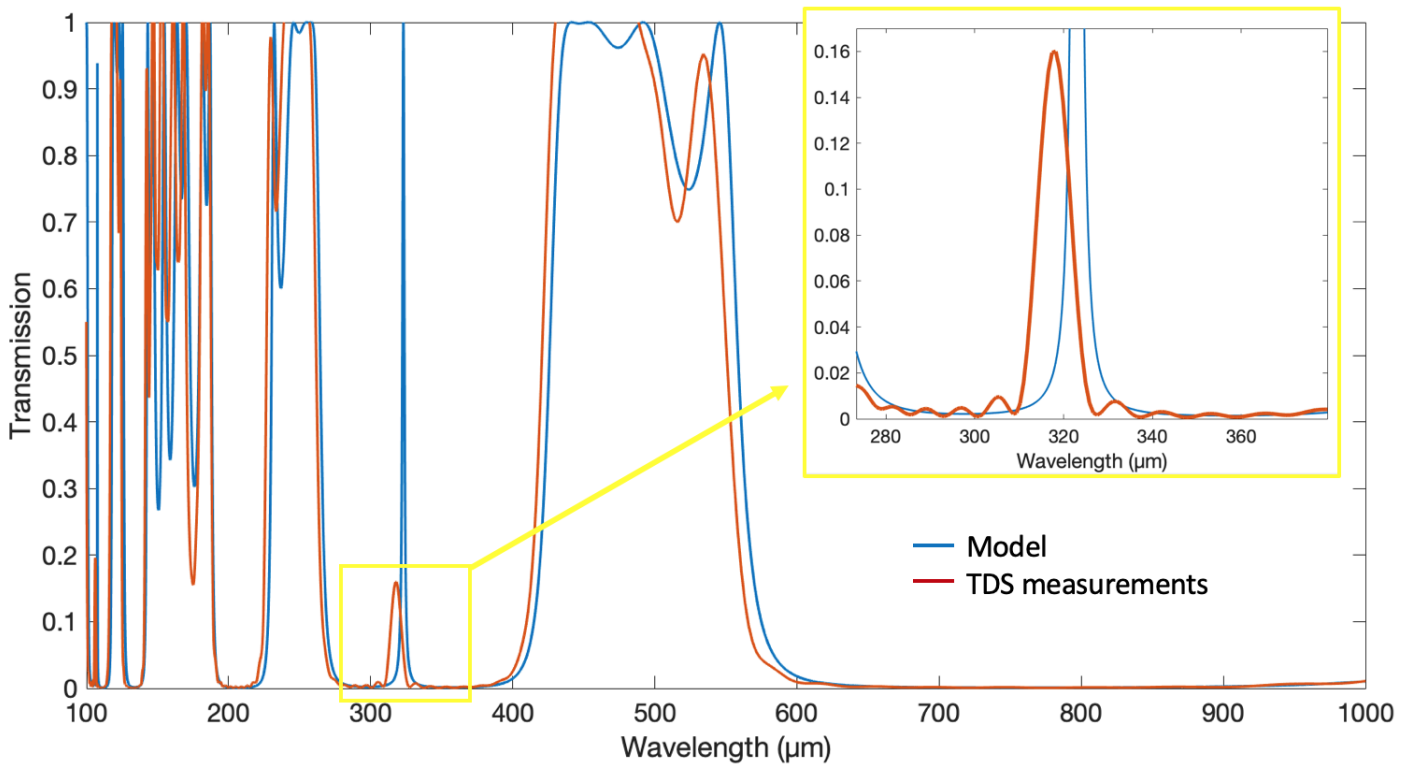


FIGURE 5.11: Comparison of the model and of the measurement : (Blue) Computed transmission for an etalon with $t_{Si} = 72.1 \mu\text{m}$ and $t_{vac} = 79.7 \mu\text{m}$, (Red) Measured transmission with the TDS at warm temperature. The yellow window highlights the sinc shape obtained with the TDS and related to the unresolved fine-line around $320 \mu\text{m}$.

the cryogenics involved in the optical system as it is a crucial aspect in all far-infrared experiments. Cooling down instruments here allows us to work with a sensitive detector and to reduce thermal noise and dielectric losses in silicon (still to be confirmed).

The Martin Puplett Interferometer

Among various kinds of FTS, the one we use is a Martin Puplett Interferometer (MPI) ((Martin and Puplett, 1970)). This configuration is often used in far-infrared since the thin beam-splitter is replaced by a polarizer, which can work over a large frequency range, unlike the conventional beam-splitter used in the visible and near-infrared. The polarizer is made of parallel metal wires which are spatially close (i.e. the distance between them is short compared to the wavelength). Then, by decomposing the incident electric field as the sum of two orthogonal polarization vectors, the polarizer will reflect the component which is parallel to the wires and transmit the component which is perpendicular to the wires. In this way, the polarizer acts as a beam-splitter ; and as long as a loss of signal through the metallic wires is not critical, then the MPI working frequency range is a serious advantage over the Michelson interferometer's ((Lesurf, 2017)). Figure 5.13 illustrates the overall MPI functioning. When the light enters the cryostat, it

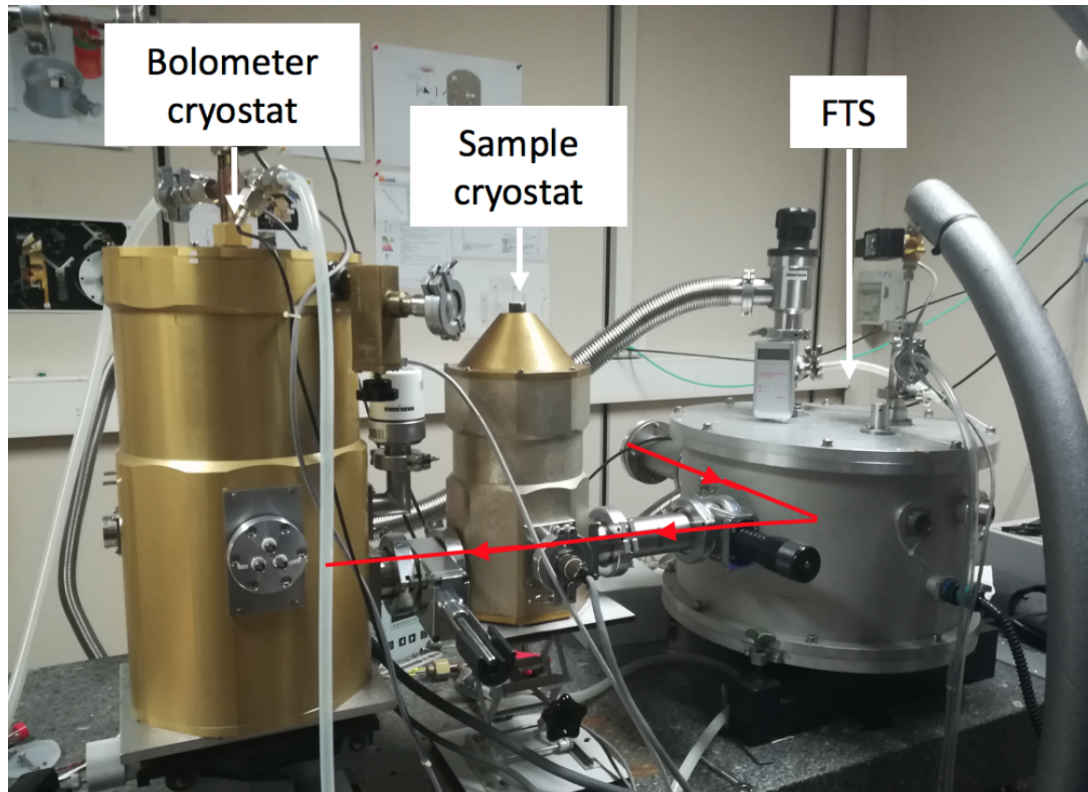


FIGURE 5.12: The optical set-up for measurements of etalons at cold temperature : the light first travels to the FTS cryostat, passes through the sample cryostat and eventually reaches the bolometer cryostat. Measurements produce interferograms which, after Fourier Transform processing, give spectra as functions of the wavelength.

is first polarized by a vertical polarizer P_1 . A 45° polarization beam-splitter BS decomposes the light into two orthogonal polarization beams. One passes through the wires and reaches a roof-top mirror (RM_1), the other is reflected and reaches the roof-top mirror RM_2 . The conventional flat mirrors in a Michelson interferometer are replaced by roof-top mirrors in the MPI because they rotate the polarization by 90° using two successive reflections. This results in transmission through (resp. reflection by) the polarizing beam-splitter of the electric component that has been first reflected (resp. transmitted). The two electric components are recombined at the beam splitter. The wave is then reflected on two parabolic mirrors (PMs) and is finally analyzed by another polarizer P_2 (whose metallic wires are in the same direction as those of P_1). This last polarizer is necessary to observe interference fringes : without this optical component one would observe a constant power on the detector. In order to perform Fourier Transform Spectroscopy, one of the two roof-top mirrors is translated, leading to a variation in the optical path difference (OPD) of the output beam which results in a modulation of power. The bolometer, at the end of the optical train, measures the power and we can derive an interferogram as a function of the mirror scan, from the zero path difference (ZPD) to a maximal travel distance. It is to mention that the FTS cryostat is cooled down to 77 K (with liquid nitrogen) during measurements to reduce the thermal background noise on the light modulation.

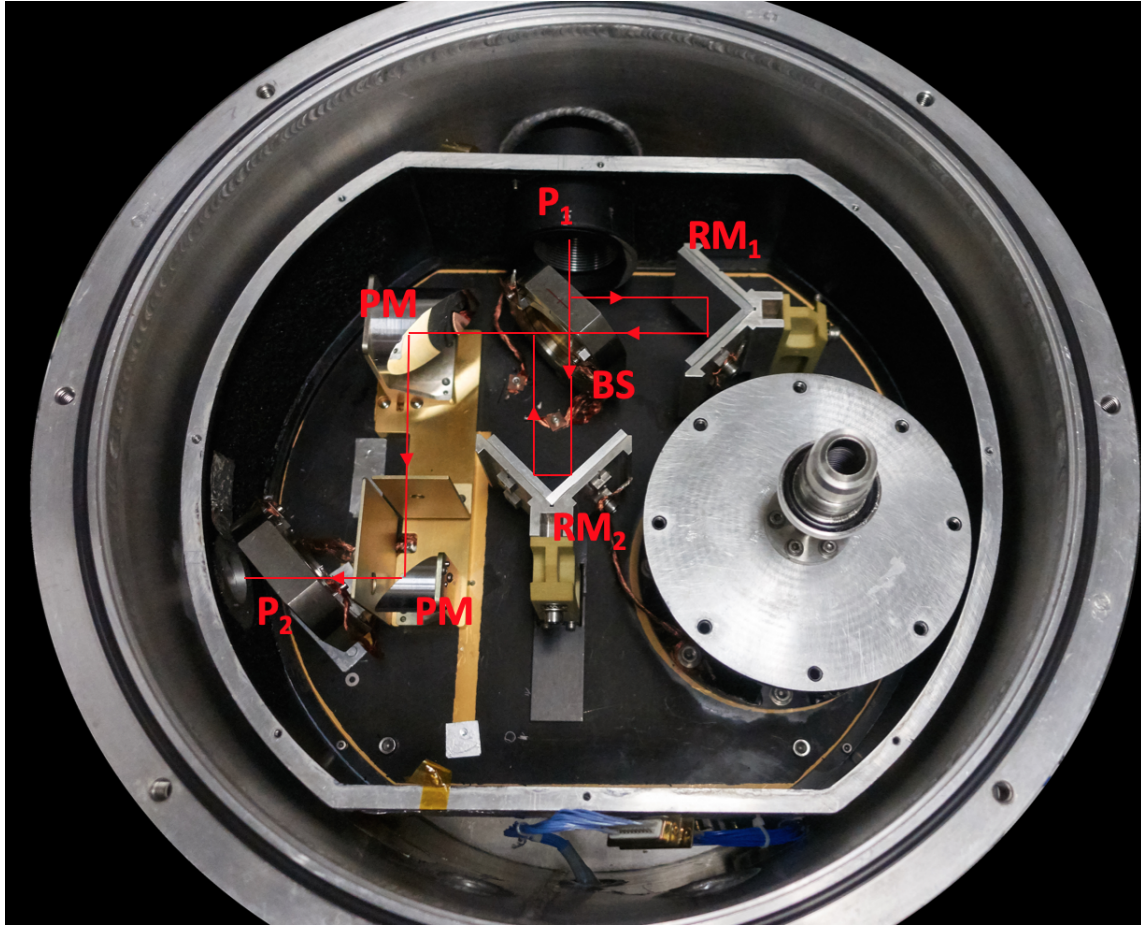


FIGURE 5.13: Cryogenic (77 K) Martin Puplett Interferometer (MPI) produces interferograms by amplitude division. The wave from the black body source is first polarized by the polarizer P_1 (wires at 45° from the orthogonal basis created by BS). It is then split into two components by the polarizer BS : each orthogonal polarization is reflected on a roof-top mirror (RM_1 and RM_2) and goes back to the polarizer BS . Eventually both components recombine, the wave is reflected on two parabolic mirrors (PM) and a polarizer P_2 (same as P_1) selects one component of the field. With P_2 it is therefore possible to observe a modulated power at the end of the FTS cryostat. Interferograms are obtained by scanning one of the two roof-top mirrors (RM_2) which changes the optical path difference of the two orthogonal electric components.

Sample cryostat

The sample cryostat is a dedicated cryostat with a single cryogenic vessel where we put the etalons under test. With this setup, the measurement of various elements can be achieved without the need to disassemble the whole experiment of figure 5.12, but only the small sample cryostat. Moreover, manual valves between the sample cryostat and the other two cryostats allow one to remove the sample cryostat without breaking the vacuum in the bolometer cryostat. The interior of the sample cryostat is pictured in figure 5.14. It contains a fixed filter holder and an aluminum wheel where etalons are mounted. Once the sample cryostat is closed, the wheel can be rotated by a manual shaft, allowing us to test one sample

after the other or after the reference. A microswitch has been installed to allow only certain positions to be reached with the help of three notches that have been milled on the circumference of the wheel at 120° from each others. For the etalon measurements, a stack of two filters on the fixed holder suppresses light outside of the $320\ \mu\text{m}$ band. Their spectral characteristics is depicted in figure 5.15. The band-pass filter (BP350) creates a narrow ($60\ \mu\text{m}$ -width) band transmission around $320\ \mu\text{m}$ and the low-pass filter (LP270) prevents any signal contamination between 100 and $200\ \mu\text{m}$, that the BP350 could let pass. These filters should allow us to measure a pure signal in the band of interest (around $320\ \mu\text{m}$), despite a small contribution from the 400 - $600\ \mu\text{m}$ band due to the etalon transmission (see figure 5.11). Concerning cryogenic aspects, the sample cryostat can be cooled down to $77\ \text{K}$ with liquid nitrogen or to $4\ \text{K}$ with liquid helium, after liquid-nitrogen pre-cooling. A copper braid forms the thermal link between the cold stage and the aluminum wheel. Thus the samples can be cooled down to 77 or $4\ \text{K}$. Two silicon diodes allow us to probe the temperature of the cold stage but also of the wheel. In most of the experiments presented in this chapter (namely the multi-layer etalon performance), we only cooled down the samples to $77\ \text{K}$, mainly for stability reasons : indeed, the cryostat has an autonomy of 6 hours at liquid nitrogen temperature while it is reduced to less than 2 hours at $4\ \text{K}$. After this thesis, we measured the effects of temperature on the losses in silicon, the results are briefly discussed at the end of section 5.2.3.

Bolometer cryostat

The bolometer cryostat is at the very end of the optical train. As the light focuses at the entrance of the detector cryostat (see figure E.3 in appendix E), we brought the detector as close as possible to the window, in order to collect the maximum amount of light. The detector is suspended by a copper plate that is directly attached to the cold tip of the cryocooler : in this way, the bolometer is thermally linked to the $300\ \text{mK}$ stage. To reach sub-Kelvin temperature, the cryostat needs to be precooled to a temperature less than $2\ \text{K}$. This is achieved with the two liquid nitrogen and liquid helium reservoirs. Then a ^3He adsorption cooler¹ allows the bolometer to reach $270\ \text{mK}$, after one or more recycling. Figure 5.16 shows the condenser, the evaporator and the pumping line of the cryocooler. The low-temperature is a prerequisite for this bolometer to work in its optimal range, although other bolometers are not that demanding and work at higher temperature ($1.7\ \text{K}$).

1. The cryocooler is made of a pump (activated charcoal), a condenser, an evaporator and a pumping line (see figure 5.16). In practice, when the cryocooler is thermalized at $\sim 1.7\ \text{K}$ due to the pumping on the helium bath, we heat the activated charcoal by applying a voltage to a resistance glued on the pumping element. The ^3He atoms which were fixed to the charcoal since the last cycling, are thus released and can travel through the pumping tube. They are then condensed at the condenser level when the saturation vapor pressure at $1.7\ \text{K}$ is reached and the liquid ^3He falls into the evaporator by gravity. Once we stop heating the resistance, the charcoal can cool down since it is thermally linked to the helium 4 tank. The charcoal pumps on the ^3He bath by adsorbing the atoms : the pressure and the temperature decrease.

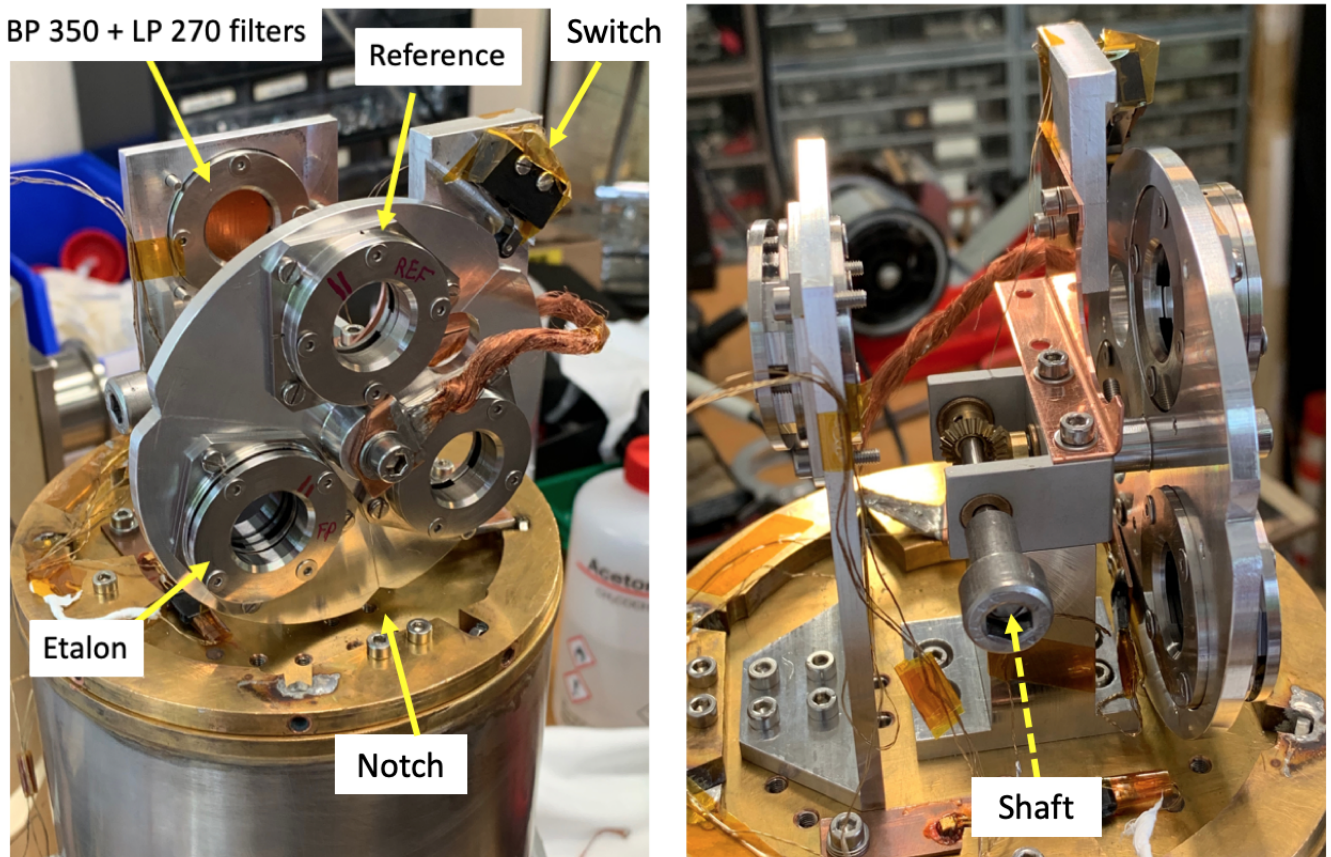


FIGURE 5.14: Pictures of the open sample cryostat shot from different angles. A maximum of three samples can be mounted on the wheel. A microswitch has been installed and three notches have been milled, to allow only certain positions that correspond to the positioning of the three samples in the optical path. Once the sample cryostat is closed, the wheel can be manually rotated from one position to the other by means of a shaft made from a fiber-epoxy tube to minimize the heat load on the cold stage. Two filters are used in this etalon experiment to reduce the power on the detector. The wheel can be cooled down to 4 K if necessary, a copper braid builds the thermal link between the cold stage and the wheel. Two probes monitor the changes in temperature of the 4 K-stage and of the wheel.

5.2.2 Measuring the finesse of multi-layer silicon etalons

After describing the optical set-up and the three cryostats that are used for measurements, we now present the results concerning the finesse of the etalons that were built.

The first real limitation that we had to face for the finesse measurements were related to the ‘short’ travelling distance that the scanning roof-top mirror was able to achieve. Indeed, from the central fringe, the mirror can travel 5 mm in one direction and 35 mm in the other direction. From equation $\delta\sigma = \frac{1}{2D_{max}}$ (section 4.1.1) and after mirroring the non-symmetric interferogram, we derive the distance between two frequency datapoints $\delta\sigma = 0.071 \text{ cm}^{-1}$, which corresponds in wavelength to $\delta\lambda = \lambda^2\delta\sigma = 0.73 \text{ }\mu\text{m}$ for $\lambda = 320 \text{ }\mu\text{m}$. With a theoretical FP resolution of $R = 215$, we might expect a limit on the FWHM of $\delta\lambda = 1.48 \text{ }\mu\text{m}$ at $\lambda = 320 \text{ }\mu\text{m}$. These short calculations indicate that there will only be a small number of datapoints in the transmission peak of the etalon. Moreover, if the signal to noise ratio is not suffi-

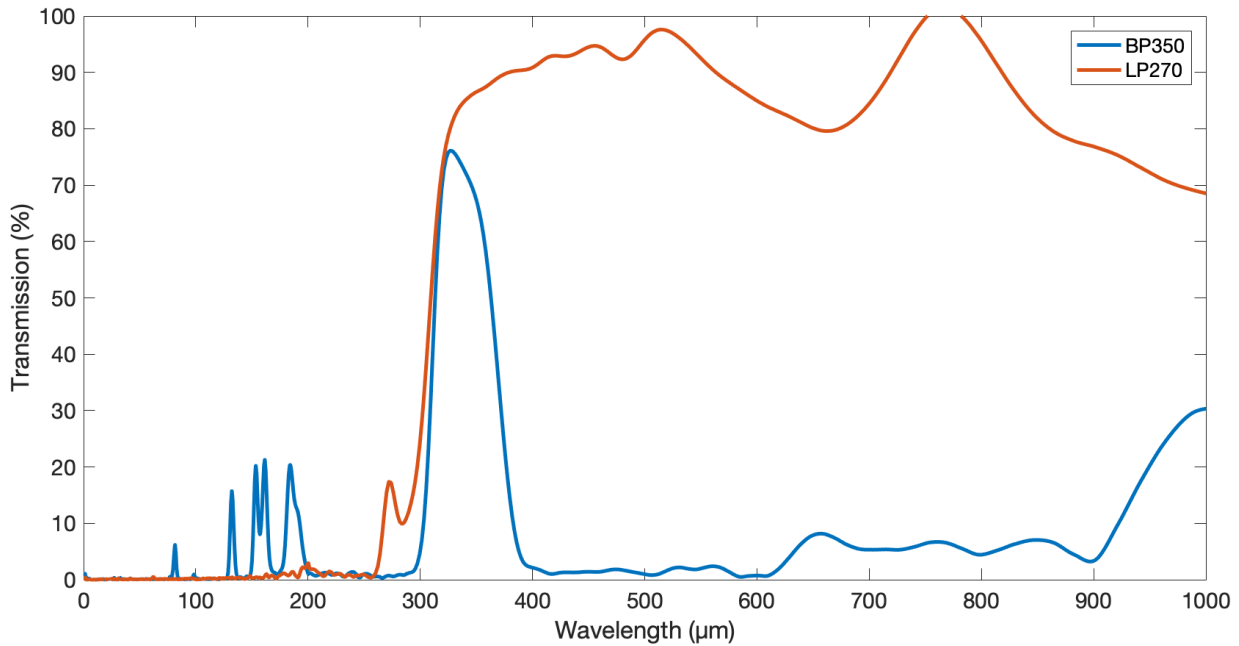


FIGURE 5.15: Transmission of the two filters used in the sample cryostat : the BP350 filter only transmits in a narrow-band around 320 μm and the LP270 filter suppresses any signal between 100 and 200 μm .

ciently high, it might be difficult to fit the data. This is the reason why we investigated an alternative analysis method that relies on the processing of the direct interferograms, instead of the Fourier Transform of interferograms. The idea is to make an assumption on the shape of the spectrum and from there, to compute the expected interferogram related to the spectrum and to fit it to the measured interferogram. From this, it is possible to derive the parameters that define the shape of the spectrum. The purpose of the two methods performed in parallel is to check that we get comparable results at the end of the analyses.

FP1 etalon

To illustrate the two methods with an example, we use the data from the 6th of June where we measured interferograms of FP1.

The first step is to process data coming from the measurements of the reference which corresponds to the open position of the wheel in figure 5.14. The measurement gives us the emission of the source radiation filtered by the bandpass on the fixed mount. We only use this spectrum to compare it to the one with the FP in the path, to derive the transmission of the FP. Moreover, this step cannot be avoided since the interferogram of the reference tells us where the zero path difference (ZPD) is for one set of measurements. Figure 5.17 illustrates the different operations of the data processing that have been applied. The MPI scanning mirror travels a distance from -20 to 20 mm in reported coordinates of the translation stage.

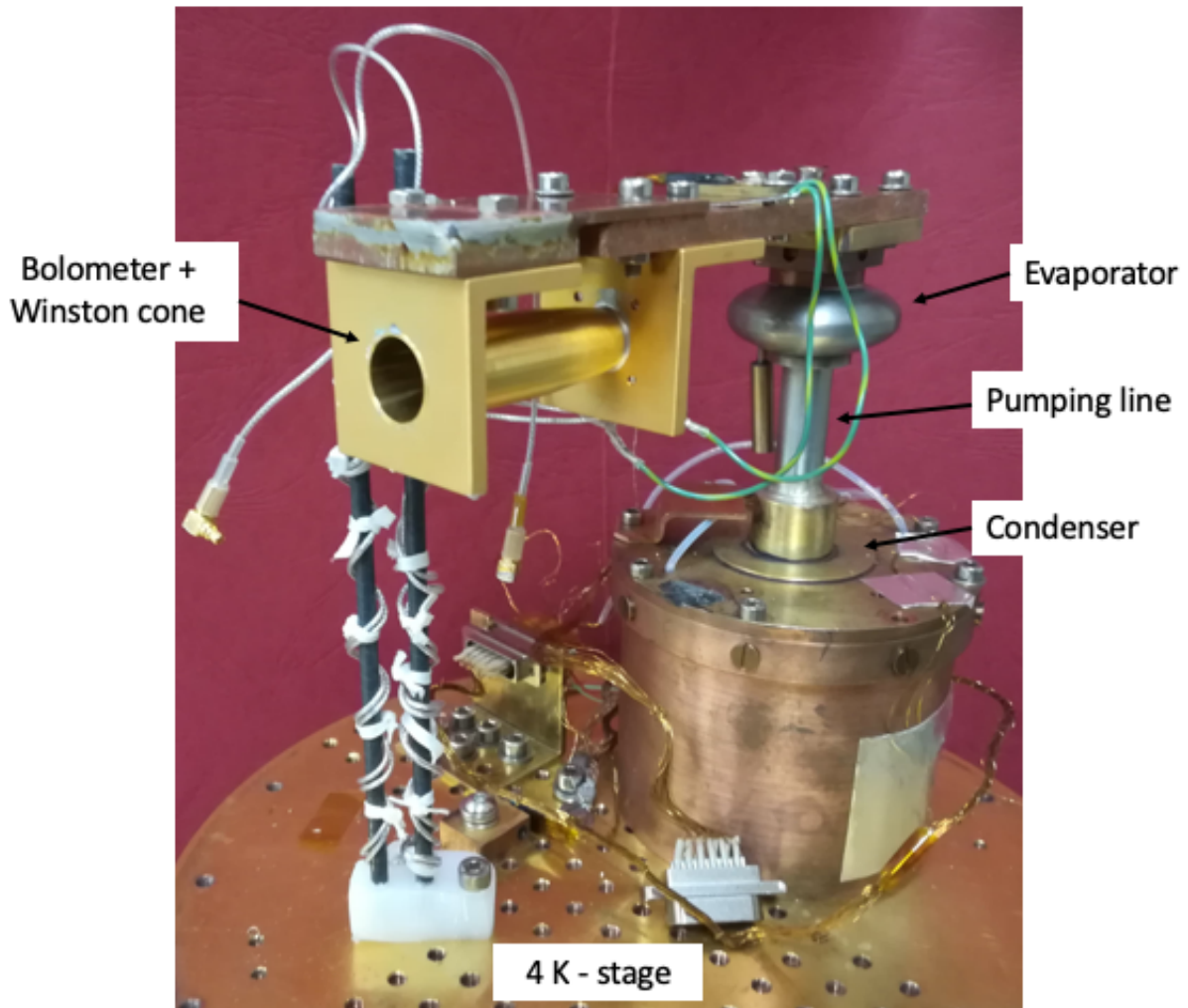


FIGURE 5.16: Open detector cryostat : the bolometer and its Winston cone is linked to the cold tip of the cryocooler. The ^3He adsorption cooler is made of an evaporator, a pumping line and a condenser.

Two interferograms have been selected for the following calculation, they are shown on (A) between ± 5 mm around the ZPD which is calculated to be at -15.0 mm for the two of them. These interferograms are obtained after thermal drift and offset corrections. Panel (B) is a zoom on the central fringes. The averaged interferogram (C) of the two interferograms gives the spectrum (D) after Fourier transform. As expected, most of the signal is detected in the $350 \mu\text{m}$ band even if there is a weak contamination signal at $470 \mu\text{m}$.

First method : Fourier transform analysis

The measured interferograms from the FP1 etalon are plotted on (A) in figure 5.18. We have selected 8 interferograms that we considered as reliable (low noise and low external perturbation data) for data processing. In the interferograms figure, presented between -16 and -14 mm, the first thing that we can notice is the shape of the measurements at the level of the ‘central fringe’ : it is a sinusoid. This pattern was

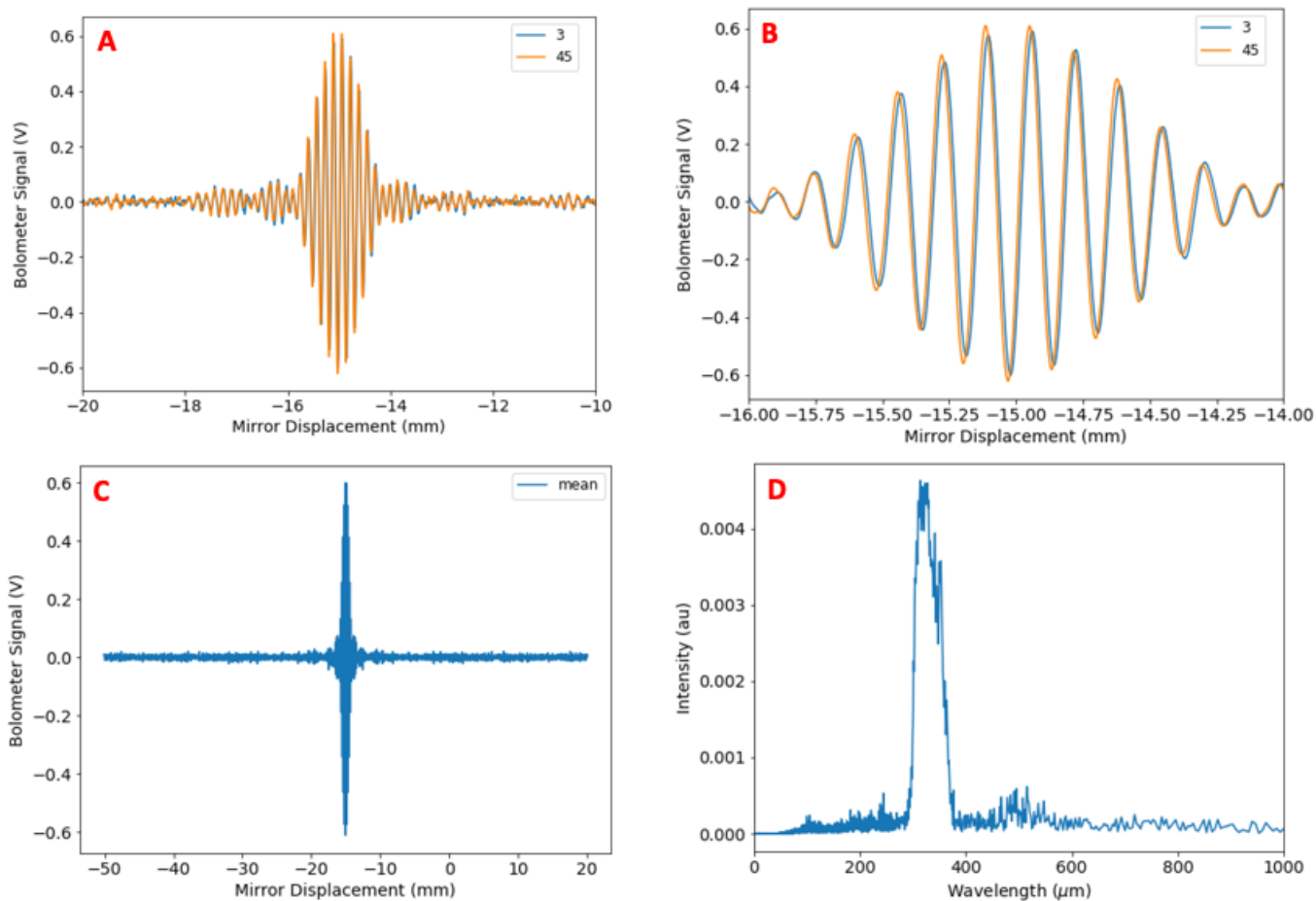


FIGURE 5.17: Results from FTS measurements in the reference position : (A) two interferograms have been selected for data processing (shown after drift and offset corrections) ; (B) Zoom on the central fringes of the two interferograms : for the two of them, the central datapoint is at -15,0 mm ; (C) Averaged (and “mirrored” (see later)) interferogram leads to the spectrum shown in (D), after Fourier transform.

expected since the Fourier Transform of a shifted Dirac function is a complex exponential and from these single measurements, we might conclude that the system we built works as a resonant system (i.e. as a FP). Panel (B) is the averaged interferogram after several operations. We have corrected the interferogram from the slow modulation that is mostly due to noise from the experimental set-up in the lab. For this operation we applied a moving average to determine a baseline and subtracted this baseline to the averaged interferogram. Next, in order to improve the spectral resolution of the spectrum derived by Fourier data processing, we have artificially increased the size of the interferogram by mirroring it with respect to the central position. Before this, we made sure that the central position was consistent with the one derived from the reference. These two operations lead to panel (B). The blue spectrum in (C) is derived from the interferogram (B) after Fourier transform.

Our objective is now to fit the spectral profile data by a Lorentzian function because this function is

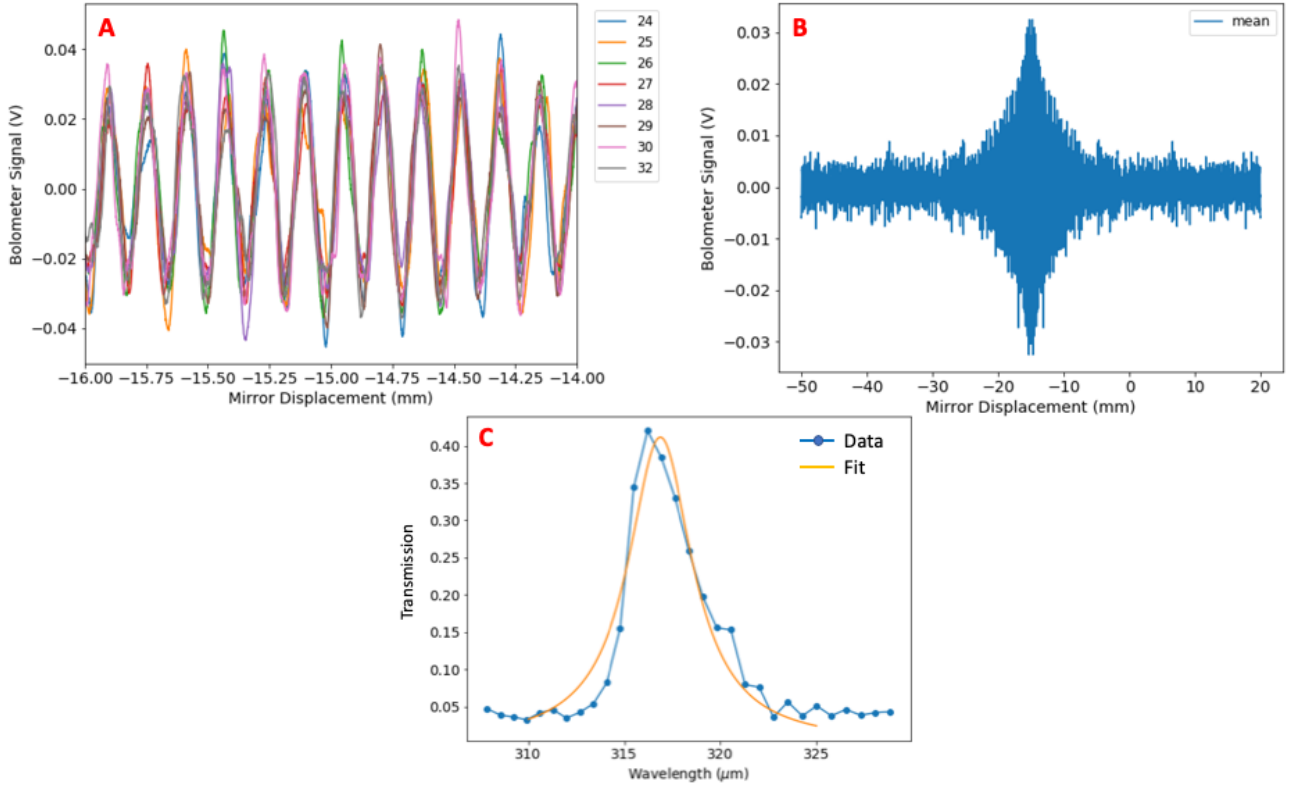


FIGURE 5.18: Results from FTS measurements of FP1 based on Fourier Transform analysis : (A) 8 interferograms have been selected for data processing, after drift and offset corrections, they are shown between ± 1 mm around the ZPD (the ‘central fringe’ is around -15 mm); (B) Averaged interferogram from the 8 measurements after correction for slow modulation and mirroring; (C) Computed transmission spectrum after Fourier Transform of the averaged interferogram and its Lorentzian fit.

representative of a resonant system, such that a Fabry-Perot interferometer. A Lorentzian function can be described by the following equation :

$$f(\lambda) = \frac{A}{1 + \alpha(\lambda - \lambda_0)^2} \quad (5.2)$$

with A the maximum of the Lorentzian function, α the parameter related to the width of the function and λ_0 which indicates the central position of the resonance. From panel (C) in figure 5.18, we derived the parameters that define the Lorentzian shape : $A = 0.41$ (in transmission), $\alpha = 0.24 \mu m^{-2}$, $\lambda_0 = 316.9 \mu m$. The corresponding fit in orange overlays the measured data on the plot. The resolving power \mathcal{R} can be deduced from the calculations of the ratio of λ_0 to the full width at half maximum (FWHM) $\delta\lambda$ which is equal to $\frac{2}{\sqrt{\alpha}}$:

$$\mathcal{R} = \frac{\lambda_0}{\delta\lambda} = \frac{\lambda_0\sqrt{\alpha}}{2} \quad (5.3)$$

For the FP1 measurements, the Fourier analysis gives a resolution \mathcal{R}_{FP1}^{FT} equal to 77.8 at $\lambda_0 = 316.9 \mu m$. The idea is now to compare the results from the conventional Fourier Transform analysis with the results

of the analysis that relies on direct interferogram processing.

Second method : direct interferogram analysis

The second method is based on the assumption that the spectrum that we expect has a Lorentzian function shape. As we have seen in the previous paragraph, this assumption is fully justified. The goal is to find the analytical function that can describe the interferogram of a Lorentzian function in order to find the parameters which fit the measured interferogram. From this, it is then possible to derive the resolving power and the resonant wavelength of the etalon, as it has been done above. The advantage of this method is that since spatial datapoints are recorded every micron (without increasing the time duration of measurements), the interferogram can be fitted with more datapoints than the spectrum.

The Fourier Transform is the mathematical operation that allows one to switch between domains : in our case, we want to find the equivalent of the wavenumber-dependent function $\hat{f}(\sigma)$ in the spatial domain. The Fourier Transform of $\hat{f}(\sigma)$ is the function $f(x)$ given by the equation :

$$f(x) = \frac{1}{\sqrt{2\pi}} \int_{-\infty}^{+\infty} \hat{f}(\sigma) e^{i2\pi\sigma x} d\sigma \quad (5.4)$$

where the wavenumber σ is expressed in m^{-1} as x accounts for the displacement of the mirror (in m). Note that here, the ‘wavenumber’ is the reciprocal variable of the distance x (and not of the optical path difference). The resonance in wavenumber can be described by the Lorentzian function :

$$\hat{f}(\sigma) = \frac{A}{1 + \alpha(\sigma - \sigma_0)^2} \quad (5.5)$$

We then use two relationships between a function and its Fourier Transform :

$$\left\{ \begin{array}{l} \hat{f}(\sigma - a) \iff f(x) e^{i2\pi ax} \\ \sqrt{\frac{2}{\pi}} \frac{a}{a^2 + 4\pi^2\sigma^2} \iff e^{-a|x|} \end{array} \right. \quad (5.6)$$

Equation 5.5 can be thus rewritten as (for $\alpha > 0$) :

$$\hat{f}(\sigma) = B \sqrt{\frac{2}{\pi}} \frac{2\pi/\sqrt{\alpha}}{4\pi^2/\alpha + 4\pi^2(\sigma - \sigma_0)^2} \quad (5.7)$$

where B is a constant coefficient. Equations 5.6 and 5.7 give the equation of the Fourier Transform $f(x)$:

$$f(x) = B \cos(2\pi\sigma_0 x) \exp\left(-\frac{2\pi |x|}{\sqrt{\alpha}}\right) \quad (5.8)$$

In practice, f is offset from the position of the central fringe x_0 which results in a slight change in the definition of f :

$$f(x) = B \cos(2\pi\sigma_0(x - x_0)) \exp\left(-\frac{|x - x_0|}{d}\right) \quad (5.9)$$

where $d = \sqrt{\alpha}/2\pi$ describes the rate of the exponential decay. With this interferogram-based method, we tried to fit the data of the figure 5.18, panel (B) to the equation 5.9. This figure shows an exponential decay in addition of the sinusoidal oscillation. As we aim at computing the resolving power, the parameters of equation 5.9 that we should derive are : x_0 the position of the central fringe, σ_0 the resonant ‘wavenumber’ and d . The resolving power \mathcal{R} can therefore be calculated since $\sigma_0 = 1/X$, where X is the spatial period of the cosine modulation (note that here $\lambda_0 = 2X$ because the OPD is two times the distance scanned by the mirror) and $\delta\sigma = \frac{2}{\sqrt{\alpha}} = \frac{1}{\pi d}$, with the formula :

$$\mathcal{R} = \frac{\pi d}{X} \quad (5.10)$$

Results from the analysis of FP1 with the second method are presented in figure 5.19. Here we only fitted the interferogram of the previous study. (A) and (B) illustrate this fit over two spatial bands : around the central position and on the decay of the exponential. The parameters that make the fit matching the data are : $X = 0.1588$ mm, $x_0 = -15.03$ mm and $d = 3.99$. With this method, the resolving power of FP1 \mathcal{R}_{FP1}^I is therefore 78.9 at $\lambda_0 = 317.6$ μm for this set of measurements, which is very close to the value \mathcal{R}_{FP1}^{FT} found with the conventional Fourier analysis.

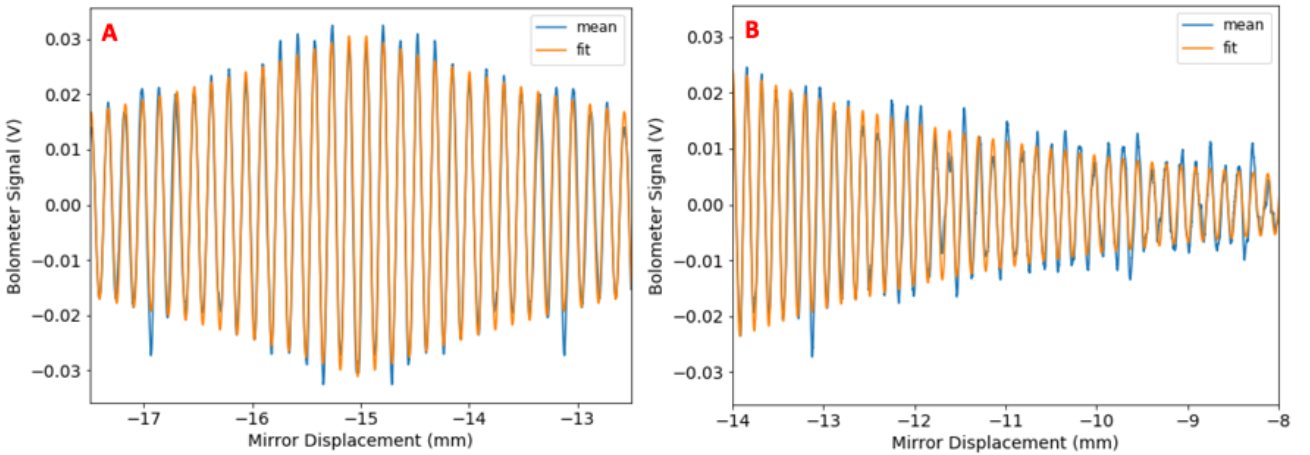


FIGURE 5.19: Results from FTS measurements of FP1 based on interferogram analysis : 8 interferograms have been used to compute an averaged interferogram. This interferogram is fitted to the interferogram expected for a Lorentzian spectrum. (A) and (B) correspond to the measured data and the fit over two different sections of the interferogram.

FP1 was the result of the assembling with four small silicon trapezoidal pieces to create each spacer

(see figure 5.7). This solution was a mean to rapidly test the multi-layer silicon FP, but the system has been improved now. However, despite a rather unstable stack (especially during the mounting), it must be mentioned that this etalon demonstrates already satisfying performance. FP2, because of the way it is built, will show better properties.

FP2 etalon

We now present the results obtained with the etalon FP2. In the following we use data of the experiment performed on the 6th of June.

Because the steps followed for the data processing have already been presented, we will not get into the details of the calculations. The methods are exactly the same as before and the important figures and fit parameters are shown here. The different steps of the Fourier analysis are shown in figure 5.20. For the fit with the Lorentzian function, we found the following parameters : $A = 0.98$, $\alpha = 1.11 \mu m^{-2}$, $\lambda_0 = 325.7 \mu m$. This gives a spectral resolution \mathcal{R}_{FP2}^{FT} of 172.1 at $\lambda_0 = 325.7 \mu m$.

The second method (interferogram fitting) deals directly with the interferogram. Results are presented in figure 5.21. The parameters of the interferogram fit are the following : $X = 0.1632$ mm, $x_0 = -15.1$ mm and $d = 9.30$. The resolution \mathcal{R}_{FP2}^I is therefore of 179.0 at $\lambda_0 = 326.4 \mu m$. Once again, the fits provided by the two methods are consistent.

As expected, the performance is far better for FP2 than for FP1, mainly for two reasons : spacer rings were made of monolithic pieces and every single layer of the FP2 has been selected for its flatness properties ($PV \leq 1 \mu m$). Furthermore, we can already discuss the discrepancy of the resonant wavelength for the two etalons. Indeed, the first one is at $\sim 317 \mu m$ while the other is close to $326 \mu m$. The shift in wavelength between etalon FP1 and etalon FP2 is probably due to the fact that two different wafers have been used to manufacture spacers, especially the one required for the FP cavity (the second wafer was most likely thicker). The nominal thickness of the small silicon sheets and spacers is very difficult to measure, especially because it is not constant over the whole wafer area. These small variations from one wafer to the other have increased the size of the cavity and this shows that the resonance of multi-layer silicon FPs as those of conventional FPs, can be tuned by scaling the cavity.

FP3 etalon

FP3 was tested on the 1st of July and the same analysis was applied to the data. Note that its measurement conditions were extremely advantageous and as a consequence, the data exhibit a very low-noise, as illustrated in figure 5.22. For the matching with the Lorentzian function, the fitting parameters : $A = 0.76$, $\alpha = 0.87 \mu m^{-2}$, $\lambda_0 = 322.1 \mu m$. The spectral resolution is therefore $\mathcal{R}_{FP3}^{FT} = 150.0$ at $\lambda_0 = 322.1 \mu m$.

The interferogram fitting is illustrated in figure 5.23 and parameters are : $X = 0.1614$ mm, $x_0 = -14.8$ mm and $d = 8.2$. Therefore we get $\mathcal{R}_{FP3}^I = 159.3$ at $\lambda_0 = 322.9 \mu m$.

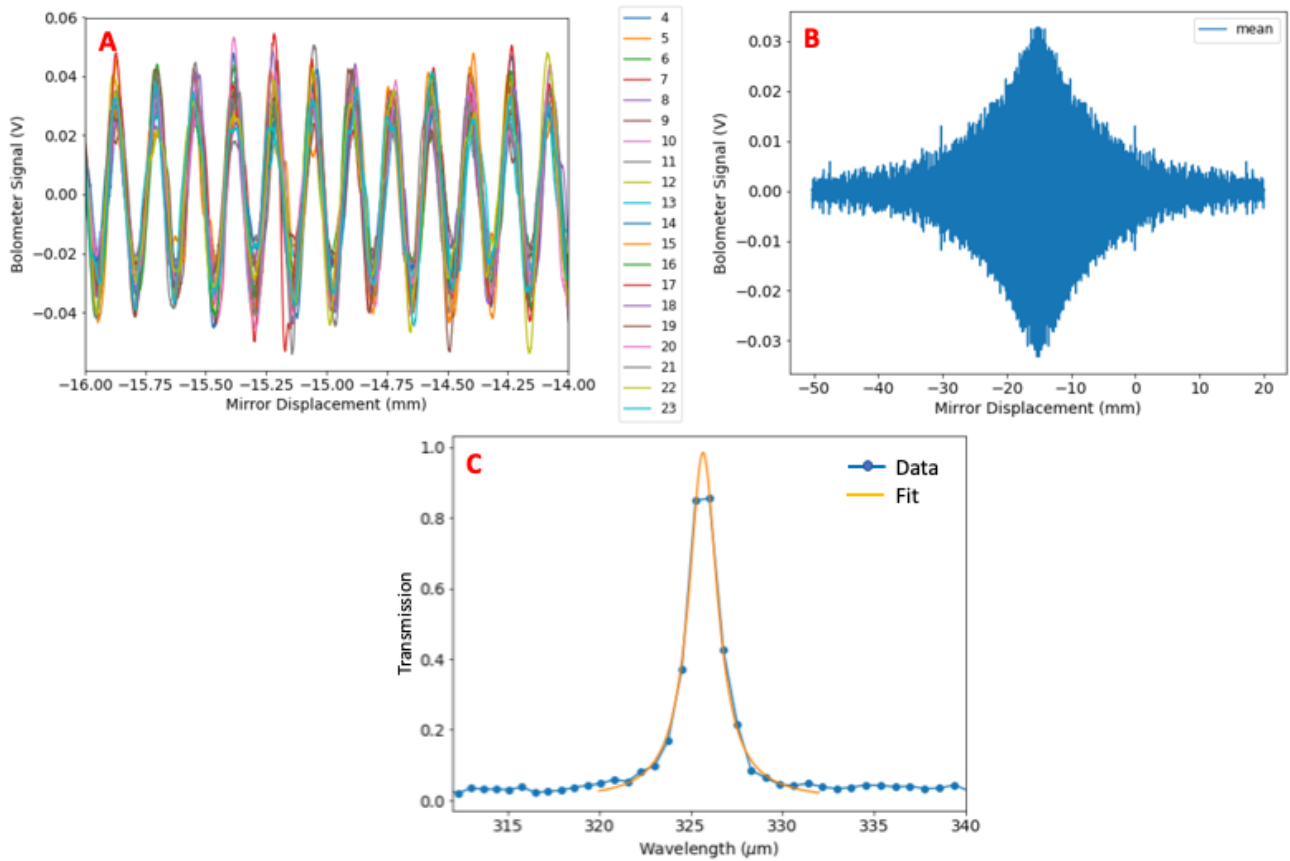


FIGURE 5.20: Results from FTS measurements of FP2 based on Fourier Transform analysis : (A) 20 interferograms have been selected for data processing, after drift and offset corrections, they are shown between ± 1 mm around the ZPD (the ‘central fringe’ is around -15 mm); (B) Averaged interferogram from the 20 measurements after correction for slow modulation and mirroring; (C) Computed transmission spectrum after Fourier Transform of the averaged interferogram and its Lorentzian fit.

Because the three-pad parts of the mechanical holders have been lapped to the sub-micron precision, it is surprising to observe that FP3 does not demonstrate better finesse performance than FP2. However, we should remind that for this etalon, we could not use homogeneous-quality silicon sheets and spacers (i.e. PV possibly greater than $1 \mu\text{m}$).

As a conclusion of this part about finesse measurements, we have demonstrated that our first FP prototypes made with multi-layer silicon plates have already reached high-finesse, close to the theoretical one (~ 215). The high resolving power of FP2 was not expected since we have shown in the first part of this chapter (section 5.1.2), that we could be limited to ~ 150 by the surface quality and by the parallelism of the silicon sheets and spacers. However, the characterization of the layers has always been done over the whole surface of samples. This might suggest that the quality of surface is far better where the light hits the etalon, i.e. on a 12 mm- diameter in the center of the etalon. Performance of the three tested etalons are summarized in table 5.1. Concerning the two methods used, the results from the two analyses are very consistent. Figure 5.24, presented here only for illustration purposes, highlights the difference in finesse of

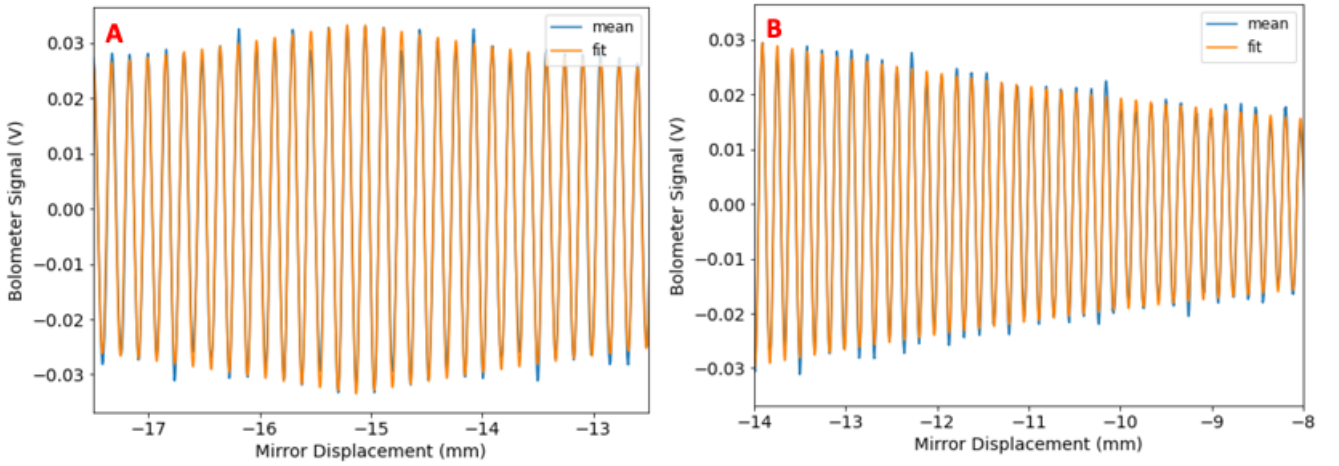


FIGURE 5.21: Results from FTS measurements of FP2 based on interferogram analysis : 20 interferograms have been used to compute an averaged interferogram. This interferogram is fitted to the interferogram expected for a Lorentzian spectrum. (A) and (B) correspond to the measured data and the fit over two different sections of the interferogram.

Etalon	Method 1 (Fourier transform analysis)		Method 2 (Interferogram analysis)	
	\mathcal{R}	λ (μm)	\mathcal{R}	λ (μm)
FP1	77.8 ± 0.2	316.9 ± 0.1	78.9 ± 0.1	317.6 ± 0.1
FP2	172.1 ± 1.0	325.7 ± 0.1	179.0 ± 0.1	326.4 ± 0.1
FP3	150.0 ± 0.2	322.1 ± 0.1	159.3 ± 0.1	322.9 ± 0.1

TABLE 5.1: Summary of the computed finesse and resonant wavelength, according to two different methods for the three etalons, with their corresponding error (derived from the variance of the fitting).

the three etalons by comparing their normalized interferogram.

From these measurements, we have learnt that the quality of the layers is essential for the overall performance of the interferometer. The intrinsic thickness of each layer should also be known. This last point has not been investigated enough in the time of this project and should be taken into consideration for the next prototypes.

5.2.3 Measuring the transmission of multi-layer silicon etalons

The efficiency, i.e. the maximal transmission, of the three etalons has not been discussed in the previous study. However, calculated transmission of each etalon has been shown on panel (C) in figure 5.18, 5.20 and 5.22. These results come from the conventional Fourier analysis. To derive the maximal transmission of the three prototypes, we have used the fit of the spectra, derived by Fourier transform of the interferograms presented above, and compare the maximum of the fit to the reference. Table 5.2 summarizes the measured transmission of FP1, FP2 and FP3 and compares them to their respective estimated transmission.

For now, we focus on the transmissions of FP1 and FP3 : respectively 41% and 76%. These numbers

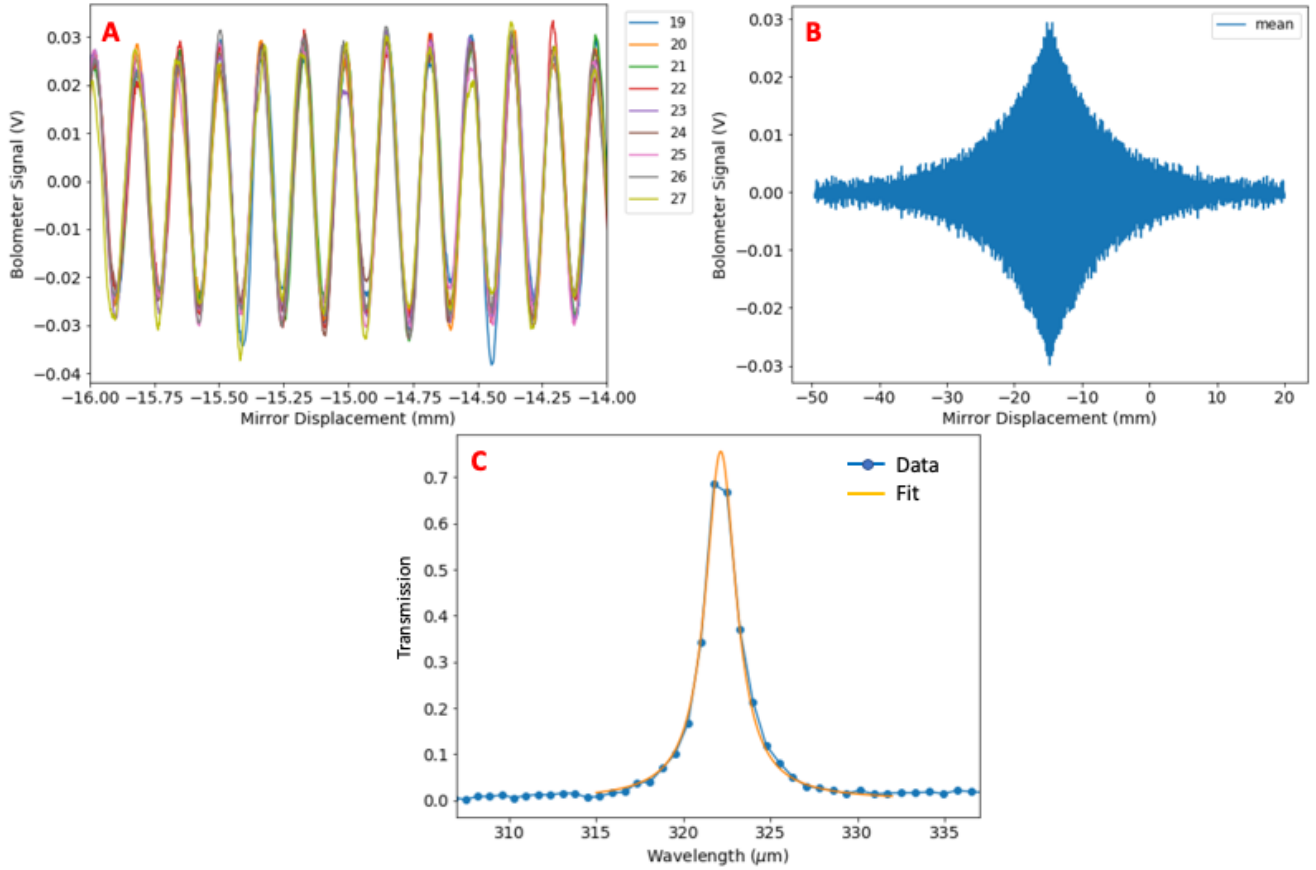


FIGURE 5.22: Results from FTS measurements of FP3 based on Fourier Transform analysis : (A) 9 interferograms have been selected for data processing, after drift and offset corrections, they are shown between ± 1 mm around the ZPD (the ‘central fringe’ is around -15 mm); (B) Averaged interferogram from the 9 measurements after correction for slow modulation and mirroring; (C) Computed transmission spectrum after Fourier Transform of the averaged interferogram and its Lorentzian fit.

should be interpreted with respect to their derived finesse : namely ~ 79 and ~ 150 (with the Fourier transform analysis). Indeed, we should understand that, assuming no diffraction and no walk-off (i.e. for a moderate finesse), the power which is transmitted through a FP is conserved. This means that if the etalon as built does not meet the specifications regarding parallelism and flatness, the 100% power expected at the resonant wavelength is re-distributed over a larger wavelength band (which makes the finesse lower). To check this with FP1 and FP3, we have first computed the total power received by an etalon with a finesse of ~ 200 at $\lambda \sim 320 \mu\text{m}$. This can be achieved by integrating the equation 5.2 with $A = 1$ and $\alpha = \frac{2\mathcal{R}}{\lambda}$ between 250 and 400 μm for example. Then, to find the maximal transmission of FP1 and FP3, we have modified the parameter A to reach the same total power with the resolving powers of 79 and 150. These short calculations provide very consistent results with respect to those measured : FP1 should transmit 40% of light and FP3 75%.

The case of FP2 is not that well-understood : if we computed the expected transmission for a finesse of ~ 172 , FP2 should transmit 86% of the light (and not 98%). The error on the measured result might

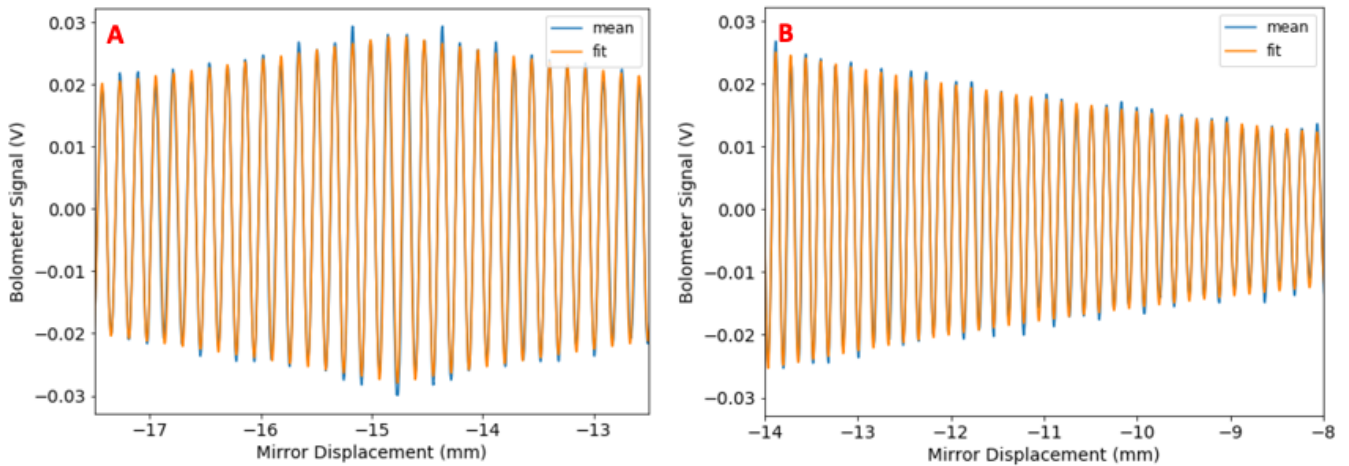


FIGURE 5.23: Results from FTS measurements of FP3 based on interferogram analysis : 9 interferograms have been used to compute an averaged interferogram. This interferogram is fitted to the interferogram expected for a Lorentzian spectrum. (A) and (B) correspond to the measured data and the fit over two different sections of the interferogram.

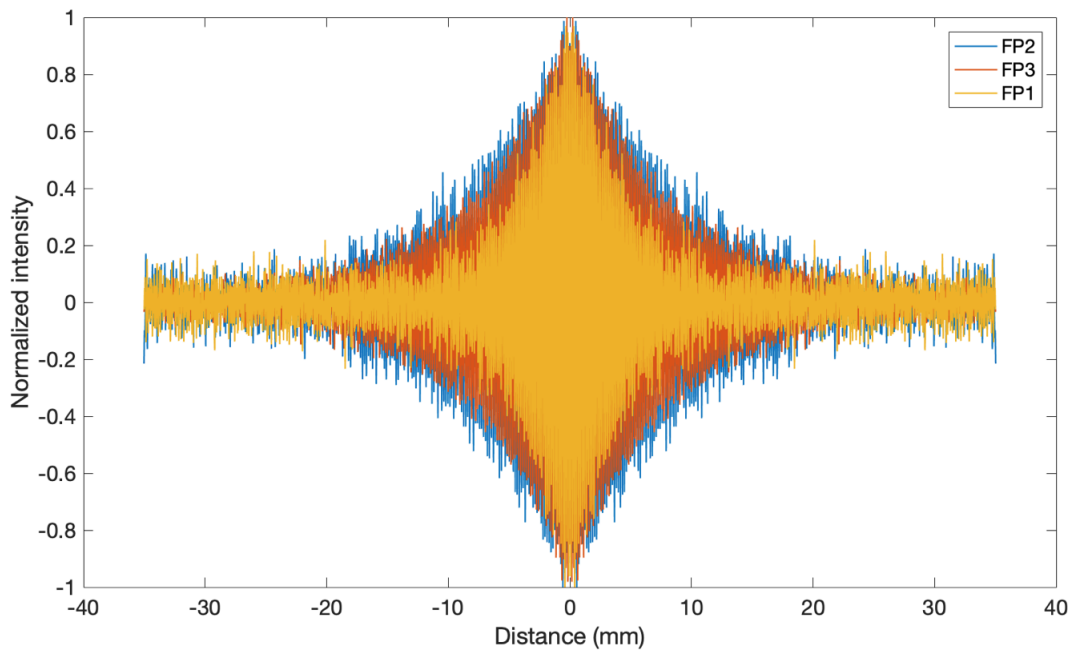


FIGURE 5.24: Normalized interferograms corresponding to the etalons FP1, FP2 and FP3. The figure highlights the difference of the decay rate experienced by the three FPs, which is related to the intrinsic finesse of each etalon.

come from the noise as well as external interference and instrumental drifts, especially for the reference which does not exhibit exactly the same spectrum in the three experiments. After analyzing the data, we understood that we should have taken more interferograms to have a less noisy reference spectrum but the signal coming from the etalons was so faint that we really payed attention to measure more etalon interferograms. For accurate transmission measurements, the quality of the reference spectrum also needs

Etalon	Measured transmission	Estimated transmission
FP1	0.41 ± 0.01	0.40
FP2	0.98 ± 0.01	0.86
FP3	0.76 ± 0.01	0.75

TABLE 5.2: Measured transmission of FP1, FP2 and FP3 etalons after data analysis (with their respective fitting error) compared to the estimated transmission.

to be ensured.

Despite the last result, we can still give an overall comparison of FPI based on dielectric mirrors (as measured) to FPI based on metallic mirrors. Figure 5.25, which is an adaptation of Douthit et al. (2018) with our measurements added, illustrates the differences in performance of the two kinds of FPIs. The noticeable result is that, with dielectric mirrors, FPIs can reach higher finesse without degrading their transmission, unlike metallic mirrors. Dielectric mirrors follow therefore a trend which is completely opposite to the behaviour of metallic mirrors. This result is explained by the fact that no observable fraction of light (within the accuracy of our test set-up) is absorbed with multi-layer silicon etalons. Thus, as the finesse becomes higher, the transmission does not fall off.

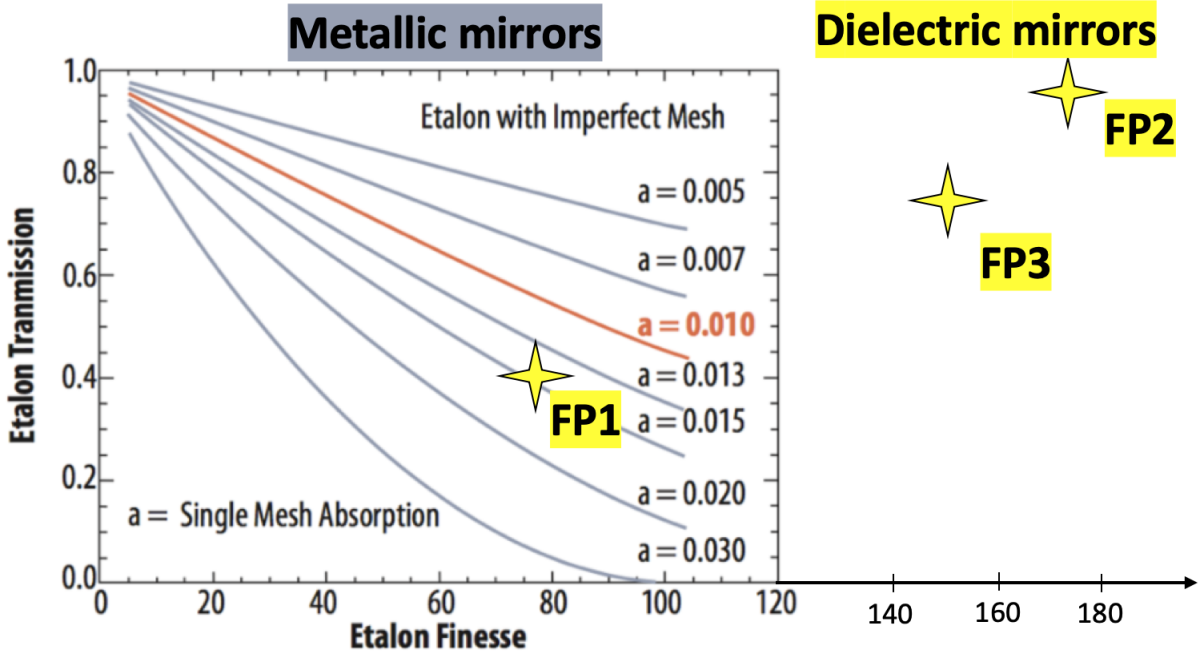


FIGURE 5.25: Adaptation from Douthit et al. (2018), where results from our measurements have been added. This figure compares the tendency of FPIs based on metallic mirrors (in grey and red) versus FPIs based on dielectric mirrors (in yellow). Unlike metallic FPIs, dielectric FPIs can reach high finesse while having high transmission : the tendency of dielectric FPIs is opposite to the one of metallic FPIs. This is only possible because the dielectric mult-layers do not exhibit any measurable absorption.

In this part, the influence of the temperature on the etalons has not been discussed because more measurements (at 300 K and 4 K, for comparison) have been performed only after this thesis. Thus, we do

not detail the measurements, but only describe the main findings, for the curiosity of the reader.

The results presented in this section have been obtained for etalons cooled down to 77 K. Since no absorption could be measured at this temperature, cooling down the etalons at lower temperature gave similar performance as at 77 K. The noticeable outcome was to observe that, at 300 K, the etalon has a similar behaviour than at lower temperature : the transmission and the finesse are both quite comparable. This result is remarkable since it shows that the high-resistivity silicon that we have used to assemble the etalons is sufficiently dielectric to prevent the system from any loss, even at warm temperature. It must also be mentioned that cooling down the system to 77 K and to 4 K has slightly shifted the resonant wavelength to lower wavelength, due to the contraction of the stack of layers.

5.3 A first step towards the coupling of the spectrometer to the bolometer

This section provides preliminary results from measurements performed at the very end of this thesis. The main purpose of this study was to demonstrate the enhancement of the absorption of the bolometer due to the Fabry Perot out of its natural spectral range, but also to exhibit a spectral capability from the coupled system, as theoretically expected (see section 4.2.4).

Sample to test

For this experiment, CEA/LETI provided us a “dummy” detector, made of a quarter-wave cavity of quartz (SiO_2), being 13- μm thick, on which a titanium nitride layer has been deposited to act as the absorbing element of the detector. This thin layer has a free-space matched impedance, which should enable it to absorb almost 100% of light at the wavelength defined by four times the size of the quarter-wave cavity ($\lambda_{cav} = 104 \mu\text{m}$ here). Figure 5.26 shows a picture of the dummy detector. On this sample, we have added an etalon with a finesse of ~ 180 , which works at $\lambda_{FP} \sim 320 \mu\text{m}$. The whole stack is absorbing at $\sim 320 \mu\text{m}$ assuming we separate the absorber from the etalon by a distance of $\sim 160 \mu\text{m}$, as described by figure 4.25. This has been achieved by interleaving two silicon spacers between the dummy detector and the etalon (illustration in figure 5.27).

Measurement set-up

In order to test the coupled system (i.e. the etalon coupled to the dummy bolometer), a different measurement set-up from the one used so far for transmission measurements, was required. In this configuration, the sample cryostat is used only for filtering while the bolometer cryostat has been totally rearranged (see figure 5.28). The idea is to perform measurements of the absorption of the samples by reflection. The bolo-



FIGURE 5.26: Dummy detector made by CEA/LETI for the coupling measurements : the detector is a quarter-wave cavity of quartz with a free-space impedance matched absorber deposited on its surface. The quarter-wave cavity is 13- μm thick and thus, the detector is optimized for wavelength $\sim 100 \mu\text{m}$.

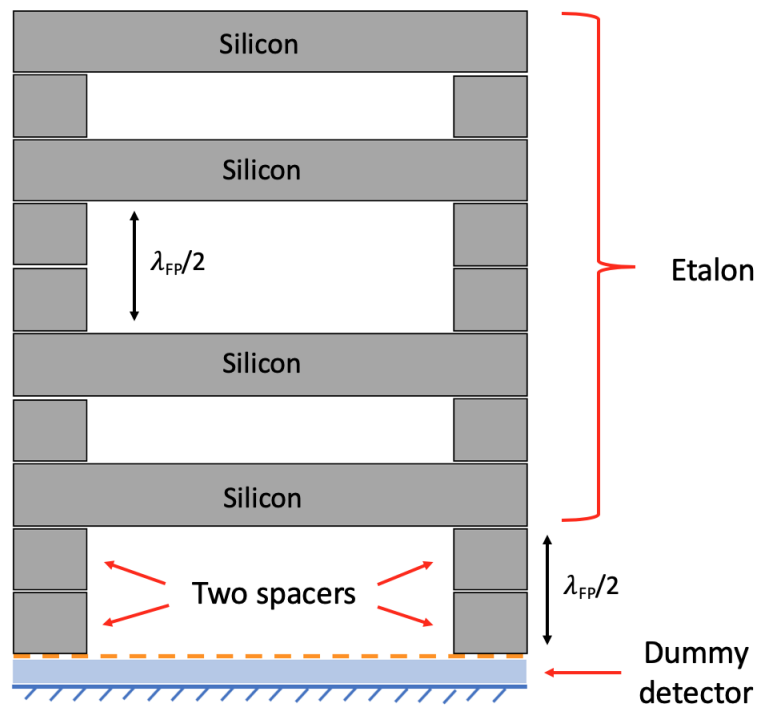


FIGURE 5.27: Scheme of the overall stack to test the coupling detector/etalon : two silicon spacers are used to separate the absorber from the etalon by a distance of $\lambda_{FP}/2$, as suggested by figure 4.25.

meter is thus no longer at the entrance of the cryostat, but the beam undergoes several reflections within the cryostat before feeding the horn of the bolometer. A revolving plate, which is thermally linked to the evaporator, has been introduced in order to switch between a reference (i.e. a mirror) and the sample to test. The motion from one position to the other is possible by the magnet attached to the revolving plate

and by external Helmholtz coils. That way, the reflection from the sample is compared to the reflection from the reference mirror and the power absorbed by the sample can be derived.

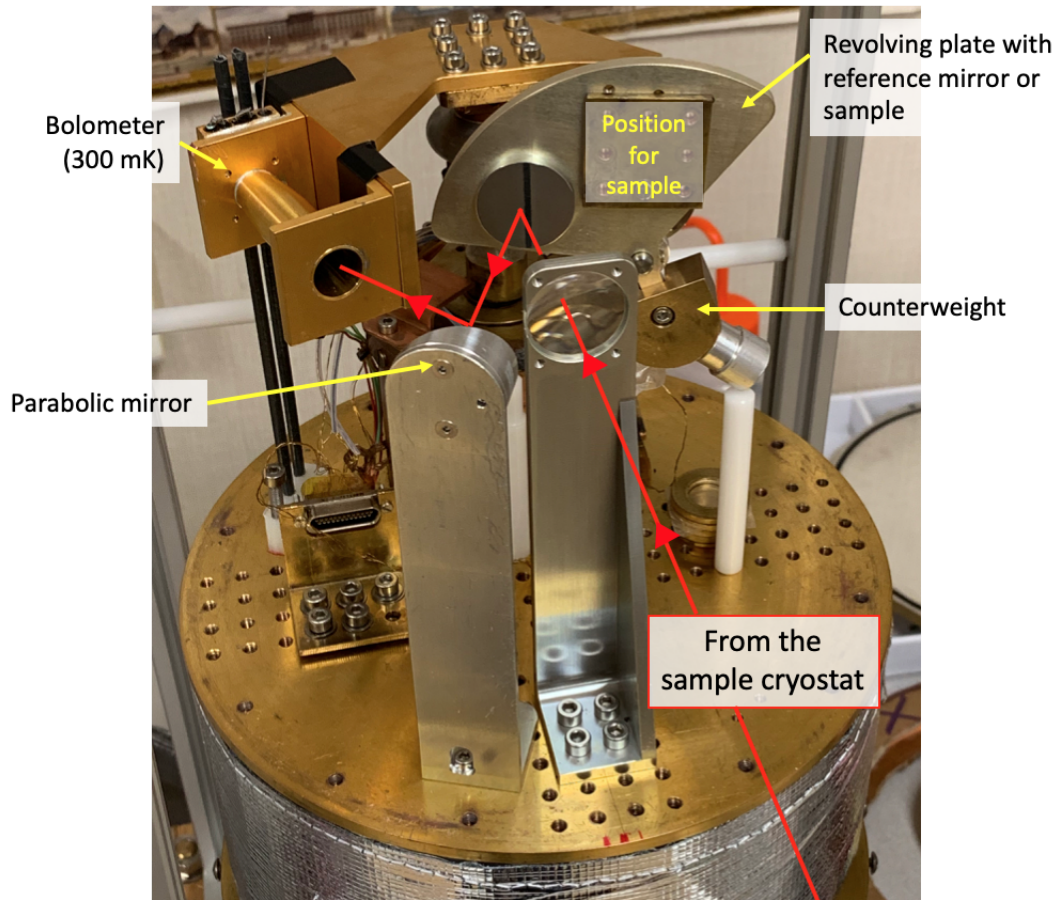


FIGURE 5.28: Internal configuration of the bolometer cryostat for reflection measurements. The light coming from the sample cryostat is reflected either on the reference mirror or the sample to test and then feeds the horn of the bolometer. The plate which carries the mirror and the sample can be rotated by a magnet attached to it (not visible on the picture) and by external Helmholtz coils.

Results

Measurements have therefore been performed with the sample being cooled down to 300 mK. First, we have measured the absorption of the bare detector alone on a large spectral band, the result is shown in figure 5.29. At $\sim 320 \mu\text{m}$, the detector is not very efficient as it absorbs about 15 % of light.

In a second measurement, we have mounted the coupled system by assembling the etalon to the detector, as described in figure 5.27, and compared the reflection from the coupled system to the one from the reference mirror. Figure 5.30 presents the absorption of the whole stack. We indeed observe a spectral pattern at $\sim 320 \mu\text{m}$; however, this ‘peak’ seems lower and wider than expected. The angle under which the beam hits the sample is probably responsible for this degradation of the spectral element. A new design of the optical train would mandatorily be needed for better performance measurements and has not been

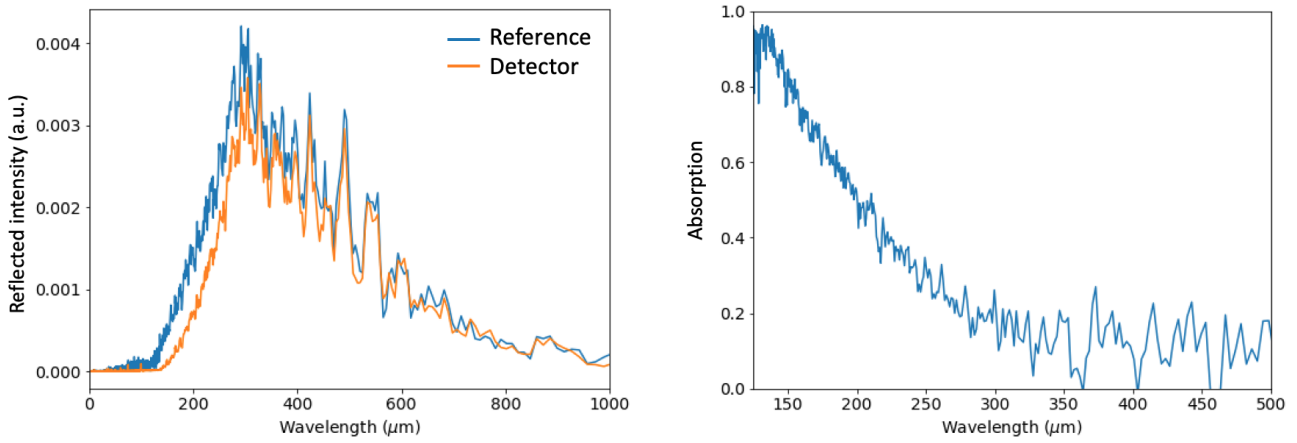


FIGURE 5.29: Measurements of the absorption of the dummy detector alone. (Left) Comparison of the reflected intensity from the reference and from the detector. (Right) Derived absorption of the bare detector.

investigated in the time of this thesis.

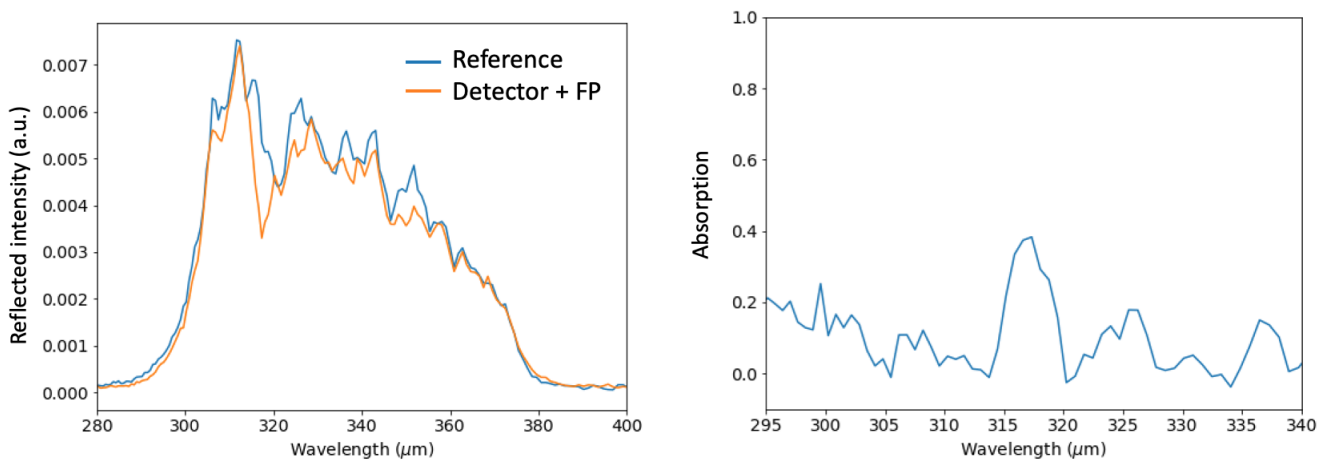


FIGURE 5.30: Measurements of the absorption of the dummy detector coupled to the etalon (finesse of ~ 180). (Left) Comparison of the reflected intensity from the reference and from the coupled system. (Right) Derived absorption of the coupled system.

5.4 Conclusions of the chapter and perspectives for the future experiments

This chapter has allowed us to experimentally verify the spectral properties of the multi-layer silicon FP that we developed in chapter 4. For this purpose, we have first demonstrated that it was possible to manufacture silicon layers with a peak-to-valley global flatness of less than $1.8 \mu\text{m}$ for every sample, and better than $1 \mu\text{m}$ for some of them. We also observed the lack of measurable wedge for the whole set of silicon layers (full sheets and spacers). These very promising geometric properties were finally confirmed by the finesse measurements. Building a FP from scratch is a way to identify, step by step, all the critical issues and to investigate innovative solutions such as the laser jet technology for designing the rings in silicon. After assembling the layers according to the model proposed by the Bragg mirror theory, we obtained three etalons to test. We could validate the simulations by measuring the transmission of the FP etalon, without being narrow-band filtered, with a warm TDS. Indeed, the model and the measurement showed almost perfect agreement over a large wavelength band. Furthermore, to be able to resolve the transmitted peak of the etalon at cold temperature, we used our cryogenic Martin-Puplett interferometer. This spectrometer has a sufficiently high spectral resolution, such that it can resolve spectral features with resolution less than 200 at $320 \mu\text{m}$, which is suitable for our experiment. We have chosen, nonetheless, to use two different analyses (one based on conventional Fourier transform, the other on the direct fit of interferograms) from which we have derived consistent results. The finesse of the three etalons built ranges from ~ 90 to 180, which is not that far from the 215 theoretical finesse. This study has, in particular, demonstrated that the quality of the layers used is very critical and that special care should be given when selecting any silicon layer for the whole assembly. In addition, the nominal thickness of the layers should be perfectly known since this can lead to a shift in wavelength, as we have experienced. Finally we have demonstrated that there is no measurable absorption in a multi-layer silicon FP at 77 K (nor at 300 K or 4 K). In particular, the maximal transmission is improved with increasing finesse and the etalons follow quite well this rule of thumb.

Preliminary results about the coupling of the spectrometer to the detector have been presented at the end of this chapter. They could be refined by improving the experimental set-up for these particular measurements. In the end, we aim at obtaining the spectral response of a notch filter with a 0% reflection around $320 \mu\text{m}$. This experiment is meant to demonstrate how a resonantly coupled FP/detector system can significantly enhance the absorption efficiency. Lastly, in the longer term, we would like to implement a cryo-mechanism that will introduce the possibility of tuning the cavity and therefore the scanning of the spectrum.

Conclusion and perspectives

Detectors with capabilities extended beyond the simple photometer are currently emerging. This thesis is focused on the development of new detectors that integrate polarimetric and spectroscopic capabilities within the detector array.

In the frame of my thesis, I had the opportunity to join the SPICA consortium at a time where everything still needed to be defined and where there was room for improvement. Polarimetric pixels have been designed for the B-BOP instrument. This instrument finds its main origin in results of the PLANCK and HERSCHEL missions which showed that the magnetic field and the evolution of filaments within star-forming regions are probably correlated. In order to map the field lines with enough sensitivity and with a greater angular resolution than PLANCK, the B-BOP arrays, cooled down to 50 mK, present a specific configuration. Indeed, the thermometers and the absorbers are designed such that each pixel is sensitive to two orthogonal polarizations of the light. In this thesis, I worked on the optimization of this design, especially the dipole antennae as it is the transducer of the electromagnetic wave. For this, I ran simulations representing the illumination of the detector by a polarized electromagnetic wave. The goal of this study was to extract characteristic values for the dimensions of the absorbers. We found out, for example, that the optimal length of dipole antennae, in a large network, is $\sim \lambda/3$. We also understood that, conversely to the usual need for matching the free-space impedance Z_0 , the optimal impedance for the absorbers is different ($\sim Z_0/2$). This is explained by the fact that the quarter-wave cavity is made of silicon oxide whose refractive index ($n = 2$) is different from the refractive index of vacuum/air and that the absorber is not a full sheet, but a structured absorber embedded in a network. In addition, the cross-polarization has been minimized and, for the design chosen for the final B-BOP detectors, estimated to be less than 0.1 %. This work, derived for the shortest wavelength detector assembly, has been extended to the two other focal planes of B-BOP. Lastly, I have used an already proven solution, to adapt the absorption of the 100 μm detector to the 200 μm and 350 μm bands. This work has enabled us to optimize the geometry of the pixels

which are currently under manufacture. Experimental characterization of the polarimetric detectors still needs to confirm these results, especially concerning the cross-polarization (critical point for the scientific mission).

The second part of this thesis deals with the implementation of the spectroscopic capability at the detector level. After evaluating which solution could be more likely used, without the need for redesigning the whole detector, I oriented our research towards Fabry-Perot interferometry (FPI). A Fabry-Perot (FP), set in a collimated beam, can be compatible with imaging assuming some converging optical elements focus the light on the detector array. However here, the idea was to bring the spectrometer very close (of the order of wavelength) to the detector to build a new interferometer. Before studying the coupling of the FP to the detector, we focused on the spectrometer and decided to initiate at CEA, in collaboration with LETI, the development of FP made only with high-resistivity silicon mirrors. This overcomes the issue of absorption experienced by state-of-the-art FPs in the far-infrared field. Later, to improve the intrinsic finesse of the spectrometer, we investigated the use of multi-layer silicon mirrors following the Bragg mirror theory. The result is that the finesse increases rapidly with a small number of layers, especially because of the high refractive index of silicon (as compared to the refractive index of vacuum/air). We chose a three-layer mirror configuration which leads to a theoretical finesse of 215. In this study, a strong coupling between the FP and the detector which is due to the impedance matching of the two optical cavities (created by the FP mirrors and the mirror of the detector backshort cavity) has also been demonstrated. This coupling enables the whole interferometer to absorb almost 100% of light, even far from the initial working range of the detector. Finally in this theoretical study, we demonstrated that a FPI with a finesse of 150 at $\sim 160 \mu\text{m}$ could be used in the focus of a focal plane without degrading too much the spatial and the spectral properties of the whole system.

The experimental work initiated at CEA started with the characterization of silicon layers made for the mirrors and the FP cavity. The samples showed already flatness performance that is close to the requirements for the range of finesse expected. First measurements, at warm temperature, enabled us to validate the model which has driven the manufacture of the FPI. Then, measurements at 77 K were performed and demonstrated that, assuming the selection of silicon layers with sufficient flatness, the multi-layer silicon FPI can reach finesse of 180 (and thus a spectral resolution of 180 at first order), close to the targeted 215. The same analysis has proved, at 77 K but also at warmer temperature, that high-resistivity silicon is a lossless material at sub-millimeter wavelengths. Indeed, the different etalons that we tested have a maximal transmission which increases with finesse and this result is not compatible with absorption by

the mirrors. The following step of this experimental study was to characterize the coupled system (i.e. the FP coupled to the detector) in order to compare its performance with the one predicted by the theory. We expect that the resonantly coupled FP/detector system can significantly enhance the absorption efficiency while adding the spectral capability to the detector. This work initiated at the very end of this thesis has already shown promising results although the experimental set-up should be adapted for more accurate measurements. Lastly, in the long term, we would like to build a 'real' spectrometer by introducing the tunability of the cavity with a cryo-mechanism.

This last thesis topic gave me the chance to lead a project from scratch. If the initial concept of the "on-chip spectrometer" was my idea, the manufacture and the characterization of the prototype has been a full team work. We have still some way to go before having a real cryogenic spectro-imager but the first experimental results have already demonstrated promising properties of the multi-layer silicon mirrors. For example, the dielectric FPs that we built could already improve the overall transmission of instruments using several FPs in series by a factor of 2 (and therefore reduce the observing time by the same factor). This also shows that progresses in micro-technologies facilitate the evolution towards integrated instruments.

Appendix A

Derivation of the Airy formula for Fabry Perot interferometry

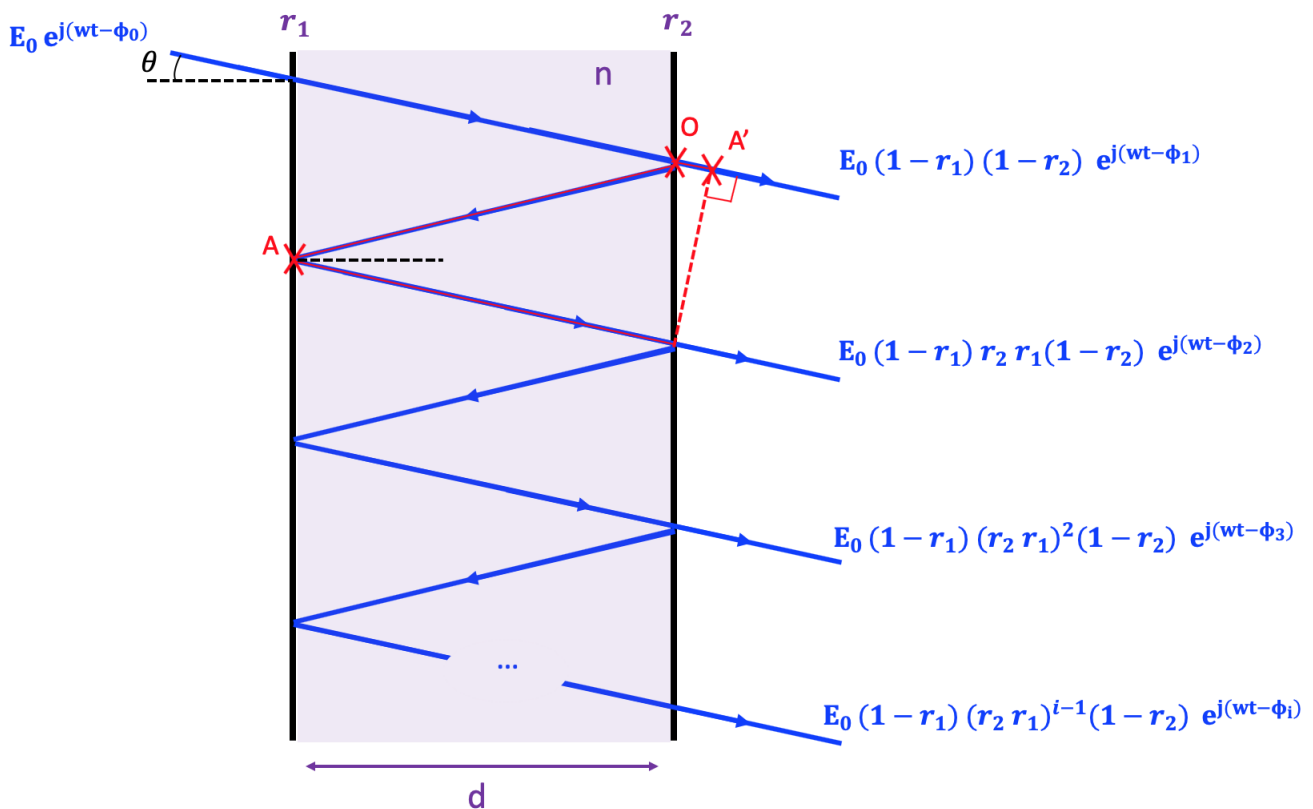


FIGURE A.1

Here we aim at deriving the Airy formula from electric field calculations to describe a multi-wave interferometer such as the Fabry-Perot Interferometer.

The transmitted wave intensity I can be computed from the transmitted electric field vector \vec{E} :

$$I = \vec{E} \cdot \vec{E}^* \quad (\text{A.1})$$

where $\vec{E} = \sum_{i=1}^{\infty} E_i \vec{u}_i$, \vec{u}_i being the unitary vector that stands for the direction of E_i . One now calculate the first outgoing waves E_1 , E_2 and E_3 :

$$E_1 = E_0 e^{j(\omega t - \phi_1)} = E_0 (1 - r_1) (1 - r_2) e^{j(\omega t - \phi_1)} \quad (\text{A.2})$$

$$E_2 = E_0 (1 - r_1) r_2 r_1 (1 - r_2) e^{j(\omega t - \phi_2)} \quad (\text{A.3})$$

$$= E_0 (1 - r_1) (r_2 r_1)^1 (1 - r_2) e^{j(\omega t - \phi_2)} \quad (\text{A.4})$$

$$E_3 = E_0 (1 - r_1) r_2 r_1 r_2 r_1 (1 - r_2) e^{j(\omega t - \phi_3)} \quad (\text{A.5})$$

$$= E_0 (1 - r_1) (r_2 r_1)^2 (1 - r_2) e^{j(\omega t - \phi_3)} \quad (\text{A.6})$$

where $I_0 = |E_0|^2$ stands for the intensity of the incident wave, r_1 and r_2 are the reflection coefficient ($R = |r|^2$ with R the power reflection coefficient) of the reflective surfaces (1) and (2) respectively and ϕ_i corresponds to the phase associated to the electric field E_i . These examples allow one to find the general relationship for any transmitted electric field :

$$E_i = E_0 (1 - r_1) (r_2 r_1)^{i-1} (1 - r_2) e^{j(\omega t - \phi_i)} \quad (\text{A.7})$$

As \vec{u}_i is the same for any electric field vector \vec{E}_i :

$$E = \sum_{i=1}^{\infty} E_i \quad (\text{A.8})$$

$$= E_0 (1 - r_1) (1 - r_2) \sum_{i=1}^{\infty} (r_1 r_2)^{i-1} e^{j(\omega t - \phi_i)} \quad (\text{A.9})$$

Calculations of any phase delay ϕ_i with respect to ϕ_1 the phase delay of \vec{E}_1 :

$$\phi_i = (\phi_i - \phi_{i-1}) + (\phi_{i-1} - \phi_{i-2}) + \dots + (\phi_2 - \phi_1) + \phi_1 \quad (\text{A.10})$$

$$= (i - 1) \Delta\phi + \phi_1 \quad (\text{A.11})$$

$$(\text{A.12})$$

where $\Delta\phi = \frac{2\pi}{\lambda} \delta$ with the optical path difference $\delta = 2OA - OA' = 2n \frac{d}{\cos \theta} - 2nd \frac{\sin^2 \theta}{\cos \theta} = 2nd \cos \theta$.

Therefore, $\Delta\phi = \frac{4\pi}{\lambda}nd \cos \theta$ and we have :

$$\phi_i = (i - 1) \times \frac{4\pi}{\lambda}nd \cos \theta + \phi_1 \quad (\text{A.13})$$

One can insert this expression in equation A.9 :

$$E = E_0 (1 - r_1) (1 - r_2) e^{j(\omega t - \phi_1)} \sum_{i=0}^{\infty} (r_1 r_2 e^{-j \frac{4\pi}{\lambda}nd \cos \theta})^i \quad (\text{A.14})$$

Since R_1 , R_2 and the complex exponential are all less than 1 in modulus, we can apply the result on geometric series :

$$E = E_0 (1 - r_1) (1 - r_2) e^{j(\omega t - \phi_1)} \frac{1}{1 - r_1 r_2 e^{-j \frac{4\pi}{\lambda}nd \cos \theta}} \quad (\text{A.15})$$

Using this equation to calculate the transmitted wave intensity, we obtain :

$$I = \vec{E} \cdot \vec{E}^* \quad (\text{A.16})$$

$$= \frac{E_0^2 (1 - r_1)^2 (1 - r_2)^2}{(1 - r_1 r_2 e^{-j \frac{4\pi}{\lambda}nd \cos \theta}) \times (1 - r_1 r_2 e^{+j \frac{4\pi}{\lambda}nd \cos \theta})} \quad (\text{A.17})$$

$$= \frac{E_0^2 (1 - r_1)^2 (1 - r_2)^2}{1 + (r_1 r_2)^2 - 2r_1 r_2 \cos(\frac{4\pi}{\lambda}nd \cos \theta)} \quad (\text{A.18})$$

$$= \frac{E_0^2 (1 - r_1)^2 (1 - r_2)^2}{1 + (r_1 r_2)^2 - 2r_1 r_2 + 4r_1 r_2 \sin^2(\frac{2\pi}{\lambda}nd \cos \theta)} \quad (\text{A.19})$$

$$(\text{A.20})$$

Fresnel equations give $r_1 = -r_2$ assuming that r_1 corresponds to the reflection amplitude at the interface A/B and r_2 is the reflection amplitude at the interface B/A. One also has : $|r_1|^2 = |r_2|^2 = |r|^2 = R$:

$$I = \frac{I_0 (1 - R)^2}{1 + R^2 - 2R + 4R \sin^2(\frac{2\pi}{\lambda}nd \cos \theta)} \quad (\text{A.21})$$

$$= \frac{I_0 (1 - R)^2}{(1 - R)^2 + 4R \sin^2(\frac{2\pi}{\lambda}nd \cos \theta)} \quad (\text{A.22})$$

$$= \frac{I_0}{1 + \frac{4R}{(1 - R)^2} \sin^2(\frac{2\pi}{\lambda}nd \cos \theta)} \quad (\text{A.23})$$

$$(\text{A.24})$$

The transmission T is :

$$T = \frac{1}{1 + \frac{4R}{(1-R)^2} \sin^2(\Delta\phi/2)} \quad (\text{A.25})$$

where $\Delta\phi = \frac{4\pi}{\lambda} nd \cos \theta$

Appendix B

Solution based on micro-structured silicon

Here, we present the detailed study based on the use of micro-structured silicon as the low-refractive index material for the multi-layer silicon FPI described in chapter 4. This solution has not been finally selected, for a question of time.

In a first attempt, we chose to use micro-structured silicon as the low refractive index material (L) in combination with bulk silicon for the high refractive index material (H). The micro-structures in the silicon are obtained by Deep Reactive-Ion Etching (DRIE) which is used to drill periodic holes in the material. The hole dimensions should be well below the wavelength in order to have an effectively homogeneous medium as seen by the wave. With the silicon etching, a material with a refractive index between that of air and the one of silicon is generated. The resulting refractive index can be controlled by adjusting the volume fraction of silicon with respect to air. This method has already been investigated by other groups for antireflective coating or for all-silicon multi-layer interference filters (Makitsubo et al. (2017); Defrance et al. (2018) for example). In the case of antireflective layers, the micro-structured silicon limits the reflection experienced by the wave on the silicon due to its high value of refractive index. CEA/LETI has also produced micro-structured silicon in the frame of the development of THz detector arrays for applications other than astronomy. One silicon window with micro-structured antireflection layer is presented in figure B.1, with a zoom on the etched holes. The refractive index of the structured silicon has been measured to be ~ 1.4 , which corresponds to holes slightly bigger than what were initially planned ($16.35 \times 16.35 \mu\text{m}$).

The idea was to braze two of these windows face to face and to etch the silicon (on the opposite side of the wafer) to $16 \mu\text{m}$. The mirror follows therefore a (HLH) configuration with (H) being the bulk silicon and (L) being the two micro-structured silicon layers facing each other and with a small spacing between them (see red marks in figure B.2, left).

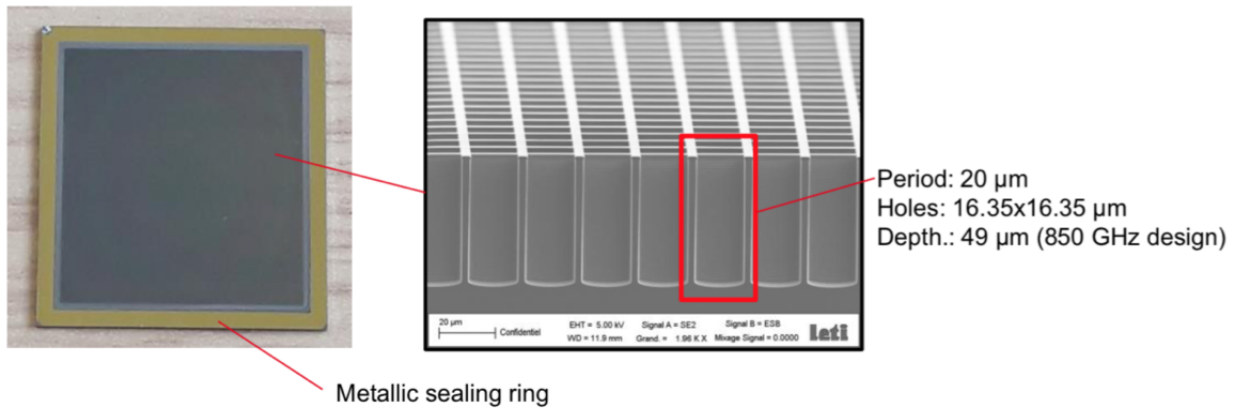


FIGURE B.1: Silicon window with micro-structured antireflection layer for THz detectors produced at CEA/LETI. The silicon window is 25.5 x 27 x 0.725 mm and the dimensions of the holes are specified on the legend of the photo (credit LETI)

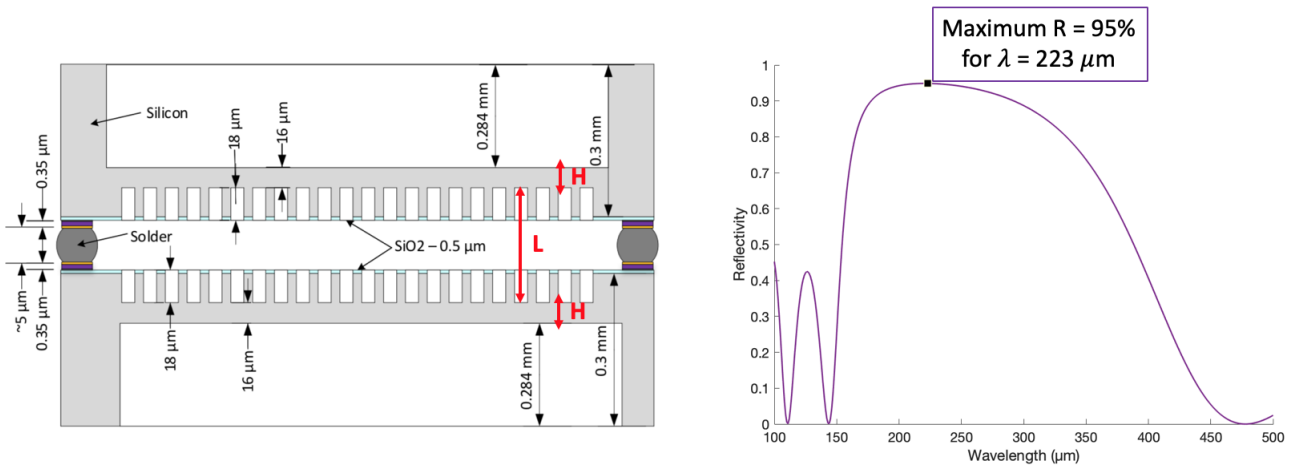


FIGURE B.2: (Left) Sketch of one mirror obtained by brazing two silicon windows with micro-structured antireflection layer and then etching the other extremity of the wafer to 16 μm . The (L) layer is formed by the two structured silicon layer interleaved by a vacuum gap. Note that the drawing is not to scale; (right) Computed reflectivity obtained for the corresponding mirror, the maximum reflectivity $R = 95\%$ is at $\lambda = 223\ \mu\text{m}$.

As it has already been mentioned, the wavelength range has evolved with the different solutions studied throughout this research project. By using the “off the shelf” micro-structured silicon, the optimized wavelength is $\lambda = 223\ \mu\text{m}$, which can be considered as sufficiently close from our initial objective (the C^+ line at 158 μm) for a first prototype. The computed reflectivity is plotted in figure B.2 (right) : it reaches 95% for $\lambda = 223\ \mu\text{m}$.

Figure B.3 presents the FPI that could be created by assembling two mirrors . The distance between the two mirrors arises from the silicon walls that should be etched to form the right cavity size ($D = 334\ \mu\text{m}$ on the sketch). For $\lambda = 222\ \mu\text{m}$, it corresponds to $\frac{3\lambda}{2}$. The whole stack has a maximal transmission of 100% at $\lambda = 222\ \mu\text{m}$ with a resolution of ~ 200 in third order, which gives a finesse of ~ 70 . This solution

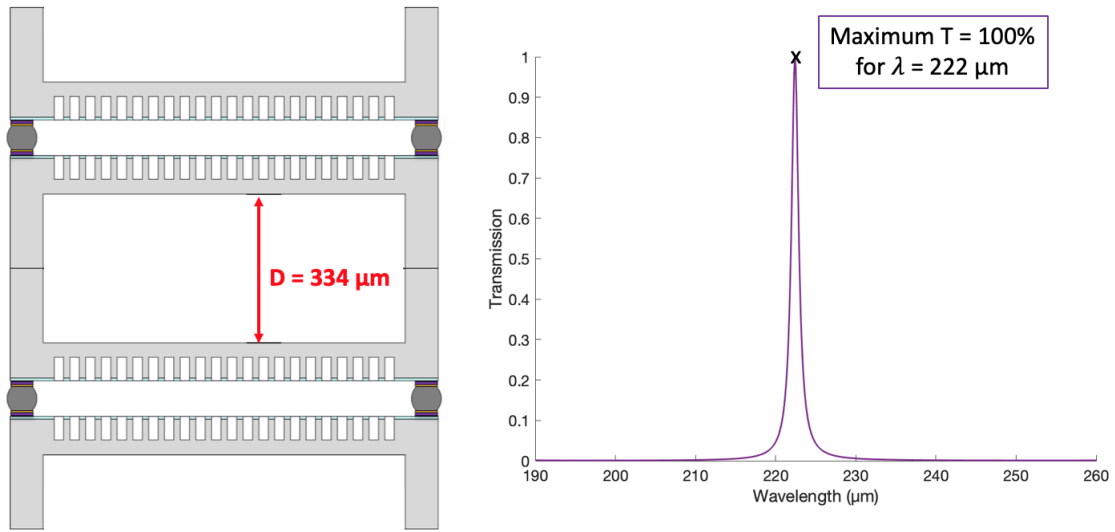


FIGURE B.3: (Left) Sketch of the whole stack that forms the FPI : two mirrors (as described by figure B.2) are separated by a distance $D = 334 \mu\text{m}$, that corresponds to $\frac{3\lambda}{2}$ at $\lambda \sim 222 \mu\text{m}$. This distance would be obtained by etching the silicon walls; (right) Computed transmission obtained for the corresponding FPI, the etalon is 100% efficient at $\lambda = 222 \mu\text{m}$.

has been studied in detail since it presents several advantages. The first one is that the micro-structured silicon was available off the shelf which means that no development would have been required for this if we accept the resonant wavelength to be $\lambda = 222 \mu\text{m}$ for the first prototype. In further experiments, we would have needed to adapt the design of the FPI to our application to avoid, for example, the silicon walls that constrain the cavity size. However the possibility to modify the value of the refractive index of the layer (L) by tuning the volume ratio of silicon to air gives the opportunity to scale the design to the need. Another strong advantage is that the whole FPI would have been only made of silicon. This implies that we avoid any issue due to different coefficients of thermal expansion (CTE) since we plan to work at 4 K. The all-silicon structure should also not present strong losses due to the many bounces in the FPI as we aim at using HRFZ silicon (still to be experimentally demonstrated). In short, the FPI solution based on micro-structured silicon looks very promising, but in the frame of this thesis, we had to move on to something simpler that came with less technological issues. One of the main issue that we had to deal with was the deep etching of the wafer to $16 \mu\text{m}$ which was not straightforward. In addition, such a thin layer, if the etching succeeded, would have made each individual silicon window very fragile. For this reason, we decided to move to another design, where we no longer use micro-structured silicon, although we should continue to investigate this solution.

Appendix C

CMB bands defined by the LiteBIRD mission

	Type	Center Frequencies [GHz]	BW	Low [GHz]	High [GHz]	Num. of wafers	TES channels	
							Opt/wf	Total
LFT 34 - 161 GHz	1	40	0.30	34	46	3	14	42
		60	0.23	53	67	3	14	42
		78	0.23	69	87	3	14	42
	2	50	0.30	43	58	4	14	56
		68	0.23	60	76	4	14	56
		89	0.23	79	99	4	14	56
	3	68	0.23	60	76	3	38	114
		89	0.23	79	99	3	38	114
		119	0.30	101	137	3	38	114
	4	78	0.23	69	87	3	38	114
		100	0.23	89	112	3	38	114
		140	0.30	119	161	3	38	114
HFT 89 - 448 GHz	5	100	0.23	89	112	3	74	222
		140	0.30	119	161	3	74	222
		195	0.30	166	224	3	74	222
	6	119	0.30	101	137	2	74	148
		166	0.30	141	191	2	74	148
		235	0.30	200	270	2	74	148
	7	235	0.30	200	270	1		
		337	0.30	286	388	1	338	338
8	280	0.30	238	322	1	338	338	
	402	0.23	356	448	1	338	338	
Total								3102
LFT								978
HFT								2124

FIGURE C.1: CMB bands defined by the LiteBIRD mission (Hazumi, 2018)

Appendix D

Calculation of the spectral and spatial effects of a Fabry Perot located in the focus of a beam for different nominal finesses.

This appendix follows the section 4.2.4 which aims at describing the behavior of a Fabry Perot interferometer (FPI) located in the focus of a beam. The following results estimate the degradation of the full width at half maximum (FWHM) of the beam after travelling through the Fabry Perot and quantify the degradation in finesse due to the focus for different nominal finesses. The motivation for these figures was to give a more general trend of the effects of a FPI, compared to the single case presented in the thesis.

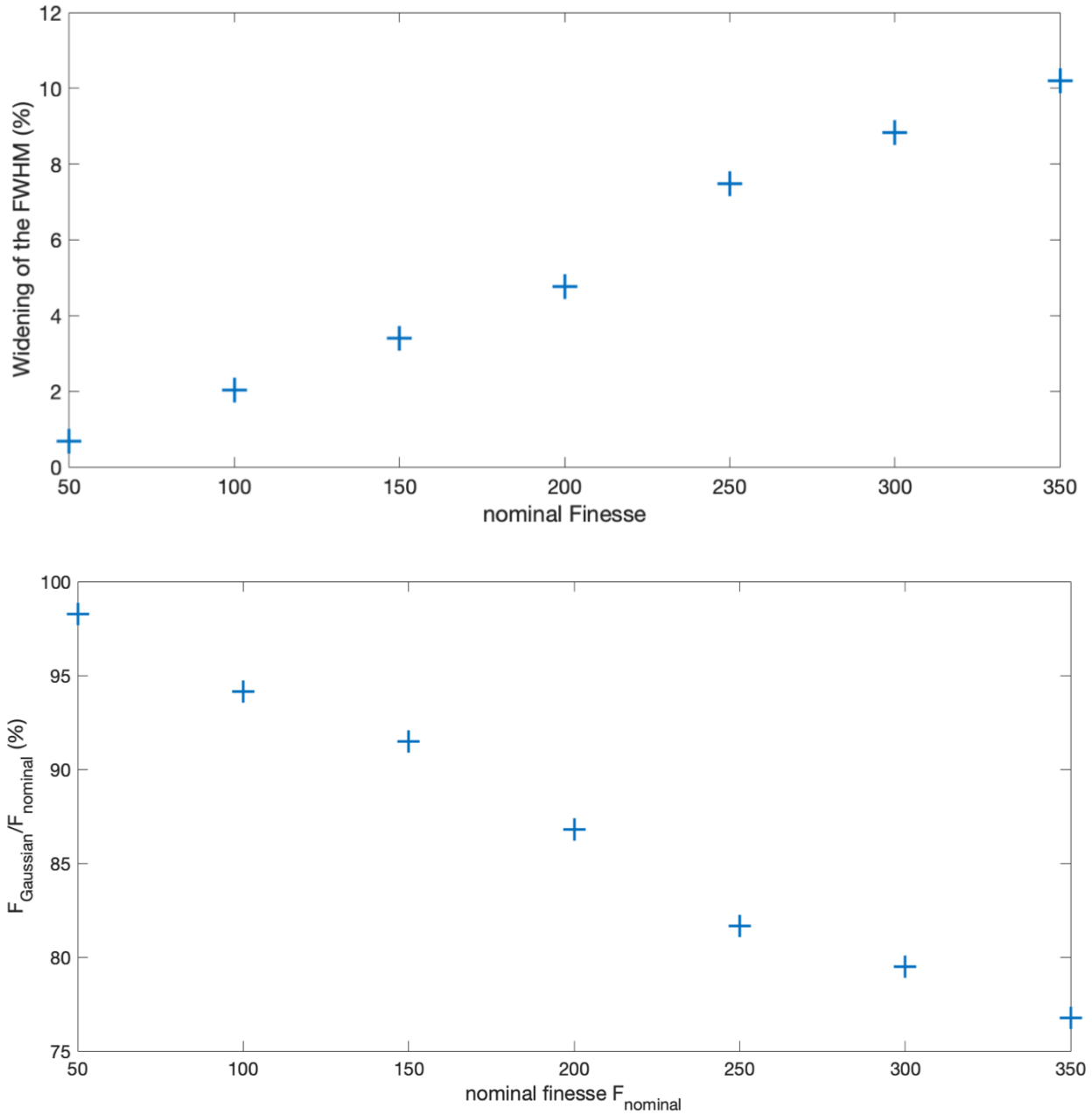


FIGURE D.1: (Top) Widening of the FWHM of the beam (in %) after travelling through the FPI for different nominal finessses between 50 and 350. (Bottom) Ratio of the finesse of a Gaussian beam travelling through the FPI to the nominal finesse (i.e. the finesse of a plane wave through the same FPI) for different nominal finessses between 50 and 350. This ratio must be less or equal to 100%.

Appendix E

Upgrade of the FTS Optical Train

Written by A. Poglitsch, internal communication.

E.1 Configuration of the system before the upgrade

The IR-FTS facility at DAp is built around a Martin-Puplett type interferometer (MPI), which is mounted on a liquid-nitrogen cooled optical bench inside a vacuum vessel (Figure E.1). All optical elements, which have to be actuated either for alignment purposes or to modulate the optical path difference (OPD), are suspended from ambient temperature mechanisms by low thermal conductivity structures and thermally linked to the LN₂ work surface by individual copper braids. Light from an ultra-high-pressure metal halide lamp enters the FTS through a polypropylene foil window; on the exit side of the FTS the optical path continues in vacuum, such that no window is needed there.

The modulated light from the MPI can then be fed either directly into the detector cryostat (IR-Labs WWW), which at the beginning of this thesis was set up for cold reflection measurements : by switching between a reference mirror and, e.g., a detector test structure, one can measure its reflectivity. The reflected light is detected with a silicon bolometer (IR-Labs XXX), which is equipped with a Winston cone to suppress any stray light from outside of its acceptance solid angle.

Alternatively, a sample cryostat (IR-Labs YYY) can be inserted into the optical path between the FTS cryostat and the detector cryostat. A wheel with several positions allows one to perform transmission measurements of several samples, in one cool-down, relative to an open position.

By the time of the start of this thesis, the entire optical train only contained one element with optical power, an offset parabolic mirror, which acted as a collimator for the light coming from the source and entering into the MPI. Given the total length of the optical path of >1m, it seemed obvious that for

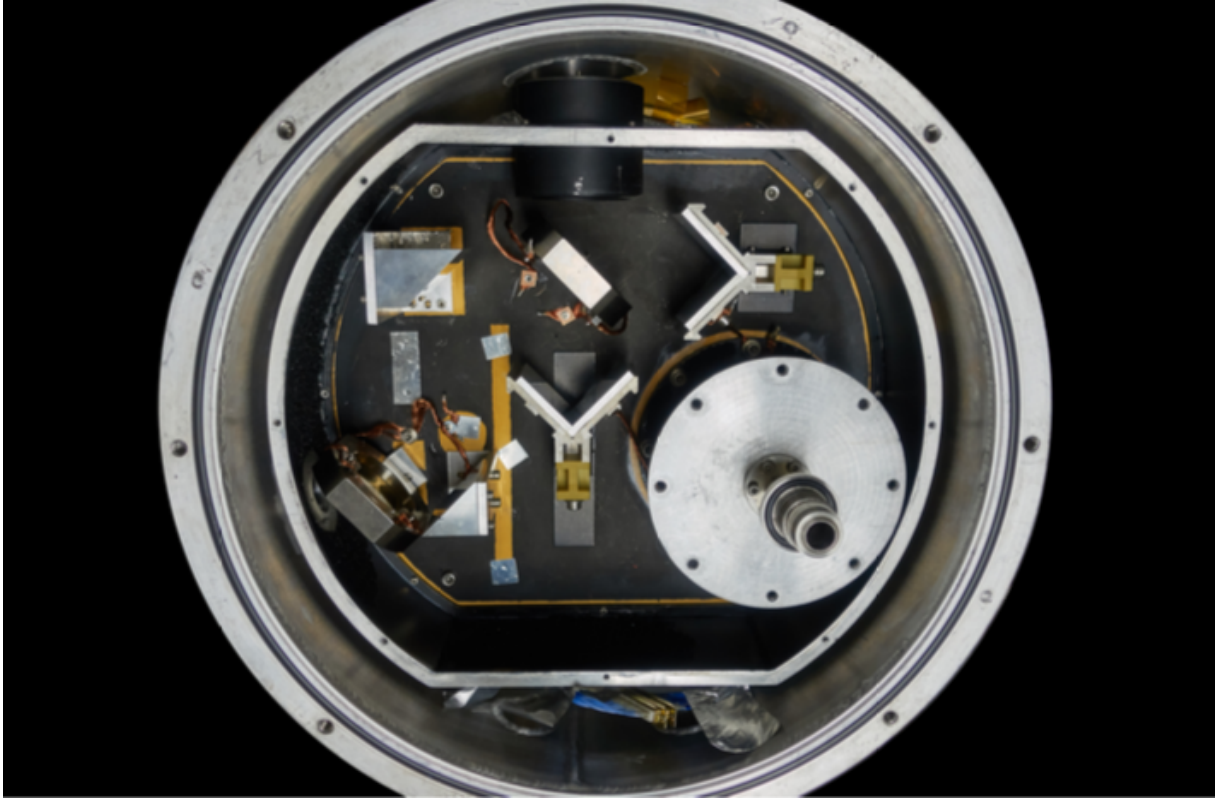


FIGURE E.1: Top view of the opened FTS cryostat with the LN₂ tank in the lower right of the picture. The collimated light from the lamp enters through the baffle tube at the top, which also contains the wire grid polarizer, and is then distributed into the two interferometer arms by the polarizing beam splitter, where also the light reflected by the roof-top mirrors is recombined on the return path. Two flat mirrors then direct the light to the cryostat exit port, where the analyzer grid completes the scheme of a Martin-Puplett interferometer.

measurements of, e.g., very narrow-band filters, with a correspondingly small amount of total transmitted power, some relay optics would be needed to increase the end-to-end étendue ($A\Omega$) of the optical system.

E.2 Upgrade of the optics design

Starting from the cryostat construction drawings and with some dimensions directly taken off the as-built hardware we could reconstruct the 3D positions of all optical surfaces in the FTS. Simple raytracing of the system (Figure E.2) then revealed an étendue of $A\Omega \sim 3 \times 10^{-8} \text{m}^2$, compared to the $A\Omega \sim 5 \times 10^{-6} \text{m}^2$ of the Winston cone. We then investigated how one could implement the necessary relay optics with a minimum amount of modifications to the existing setup, but substantial improvements in étendue. One further constraint was to introduce no extra complications in the optical alignment; in particular, the alignment should still be possible with visible light. This requirement dictated the use of a combination of (optical quality) mirrors and of lenses made from a material with the same refractive index in the FIR/submm as in the visible. The resulting, new optical scheme is presented in Figure E.3.

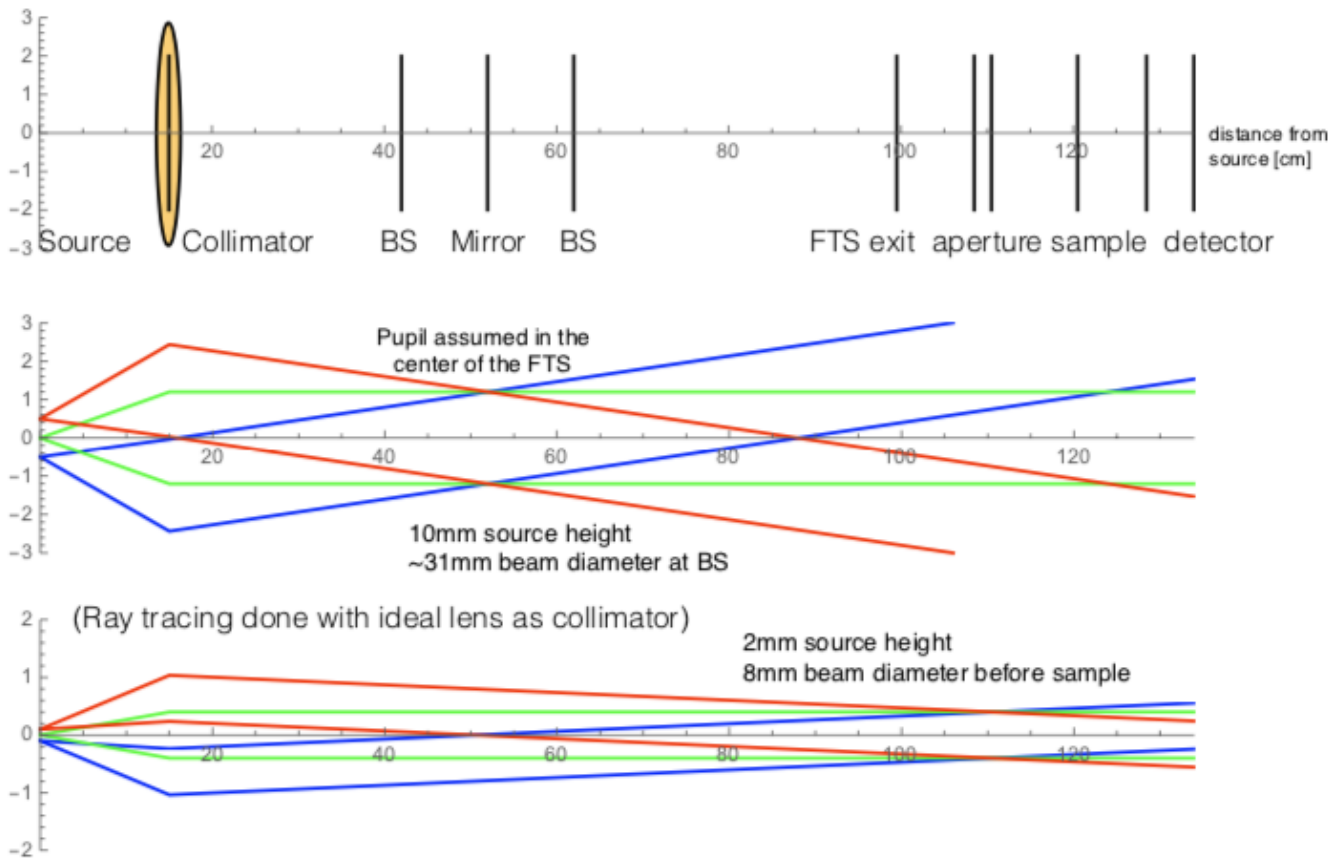


FIGURE E.2: Top : “unfolded” optical schematic of the FTS from source to detector in the configuration of Martin-Puplett interferometer plus detector cryostat. The sample position inside the detector cryostat is occupied either by a reference mirror or by the test item measured in reflection. Marked as “aperture” is the position of the cold stop at the entrance to the detector cryostat. Middle : assessment of the étendue ($A\Omega$), which the Martin-Puplett interferometer – in principle – could provide. Bottom : limited by the cold stop at the detector cryostat and the Winston cone on the detector, only a very small fraction of the available light is used in the original setup.

The improvement in étendue is quite substantial : instead of $A\Omega \sim 3 \times 10^{-8} \text{m}^2$ we can now have $A\Omega = 5.5 \times 10^{-6} \text{m}^2$, if the cold stop at the detector cryostat entrance is increased to a diameter of 10mm. With the original 8mm diameter aperture one still can achieve $A\Omega > 3 \times 10^{-6} \text{m}^2$, up by two orders of magnitude from the original configuration.

The extra étendue is, however, bought at the expense of some loss in transmission, as the TPX material shows noticeable absorption already in the submm, which increases toward the FIR (Figure E.4). On the other hand, since the spectrum of the lamp is roughly that of a rather warm blackbody, the modulated power reaching the detector is still increasing down to $100 \mu\text{m}$ and only decreasing slightly between $100 \mu\text{m}$ and $50 \mu\text{m}$, such that the gain in étendue is leading to a substantially increased measuring efficiency over the wavelength band of interest.

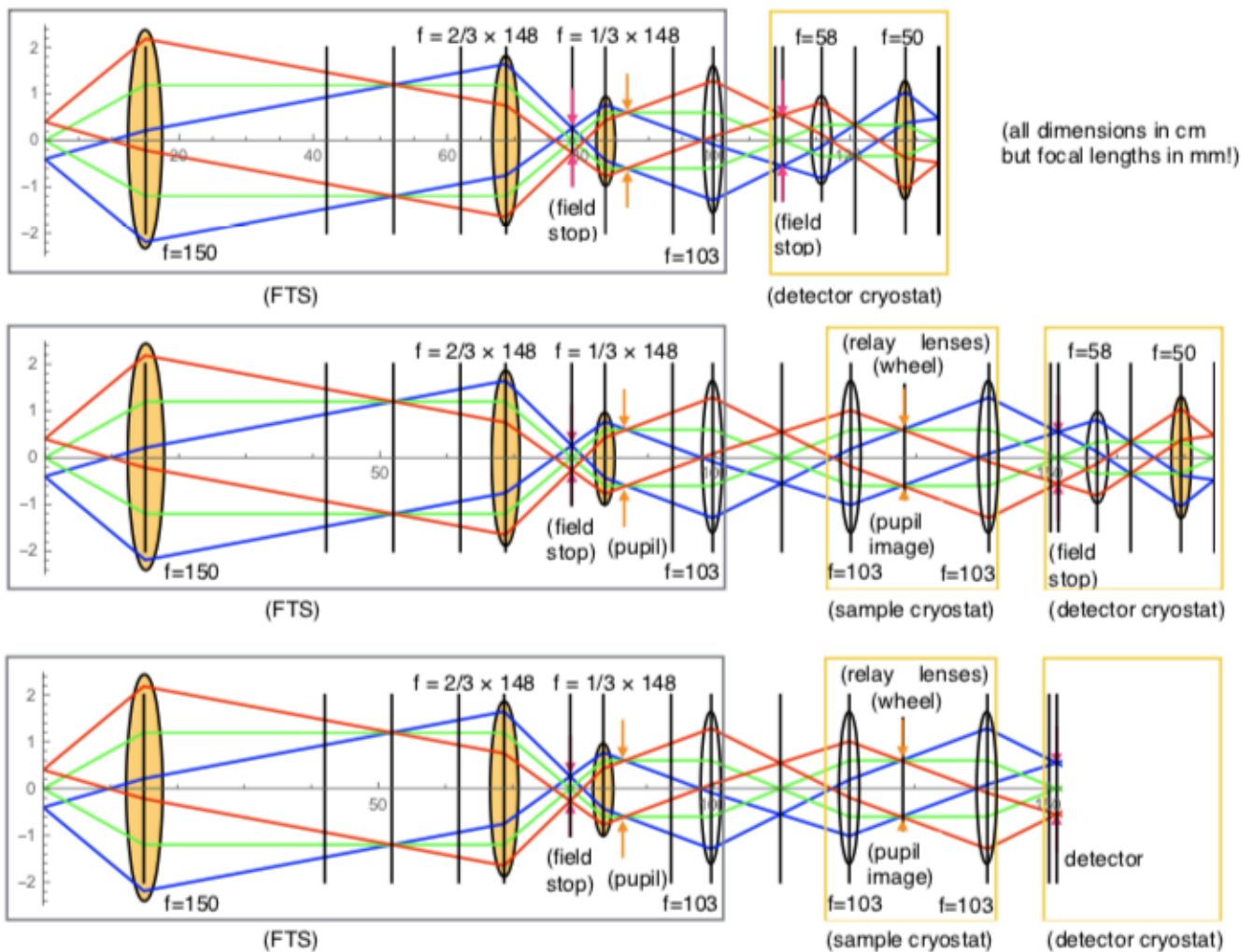


FIGURE E.3: Gold-coloured elements represent curved mirrors, transparent elements are lenses. Top : “unfolded” new optical schematic of the FTS from source to detector in the configuration of Martin-Puplett interferometer plus detector cryostat. Two additional, off-axis parabolic mirrors are used to form an intermediate focus, where a field stop can be placed, and to re-collimate the light to a suitable beam diameter, with the bonus of introducing a proper pupil stop. A relay lens attached to the cold “snout” inside the exit vacuum flange of the FTS cryostat re-focuses the light in the cold entrance aperture of the detector cryostat. A second lens is used to re-collimated the light, with a pupil image at the position of the sample/reference mirror. Finally, the light is adapted to the geometry of the Winston cone by an off-axis parabolic mirror. Middle : with two additional relay lenses, it is possible to insert the sample cryostat for transmission measurements without changing the beam path as seen by the detector cryostat. Bottom : simplified configuration actually used for the Fabry-Pérot transmission measurements.

E.3 Implementation of the FTS optics upgrade

A photo of the upgraded FTS is shown in Figure E.5. The two parabolic mirrors were diamond-machined from aluminium 6061 to our specified dimensions at LT-Ultra and mounted on a small optical bench, which is bolted onto the LN₂ work surface using already existing, tapped holes. The TPX for the lenses was purchased as a solid cylinder from Goodfellow and machined and polished by a local optics shop according to

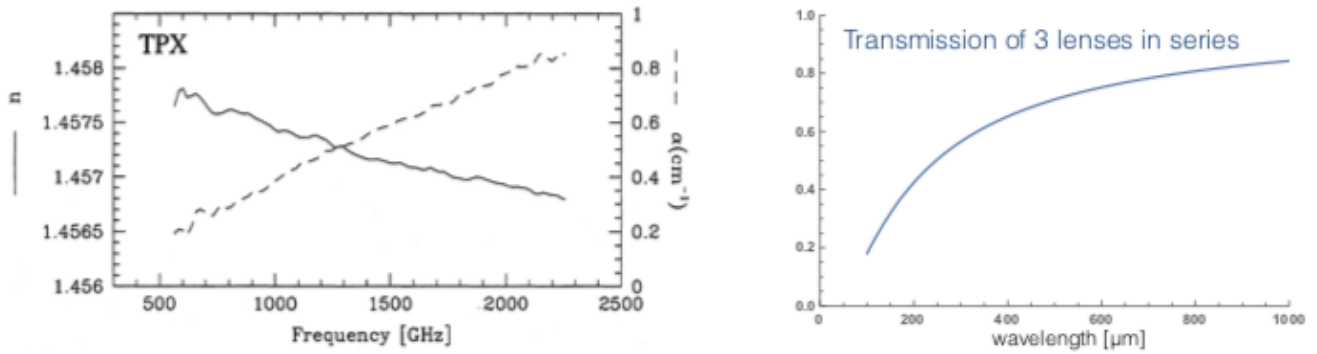


FIGURE E.4: Left : refractive index and absorption coefficient of TPX at 295K. Right : transmission of three lenses in series, as used for the Fabry-Pérot transmission measurements.

our optical prescription. The focal lengths of the lenses have been verified with a collimated light source at our lab.

The new optics – initiated originally to improve the coupling of the light from the MPI into the detector cryostat – already required one lens with a “promising” focal length ($f=103\text{mm}$), and to save manufacturing overhead and time we considered to re-use the same prescription also for the extra relay optics needed to insert the sample cryostat for transmission measurements into the optical path. As it turned out, this could be achieved by simply adding the right distance between the FTS cryostat and the sample cryostat, realized with a custom-length vacuum extension tube (Figure E.6). With this configuration we create a $\sim 12\text{mm}$ diameter pupil image in a collimated beam on the sample wheel, which is well matched to the dimensions of typical structures we investigate, including the new Fabry-Perot interferometers.

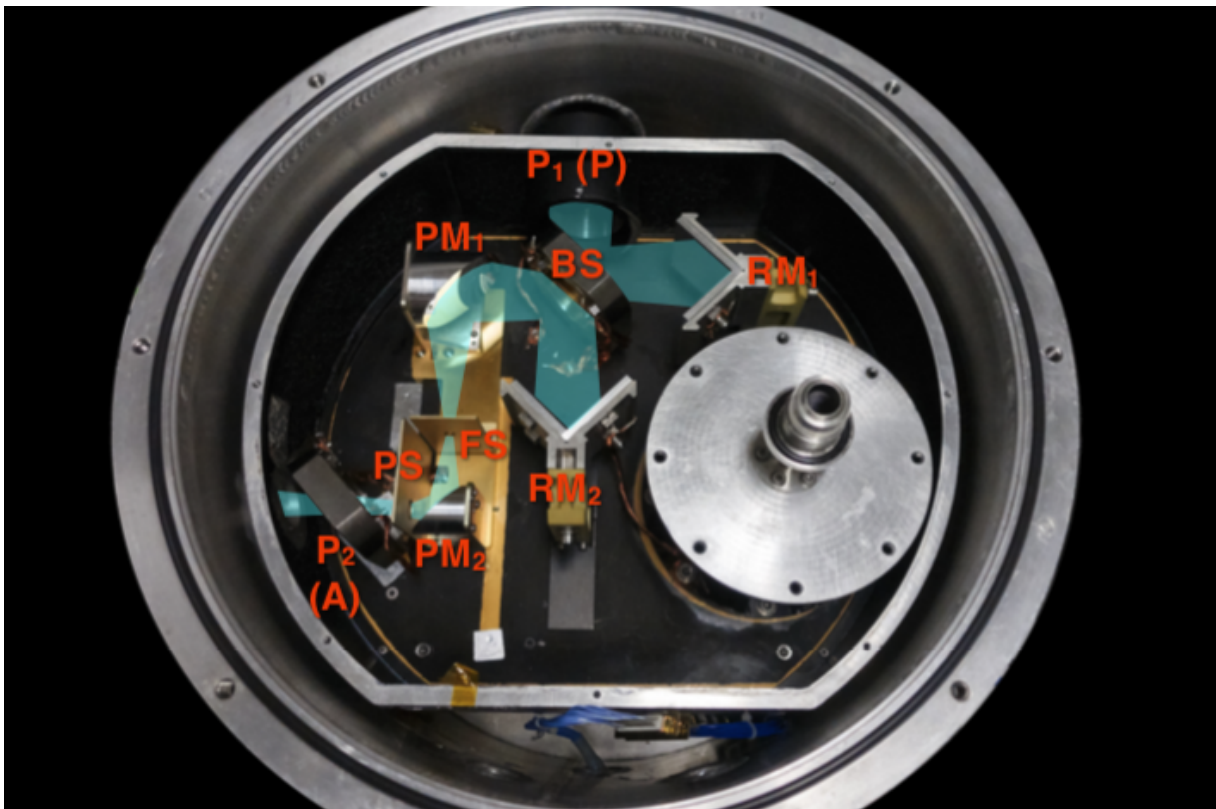


FIGURE E.5: Top view of the opened FTS cryostat after the optics modification. Compared to the original configuration, the two flat mirrors have been replaced with off-axis parabolas (PM_1 and PM_2), and a lens has been added on the cold “snout” in the exit flange (not visible in this photo). To reduce stray light we have also added a field stop (FS) and a pupil stop (PS). Otherwise, the polarizer (P_1), beam splitter (BS), roof-top mirrors (RM) and analyzer (P_2) have not been touched. The simulated illumination of the optical path is only approximate.

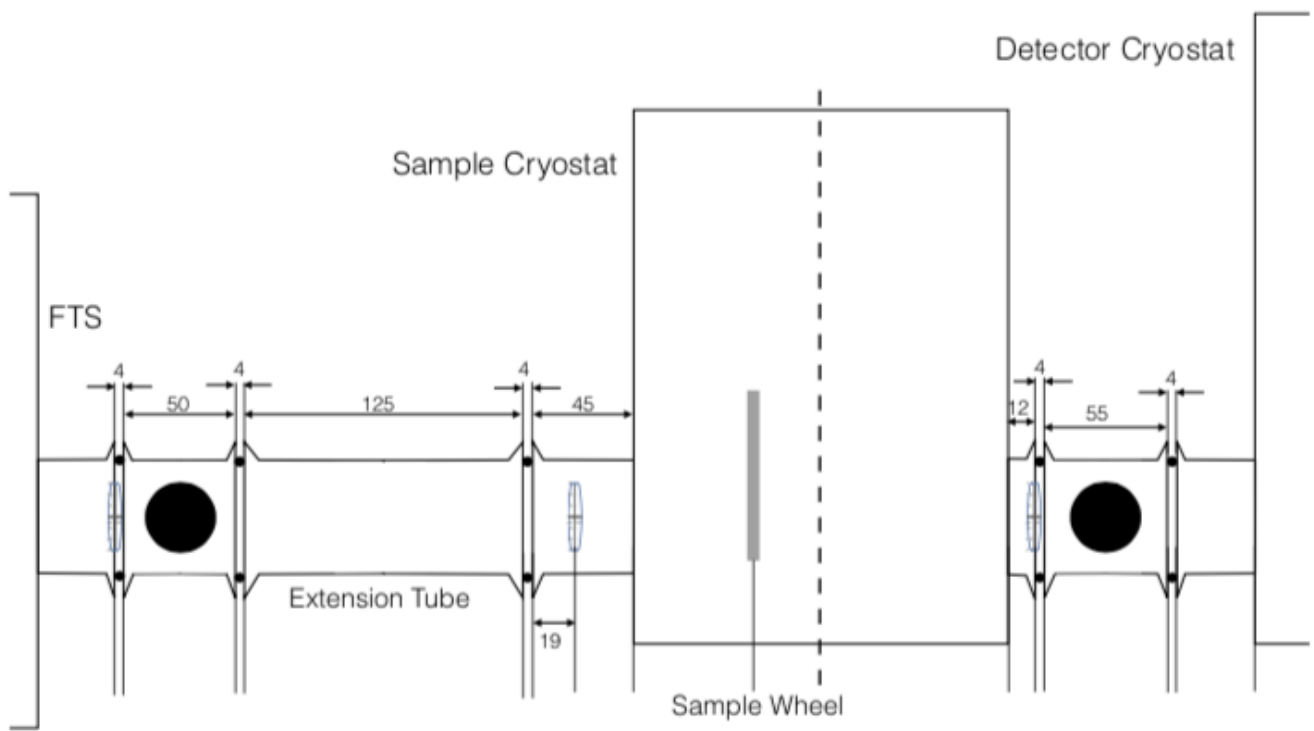


FIGURE E.6: Schematic view of the sample cryostat inserted in the path between the FTS cryostat and the detector cryostat. The two relay lenses are mounted inside the entrance and exit vacuum flanges of the cryostat, respectively. The extension tube is necessary to replicate the focus and pupil distances as seen by the detector cryostat without the sample cryostat and its relay optics.

Bibliography

- Adami, O., Rodriguez, L., Reveret, V., Aliane, A., Poglitsch, A., Sauvageot, J.-L., Bounissou, S., Goudon, V., and Dussopt, L. (2018). Characterization of doped silicon thermometers for very high sensitivity cryogenic bolometers. *Journal of Low Temperature Physics*, 193.
- Adami, O.-A., Rodriguez, L., Poglitsch, A., Bounissou, S., Reveret, V., Aliane, A., Goudon, V., and Dussopt, L. (2019). Highly sensitive polarimetric camera (B-BOP) for the SPICA mission. *Applied Optics*, 58-2 :398–403.
- Ade, P., Aghanim, N., Ahmed, Z., Aikin, R., Alexander, K., Arnaud, M., Aumont, J., and et al. (2015). A joint analysis of BICEP2/Keck array and planck data.
- Ade, P., Pisano, G., Tucker, C., and Weaver, S. (2006). A review of metal mesh filters. *Proceedings of SPIE - The International Society for Optical Engineering*, 6275.
- Aliane, A., Solana, M., Rabaud, W., Saminadayar, L., Agnese, P., Goudon, V., Dussopt, L., Vialle, C., Baghe, E., Pocas, S., Carle, L., Lio Soon Shun, N., Becker, S., Reveret, V., Rodriguez, L., Hamelin, A., Poglitsch, A., Bounissou, S., and Adami, O. (2018). Superconducting Ti/TiN thin films for mm-wave absorption.
- Alpher, R. and Herman, R. (1948). Evolution of the Universe. *Nature*, 162 :774–775.
- André, P., Francesco, J. D., Ward-Thompson, D., Inutsuka, S., Pudritz, R., and Pineda, J. (2013). From filamentary networks to dense cores in molecular clouds : Toward a new paradigm for star formation. *arXiv*.
- André, P., Hughes, A., Guillet, V., Boulanger, F., Bracco, A., Ntormousi, E., Arzoumanian, D., and et al. (2019). Probing the cold magnetized universe with SPICA-POL (B-BOP).
- Arzoumanian, D., André, P., Didelon, P., Konyves, V., Schneider, N., Men'shchikov, A., Sousbie, T., and et al. (2011). Characterizing interstellar filaments with Herschel in IC 5146. *Astronomy and Astrophysics*, 529.

- Arzoumanian, D., André, P., Konyves, V., Palmeirim, P., Roy, A., Schneider, N., Benedettini, M., and et al. (2018). Characterizing the properties of nearby molecular filaments observed with Herschel. *Astronomy and Astrophysics*, 621.
- Bacon, R. and Monnet, G., editors (2017). *Optical 3D-Spectroscopy for Astronomy*. John Wiley and Sons.
- Bandler, S. (2010). Magnetic calorimeter arrays for x-ray astronomy.
- Bayer, B. (1976). Color imaging array. US Patent 3,971,065.
- Bennett, C., Fixsen, D., Hinshaw, G., Mather, J., Moseley, S., Wright, E., R.E. Eplee, J., and et al. (1994). Morphology of the interstellar cooling lines detected by COBE. *Astrophysical Journal*, 434-2 :587–598.
- Benoit, A., Ade, P., Amblard, A., Ansari, R., Aubourg, E., Bargout, S., and et al, J. B. (2004). First detection of polarization of the submillimetre diffuse galactic dust emission by Archeops. *Astronomy and Astrophysics*, 424 :571–582.
- Bernard, J.-P. (2005). PILOT : Measuring polarization in the interstellar medium. In *17th ESA Symposium on European Rocket and Balloon Programmes and Related Research*.
- Billot, N. (2007). *Etalonnage d'un nouveau type de détecteur bolométrique pour l'instrument PACS de l'Observatoire Spatial Herschel*. PhD thesis, Université Paris Sud - Paris XI.
- Bock, J. (2008). Planar antenna-coupled bolometers for CMB polarimetry. Technical report, NASA Jet Propulsion Laboratory.
- Bock, J., Chen, D., Mauskopf, P., and Lange, A. (1995). A novel bolometer for infrared and millimeter-wave astrophysics. *Space Science Reviews*, 74 :229–235.
- Bouchareine, P. (1994). *Spectrométrie Optique*. Techniques de l'Ingenieur.
- Bounissou, S., Reveret, V., Rodriguez, L., Poglitsch, A., Aliane, A., Adami, O.-A., Goudon, V., and et al. (2018). Electromagnetic simulations of newly designed semiconductor bolometers for submillimeter observations. *Journal of Low Temperature Physics*, 193 :428–434.
- Bradford, C., Stacey, G., Swain, M., Nikola, T., Bolatto, A., Jackson, J., Savage, M., and et al. (2002). SPIFI : a direct-detection imaging spectrometer for submillimeter wavelengths. *Applied optics*, 41 :2561–74.
- Brooker, G., editor (2003). *Modern Classical Optics*. Oxford Master Series in Atomic, Optical and Laser Physics.

- Burmeister, O., Britzger, M., Thuring, A., Friedrich, D., Bruckner, F., Danzmann, K., and Schnabel, R. (2010). All-reflective coupling of two optical cavities with 3-port diffraction gratings. *Optics Express*, 18-9.
- Button, K., editor (1982). *Infrared and Millimeter Waves V6 - First edition*. Academic Press.
- Buzzi, C. (1999). *Developpement de bolometres monolithiques silicium refroidis à 0,3 K pour le satellite FIRST (Far Infrared and Submillimeter Telescope)*. PhD thesis, Universite Grenoble 1.
- Chevance, M. (2016). *The physical processes in the interstellar medium of the Magellanic Clouds*. PhD thesis, Universite Sorbonne Paris Cite.
- Clegg, P.-E., Ade, P., Armand, C., Baluteau, J.-P., Barlow, M., Buckle, M., Berges, J.-C., and et al. (1996). The ISO Long-Wavelength Spectrometer. *Astronomy and Astrophysics*, 315 :L38–L42.
- Collet, E. (2005). *Field Guide to Polarization*. SPIE press book.
- Connes, P., Smyth, M., Hadni, A., and Gerbaux, X. (1988). Heinrich Rubens, Herbert Hollnagel, and Fourier transform spectroscopy. *Optics News*, 14 :6–14.
- Cormier, D. (2012). *The physical properties in the interstellar medium of low-metallicity dwarf galaxies*. PhD thesis, Universite Sorbonne Paris Cite.
- Cormier, D., Madden, S., Lebouteiller, V., Abel, N., Hony, S., Galliano, F., A. Remy-Ruyer, A., and et al. (2015). The Herschel Dwarf Galaxy Survey. I. Properties of the low-metallicity ISM from PACS spectroscopy. *Astronomy and Astrophysics*, 578.
- Cothard, N., Stacey, G., Niemack, M., and K.Vetter (2018). Optimizing the Efficiency of Fabry-Perot Interferometers with Silicon-Substrate Mirrors. In *Advances in Optical and Mechanical Technologies for Telescopes and Instrumentation III*.
- Crutcher, R. (2012). Magnetic fields in molecular clouds. *Annual Review of Astronomy and Astrophysics*, 50(1) :29–63.
- Dai, J., Zhang, J., Zhang, W., and Grischkowsky, D. (2004). Terahertz time-domain spectroscopy characterization of the far-infrared absorption and index of refraction of high-resistivity, float-zone silicon. *Journal of The Optical Society of America B-optical Physics*, 21.
- Davis, G., Furniss, I., Towson, W., Ade, P., Emery, R., Glencross, W., Naylor, D., and et al. (1995). Design and performance of cryogenic, scanning Fabry-Perot interferometers for the Long-Wavelength Spectrometer on the Infrared Space Observatory. *Applied optics*, 34 :92–107.

- Day, P., LeDuc, H., Mazin, B., Vayonakis, A., and Zmuidzinas, J. (2003). A broadband superconducting detector suitable for use in large arrays. *Nature*, 425 :817–821.
- Defrance, F., Jung-Kubiak, C., Sayers, J., Connors, J., deYoung, C., Hollister, M., Yoshida, H., and et al. (2018). A 1.6 :1 Bandwidth Two-Layer Antireflection Structure for Silicon Matched to the 190-310 GHz Atmospheric Window. *Applied Optics*, 57.
- Désert, F.-X., Adam, R., Ade, P., André, P., Aussel, H., Beelen, A., and et al. (2016). NIKA2, a dual-band millimetre camera on the IRAM 30 m telescope to map the cold universe. *SF2A*, pages 439–442.
- Douthit, G., Stacey, G., Nikola, T., Henderson, C., Gull, G., Rossi, K., Kutryrev, A., and Moseley, S. (2018). Development of the Fabry-Perot interferometers for the HIRMES spectrometer on SOFIA. volume 10708. SPIE.
- Dowell, C., Allen, C., Babu, S., Freund, M., Gardner, M., Grosetha, J., Jhabvala, M., and et al. (2003). SHARC II : a caltech submillimeter observatory facility camera with 384 pixels. In *Millimeter and Submillimeter Detectors for Astronomy*. SPIE.
- Downey, P., Jeffries, A., Meyer, S., Weiss, R., Bachner, F., Donnelly, J., Lindley, W., Mountain, R., and Silversmith, D. (1984). Monolithic silicon bolometers. *Applied Optics*, 23-6 :910–914.
- Doyle, S., Mauskopf, P., Naylor, J., Porch, A., and Duncombe, C. (2008). Lumped Element Kinetic Inductance Detectors. *Journal of Low Temperature Physics*, 151 :530–536.
- Efros, A. and Shklovskii, B. (1975). Coulomb gap and low temperature conductivity of disordered systems. *J. Phys. C : Solid State P.*, 8 :L49–L51.
- Endo, A., Baselmans, J., der Werf, P. V., Knoors, B., Javadzadeh, S., Yates, S., Thoen, D., and et al. (2012). Development of DESHIMA : A redshift machine based on a superconducting on-chip filterbank. In *Millimeter, Submillimeter, and Far-Infrared Detectors and Instrumentation for Astronomy VI*. SPIE.
- Engel, C., Ade, P., Bernard, J.-P., Bernardis, P. D., Bouzit, M., Giard, M., and et al, M. G. (2009). Status of the PILOT balloon-borne experiment. In *19th ESA Symposium on European Rocket and Balloon Programmes and Related Research*.
- Fabry, C. and Perot, A. (1901). On a new form of interferometer. *Astrophysical Journal*, 13 :265–273.
- Fante, R. L. and McCormack, M. T. (1988). Reflection properties of the Salisbury screen. *IEEE Transactions on Antennas and Propagation*, 36(10) :1443–1454.
- Fellgett, P. (1958). Spectromètre interférentiel multiplex pour mesures infra-rouges sur les étoiles. *Journal of Physics*, 19 :237–240.

- Ferrec, Y. (2010). Spectro-imageurs. Technical report, Techniques de l'Ingenieur.
- Fischer, C., Beckmann, S., A.Bryant, Colditz, S., Fumi, F., Geis, N., and et al. (2018). FIFI-LS : The Field-Imaging Far-Infrared Line Spectrometer on SOFIA. *Journal of Astronomical Instrumentation*, 07.
- Fleischmann, A., Link, M., Daniyarov, T., Rotzinger, H., Enss, C., and Seidel, G. (2004). Metallic magnetic calorimeters (MMC) : detectors for high-resolution X-ray spectroscopy. *Nuclear Instruments and Methods in Physics Research*, 520 :27–31.
- Gamow, G. (1948). The Evolution of the Universe. *Nature*, 162 :680–682.
- Geelen, B., Tack, N., and Lambrechts, A. (2014). A compact snapshot multispectral imager with a monolithically integrated, per-pixel filter mosaic. In *Advanced Fabrication Technologies for Micro/Nano Optics and Photonics VII*. SPIE.
- Graauw, T. D., Helmich, F., Phillips, T., Stutzki, J., Caux, E., Whyborn, N., Dieleman, P., and et al. (2010). The Herschel-Heterodyne Instrument for the Far-Infrared (HIFI). *Astronomy and Astrophysics*, v.518 (2010), 518.
- Grabarnik, S., Wolffenbuttel, R., Emadin, A., Loktev, M., Sokolova, E., and Vdovin, G. (2007). Planar double-grating microspectrometer. *Optics express*, 15 :3581–8.
- Griffin, M. J., Abergel, A., Abreu, A., Ade, P. A. R., André, P., Augueres, J.-L., and Babbedge, T. (2010). The Herschel-SPIRE instrument and its in-flight performance. *Astronomy and Astrophysics*, 518.
- Hadley (1957). Theory of superconductivity. *Physical Review*, 108-5 :1175–1204.
- Hadley, L. and Dennison, D. (1947). Reflection and transmission interference filters. *Journal of the Optical Society of America*, 37-6 :451–465.
- Hailey-Dunsheath, S., Shirokoff, E., Barry, P. S., Bradford, C. M., Chattopadhyay, G., P.Day, Doyle, S., and et al. (2015). Status of SuperSpec : A Broadband, On-Chip Millimeter-Wave Spectrometer. In *Millimeter, Submillimeter, and Far-Infrared Detectors and Instrumentation for Astronomy VII*. SPIE.
- Hall, J. (1949). Observations of the polarized light from stars. *Science*, 109 :166–167.
- Haller, E. (1994). Advanced far-infrared detectors. *Infrared Physics Technology*, 35-2/3 :127–146.
- Hazumi, M. (2018). LiteBIRD for B-mode from space.
- Hernandez, G. (1986). *Fabry-Perot Interferometers*. Cambridge University Press.
- Herschel, W. (1800). XIV. Experiments on the refrangibility of the invisible rays of the sun. *The Royal Society Publishing*, 90.

- Hildebrand, R. (1988). Magnetic fields and stardust. *Quarterly Journal of the Royal Astronomical Society*, 29.
- Hilsum, C. (1954). Infrared absorption of thin metal films. *Journal of the Optical Society of America*, 44-3 :188–191.
- Hiltner, A. (1949). Polarization of radiation from distant stars by the interstellar medium. *Nature*, 163 :283.
- Hochheimer, B. F. and Bradley, C. F. (1969). A Fourier Transform Spectrometer for the 10-10,000 cm^{-1} Spectral Region. *Applied Optics*, 8(3) :557–562.
- Holland, W. and Duncan, W. (2002). Bolometers for submillimeter and millimeter astronomy. In *Single-Dish Radio Astronomy : Techniques and Applications*. ASP Conference Series.
- Hollenbach, D. (1990). Photodissociation regions. In *The Evolution of the Interstellar Medium*, volume 12 of *Astronomical Society of the Pacific Conference Series*, pages 167–181.
- Holmes, W., Bock, J., B.P.Crill, Koch, T., Jones, W., Lange, A., and Paine, C. (2008). Initial test results on bolometers for the Planck high frequency instrument. *Applied Optics*, 47-32 :5996–6008.
- Jones, W., Bhatia, R., Bock, J., and Lange, A. (2002). A Polarization Sensitive Bolometric Detector for Observations of the Cosmic Microwave Background. In *SPIE proceedings*.
- Kimmitt, M. (1970). *Far Infrared techniques*. Pion Ltd.
- Kogelnik, H. and Li, T. (1966). Laser beams and resonators. *Applied Optics*, 5-10 :1550–1557.
- Koshida, N., editor (2008). *Device Applications of Silicon Nanocrystals and Nanostructures*. Springer Science and Business Media.
- Lamarre, J. (1986). Photon noise in photometric instruments at far-infrared and submillimeter wavelengths. *Applied Optics*, 25-6 :870–876.
- Lamarre, J.-M., Puget, J.-L., Ade, P., Bouchet, F., Guyot, G., and et al. (2010). Planck pre-launch status : The HFI instrument, from specification to actual performance. *Astronomy and Astrophysics*, 520 :A9.
- Lambrechts, A., Gonzalez, P., Geelen, B., Soussan, P., Tack, K., and Jayapala, M. (2014). A CMOS-compatible, integrated approach to hyper- and multispectral imaging. In *Proceedings of 2014 IEEE International Electron Devices Meeting*.
- Langley, S. P. (1881). The bolometer. *Nature*, 25 :14–16.
- Langley, S. P. (1900a). Description of the observatory buildings and the apparatus employed in the research-adjustments of apparatus. Technical report, Astrophysical Observatory of the Smithsonian Institution.

- Langley, S. P. (1900b). Limitations of the research - sources of error now existing. Technical report, Astrophysical Observatory of the Smithsonian Institution.
- Langley, S. P. (1900c). Methods of procedure in preparing and comparing bolographs. Technical report, Astrophysical Observatory of the Smithsonian Institution.
- Langley, S. P. (1902). Annals of the Astrophysical observatory of the Smithsonian Institution, Volume I. *Monthly Weather Review*, 30(5) :258–260.
- Le Coarer, E., Blaize, S., Benech, P., Stefanon, I., Morand, A., Lerondel, G., Leblond, G., and et al. (2007). Wavelength-scale stationary-wave integrated Fourier-transform spectrometry. *Nature Photonics*, 1 :473–478.
- Le Coarer, E., Boussey, J., Blaize, S., Kern, P., and et al. (2010). SWIFTS : on-chip very high spectral resolution spectrometer. In *International conference on space Optics - ICSO*. ESA.
- Lee, S., Gildemeister, J., Holmes, W., Lee, A., , and Richards, P. (1998). Voltage-biased superconducting transition-edge bolometer with strong electrothermal feedback operated at 370 mK. *Applied Optics*, 37-16 :3391–3397.
- Lesurf, J. (2017). *Millimetre-wave optics, devices and systems*. CRC Press.
- Li, M., Allen, C., Gordon, S., Kuhn, J., Mott, D., Stahle, C., and Wang, L. (1999). Fabrication of pop-up detector arrays on si wafers. In *Conference on Micromachining and Microfabrication Process Technology V*. SPIE.
- Lippmann, G. (1891). La photographie des couleurs. *Comptes Rendus Hebdomadaires des Seances de l'Academie des Sciences*, 112-5 :274–275.
- Lippmann, G. (1894). Sur la théorie de la photographie des couleurs simples et composées par la méthode interférentielle. *Journal de Physique Théorique et Appliquée*, 3-1 :97–107.
- Loettgers, A. (2003). Samuel Pierpont Langley and his Contributions to the Empirical Basis of Black-Body Radiation. *Physics in Perspective*, 5.
- Low, F. (1961). Low-temperature germanium bolometer. *Journal of the Optical Society of America*, 51 :1300–1304.
- Macleod, H. (2010). *Thin-Film Optical Filters, Fourth Edition*. CRC Press.
- Makitsubo, H., Wada, T., Kataza, H., Mita, M., Suzuki, T., and Yamamoto, K. (2017). Fabrication and analysis of three-layer all-silicon interference optical filter with sub-wavelength structure toward high performance terahertz optics. *Journal of Infrared, Millimeter, and Terahertz Waves*, 38(2) :206–214.

- Martignac, J. (1998). Étude de l'absorption des ondes submillimétriques par des structures métalliques utilisées pour des bolomètres fonctionnant à 300 mK.
- Martin, D. and Pulett, E. (1970). Polarised interferometric spectrometry for the millimetre and submillimetre spectrum. *Infrared Physics*, 10-2 :105–109.
- Mather, J., Cheng, E., Jr., R. E., Isaacman, R., Meyer, S., Shafer, R., Weiss, R., and et al. (1990). A preliminary measurement of the cosmic microwave background spectrum by the Cosmic Background Explorer (COBE) satellite. *Astrophysical Journal*, 354 :37–40.
- Mather, J. C., Fixsen, D. J., Shafer, R. A., Mosier, C., and Wilkinson, D. T. (1999). Calibrator design for the COBE far-infrared absolute spectrophotometer (FIRAS). *The Astrophysical Journal*, 512-2 :511–520.
- McCarrick, H., Abitbol, M., Flanigan, D., Johnson, B. R., Ade, P., Barry, P., Bryan, S., and et al. (2016). Development of dual-polarization LEKIDs for CMB observations. In *Millimeter, Submillimeter, and Far-Infrared Detectors and Instrumentation for Astronomy VIII*. SPIE.
- McCarrick, H., Flanigan, D., Jones, G., Johnson, B., Ade, P., Araujo, D., Bradford, K., and et al. (2014). Horn-coupled, commercially-fabricated aluminum lumped-element kinetic inductance detectors for millimeter wavelengths. *Review of Scientific Instruments*, 85 :123117,1–16.
- McCarrick, H., Jones, G., Johnson, B. R., Abitbol, M., Ade, P., Bryan, S., and et al. (2017). Design and performance of dual-polarization lumped-element kinetic inductance detectors for millimeter-wave polarimetry. *Astronomy and Astrophysics*.
- Moseley, S., Dowell, C., Allen, C., and Phillips, T. (2000). Semiconducting pop-up bolometers for far-infrared and submillimeter astronomy. In *Imaging at Radio through Submillimeter Wavelengths*. ASP Conference Series.
- Nakajima, K. and Usami, N. (2009). *Crystal Growth of Si for Solar Cells*. Springer.
- Naylor, D., Veenendaal, I., Gom, B., Fulton, T., Jellema, W., Ade, P., and Eggen, M. (2017). A novel design for a cryogenic Fabry-Perot interferometer. In *42nd International Conference on Infrared, Millimeter, and Terahertz Waves (IRMMW-THz)*.
- Neu, J. and Schmuttenmaer, C. (2018). Tutorial : an introduction to Terahertz time domain spectroscopy (THz-TDS). *Journal of Applied Physics*, 124-23.
- Ojeda, J. and Dittrich, M. (2012). Fourier transform infrared spectroscopy for molecular analysis of microbial cells. *Methods in molecular biology (Clifton, N.J.)*, 881 :187–211.

- Page, L., Hinshaw, G., Komatsu, E., Nolta, M., Spergel, D., Bennett, C., Barnes, C., and et al. (2007). Three-Year Wilkinson Microwave Anisotropy Probe (WMAP) Observations : Polarization Analysis. *The Astrophysical Journal Supplement Series*, 170(2) :335–376.
- Parshley, S., Vavagiakis, E., Nikola, T., and Stacey, G. (2014). A miniature cryogenic scanning Fabry-Perot interferometer for mid-IR to submm astronomical observations. In *Proceedings of SPIE - The International Society for Optical Engineering*, volume 9147, page 914745.
- Penzias, A. and Wilson, R. (1965). A Measurement of Excess Antenna Temperature at 4080 Mc/s. *Astrophysical Journal*, 142 :419–421.
- Perot, A. and Fabry, C. (1899). On the application of interference phenomena to the solution of various problems of spectroscopy and metrology. *Astrophysical Journal*, 9 :87.
- Piat, M. (2008). *De PLANCK à BPOL : Développements instrumentaux pour la caractérisation de la polarisation du Fond Diffus Cosmologique*. PhD thesis, Université Paris-Diderot - Paris VII.
- Pilbratt, G., Riedinger, J., Passvogel, T., Crone, G., Doyle, D., Gageur, U., and et al. (2010). Herschel Space Observatory - An ESA facility for far-infrared and submillimetre astronomy. *Astronomy and Astrophysics*, 518.
- Planck Collaboration (2016). Planck intermediate results - XXXV. Probing the role of the magnetic field in the formation of structure in molecular clouds. *Astronomy and Astrophysics*, 586.
- Planck Collaboration (2018). Planck 2018 results. I. Overview and the cosmological legacy of Planck.
- Poglitsch, A., Beeman, J. W., Geis, N., Genzel, R., Haggerty, M., Haller, E. E., and Jackson, J. (1991). The MPE/UCB far-infrared imaging Fabry-Perot interferometer (FIFI). *International Journal of Infrared and Millimeter Waves*, 12 :859–884.
- Poglitsch, A., Katterloher, R., Hoenle, R., Beeman, J., Haller, E., Richter, H., U.Groezinger, and et al. (2003a). Far-infrared photoconductor arrays for Herschel and SOFIA. volume 4855. SPIE.
- Poglitsch, A., Waelkens, C., Bauer, O., Cepa, J., Feuchtgruber, H., Henning, T., Hoof, C. V., and et al. (2003b). The Photodetector Array Camera and Spectrometer PACS for the Herschel Space Observatory. *Space Telescopes and Instrumentation I : Optical, Infrared, and Millimeter*, 6265.
- Pracht, U., Scheffler, M., Dressel, M., Kalok, D., Strunk, C., and Baturina, T. (2012). Direct observation of the superconducting gap in thin film of titanium nitride using terahertz spectroscopy. *Physical Review B*, 86.
- R.C. Kennicutt, J. (1998). The Global Schmidt Law in Star-forming Galaxies. *The Astrophysical Journal*, 498(2) :541–552.

- Reveret, V. (2004). *Etude de faisabilité d'une caméra bolométrique pour l'imagerie à haute résolution spatiale à 1,3mm de longueur d'onde pour l'IRAM*. PhD thesis, Université Pierre et Marie Curie - Paris VI.
- Reveret, V., Rodriguez, L., and Agnese, P. (2010). Enhancing the spectral response of filled bolometer arrays for submillimeter astronomy. *Applied Optics*, 49 :6726–36.
- Richards, P. (1994). Bolometers for infrared and millimeter waves. *Journal of Applied Physics*, 76 :1 – 24.
- Rieke, G. (2003). *Detection of Light : From the ultraviolet to the submillimeter - 2nd edition*. Cambridge University Press.
- Risacher, C., Gusten, R., Stutzki, J., Hubers, H.-W., Aladro, R., Bell, A., Buchbender, C., and et al. (2018). The upGREAT dual frequency heterodyne arrays for SOFIA. *Journal of Astronomical Instrumentation*, 7-4.
- Rodriguez, L. (2012). Les bolomètres résistifs. In *Workshop - Detection des rayonnements tres basses temperatures*.
- Rodriguez, L., Poglitsch, A., Aliane, A., Martignac, J., Dubreuil, D., Bounissou, S., Reveret, V., and et al. (2018). BRAHMS-sensitive bolometer arrays for the SPICA imaging polarimetry. *Journal of Low Temperature Physics*, 193.
- Roelfsema, P., Shibai, H., Armus, L., Arrazola, D., Audard, M., Audley, M., Bradford, C., and et al. (2018). SPICA-A Large Cryogenic Infrared Space Telescope : Unveiling the Obscured Universe. *Publications of the Astronomical Society of Australia*, 35.
- Rohlfs, K. and Wilson, T. (2004). *Tools of Radio Astronomy - 4th edition*. Springer.
- Rommelueire, S., Guerineau, N., Haidar, R., Deschamps, J., Borniol, E. D., Million, A., Chamonal, J.-P., and Destefanis, G. (2008). Infrared focal plane array with a built-in stationary Fourier-transform spectrometer : basic concepts. *Optics Letters*, 33-10.
- Rosset, C., Tristram, M., Ponthieu, N., Ade, P., Aumont, J., Catalano, A., Conversi, L., and et al. (2010). Planck pre-launch status : High frequency instrument polarization calibration. *Astronomy and Astrophysics*, 520.
- Sakai, K. and Genzel, L. (1983). Far Infrared Metal Mesh Filters and Fabry-Perot Interferometry. *Reviews of Infrared and Millimeter Waves*, 1 :155–247.
- Schmidt, M. (1959). The rate of star formation. *Astrophysical Journal*, 129 :243.

- Schneider, S. and Elmegreen, B. (1979). A catalog of dark globular filaments. *Astrophysical Journal, Supplement*, 41 :87–95.
- Sellar, R. and Boreman, G. (2005). Classification of imaging spectrometers for remote sensing applications. *Optical Engineering - OPT ENG*, 44.
- Simon, F. (1935). Application of low temperature calorimetry to radioactive measurements. *Nature*, 3135 :763.
- Smoot, G., Bennett, C., Kogut, A., Wright, E., Aymon, J., Boggess, N., Cheng, E., and et al. (1992). Structure in the COBE differential microwave radiometer first-year maps. *Astrophysical Journal*, 396-1 :L1–L5.
- Stacey, G., Geis, N., Genzel, R., Lugten, J., Poglitsch, A., Sternberg, A., and Townes, C. (1991). The 158 micron [CII] line : a measure of global star formation activity in galaxies. *The Astrophysical Journal*, 373 :423–444.
- Stacey, G., Hayward, T., Latvakoski, H., and Gull, G. (1993). KWIC : a widefield mid-infrared array camera/spectrometer for the KAO. *Proceedings of SPIE - The International Society for Optical Engineering*.
- Suzuki, A., Ade, P., Akiba, Y., Alonso, D., Arnold, K., Aumont, J., Baccigalupi, C., and et al. (2018). The LiteBIRD Satellite Mission - Sub-Kelvin Instrument. *Journal of Low Temperature Physics*.
- Suzuki, A., Arnold, K., Edwardsy, J., Engargiolaz, G., Ghribi, A., Holzapfel, W., and Lee, A. (2012). Multi-chroic dual-polarization bolometric detectors for studies of the Cosmic Microwave Background. *Journal of Low Temperature Physics*, 176-5/6 :650–656.
- Swinyard, B. and Wild, W. (2013). Far-infrared imaging and spectroscopic instrumentation. *ISSI Scientific Reports Series*.
- Synova S.A. (2019). Synova company website. <https://www.synova.ch/>. Last accessed 08/08/2019.
- The Event Horizon Telescope Collaboration (2019). First M87 Event Horizon Telescope Results. II. Array and Instrumentation. *The Astrophysical Journal Letters*, 875.
- Tielens, A. (2005). *The physics and chemistry of the Interstellar medium*. UK Cambridge University Press.
- Ulrich, R. (1967). Far-infrared properties of metallic mesh and its complementary structure. *Infrared Physics*, 7(1) :37 – 55.
- Ulrich, R., Renk, K., and Genzel, L. (1963). Tunable Submillimeter Interferometers of the Fabry-Perot Type. *Microwave Theory and Techniques, IEEE Transactions*, 11 :363 – 371.

- Vuichard S.A. (2019). Vuichard company website. <https://vuichard.fr/>. Last accessed 08/08/2019.
- Ward-Thompson, D. and Whitworth, A. (2011). *An introduction to star formation*. Cambridge University Press.
- Weintraub, D., Goodman, A., and Akeson, R. (2000). *Polarized Light from Star-Forming Regions*, volume Protostars and Planets IV, pages 247–272. University of Arizona Press.
- Winston, R. (1970). Light collection within the framework of geometrical optics. *Journal of the Optical Society of America*, 60-2 :245–247.
- Wood, K. (1997). Scattering and dichroic extinction : Polarimetric signatures of galaxies. *The Astrophysical Journal*, 477(1) :L25–L28.
- Zmuidzinas, J. (2003). Thermal noise and correlations in photon detection. *Applied Optics*, 42-25 :245–247.

Titre : Instrumentation compacte pour l'astronomie: intégrer la spectroscopie et la polarisation au niveau du détecteur

Mots clés : détecteurs, polarisation, spectroscopie

Résumé : Cette thèse étudie la possibilité d'intégrer plusieurs fonctions instrumentales au sein de la matrice de bolomètres pour les observations dans le domaine du sub-millimétrique. Ceci est désormais envisageable grâce aux progrès des micro-technologies.

Dans un premier temps, nous avons optimisé le design des pixels polarimétriques inventés pour l'instrument B-BOP du futur observatoire spatial SPICA. Ce travail a notamment permis de quantifier la cross-polarisation (1/1000) et de repenser la géométrie des pixels afin d'obtenir des détecteurs mieux adaptés au rayonnement incident.

Cette thèse a également été l'occasion, et ce de manière indépendante à la polarimétrie, de réfléchir à l'intégration de la spectroscopie au sein du plan focal. Pour cela, nous nous sommes orientés vers de l'interférométrie de type Fabry Perot (FP). Un FP dans un faisceau collimaté présente l'avantage d'être très facilement compatible avec l'imagerie. Toutefois, nous avons choisi d'intégrer le spectromètre au plus près du détecteur (et donc dans le faisceau convergent). Nous avons également initié le développement de FP

tout silicium (Si) à haute résistivité afin de réduire les pertes dues aux miroirs métalliques, conventionnellement utilisés dans nos gammes de longueurs d'onde. Afin d'améliorer les performances spectrales du FP, les miroirs sont fabriqués via un empilement de couches de silicium interposés de vide tels des miroirs de Bragg. Cela permet d'augmenter rapidement le coefficient de réflexion des miroirs sans toutefois en augmenter trop la complexité: une finesse de 215 est, par exemple, attendue à 320 μm pour un FP utilisant des miroirs Si/vide/Si. Ensuite, nous avons étudié le couplage détecteur/FP qui se voit renforcé par la résonance des deux cavités optiques formées par le système complet. Enfin, des calculs ont montré qu'un FP avec une finesse raisonnable (~ 150) mis dans le plan focal ne dégrade que très peu l'imagerie et la spectroscopie.

A la fin de cette thèse, plusieurs étalons FP ont été réalisés et ont déjà démontré des propriétés intéressantes: une résolution spectrale de 180 a notamment été obtenue. En plus de cela, les mesures ont montré que le silicium avait une absorption négligeable à 77 K.

Title : "On-chip" astronomical instrumentation: bringing polarimetric and spectroscopic capabilities to the detector level

Keywords : detectors, polarization, spectroscopy

Abstract : This thesis assesses the potential of gathering several instrumental functions into a bolometer array for sub-millimetric astronomical observations. This possibility is now conceivable thanks to the recent progress made in micro-technologies.

First, we optimized the design of polarimetric pixels invented for the B-BOP instrument of the future space observatory SPICA. This work enabled the quantification of the cross-polarization (1/1000) and to rethink the geometry of the pixels in order to obtain detectors better matched to incident radiation.

This thesis has also been an opportunity to deal with the integration of spectroscopy within the focal plane, independently from the polarimetry aspect. We accordingly focused on Fabry-Perot (FP) interferometry, as an FP in a collimated beam can be well-suited for imaging. Nonetheless, we chose to integrate the spectrometer closer to the detector (and thus in the convergent beam). We also initiated the development of an FP

made from high-resistivity silicon (Si) in order to lower the losses due to metallic mirrors, generally used in this range of wavelengths. With the objective to enhance the spectral capabilities of the FP, mirrors are built as a stack of silicon layers, separated by vacuum (Bragg mirrors). This increases the reflectivity of the mirrors while keeping the complexity to a reasonable level : a finesse of 215, for instance, is expected at 320 μm for a FP using Si/vacuum/Si mirrors. As a next step, we studied the detector/FP coupling which is enhanced by the resonance of two optical cavities formed by the whole system. Eventually, calculations showed that an FP with a moderate finesse (~ 150) put in the focal plane barely deteriorates imaging or spectroscopy.

By the end of this thesis, several FP etalons have been built and have already demonstrated favorable properties: we obtained a spectral resolution of 180. Moreover, measurements showed that silicon has a negligible absorption at a temperature of 77 K.

